Swansea University
Prifysgol Abertawe

Design of Ancillary Services for Battery Energy Storage Systems to Mitigate Voltage Unbalance in Power Distribution Networks

By
Ioannis Mexis

Submitted to Swansea University in fulfilment of the requirements for the Degree of Doctor of Philosophy

Department of Electronic and Electrical Engineering
Swansea University

January 2023

Abstract

In light of the increasing penetration of single–phase loads and generation in the power system, voltage unbalance issues are expected to exacerbate. Single–phase connected photovoltaic (PV) panels may cause unequal three–phase power flows, resulting in unbalanced grid currents and voltages. In addition, the random charging behaviour of Plug–in Hybrid Electric Vehicles (PHEVs) equipped with single–phase on–board chargers is expected to further contribute to voltage unbalance rise as the number of these devices grows. If voltage unbalance increases to unacceptable levels, it may have adverse effects on power system operation and on the equipment connected to it. Traditionally, the phase swapping technique has been deployed by distribution system operators for voltage unbalance mitigation, while other mitigating techniques include the deployment of power electronics-based devices. The majority of the devices reported in the literature are based on three-phase configurations, including series and parallel active power filters, unified power quality conditioners (UPQCs), static synchronous compensators (STATCOMs) and, more recently, three-phase distributed generation (DG) inverters.

This research proposes the use of single-phase battery energy storage systems (BESSs) for the provision of phase balancing services, which has been considered only in a few literature works, with most of these research papers focusing on three-phase BESSs. In this thesis, a novel control strategy is proposed for single-phase BESS units to compensate voltage unbalance by injecting both active and reactive power simultaneously. The proposed approach is based on the coordinated operation of three independent single-phase BESS inverters using local voltage and current measurements.

Initially, a comprehensive literature review is performed with the following aims: a robust classification of the ancillary services currently offered by BESSs, harmonisation of the notation found in the literature for ancillary services, and identification of potential future applications of BESSs to power grids with large number of Low Carbon Technologies (LCTs). Then, the effectiveness of the proposed voltage unbalance compensation method is validated in the simulation environment, where two realistic models of distribution systems are developed. Next, the impact of increasing PV and EV penetration levels on voltage unbalance for a typical UK distribution system is assessed based on a deterministic approach. The control strategy is validated experimentally by carrying out Hardware-In-The-Loop (HIL) tests. Finally, an equivalent model of the distribution system and BESS inverter is derived, which allows to carry out a preliminary probabilistic study to cater for the uncertainties related to the location and size of the PVs and EVs, and to evaluate the voltage unbalance levels without and with the BESSs controlled to provide voltage unbalance compensation.

It is concluded that the proposed BESS control system may effectively reduce the voltage unbalance levels under various loading and generating conditions.

Declarations

This work has not previously been accepted in substance for any degree and is not being concurrently submitted in candidature for any degree.

Signed: [redacted]

Date: 24/01/2023

This thesis is the result of my own investigations, except where otherwise stated. Other sources are acknowledged by footnotes giving explicit references. A bibliography is appended.

Signed: [redacted]

Date: 24/01/2023

I hereby give consent for my thesis, if accepted, to be available for electronic sharing.

Signed: [redacted]

Date: 24/01/2023

The University's ethical procedures have been followed and, where appropriate, that ethical approval has been granted.

Signed: [redacted]

Date: 24/01/2023

Contents

List of Figures

List of Tables

List of Symbols[1]

Symbol	Unit	Definition
$\boldsymbol{\alpha} = e^{j\frac{2\pi}{3}}$		Fortesque operator
$\alpha\beta 0$		$\alpha\beta 0$ stationary reference frame
abc		abc stationary reference frame
C_f	[F]	Capacitance of the inverter output filter
$dq0$		$dq0$ rotating reference frame
f_s	[Hz]	Sampling frequency
f_{sw}	[Hz]	Switching frequency
i_{gx}	[A]	Current of phase-x inverter
$i_{g\alpha}, i_{g\beta}$	[A]	Inverter current in the $\alpha\beta 0$ stationary reference frame
$\boldsymbol{I_{fx}}$	[A]	Feeder current phasor at phase-x
$\boldsymbol{I_{x,ref}}$	[A]	Reference current phasor of phase-x inverter
$\boldsymbol{I_{f1}}$	[A]	Positive-sequence component of phase-a feeder current
$\boldsymbol{I_{f2}}$	[A]	Negative-sequence component of phase-a feeder current
$\boldsymbol{I_{f0}}$	[A]	Zero-sequence component of phase-a feeder current
i_{fx}	[A]	Feeder current at phase-x
$v_{g\alpha}, v_{g\beta}$	[V]	Inverter terminal voltage in the $\alpha\beta$-stationary reference frame
ω_0	[rad/s]	Fundamental frequency
$\ell_o, \ell_{cb1}, \ell_{cb2}$	[m]	Lengths of overhead lines and cables
L_f	[Ω]	Inductance of the inverter output filter
$P_{x,ref}$	[W]	Reference active power of phase-x inverter
P_{fx}	[W]	Active power of phase-x load
p_x	[W]	Active power of phase-x inverter
Q_{fx}	[var]	Reactive power of phase-x load
$Q_{x,ref}$	[var]	Reference reactive power of phase-x inverter
q_x	[var]	Reactive power of phase-x inverter
R_f	[Ω]	Resistance of the inverter output filter
S_k	[VA]	Short-circuit power
$S_{x,ref}$	[VA]	Reference apparent power of phase-x inverter
T_s	[s]	Sampling time
V_{dc}	[V]	DC voltage

[1] Bold font is used to represent phasor quantities. Lowercase and uppercase letters are used to represent instantaneous and constant values of voltage, current and power, respectively. The subscript x is equal to $x = \{a, b, c\}$.

v_{gx}	[V]	Voltage of phase-x inverter
$\boldsymbol{V_{gx}}$	[V]	Voltage phasor of phase-x inverter
$\boldsymbol{V_{gx1}}$	[V]	Positive-sequence component of phase-x inverter voltage
$\boldsymbol{V_{gx2}}$	[V]	Negative-sequence component of phase-x inverter voltage
$\boldsymbol{V_{gx0}}$	[V]	Zero-sequence component of phase-x inverter voltage
V_n	[V]	Nominal voltage

Acronyms

AC	Alternating Current
AD	Anderson-Darling
ADC	Analogue-to-Digital Converter
AF	Active Filter
BESS	Battery Energy Storage System
CPU	Central Processing Unit
DC	Direct Current
DERs	Distributed Energy Resources
DG	Distributed Generation
GI	Generalized Integrator
HRTIM	High Resolution Timer
IEC	International Electrotechnical Commission
IGBT	Insulated-gate bipolar transistor
I/O	Input/Output
LPF	Low Pass Filter
NEMA	National Equipment Manufacturer's Association
OSG	Orthogonal Signal Generator
PCC	Point of Common Coupling
PD	Primary Distribution
PEVs	Plug-in Electric Vehicles
PI	Proportional Integral controller
PLL	Phase Locked Loop
PR	Proportional Resonant Controller
PVUR	Phase Voltage Unbalance Rate
PWM	Pulse Width Modulation
SD	Secondary Distribution
SOGI	Second Order Generalized Integrator
STATCOM	Static Synchronous Compensator
SVC	Static Voltage Compensator
TF	Transfer Function
UPQC	Unified Power Quality Conditioner
VCO	Voltage Controlled Oscillator
VSI	Voltage Source Inverter
XHP	eXtra High Performance

Acknowledgements

Firstly, I would like to express my deepest gratitude to Dr. Grazia Todeschini, who was my supervisor in the first two years of my PhD, for giving me the opportunity to study a PhD. I could not have undertaken this journey without her continuous guidance and consistent support. Her wealth of technical knowledge, meticulous editing of my manuscripts and encouraging words ensured the quality of my research work, but also helped me grow both on a personal and professional level.

Additionally, I would like to express my sincere thanks to Dr. Zhongfu Zhou, who was my supervisor during the last year of my PhD, for his enthusiasm and our extensive discussions, which helped me develop a better understanding of the subject. His valuable technical suggestions were crucial towards the improvement and completion of my work. I would like to extend my thanks to my third supervisor, Professor Mike Jennings.

I am also grateful to the members of the thesis committee, Professor Li Ran and Professor Karol Kalna, for their constructive feedback and suggestions that resulted in significant improvement of my work.

Special thanks go to the faculty, staff, colleagues and students from the Electronic and Electrical Engineering Department for having provided a supportive and friendly environment where I was able to work efficiently and serenely.

Most importantly, I would like to express my deepest gratitude to my family for their unconditional and continuous love and support.

Chapter 1

Introduction

1.1 Overview of battery energy storage in power systems

Modern power systems are characterised by the proliferation and penetration of distributed energy resources (DERs), which have been causing a transition from centralised to decentralised energy generation. In the last decade, an increasing number of these resources, such as photovoltaic (PV) distributed generation and plug-in electric vehicles (PEVs), has been deployed in distribution networks worldwide. This trend is expected to continue and to further accelerate in order to meet Net Zero targets set by a number of countries worldwide.

The introduction of PEVs results in increased flexibility to the load patterns, while PVs can provide carbon free electricity generation [3], [4]. Despite the potential benefits of these technologies, their adoption introduces a series of technical and economical challenges. One of the most prominent issues is the difficulty to maintain power balance between electricity generation and consumption, which becomes more challenging to achieve due to the inherent intermittency of renewable energy sources (RESs) [4].

Another issue to be considered is voltage regulation. For example, reverse power flow may occur upstream of the PV units during periods of high PV generation and low demand, therefore resulting in overvoltages at different nodes of the network, and increasing the number of operations of switched shunt capacitor banks, load tap changers and line voltage regulators, thereby reducing the reliability of these devices [5], [6].

Finally, the integration of power-electronics based devices threatens to degrade the power quality, since they inject harmonic components in the grid [7], [8]. Among others,

the retirement of fossil–based plants becomes an increasing concern for system operators, since it leads to the decrease of the system inertia [9].

In the context of these challenges, energy storage systems are expected to support the integration of high levels of variable renewable generation and different load schemes, since they are capable of decoupling the timing of generation and consumption [3]. Electrochemical energy storage systems, otherwise known as battery energy storage systems (BESSs), are gaining significant attraction for applications in power systems due to their valuable characteristics, including fast response time, scalability and modularity [3], [10], [11]. In addition to acting as an energy buffer and mitigating the mismatch between generation and demand, BESSs have the capability of providing numerous ancillary services [10], [12].

The term 'ancillary services' refers to a variety of control algorithms that allow providing support to the electrical power system with the aim of ensuring the secure and reliable transmission of power to the customers [13], [14]. Their importance has grown in the last few years due to the increased penetration of distributed generation. Among others, they include voltage support, frequency regulation, transmission congestion relief and peak shaving [15].

BESSs have been used to provide ancillary services at various voltage levels for different stakeholders, which include power system operators, utilities and residential customers. For example, BESSs are used to store excessive generation from RESs; they are deployed at customers' facilities by acting as 'emergency supply'; they are used to defer network upgrade or in energy arbitrage applications [3], [13], [16]. In addition to the aforementioned services, there is a significant potential to expand the use of BESSs to additional emerging applications, including harmonic mitigation and provision of synthetic inertia [9], [17], [18].

Considering more specifically the UK power grid, an increasing deployment of low carbon technologies (LCTs), i.e. PVs, EVs, heat pumps (HPs) and other smart appliances (SAs) at distribution level is expected in the next decades in order to reach the UK government's Net Zero target by 2050. Based on the projections published by the UK Electricity System Operator (ESO), the amount of distributed generation in the UK will continue to experience a steady growth in the future. At the same time, electrification of transportation and heat will lead to a significant increase in load levels [19]. Simultaneously, a large number of BESSs have already been installed in the UK, and they are utilised in a wide variety of ancillary services. However, due to the expected changes in the energy generation and demand patterns, there is a potential for a significantly larger number of installations and new areas of applications.

A potential area of application for BESSs is their deployment for voltage unbalance

compensation. Voltage unbalance levels are expected to increase in future power grids, mostly due to the cumulative large power rating and the variable output of single-phase loads and generating units (such as PEVs and distributed generation), which are deployed to the distribution system at an increasing rate during the last years. High levels of voltage unbalance can cause detrimental effects including equipment ageing and outages [1]. Among the main concerns for the distribution system operators are voltage band management across the three phases, neutral conductor overloading and transformer overheating due to zero-sequence fundamental currents. In addition, the flow of unbalanced currents may lead to higher network losses and reduce the effective utilization of the distribution line capacity.

One common mitigating solution to voltage unbalance consists in maintaining load symmetry on the three phases by phase swapping, but this approach may not be possible in systems with large penetration of single-phase equipment [3]. Alternatively, active compensation equipment can be installed in the distribution system, i.e. power electronics-based devices controlled to inject active and reactive power to compensate voltage unbalance. These include wind/solar inverters and dedicated power quality devices, e.g. static synchronous compensator (STATCOM). Despite the potential benefits of using BESSs for voltage unbalance compensation, due to their declining prices, flexibility to control both active and reactive power (four-quadrant operation) and relatively stable DC voltage, such application is a relatively unexplored research area. Only a few literature works consider using BESSs for providing phase balancing services, and most of these research papers focus on three-phase BESSs.

1.2 Research objectives

The aim of this research is to investigate the application of BESSs for voltage unbalance compensation. More specifically, the focus is placed on the use of single-phase BESSs, which are deployed in the distribution system, and they are controlled to compensate voltage unbalance by injecting and absorbing both active and reactive power. The proposed control strategy can be implemented as ancillary service, in addition to other functions such as, for example, load balancing.

Based on the increasing number of disruptive single-phase loads and generating units connected to the distribution grid, voltage unbalance may increase to levels above the regulatory limits at distribution networks in the future. New connections of the aforementioned devices make the phase unbalance conditions to be more variable over time, thus rendering the deployment of active mitigating techniques more suitable to ensure that voltage unbalance levels do not violate the limits defined in the relevant standards.

In this context, the proposed use of the BESSs has many practical implementations in distribution networks, since they can be deployed to provide phase balancing services during periods of high voltage unbalance, while performing load balancing during periods when voltage unbalance is not an issue. For this purpose, the single-phase BESS units can be connected either at the substation or at other busbars along the distribution feeder. Although it is identified that the proposed control strategy can be deployed to other assets including energy storage, such as EVs, this research focuses only on voltage unbalance mitigation for stand-alone battery units.

The main research objectives were set as follows:

1. Perform a comprehensive literature review on BESS technology and its applications in power systems, and identify potential future developments, with the focus placed in the UK electricity grid. Revise the literature on state-of-the art voltage unbalance compensation strategies.
2. Develop a novel control system for single-phase BESSs to mitigate voltage unbalance in realistic distribution systems characterized by varying penetration of PVs and EVs.
3. Develop realistic distribution system models using real load, PV and EV data.
4. Perform numerical validation of the developed voltage unbalance mitigation strategy in the simulation environment.
5. Perform experimental validation of the proposed control strategy by Hardware-In-The-Loop (HIL) experiments.
6. Evaluate the impact of increasing penetration of PVs and EVs on voltage unbalance in the distribution system, and compare the voltage unbalance levels without and with the BESSs controlled to mitigate voltage unbalance.

1.3 Thesis original contributions

The main contributions of this thesis are summarised as follows:

1. Potential future applications of BESSs relevant to the UK electricity network and more in general to power grids with large numbers of LCTs have been identified; a robust classification of the ancillary services currently offered by BESSs has been carried out, and the notation found in the literature has been harmonised; a classification suitable for the UK was identified.
2. A voltage unbalance compensation strategy based on the coordination of three single-phase BESS inverters to mitigate voltage unbalance by independently controlling both their active and reactive power has been developed.

3. The performance of the developed control scheme has been evaluated considering two realistic distribution network models, which are built based on the configuration, parameters, loads and LCTs corresponding to typical European distribution networks, such as those found in the UK and in Germany. Both these networks were used to validate the proposed voltage unbalance mitigation strategy due to data availability. Various BESS locations along the feeders were tested to carry out a sensitivity analysis and examine the impact of varying location on the voltage unbalance factor, transformer neutral current and BESS size.
4. Experimental validation of the proposed voltage unbalance compensation strategy via HIL experiments has been carried out.
5. Assessment of the impact of increasing penetration of PV and EV profiles on voltage unbalance for typical UK distribution systems has been performed. The above objective was fullfiled by realizing simulations based on a deterministic approach.
6. The conclusions of the deterministic simulations were reinforced by a preliminary statistical analysis that caters for the uncertainties related to the location and size of the PVs and EVs. To this end, a simple yet effective model has been developed to allow for running the probabilistic simulation scenarios with the aim to evaluate the voltage unbalance levels without and with the BESSs controlled to provide voltage unbalance compensation.

1.4 Thesis outline

This thesis is organized as follows:

Chapter 1: A general overview of the role and applications of battery energy storage systems in power systems is provided. The objectives of the present research are explicitly stated, followed by the description of the original contributions of the thesis. Finally, a list of the publications carried out during the period of the PhD studies is provided.

Chapter 2: This chapter presents a brief literature review on the BESS technologies and their applications in power systems. The main BESS projects in the UK are presented and classified. Additionally, a classification of the most commonly deployed ancillary services is carried out. A detailed review on the topic of voltage unbalance is carried out, and the focus is placed on the systematic recording of both existing and potential mitigating solutions. The BESS model is presented.

Chapter 3: The developed voltage unbalance compensation strategy is introduced. The inverter control system developed to regulate the active and reactive power of each BESS is analysed.

Chapter 4: Deterministic validation of the proposed control scheme is carried out

by means of simulations. First, a network with a single feeder is modelled, and static three-phase loads are applied to test the effectiveness of the voltage unbalance mitigation strategy under various load distributions and for varying number of BESSs; second, a distribution network model based on typical values of German distribution systems is built. Realistic single-phase load demands are modelled, and the effectiveness of the control scheme is evaluated for different locations within the distribution system.

Chapter 5: Deterministic validation of the proposed control strategy is performed by building a typical UK distribution system model based on realistic network parameters, load, PV and EV profiles found in the literature. Different locations within the distribution system are examined for the BESS units, which are controlled to perfom voltage unbalance mitigation. Additionally, a deterministic assessment of the impact of increasing PV and EV penetration levels on voltage unbalance is carried out.

Chapter 6: Hardware-In-The-Loop (HIL) experiments are carried out to validate the control algorithm in real-time using the OPAL-RT simulation platform.

Chapter 7: A probabilistic study is carried out with the aim to assess the impact of the PV and EV profiles on voltage unbalance in the distribution system. A Current Source-based model is developed, and different probabilistic scenarios are simulated with the aim to evaluate and compare the voltage unbalance levels without and with the BESS controlled to provide voltage unbalance compensation.

Chapter 8: Finally, the main contributions and achievements are summarised, followed by recommendations for future work on the subject of voltage unbalance mitigation by single-phase BESS units.

1.5 List of publications and other activities

Journal Articles:

1. I. Mexis, G. Todeschini, Z. Zhou, "Coordinated Control of Three Single–Phase BESS Inverters Using Local Measurements to Mitigate Voltage Unbalance," IEEE Transactions on Energy Conversion, vol. 37, no. 4, pp. 2941-2951, Dec. 2022, https://doi.org/10.1109/TEC.2022.3202137
2. Mexis, I.; Todeschini, G. "Battery Energy Storage Systems in the United Kingdom: A Review of Current State-of-the-Art and Future Applications," Energies 2020, vol. 13, no. 14, p. 3616. https://doi.org/10.3390/en13143616

Conference contributions:

1. I. Mexis, G. Todeschini, F. Möller and J. Meyer, "Mitigation of Voltage Unbalance in Rural Low Voltage Networks Using Single-phase BESS Inverters," CIRED 2021 - The 26^{th} International Conference and Exhibition on Electricity Distribution, 2021, pp. 789-794, https://doi.org/10.1049/icp.2021.1998
2. I. Mexis and G. Todeschini, "Voltage Unbalance Mitigation by Novel Control of BESS Single–phase Inverters," 2020 IEEE PES Innovative Smart Grid Technologies Europe (ISGT-Europe), 2020, pp. 146-150, https://doi.org/10.1109/isgt-europe47291.2020.9248770

Poster presentations:

1. I. Mexis, G. Todeschini, "Voltage Unbalance Mitigation in Distribution Networks Using Single-Phase BESS Inverters," 2021 IEEE Power and Energy Society General Meeting, Virtual Event, 26-29 July 2021.

Panel presentations:

1. I. Mexis, "Deployment of single-phase BESS inverters for voltage unbalance mitigation in distribution systems with high penetration of low-carbon technologies," Panel session: Power quality assessment for networks with high penetration of renewable energy sources, 2022, 12-15 June, Online, 17^{th} International Conference on Probabilistic Methods Applied to Power Systems (PMAPS). https://www.pmaps2022.org/presentation-slides/

Chapter 2

Literature Review

2.1 Introduction

The aim of this chapter is to provide a comprehensive literature review around the topic of Battery Energy Storage[1]. First, projects that have been implemented in the UK up to date are presented, followed by a brief description of the main BESS technologies used in these projects. A classification of the most commonly deployed ancillary services is implemented, and a detailed discussion around the topic of voltage unbalance is carried out, including a description of its causes, consequences, as well as of state-of-the-art and emerging mitigating solutions. The chapter closes with a presentation of the BESS model used to carry out the simulation studies on voltage unbalance mitigation.

2.2 BESS projects in the UK

A list of BESS projects installed in the U.K. is provided in Table 2.1, based on the U.K. Renewable Energy Association (REA) and the United States Department of Energy (DOE) database [20, 21]. Only projects under operational status are included, while projects that are either announced, contracted or under construction are not listed. Table 2.1 mainly focuses on projects installed at voltages above 3.3 kV. Based on these criteria, at the moment of this writing (January 2023), twenty-four BESS projects have been identified, for a total installed power equal to approximately 25.5 MW.

The projects are listed by decreasing rated power, and for each project, location, technology adopted, ancillary service(s) provided and rated voltage are shown. The abbreviations used in the table are listed in the Acronyms section of the thesis. In Table

[1]The majority of the work presented in this chapter has been published in [1].

2.1, the distinction between primary and secondary distribution is based on the definition provided in [22]. Thus, the term "primary distribution" (PD) implies that $V > 33$ kV, while the term "secondary distribution" (SD) is used when the voltage level is $V \leq 33$ kV. BESSs are connected to the grid by means of a transformer: in the table, the rated voltage values refer to the high side of the transformer, corresponding to the point of connection (PoC).

Based on the ratings shown in Table 2.1, the majority of the projects is installed at voltages below 33 kV. This is mostly due to the cost of BESSs with increasing voltage levels. Additionally, the majority of DERs are installed at voltages below 33 kV, thus making demand response management more challenging at low voltages and justifying the connection of the battery units.

Among the projects, the most significant ones are shortly described below, while more details can be found in the references provided:

Project 1 is the largest battery energy storage facility in the U.K. and Ireland, installed within Kilroot coal-fired generation plant, with the aim of providing frequency regulation for the Irish electricity system (including both Ireland and Northern Ireland), which is characterised by high penetration of onshore wind energy [38].

Project 2 is the Smarter Network Storage project, which aims at investigating various capabilities and revenue streams of BESSs. To this end, a 6 MW/10 MWh BESS is deployed in a 33/11 kV primary substation in Leighton Buzzard [23].

Projects 3, 11, 12, 15, 16 and 17 are part of the Northern Powergrid's Customer-Led Network Revolution (CLNR) project, which aims at assessing the potential for new network technologies and flexible customer response. For this purpose, six battery storage units are connected at three different locations, representing different grid conditions, with the placements offering a representative sample of 80% of the entire U.K. power grid. The provided services include voltage support, electric energy time shift and stationary transmission/distribution upgrade deferral [24, 25].

Project 4 has been funded by the Engineering and Physical Sciences Research Council with the aim to investigate the potential of Li-ion titanate batteries for frequency regulation services. Therefore, BESSs of 2 MW are connected to the 11 kV Western Power Distribution's Willenhall substation [21].

Project 5 refers to the use of BESS for alleviating network constraints that are limiting the number of generators able to connect to the distribution network. To this end, Li-ion BESSs of 2 MW are connected to the 33 kV distribution grid of Orkney island to facilitate the penetration of renewable generation and defer further network investments [28, 29].

Project 6 is of particular interest, since it refers to the deployment of a BESS at the Hywind offshore wind farm in Scotland, which constitutes the world's first floating wind

Table 2.1: Transmission and distribution BESS projects in the U.K.

No	Location	Technology	Rated Power (kW)	Service Provided	Voltage Level
1	Carrickfergus, Northern Ireland	Li-ion	10,000	Frequency regulation	TR, V = 275 kV
2	Leighton Buzzard, England [23]	Li-ion	6000	Electric energy time shift, Frequency regulation Electric supply reserve capacity, Spinning reserve TS/DS upgrade deferral	SD, V = 11 kV
3	Rise Carr, England [24, 25]	Li-ion	2500	Voltage support, Electric energy time shift TS/DS upgrade deferral	SD, V = 6.6 kV
4	Wolverhampton, England [21, 26, 27]	Li-ion titanate	2000	Frequency regulation, Power reliability Power quality enhancement	SD, V = 11 kV
5	Kirkwall, Scotland [28, 29]	Li-ion	2000	Transmission congestion relief	SD, V = 11 kV
6	Peterhead, Scotland [30]	Li-ion	1000	Renewables capacity firming	SD, V = 33 kV
7	Dorset, England	Li-ion	598	Electric supply reserve capacity, Spinning reserve On-site renewable generation shifting, Renewables capacity firming	SD, V = 11 kV
8	Butleigh, England [31]	Li-ion	300	Electric bill management, Electric energy time shift Renewables capacity firming, Renewables energy time shift	SD, V = 11 kV
9	Berkshire, England	Li-ion	250	On-site renewable generation shifting Renewables capacity firming	SD, V = 11 kV
10	Milton Keynes, England [32, 33]	$NaNiCl_2$	250	TS/DS upgrade deferral, Voltage support Spinning reserve, Electric supply reserve capacity, Transmission congestion relief	SD, V = 11 kV
11	Rise Carr, England [24, 25]	Li-ion	100	Voltage support, Electric energy time shift TS/DS upgrade deferral	SD, V = 6.6 kV
12	Denwick, England [24, 25]	Li-ion	100	Voltage support, Electric energy time shift TS/DS upgrade deferral	SD, V = 20 kV
13	Slough, England [34]	Li-ion	75	Renewables energy time shift Renewables capacity firming	SD, V = 0.24 kV
14	Isle of Eigg, Scotland [35, 36, 37]	P_bA_c	60	On-site renewable generation shifting, Frequency regulation, Voltage support, Electric supply capacity	SD, V = 3.3 kV
15	Rise Carr, England [24, 25]	Li-ion	50	Voltage support, Electric energy time shift TS/DS upgrade deferral	SD, V = 6.6 kV
16	Wooler, England [24, 25]	Li-ion	50	Voltage support, Electric energy time shift TS/DS upgrade deferral	SD, V = 20 kV
17	Maltby, England [24, 25]	Li-ion	50	Renewables capacity firming, Renewables energy time shift, TS/DS upgrade deferral	SD, V = 0.23 kV
18	Isle of Muck, Scotland [37]	P_bA_c	45	On-site renewable generation shifting Electric supply capacity	SD, V = 3.3 kV
19	Isle of Rum, Scotland [37]	P_bA_c	45	On-site renewable generation shifting Electric supply capacity, Renewables energy time shift	N/A
20	Isle of Foula, Scotland [37]	P_bA_c	16	On-site renewable generation shifting Renewables energy time shift	SD, V = 3.3 kV
21	Horse Island, Scotland [37]	P_bA_c	12	Renewables capacity firming, Electric supply capacity On-site renewable generation shifting	N/A
22	Flat Holm Island, Wales	P_bA_c	5	On-site renewable generation shifting Electric supply capacity, Renewables energy time shift	N/A
23	Wokingham, England	VRF	5	Electric energy time shift Renewables energy time shift	N/A
24	Cardiff, South Wales	Li-ion	2	Electric bill management	N/A

Table 2.2: List of ancillary services provided by BESSs for the projects included in Table 2.1.

Service No.	Service Name
1	Voltage support
2	Frequency regulation
3	Load following
4	Electric supply reserve capacity
5	Black start
6	Renewable capacity firming
7	Electric energy time shift
8	Load levelling
9	Peak shaving
10	Electric supply capacity
11	TS/DS upgrade deferral
12	Transmission congestion relief
13	Power quality enhancement
14	Power reliability
15	Electric bill management

farm [21]. As detailed in [30], this project presents major opportunities in a wide range of applications, including: capture of wind overshoots, reduction of balancing costs, increase of power market value, and other ancillary services.

Projects 7 and 9 are related to the installation of 250 kWh commercial-scale Li-ion BESS units within solar farms, showing that battery units have the potential to support the effective utilization of solar power and to foster its penetration to the generation mix [21].

Project 8 constitutes one of the first industrial-scale BESS facilities in the U.K., with a 300 kW/640 kWh Li-ion BESS being connected to a solar farm in Somerset. One of the aims of the project is to raise awareness on the potential benefits from the deployment of BESSs at the industrial scale among investors and developers. Furthermore, these systems can be utilised by the local distribution system operator (Western Power Distribution) with the aim of enhancing the network power quality [31].

Project 10 refers to five 50 kW/100 kWh BESS units, installed in one of Western Power Distribution's substations, with the focus being placed on investigating the use of BESSs for deferral of grid investments, and evaluating the use of smaller distributed units across the network against single units deployed at a specific location [33, 32].

Project 13 is the first project funded by the Low Carbon Networks Fund that locates the BESS units close to the residential customers, rather than at the substation [34].

Projects 14, 18, 19, 20, 21 and 22 are installed in remote islands, and are functional to

the development of renewable-powered microgrids (MGs). The objective of these projects is to reduce the reliance on diesel generators and smooth renewable generation. The services provided by the BESS units include: time shifting of the excess energy generated by RESs during low demand times to high demand times, and electric supply capacity [36, 37].

Projects 23 and 24 are customer-owned, and they refer to the use of batteries together with PV systems to achieve time shifting of renewable energy and to reduce the electric bill, with the customer in Project 24 being the first British owner of a Tesla Powerwall.

Regarding the battery technology, lithium-ion is the most deployed, followed by the more mature technology of lead-acid, whereas three of the projects differentiate from this trend, featuring the technologies of Li-ion titanate, vanadium redox flow (VRF) and sodium-nickel-chloride [39, 40]. A description of the characteristics of each technology will be given in Section 2.3.

BESSs have been utilised for the provision of a wide variety of ancillary services [20, 21] that are listed in Table 2.2. These services will be classified in Section 2.4, and the numbering used in Table 2.2 will be referred to in this section to provide the location of each application within the power system.

2.3 BESS technologies

For power system applications two parameters are commonly used to characterise BESS units. The first is the power capability (W), shown in Table 2.1, corresponding to the rate at which energy can be transferred to or from the battery (this quantity is also referred to as "rated power flow"). The second is the amount of energy that can be stored in the device, or capacity (Wh). These two parameters are not independent of each other: optimising the design in terms of power-to-energy ratio to meet the needs of a specific application (power or energy) leads to more cost-effective solutions [41].

Both characteristics depend on the battery chemistry, and therefore as part of this literature review, the most popular BESS technologies are presented. While a large variety of technologies for rechargeable batteries are available for grid applications, this work focuses on the ones deployed for the projects presented in Table 2.1: lead-acid, lithium-ion, sodium nickel chloride and vanadium redox flow. In this thesis, a summary of the advantages, disadvantages and research trends for these technologies is provided, while a more detailed description of the above can be found in the work published by the author in [1]. Subsection 2.3.1 provides a brief description of the aforementioned battery technologies, while their advantages, disadvantages and technical characteristics are summarized in Subsection 2.3.2.

2.3.1 Battery technologies deployed in the UK projects

- Lead-acid: Lead-acid is the most mature battery technology, featuring low cost and dominating in applications where low energy density and limited life cycle are not an issue [42, 43]. However, their low cycling capability (or short cycle number) may have a negative impact on the economics of the interconnected system in utility applications. Based on [44], there is high potential for the advanced lead-acid batteries to provide improvements in terms of energy density and life cycle.

- Lithium-ion: During the last years, lithium-ion batteries have undergone an increasing deployment in stationary installations, driven by the significant experience gained from their development in other types of applications, such as electric and hybrid vehicles [45, 46]. They feature the highest energy density, thus offering a huge potential for deployment in a wide range of energy storage systems [47]. Other advantages are their high power density and efficiency, long cycle numbers, low discharge rate as well as no-memory effect [10, 48, 49, 50]. One of the main issues for Li-ion is the heating of their internal resistance, which can cause battery's failure, therefore overcurrent and overvoltage systems should operate in parallel to ensure appropriate protection, leading to increased battery's cost [49], [51]. Besides, there are known concerns regarding the availability of adequate resources for large-scale energy storage applications [46]. Improvements to the basic configuration have been obtained by adding fibre and nano-composite improvements to the anode, thereby achieving higher power, higher reversibility and increased life cycle, while the use of solid electrolytes and electrolyte salts has reduced the acidity and the safety risks [46]. Advanced lithium energy storage systems can increase the energy density, due to the use of nanowire silicon in the anode [51, 52, 46].

- Vanadium redox flow: Vanadium redox flow (VRF) batteries are the most widely employed flow batteries. They differ from conventional batteries in terms of storing process, since they utilise two external tanks for the storage of the electrolyte, which is pumped through the electrochemical cells during the process of charging and discharging.[10, 53]. Their advantages include: large number of cycles, flexibility in the design of power and energy capacities, low standby losses and simple cell management [10, 54], possibility to provide continuous power with a discharge duration time longer than 24 h, ability to be brought up to full power promptly and high energy efficiency [12, 50, 55]. Additionally, VRF batteries do not cause significant safety and environmental issues, they have low maintenance cost and can be idle for long time periods without losing their storage capacity [56]. How-

ever, VRF batteries are relatively expensive, featuring high capital and running costs [10, 12, 47]. They are more suitable for peak-shaving and energy time-shifting applications, due to the relatively low energy density of the vanadium electrolyte [45, 54, 57]. Significant research effort is put on reducing the cost and on increasing the storage system's power density via the use of thinner and more active reaction felts [45].

- Sodium nickel chloride: Finally, the sodium nickel chloride batteries are characterised by high energy density, long life cycle and are practically maintenance-free [10]. Due to the characteristics of long life cycle, long discharge time and fast response, they are well suited to applications that engage bulk energy storage such as the ones within transmission systems, railway transportation and large renewable energy plants [56]. This claim is further expanded in [58], where the high suitability and compatibility of the electrical characteristic of this battery (e.g., its volumetric and gravimetric energy densities) with large-scale stationary storage is highlighted. Within their drawbacks are their high cost and self-discharge [50]. Their main limitation is the required heat to keep the molten state temperature.

2.3.2 Summary of battery technologies

Table 2.3 summarizes the main advantages and disadvantages of the main battery technologies currently deployed for power systems applications.

Table 2.4 provides a summary of the main characteristics of the technologies described above. The characteristics considered include: power and energy rating, life cycle, life span, efficiency, energy and power density, response and discharge time, energy and power capital cost. For each metric, a range of variability is provided, based on the references listed.

For some characteristics, such as power ratings, there is a clear advantage of some technologies versus others-more specifically, Pb-acid and Li-ion batteries. For other characteristics, such as efficiency, the performance of various technologies is closer, since efficiency values higher than 90% have been reported for all of them. For some other characteristics, such as the energy density of Pb-acid energy storage, a significant variability is observed. This may be due to different manufacturing processes or test conditions.

Based on the results shown in the summary table and the technology review carried out above, one can conclude that BESS energy technology is changing rapidly. Thus, it is likely that in the future more diversified types of batteries will be deployed for transmission and distribution applications, while at the moment the great majority of projects listed in Table 2.1 adopt Li-ion batteries.

Table 2.3: Main advantages and disadvantages of the BESS technologies described in Section 2.3.

Technologies	Advantages	Disadvantages
Pb-acid	mature technology low cost [42, 43] tolerance against misuse [3] low maintenance requirements large storage capacity [10, 59] spill-proof [56] fast response time low daily self-discharge rate [12]	bulky (low energy density and specific energy [49]) increased cost under low temperature operation [12] reduced lifespan at prolonged discharged state [60, 61] low cycling capability low DOD [56] hazardous for the environment [59, 51, 50, 62]
Li-ion	high energy density [47] high power density high efficiency long life cycle low discharge rate no-memory effect [10, 48, 49, 50] stable discharge voltage wide operating temperature high cycle efficiency [59] packaging flexibility [63] recyclable lithium oxides and salts [51] high specific energy rapidly decreasing costs excellent charge retention high cell voltages very good performance at low temperatures high DOD [46]	increased cost due to protection circuits and packaging [51] availability [46] safety and environmental issues [48] temperature-dependent life cycle [12, 52]
VRF	long life cycle flexible design of power and energy capacity [52] low standby losses simple cell management [10, 54] high energy efficiency [12], [50, 55] low maintenance cost [56] large storage capacity high power output and energy conversion rate suitability for large-scale energy storage [59] low self-discharge [12] durable performance [52] overcharge tolerance high DOD [51, 64]	high cost large layout high capital and running costs [10, 12, 47] unsuitable for small-scale storage applications [51, 52, 62] low energy density [45, 54, 57]

Table 2.3: *Cont.*

Technologies	Advantages	Disadvantages
$NaNiCl_2$	high energy density long life cycle maintenance-free [10] long discharge time fast response [56, 58] high efficiency [51]	high cost high self-discharge [50] heat required to keep the molten state temperature

Table 2.4: Technical characteristics of the BESS technologies deployed in U.K. projects.

Characteristics/Technologies	Pb-acid	Li-ion	VRF	$NaNiCl_2$
Power rating [MW]	0–50 [46]	0/10–50/100 [11, 60, 50, 46, 65]	0.005/1–1.5/10 [48, 52, 50, 65]	0/0.001–0.3/1 [48, 52]
Energy rating [MWh]	0.1/0.25–50/100 [13, 48]	10^{-5}/4–10/100 [12, 13, 48, 65]	0.01/4–10/40 [48, 65]	0.12–5 [48]
Life cycle [cycles x 10^3]	0.1/0.5–2/3 [46, 66, 67]	0.25/4.5–5/20 [11, 12, 40, 48, 50, 46, 65, 66]	2–5/13+ [12, 40, 48, 52, 50, 65]	2.5/4–4.5 [48, 52]
Life [years]	3/5–15/20 [40, 50, 46, 66]	2/5–15/20 [11, 48, 50, 46, 66]	2/10–15/20 [48, 52, 50, 46]	10–14/15 [48, 52]
Efficiency [%]	70/75–85/92 [50, 66]	70/85–90/100 [11, 48, 52, 50, 46, 65, 66, 67]	60/85–88/90 [48, 52, 50, 46, 65]	85–90 [48, 52]
Energy density [Wh/l]	50–90 [48, 66]	200–500/600 [48, 52, 50]	15/16–33 [12, 48, 50]	150–180 [48, 52]
Power density [W/l]	10–400/700 [48, 46]	1300/1500–10000 [12, 48]	0.5–2 [48]	220–300 [48, 52]
Response time	5–10 ms, ¡1/4 cycle, a few ms [11, 12, 48]	20–1000 ms, ¡1/4 cycle, a few ms [11, 12, 40, 48, 66]	¡1/4 cycle, a few ms [40, 48]	a few ms [48]
Discharge time	a few min –4/20+ h [13, 66]	6 min/2 h–4/5 h [50, 65, 66]	s–8/10 h [48, 52, 50]	s/min–h [48, 52]
Energy capital cost [$/kWh]	200–400 [48, 50]	600/900–1700/2500 [48, 52, 50, 65, 68]	150/750–830/1000 [48, 52, 50, 65]	100/200–500/1000 [48, 52]
Power capital cost [$/kW]	300–600 [48, 50]	1200/1800–4000/4100 [48, 52, 50, 65, 68]	600–1500 [48, 52, 50]	l150/300–400/1800 [48, 52]

2.4 Ancillary services provided by BESSs in power systems

This section summarizes the work carried out in [1], which provides a detailed description of the most common ancillary services provided by BESS projects in the U.K. and presented in Table 2.2. A classification of the ancillary services provided by BESS connected to the transmission and distribution system in the U.K. is presented, and their location within the power system is provided.

Based on the existing literature, the terminology used for ancillary services and their classification varies broadly [69]. A commonly employed approach to classify these services is based on the power rating of the system and the discharge time [70]. Under this

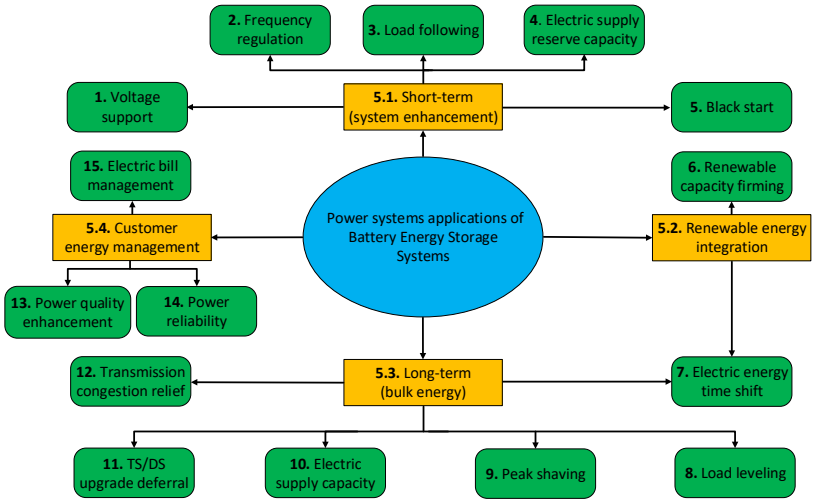

Figure 2.1: Classification of the ancillary services provided by BESSs connected to the transmission and distribution system in the UK [1].

approach, services are divided into power and energy applications, depending on if their discharge duration is less or more than 30 min respectively [71, 67, 72].

In this thesis, an alternative approach is adopted, based on the work presented in [13], because it is deemed more appropriate to categorise the ancillary services provided by BESSs in the U.K. Therefore, ancillary services are divided in four families:

- Short-term (system enhancement): to ensure the stability, robust operation and reliability of the electrical grid via the provision of rapid-response services, responding to small-time scale (seconds to several minutes) fluctuations in generation and demand.
- Customer energy management: to enhance the power quality of a specific part of the grid by mitigating short-term power delivery issues, e.g., supply interruptions and voltage dips.
- Long-term (bulk energy): to boost the system's efficiency and reduce the electricity costs by providing services that operate over a long period of time, which can be several hours.
- Renewable energy integration: to enhance the energy-efficient and cost-effective penetration and operation of RESs into the grid. This can be achieved by smoothing the output and control the ramp rate of RESs in order to eliminate rapid voltage and power swings on the grid. Since this thesis is focused on the U.K., where RESs are gradually overtaking the coal-fired generation, it seems reasonable to consider the renewable energy related applications as a distinct family of applications [3].

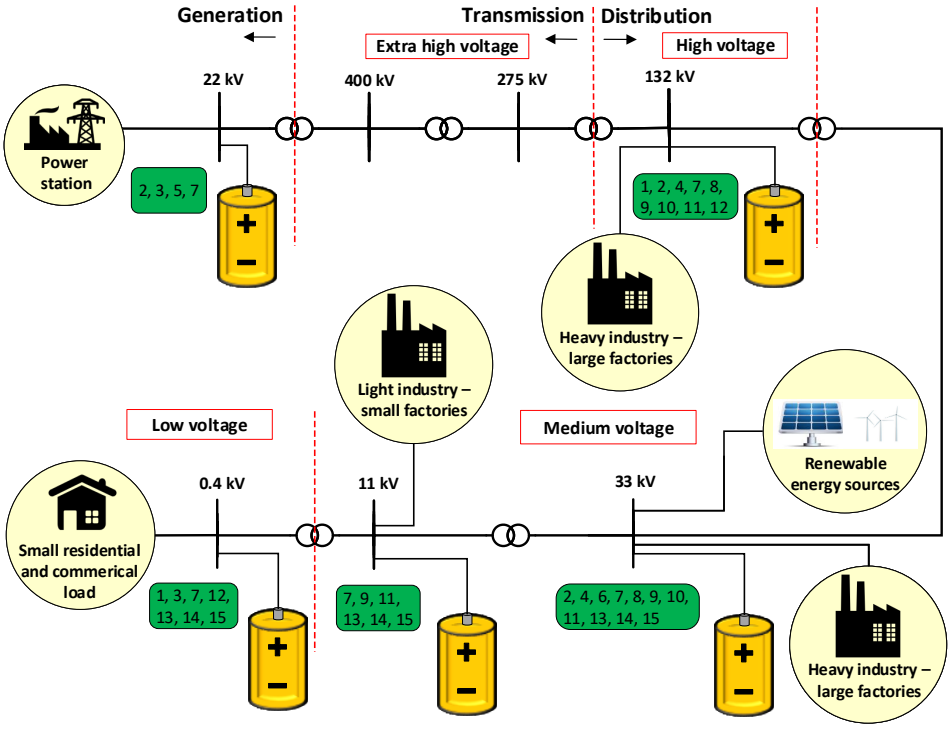

Figure 2.2: Location of each application of BESSs in the electricity supply chain [1].

Figure 2.1 illustrates the four main families of ancillary services listed above. For simplicity, each one of the ancillary services listed in Table 2.2 is associated to one family, although the authors recognise that some services could have been associated to more than a family. A more detailed description of each application family and of the corresponding services is provided in [1].

Figure 2.2 presents a simplified representation of the U.K. electricity network, including electricity generation, transmission and distribution (primary and secondary), interconnected loads and BESS units[2]. The figure illustrates the location of each application within the electrical grid [69, 73]. The different ancillary services are referred to by using the numbers provided in Table 2.2.

Each ancillary service may be deployed at different locations in the power system, although some applications may be more specific for certain voltage levels. For example, electric bill management is expected to be deployed at lower voltage levels, close to the customers. However, the figure highlights the flexibility and wide-spread applications of

[2]In Figure 2.2, the renewable energy sources are connected at the 33 kV busbar. However, in the practice, they can be connected at higher or lower voltage levels in the electricity supply chain.

both BESSs and ancillary services.

2.5 Voltage unbalance mitigation

This section elaborates on the causes and consequences of voltage unbalance in distribution networks. A comprehensive review of the state-of-the-art and emerging mitigating solutions is provided, including both passive and active mitigating techniques; special focus is placed on the literature works referring to voltage unbalance mitigation by means of BESSs.

2.5.1 Definition of voltage unbalance

In a three-phase system, a set of three voltage or current phasors is balanced if the two following conditions apply: the phasors are equal in magnitude and they are shifted symmetrically by a phase angle of 120^o to each other. If one or both of the above conditions do not apply, the phasors (and, consequently, the voltages) are unbalanced. Alternatively, the set of phasors is defined as balanced if it is decomposed only into positive-sequence voltages (currents) [74]. Considering that synchronous generators are designed to provide balanced three-phase voltages, and the amount of unbalance caused by the grid equipment in the MV and HV network level is negligible, voltage unbalance in LV networks is mainly excited due to local causes, as it will be described in Subsection 2.5.2. These include uneven allocation of single-phase loads and presence of single-phase DERs, among others.

The most commonly used metrics for the quantification of voltage unbalance are those defined by the following communities: the Institute of Electrical and Electronics Engineers (IEEE), the International Electrotechnical Commission (IEC) and the National Equipment Manufacturer's Association (NEMA) of the United States [74], [75]. These metrics are slightly different from each other, and will be briefly summarised below.

Based on the IEC definition, voltage unbalance is quantified by the negative–sequence and the zero–sequence voltage unbalance factors (k_{v2} and k_{v0}), defined as the ratio of the negative–sequence ($\boldsymbol{V_2}$) and the zero–sequence ($\boldsymbol{V_0}$) to the positive–sequence voltage fundamental component ($\boldsymbol{V_1}$), respectively [76], [77]:

$$k_{v2} = \frac{|\,\boldsymbol{V_2}\,|}{|\,\boldsymbol{V_1}\,|} \tag{2.1}$$

$$k_{v0} = \frac{|\,\boldsymbol{V_0}\,|}{|\,\boldsymbol{V_1}\,|} \tag{2.2}$$

The IEC definition directly represents the phenomena of interest without approximation, and it is commonly referred to as true unbalance. According to IEC 61000–2–2, the compatibility level for k_{v2} is 2%, although stricter limits may be imposed by some DNOs [74]. Compatibility levels are not provided for k_{v0}.

Phase voltage unbalance rate (PVUR) is used by IEEE, and it is defined as the ratio of the maximum deviation of the phase-to-neutral voltage from the average phase-to-neutral voltage to the average phase-to-neutral voltage:

$$\text{PVUR} = \frac{\Delta V_{ph,max}}{V_{ph,av}} \tag{2.3}$$

The NEMA definition is similar to the IEEE definition, except for using phase-to-phase instead of phase voltages. In the context of this work, the IEC definition is adopted and, since the standards provide guidances for this quantity only, k_{v2} is chosen as the metric to quantify voltage unbalance.

2.5.2 Causes of voltage unbalance in power systems

Generally, domestic customers in the UK are connected to single-phase supply along single-phase laterals, and they are allocated to the three phases unevenly [78], [79]. In addition, a random phase is chosen for a new customer connected to the network, therefore leading to voltage unbalance between the three phases. Even for countries where the customers are connected to three-phase supply, such as in Denmark, the single-phase appliances are not evenly allocated across the three phases, and the phase connectivity is not controlled or known by the network operator [80]. Voltage unbalance can also be excited by unbalanced three-phase loads, such as arc furnaces [81].

Another typical cause of unbalance is the structural asymmetries of the single-phase laterals over the three phases of the grid. The inherent asymmetry of the distribution lines involves asymmetrical self and mutual impedances, therefore giving rise to voltage unbalance across the distribution system [79].

Additionally, voltage unbalance is excited due to random load patterns, even assuming an even allocation of the customers across the three phases. Especially in the last decade, an increasing number of distributed energy resources (DERs), such as photovoltaic (PV) distributed generation and plug-in electric vehicles (PEVs), has been deployed in distribution networks worldwide [1]. This trend is expected to continue and to further accelerate in order to meet Net Zero targets. Since a large portion of these devices is single-phase connected, and given the cumulative large power rating and their variable output, voltage unbalance levels are expected to increase across distribution feeders and at the substations.

Finally, the incidence of unbalanced faults, such as phase-to-phase or phase-to-ground short circuit, single-phase broken-line fault, etc. can excite voltage unbalance [79].

2.5.3 Consequences of voltage unbalance in power systems

The increase of voltage unbalance to unacceptable levels may have adverse effects on power system operation and on the equipment connected to it. A negative impact of voltage unbalance is the waste of network capacity, which leads to increased investment costs both for individual networks and DNOs, as shown in [82], [83]. More specifically, when one of the phases of a three-phase LV feeder is heavily loaded, the investment in network reinforcement will be required earlier compared to the case when all three phases are balanced [84]. Furthermore, under unbalanced current operation, the serviceable loading capacity of distribution transformers and LV cables is decreased, and they cannot be used up to their nominal ratings [74], [81]. Phase unbalance can also be a limiting factor for the connection of distributed generation [85].

Voltage unbalance can additionally lead to the rise of energy losses on the three phases, neutral and ground conductors, both at the transformer and feeder level. As reported in [74], the energy losses induced by phase unbalance constitute a considerable amount of the total losses in the LV network [79].

Furthermore, another negative impact caused by high levels of voltage or current unbalance is the misoperation of the protection relays, which can cause nuisance tripping [74]. Phase unbalance causes the flow of ground currents, which may trip the protection devices, as in the case of a variable-frequency drive (VFD).

Finally, voltage unbalance can cause degradation of the efficiency and increase in the losses of induction motors, and it is identified by DOE as the primary reason for their overheating and premature failure. More specifically, low levels of voltage unbalance may lead to significant current unbalance levels due to the low negative-sequence impedance value compared to the value of the positive-sequence impedance of an induction motor [79].

A summary of the above desribed causes and consequences of voltage unbalance in distribution networks is provided in Figure 2.3.

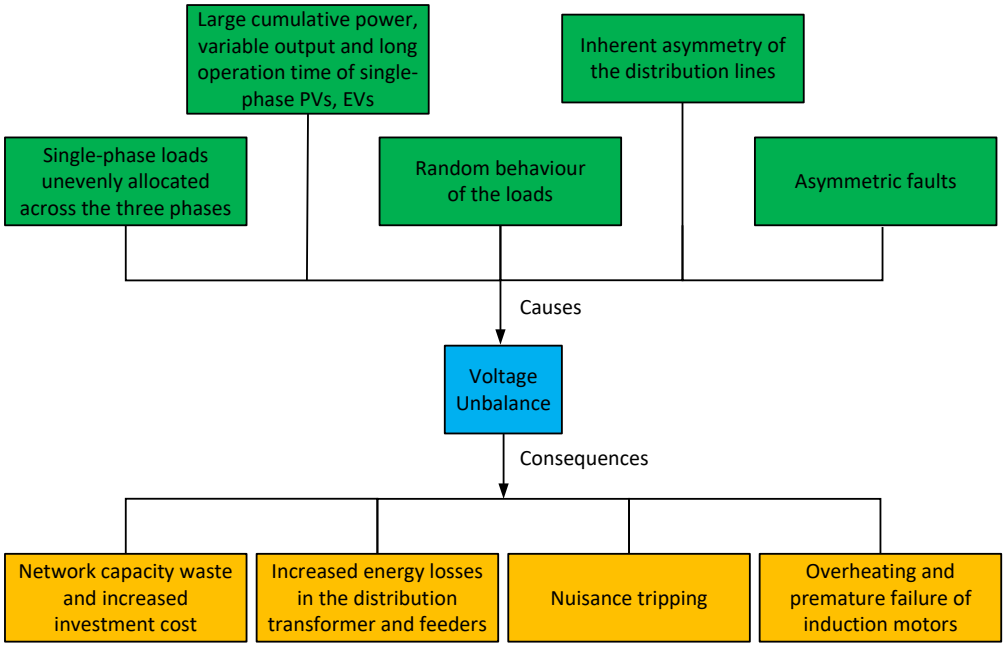

Figure 2.3: Causes and consequences of voltage unbalance.

2.5.4 Voltage unbalance mitigation techniques

As a result of the challenges described in the previous subsections, to maintain a balanced system operation, distribution network operators (DNOs) are exploring new approaches to improve voltage profiles and reduce the levels of current and voltage unbalance.

Voltage unbalance has been traditionally tackled by trying to distribute equally the loads on the three phases, by using delta-connected systems, and by applying transposition on long lines [1]. Additionally, it is possible to replace the LV cables with cables of larger cross-sectional area [74]. This results in reduced voltage drop along the feeders, therefore the difference among the voltage amplitudes at the three phases is decreased at the feeder end [86]. When these mitigating solutions are not viable, active filters can be deployed [87, 88]. Series and parallel active power filters have been proposed for voltage unbalance compensation by injecting negative-sequence voltage and current, respectively [89]. Furthermore, voltage unbalance can be reduced by controlling unified power quality conditioners to inject both negative-sequence voltage and current or by static synchronous compensators controlled to inject positive- and negative-sequence reactive power [90]. The installation of phase balancers in LV feeders is another option for

mitigating the unbalance [74]. However, the aforementioned solutions incur in high costs for DNOs [91].

Alternatively, power converters used for distributed generation (DG) may provide voltage unbalance compensation as an ancillary service by regulating their reactive power output [1], [2]. However, the effectiveness of this method is limited to low voltage (LV) networks with high R/X values. In [87, 91], three-phase inverters for wind and solar generation are controlled to compensate voltage unbalance at the PCC by injecting negative-sequence active and reactive power, while in [92] the negative- and zero-sequence grid current components are compensated by single-phase DG inverters. A supervisory controller manages the units by calculating the reactive power references for each inverter in real time [93]. The control strategy presented in [94] enables the synergic action of single-phase and three-phase PV inverters for voltage unbalance mitigation, with a central controller located at the PCC evaluating the required compensating active and reactive power signals to be dispatched to the inverters. More recently, decentralized and distributed control schemes based on the Steinmetz design have been proposed to control the reactive power injections of single-phase distributed PV inverters for voltage unbalance mitigation [95].

All the works cited above refer to the use of wind/solar inverters. Despite the potential benefits of using Battery Energy Storage Systems (BESSs) for voltage unbalance compensation, due to their declining prices, flexibility to control both active and reactive power (four-quadrant operation) and relatively stable DC voltage, such application is a relatively unexplored research area. Only a few literature works consider using BESSs for providing phase balancing services, and most of these research papers focus on three-phase BESSs. In [96], a control scheme is proposed for three-phase PV/BESS inverters installed across a distribution system to balance the voltage at the LV busbar; a central controller receives measurements from a smart meter installed at the MV/LV transformer and calculates the negative-sequence reference set-points sent to each inverter. A three-phase community energy storage (CES) system was proposed in [97] to alleviate the neutral current and neutral-to-ground voltage rise caused by the variable PV output and unbalanced loads in a multi-grounded three-phase four-wire distribution system. The CES system was controlled to dynamically balance the power exchange with the grid utilizing the minimum amount of power.

The provision of unbalance compensation by single-phase BESS has been described only by a few authors. In [98], PEVs single-phase batteries were coordinated to inject and absorb reactive power to mitigate the current unbalance. However, since the active power exchange remains unaltered, the effectiveness of this method is limited for distribution systems with high PV and EV penetration levels. In [99], the control of a single-phase

BESS connected at the same phase as a PV inverter and a load reduces the voltage unbalance and the network power losses by acting as a load or generator when the PV output is greater or lower than the load, respectively. Nevertheless, the proposed control scheme results in voltage unbalance levels above the statutory limit and increased network losses when the BESS is connected at different phase from the PV and the load. Distributed control strategies for single-phase distributed BESSs were proposed in [100] to balance the active powers at the point of common coupling (PCC) of the distribution system. In [101], the power balancing algorithm proposed in [97] was applied to single-phase battery storage devices integrated with PV systems in the distribution feeder to balance the power flows at each bus, by storing surplus energy during PV peak generation period and releasing the stored energy during the evening peak load.

The literature review performed has shown that there is still room for further application of BESSs for unbalance compensation, since this is a relatively new research area. However, in contrast with active filter operation, compensation of voltage unbalance involves charging and discharging of the energy storage unit, and may have an impact on the state of charge (SOC) and the lifetime of the battery [102]. This issue is common to other ancillary services, and it was described more in details in [1].

2.6 BESS model

The configuration of the BESS model was determined based on the literature review carried out on BESS technologies and inverter configurations utilized for voltage unbalance mitigation. This section presents the two main components of the BESS model: the battery (Subsection 2.6.1) and the inverter (Subsection 2.6.2).

2.6.1 Battery model

A built-in Simulink block is used to model the battery of the BESS. This block implements a generic battery model that represents most popular technologies. In the case under study, a Li-ion battery is connected to the dc side of each BESS inverter. This technology is chosen since it is the most common for power system applications [1], as discussed in Section 2.2, and the following assumptions apply to the model [103]:

- The temperature and ageing (due to cycling) effects on the battery are not simulated.
- The internal resistance is assumed to be constant during the charge and discharge cycles and it does not vary with the current amplitude.

- The default values are chosen for the model parameters of the Li-ion battery cell. The Simulink software derives these values from the data sheet of the corresponding battery technology and its typical discharge characteristics, which are assumed to be the same with the charge characteristics.
- The battery capacity does not change with the current amplitude - there is no Peukert effect [103].
- The self–discharge of the battery is not represented. This can be modelled by adding a large resistance in parallel with the battery terminals.
- The battery has no memory effect.

The lithium-ion battery is modelled using the following equations, depending on if the battery is charging or discharging:

- Discharge model ($i^* > 0$):

$$f_d(it, i^*, i) = E_0 - K \cdot \frac{Q}{Q - it} \cdot i^* - K \cdot \frac{Q}{Q - it} \cdot it + A \cdot e^{(-B \cdot it)} \tag{2.4}$$

- Charge model ($i^* < 0$):

$$f_c(it, i^*, i) = E_0 - K \cdot \frac{Q}{it + 0.1 \cdot Q} \cdot i^* - K \cdot \frac{Q}{Q - it} \cdot it + A \cdot e^{(-B \cdot it)} \tag{2.5}$$

where $f_d(it, i^*, i)$ and $f_c(it, i^*, i)$ are the battery discharge and charge voltage, respectively, E_0 is the constant voltage (in V), K is the polarization constant (in V/Ah) or polarization resistance (in Ohms), i^* is the low frequency current dynamics (in A), i is the battery current (in A), it is the extracted capacity (in Ah), Q is the maximum battery capacity (in Ah), A is the exponential voltage (in V), B is the exponential capacity (in Ah^{-1}).

To satisfy the required operating conditions for a specific application, i.e. achieve the desired operating voltage and capacity of the BESS, N_s and N_p battery cells have to be connected in series and in parallel, respectively, as shown in Figure 2.4. The number of cells connected in series and in parallel are calculated based on the required operating voltage and capacity of the BESS, respectively:

$$N_s = \frac{V_{bn}}{V_{cn}} \tag{2.6}$$

$$N_p = \frac{C_{bn}}{C_{cn}} \tag{2.7}$$

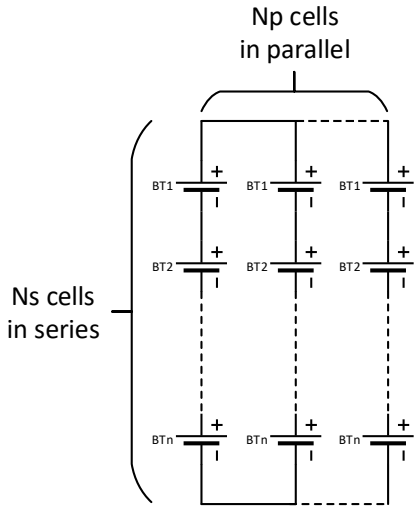

Figure 2.4: Li-ion battery consisting of Ns cells connected in series and Np cells connected in parallel.

where V_{bn} is the BESS nominal voltage (V), V_{cn} is the battery cell nominal voltage (V), C_{cn} is the battery cell rated capacity (Ah) and C_{bn} is the BESS rated capacity (Ah), which can be rewritten as:

$$C_{bn} = \frac{E_{bn}}{V_{bn}} \tag{2.8}$$

where E_{bn} is the BESS rated capacity (Wh). Substituting (2.8) to (2.7), the number of parallel connected cells is equal to:

$$N_p = \frac{E_{bn}}{V_{bn} C_{cn}} \tag{2.9}$$

The BESS rated capacity is obtained as the product of the inverter rated power (P_{inv}) and the BESS operating time (t_{op}):

$$E_{bn} = P_{inv} t_{op} \tag{2.10}$$

In the context of this work, the operating time for providing the unbalance compensation service was chosen as 10 h, assuming that the BESS provides this service during the daytime. The inverter rated power was chosen equal to $P_{inv} = 9$ kW, as discussed in Subsection 2.6.2. Therefore, the BESS rated capacity is equal to $E_{bn} = 90$ kWh, and this rating was used throughout the simulations carried out in Chapter 4 and Chapter 5 to validate the voltage unbalance mitigation strategy.

Table 2.5: Parameters of the Li–ion battery cell.

Parameters	Symbols	Values	Units
Nominal voltage	V_{cn}	7.2	V
Rated capacity	C_{cn}	5.4	Ah
Initial state–of–charge	SOC_{in}	80	%
Battery response time	t_r	30	s
Maximum capacity	$C_{c,max}$	5.4	Ah
Cut-off voltage	V_{co}	5.4	V
Fully charged voltage	V_{cf}	8.3807	V
Nominal discharge current	I_{dn}	2.3478	A
Internal resistance	R_{int}	0.013333	Ohm
Capacity at nominal voltage	$C_{cn}^{'}$	4.8835	Ah
Exponential zone [voltage, capacity]	$[V_{ce}\ C_{ce}]$	[7.7788 0.2653]	[V Ah]

Table 2.5 summarizes the parameters of the individual Li-ion battery cell. To model a series and parallel combination of cells, the parameters of Table 2.5 are modified as follows: the voltage parameters $(V_{cn}, V_{co}, V_{cf}, V_{ce})$ are multiplied with N_s, the capacity $(C_{cn}, C_{c,max}, C_{cn}^{'}, C_{ce})$ and current parameters (I_{dn}) are multiplied with N_p, and the internal resistance (R_{int}) is multiplied with $\frac{N_s}{N_p}$. The values of N_s and N_p are provided in the next section.

2.6.2 Single-phase BESS inverter model

The single-phase BESS inverter was modelled as a single-phase full-bridge voltage source inverter (VSI) shown in Figure 2.5. The inverter consists of four IGBT switches (Q1-Q4), which are forced-commutated devices, and four diodes that are connected in antiparallel to the switches. As it will be shown in later chapters, the single-phase inverter is connected either at the busbar at the secondary side of the distribution transformer or at a busbar along the distribution feeder.

The inverter nominal phase-to-neutral voltage is equal to $V_{LN,rms} = 230$ V or $V_{LN,peak} = 325$ V. Since the BESS rated dc voltage should be larger than the grid voltage under any operating conditions, including overvoltage, V_{bn} should be above $1.1 \times 325 = 357.5$ V [104]. Therefore, $N_s = 70$ battery cells were connected in series, leading to a BESS nominal voltage equal to $V_{bn} = 504$ V. In addition, the inverter rated power was chosen equal to $S_{inv} = 9$ kvar, since the choice of this rating was shown to result in a satisfactory performance on mitigating the voltage unbalance levels, which stayed below the regulatory limits for most of the generation and load operating conditions examined throughout the simulations presented in Chapter 4, 5 and 7. In a practical application, the optimum bat-

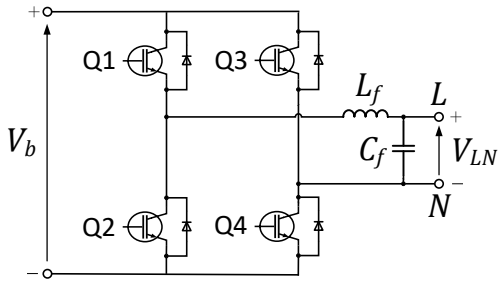

Figure 2.5: Single-phase full-bridge voltage source inverter.

tery rating will be chosen as a compromise between performance, cost, ancillary services provided and their remuneration. The validation of the chosen inverter rating is carried out in Appendix A. Substituting $E_{bn} = 90$ kWh, $V_{bn} = 504$ V and $C_{cn} = 5.4$ Ah to (2.9), the number of parallel connected cells for the BESS unit was chosen equal to:

$$N_p = \frac{90000}{504 \cdot 5.4} = 33.064 \approx 34 cells \tag{2.11}$$

Purely resistive snubbers are simulated by setting the snubber capacitance and resistance equal to $C_s = \text{inf}$ and $R_s = 10^5\ \Omega$, respectively [105]. Thus, the power electronic devices are simulated with virtually no snubbers, and the leakage currents are negligible due to the very large resistance value. In addition, the conduction losses and the forward voltage of the IGBT and the diode are neglected[3]. The switching frequency is set equal to $f_{sw} = 10$ kHz. The inverter is connected to the grid through an LC filter, which filters out the high frequency switching harmonics of the output voltage and current. Table 2.6 summarizes the chosen parameters.

[3]These approximations are acceptable for the purpose of this work, where the interest is focused on the impact of the proposed control strategy on the electrical power system, rather than on the individual inverter.

Table 2.6: Parameters of the VSI and output filter.

Parameters	Values
Nominal dc voltage	$V_{bn} = 504$ V
Nominal ac voltage	$V_{LNn} = 230$ V
Rated apparent power	$S_{inv} = 9$ kVA
LC filter	$R_f = 0.135\ \Omega$, $L_f = 3.6$ mH, $C_f = 8\ \mu$F
Switching frequency	$f_{sw} = 10$ kHz
Snubber resistance and capacitance	$R_s = 10^5\ \Omega$, $C_s = inf$
IGBT internal resistance	$R_{on} = 10^{-3}\ \Omega$
IGBT and Diode forward voltage	$V_f = V_{fd} = 0$ V

2.7 Conclusions

This chapter presented a literature review dealing with applications of BESS in distribution systems. Various BESS projects in the UK were presented, showing that there has been a trend towards utilizing BESSs for time-shifting applications and for deferring investments for the upgrade of the transmission system (TS) and distribution system (DS). Additionally, BESSs have been utilised for the provision of ancillary services such as voltage support, which is gaining increasing importance due to the growing penetration of variable generation and load patterns into the grid. Different BESS technologies deployed in the UK projects were discussed, showing that while the majority of them is based on Li-ion batteries, more diversified types of batteries are expected to be utilized in future applications. A robust classification of the ancillary services currently offered by BESSs was performed, and the notation found in the literature was harmonised.

A comprehensive literature review on the topic of voltage unbalance was carried out. It has been reported that the uneven allocation of single-phase loads, the random load behaviour and the inherent structural asymmetries present in distribution networks are the main causes of voltage unbalance, while disruptive single-phases loads and generating units, such as PVs and EVs, can become major contributors to the rise of voltage unbalance levels as their number grows. Voltage unbalance can have multiple negative effects on the power system, including: increased energy losses, reduced efficiency and degradation of induction motors, and waste of the network capacity, which may lead to increased network investment costs.

State-of-the-art and potential voltage unbalance mitigation techniques have been presented, including both passive (e.g. corrective actions implemented by the utilities) and active (e.g. use of power electronic equipment controlled to inject active and reactive

power to compensate for voltage unbalance) techniques. The literature review has shown that the installation of equipment such as active power filters may increase the total investment cost, and therefore there has been an increasing interest towards the deployment of DG inverters for the provision of voltage unbalance mitigation services, since they are not operating at full rating all the time due to the intermittent nature of RESs. Therefore, utilizing their available power rating to address voltage unbalance issues is a promising idea. Alternatively, voltage unbalance compensation could be provided either by behind-the-meter or front-of-the-meter BESS units, which can be utilized in a stand-alone setup or they can be collocated with other renewable energy resources, such as PVs. The majority of the literature works propose voltage unbalance compensation strategies deployed to three-phase BESSs, while only a few of them consider the application of single-phase BESSs for unbalance mitigation in LV networks. This research is aimed to fill this gap, and the proposed mitigation technique will be introduced in Chapter 3.

Finally, the BESS model used in this work was presented. The basic modelling principles and parameters of the adopted Li-ion battery and single-phase full-bridge voltage source inverter models were provided. These models are used in Chapter 4 and Chapter 5 to validate the developed control strategy.

Chapter 3

Voltage Unbalance Mitigation Strategy for Single-Phase Battery Energy Storage Inverters

3.1 Introduction

This chapter presents the proposed voltage unbalance mitigation strategy for single-phase BESS inverters. A detailed description of the strategy developed to mitigate voltage unbalance in unbalanced power distribution systems is provided, followed by a detailed discussion of the BESS control strategy developed to regulate the active and reactive power output of each single–phase BESS inverter.[1]

3.2 Voltage unbalance compensation strategy

Figure 3.1 illustrates the configuration of three single-phase BESS units connected at a generic bus (labelled 'bus j') of the distribution system and the control system layout. This representation means that the BESS units may be connected either at the substation busbar or at any other three-phase busbar.

The downstream single-phase loads are represented by their active and reactive power

[1] Part of the work presented in this chapter has been published in [2], [106].

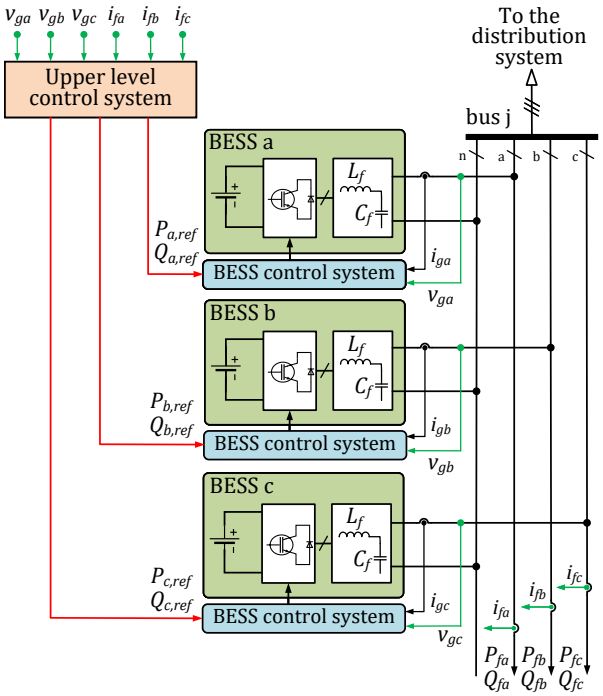

Figure 3.1: Schematic of the three single-phase BESS units connected to the distribution system for providing voltage unbalance compensation.

values P_{fi}, Q_{fi}, with i = a, b, c. It is worth noticing that the term 'load' is used loosely here, as both passive and active elements (such as PVs and EVs) may be connected to the distribution feeder, and the net power may be positive or negative, and varying in time. It is assumed that the loads are non-uniformly distributed, so that the power flow in the three phases will be different thus leading to unbalanced voltages at bus j. Additionally, the presence of structural asymmetries in the medium-voltage (MV) network introduces background unbalance, which is added to the voltage unbalance caused by unequal load distribution. Differences in mutual impedances between phase conductors cause different voltage drops, depending on their spatial configuration. Low voltage networks generally introduce a small amount of voltage unbalance due to mutual impedance mismatch, therefore the coupling between the three phases is not considered in this work [107].

The proposed control system is composed of two distinct parts: the upper level control system and the BESS control system. The upper level control system coordinates the three units by providing active and reactive power reference to each BESS inverter, based on voltage measurements and feeder current measurements at bus j (v_{gi} and i_{fi}, with i = a, b, c). The BESS control system regulates the active and reactive power and generates

the switching pulses for the inverter based on power references ($P_{i,ref}$, $Q_{i,ref}$), voltage measurements (v_{gi}) and inverter output current measurements (i_{gi}).

The aim of the proposed strategy is to control the inverters to inject negative- and zero-sequence fundamental current components to be equal in magnitude and 180^o out of phase compared to the sequence components of the feeder current. As a result, only the positive-sequence current component flows upstream bus j. The upper level control system is described in details in Subsection 3.2.1, while Section 3.3 presents the BESS control system.

3.2.1 Upper level control system

Figure 3.2 presents a detailed representation of the upper level control system. While the use of reference currents is a suitable approach for locally connected three-phase inverters controlled to mitigate voltage unbalance, reference powers, such as active and reactive power, are more suited when applying coordinated control strategies between various network components [94], [108]. Therefore, in the context of this work, the deployment of an upper level controller is proposed for the calculation of the power commands, which are sent to the single-phase BESS units. While in this work it is assumed that the BESS units are connected at the same bus, the applicability of the proposed power-based control approach can also be extended to the coordination of BESS units connected at different buses for voltage unbalance mitigation or the coordination of BESS units with other devices, such as EVs. A possible alternative configuration for the three BESS inverters consists in using a common DC link, where the tree BESSs are connected in parallel. This topology introduces further challenges related to the BESS SOC control, among others, and has not been considered in this work, which rather focuses on mitigating voltage unbalance by controlling three separate single-phase BESS inverters,

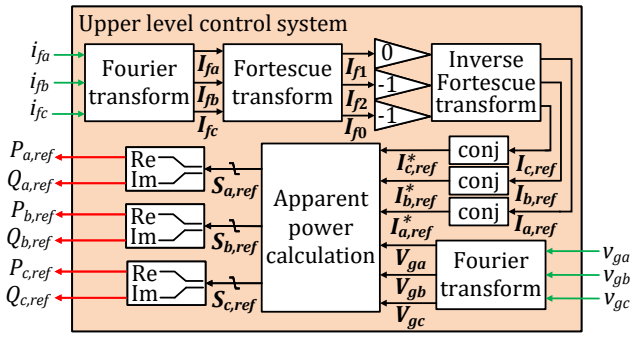

Figure 3.2: Upper level control system structure.

which may be deployed at the same busbar or far from each other in a practical setting.

Figure 3.2 shows that both current and voltage signals i_{fi} and v_{gi} are transformed to the phasor domain by applying the Fourier transformation (appendix B), therefore leading to the signals [$\boldsymbol{I_{fa}}$, $\boldsymbol{I_{fb}}$, $\boldsymbol{I_{fc}}$] and [$\boldsymbol{V_{ga}}$, $\boldsymbol{V_{gb}}$, $\boldsymbol{V_{gc}}$]. The Fortescue transformation is then applied to obtain the current symmetrical components [$\boldsymbol{I_{f1}}$, $\boldsymbol{I_{f2}}$, $\boldsymbol{I_{f0}}$], which are calculated as follows:

$$\begin{bmatrix} \boldsymbol{I_{f1}} \\ \boldsymbol{I_{f2}} \\ \boldsymbol{I_{f0}} \end{bmatrix} = \frac{1}{3} \begin{bmatrix} 1 & \boldsymbol{\alpha} & \boldsymbol{\alpha^2} \\ 1 & \boldsymbol{\alpha^2} & \boldsymbol{\alpha} \\ 1 & 1 & 1 \end{bmatrix} \begin{bmatrix} \boldsymbol{I_{fa}} \\ \boldsymbol{I_{fb}} \\ \boldsymbol{I_{fc}} \end{bmatrix} \tag{3.1}$$

where the phasors [$\boldsymbol{I_{f1}}$, $\boldsymbol{I_{f2}}$, $\boldsymbol{I_{f0}}$] represent the load positive–, negative– and zero–sequence components, while the phasors [$\boldsymbol{I_{fa}}$, $\boldsymbol{I_{fb}}$, $\boldsymbol{I_{fc}}$] are the fundamental load currents, and $\boldsymbol{\alpha} = \boldsymbol{e^{j\frac{2\pi}{3}}}$ is the phasor rotation operator, which rotates a phasor counterclockwise by 120^o.

Since the BESS inverter is expected to inject both the zero- and the negative-sequence current components of the feeder current, $\boldsymbol{I_{f2}}$ and $\boldsymbol{I_{f0}}$ are multiplied with -1, while $\boldsymbol{I_{f1}}$ is multiplied by zero. The inverse Fortesque transformation is then applied to the modified symmetrical current components to calculate the reference current phasors [$\boldsymbol{I_{a,ref}}$, $\boldsymbol{I_{b,ref}}$, $\boldsymbol{I_{c,ref}}$], which are given by the following equation:

$$\begin{bmatrix} \boldsymbol{I_{a,ref}} \\ \boldsymbol{I_{b,ref}} \\ \boldsymbol{I_{c,ref}} \end{bmatrix} = \begin{bmatrix} 1 & 1 & 1 \\ \boldsymbol{\alpha^2} & \boldsymbol{\alpha} & 1 \\ \boldsymbol{\alpha} & \boldsymbol{\alpha^2} & 1 \end{bmatrix} \begin{bmatrix} 0 \\ \boldsymbol{-I_{f2}} \\ \boldsymbol{-I_{f0}} \end{bmatrix} \tag{3.2}$$

The reference current phasors are multiplied with the voltage phasors [$\boldsymbol{V_{ga}}$, $\boldsymbol{V_{gb}}$, $\boldsymbol{V_{gc}}$] to calculate the reference active and reactive power commands ($P_{i,ref}$, $Q_{i,ref}$) for each BESS inverter. The formulations of the reference powers are:

$$\boldsymbol{S_{a,ref}} = P_{a,ref} + jQ_{a,ref} = \boldsymbol{V_{ga}}(\boldsymbol{-I_{f2}^* - I_{f0}^*}) \tag{3.3}$$

$$\boldsymbol{S_{b,ref}} = P_{b,ref} + jQ_{b,ref} = \boldsymbol{V_{gb}}(\boldsymbol{-\alpha^* I_{f2}^* - I_{f0}^*}) \tag{3.4}$$

$$\boldsymbol{S_{c,ref}} = P_{c,ref} + jQ_{c,ref} = \boldsymbol{V_{gc}}(\boldsymbol{-\alpha^{2*} I_{f2}^* - I_{f0}^*}) \tag{3.5}$$

From Eqs. (3.3)-(3.5), the three BESS units are controlled to supply the zero- and negative-sequence current to the load, as shown in Figure 3.3, therefore only the positive-sequence current flows through bus j. As a result of the improved current symmetry, the voltage drops across the downstream distribution system are altered, with the voltage deviations between the three phases being reduced at the remaining buses.

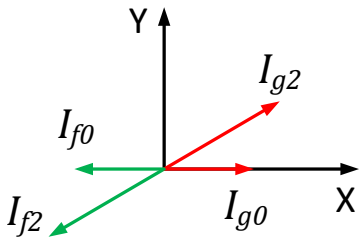

Figure 3.3: Zero- and negative-sequence components of the feeder current and inverter current.

In Eqs. (3.3)-(3.5), $\boldsymbol{V_{gi}} = \boldsymbol{V_{gi1}} + \boldsymbol{V_{gi2}} + \boldsymbol{V_{gi0}}$, where $\boldsymbol{V_{gi1}}$, $\boldsymbol{V_{gi2}}$ and $\boldsymbol{V_{gi0}}$ are the positive-, negative- and zero-sequence voltage components of phase-i inverter, for $i = a, b, c$. In steady-state conditions, once the BESS control systems regulate the active and reactive powers to the reference value, the negative- and zero-sequence voltage components at bus j are eliminated. Substituting $\boldsymbol{V_{gi2}} = 0$ and $\boldsymbol{V_{gi0}} = 0$ in Eqs. (3.3)-(3.5), it can be seen that the power exchanged between each BESS and the system is determined as the product of two terms: the positive-sequence voltage component and the sum of the negative- and zero-sequence current component, i.e.:

$$\boldsymbol{S_{a,ref}} = \boldsymbol{V_{ga1}}(-\boldsymbol{I^*_{f2}} - \boldsymbol{I^*_{f0}}) \tag{3.6}$$

$$\boldsymbol{S_{b,ref}} = \boldsymbol{V_{gb1}}(-\boldsymbol{a^*I^*_{f2}} - \boldsymbol{I^*_{f0}}) \tag{3.7}$$

$$\boldsymbol{S_{c,ref}} = \boldsymbol{V_{gc1}}(-\boldsymbol{a^{2*}I^*_{f2}} - \boldsymbol{I^*_{f0}}) \tag{3.8}$$

By adding Eqs. (3.6)-(3.8), the total apparent power exchanged between the three BESSs and the system is obtained as:

$$\boldsymbol{S_{t,ref}} = -\boldsymbol{I^*_{f2}}(\boldsymbol{V_{ga1}} + \boldsymbol{\alpha^*V_{gb1}} + \boldsymbol{\alpha^{2*}V_{gc1}}) - \boldsymbol{I^*_{f0}}(\boldsymbol{V_{ga1}} + \boldsymbol{V_{gb1}} + \boldsymbol{V_{gc1}}) \tag{3.9}$$

Due to the properties of the symmetrical components, in Eq. (3.9) the total apparent power exchanged between the BESS and the system will be zero. This means that at any point in time, either two BESS units will be charging and the third unit will be discharging, or the two BESS units will be discharging and the third unit will be charging active power to achieve voltage unbalance mitigation. The same principle applies for the generation or dissipation of the reactive power.

For the case when the desired operation cannot be achieved by the three BESS simultaneously (because of maintenance or unavailability of charge from the battery, for example), the proposed strategy still has positive impact in mitigating voltage unbalance, but it is less effective. This behaviour will be demonstrated both in the offline simulations and in the experiments in later chapters.

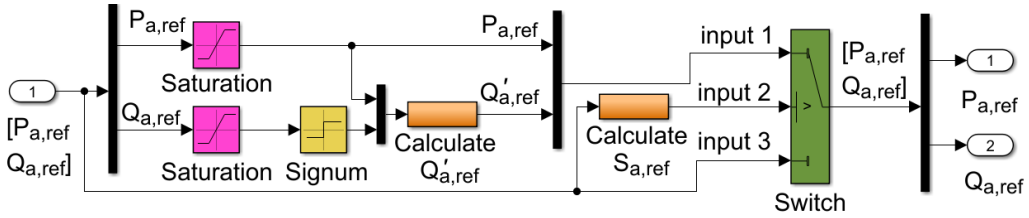

Figure 3.4: Simulink implementation of the apparent power limiter.

Notably, when the BESS cannot provide active power due to lack of charge or outages, the inverter can still inject reactive power, thus emulating the operating conditions described in [1], [98]. More formally, this condition is achieved by setting $P_{ref} = 0$ in the upper level controller.

To ensure that each BESS inverter does not exceed its nominal apparent power rating, a power limiting scheme has been developed. Its structure is demonstrated in the Simulink block diagram of Figure 3.4, which refers to phase-a BESS inverter, while the same logic applies to phase-b and phase-c BESS inverters. Based on this block diagram, the reference apparent power is calculated as:

$$S_{a,ref} = \sqrt{P_{a,ref}^2 + Q_{a,ref}^2} \tag{3.10}$$

and it is fed through input 2 to the 'Switch' block. The reference power is compared to the rated apparent power of the inverter ($S_n = 9$ kVA) inside this block, which passes in the output the reference active and reactive power signals either through input 1 or input 3, based on the following logic:

- $S_{a,ref} \leq S_n$: The reference active and reactive power signals $P_{a,ref}$ and $Q_{a,ref}$ pass through input 3, with their values remaining unchanged, as they were calculated by the voltage unbalance mitigation algorithm.
- $S_{a,ref} > S_n$: The reference active and reactive power signals pass through input 1, after having being modified as follows: two 'Saturation' blocks are used to ensure that $P_{a,ref}$ and $Q_{a,ref}$ do not exceed their nominal values, i.e. $\mid P_{a,ref} \mid \leq S_n$ and $\mid Q_{a,ref} \mid \leq S_n$. Since voltage unbalance mainly arises due to load active power mismatch, priority is given to active against reactive power injection/absorption. To this end, $P_{a,ref}$ passes unchanged, while the reactive power is recalculated as:

$$Q_{a,ref}^{'} = \text{sign}(Q_{a,ref}) \cdot \sqrt{S_n^2 - P_{a,ref}^2} \tag{3.11}$$

The 'Signum' block output is: $\text{sign}(Q_{a,ref}) = 1$, for $Q_{a,ref} > 0$ and $\text{sign}(Q_{a,ref}) = -1$, for $Q_{a,ref} < 0$.

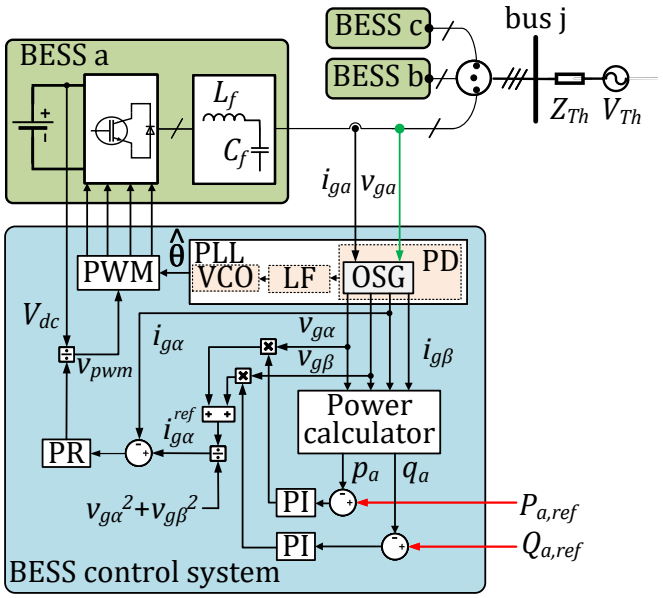

Figure 3.5: Phase-a BESS inverter and BESS control system.

3.3 BESS inverter control

This section elaborates on the single-phase BESS control system. The control system for phase-a BESS unit is shown in Figure 3.5 for simplicity. The control for phase-b and phase-c units is identical. In this figure, the three-phase network Thevenin equivalent is included. The inputs to the BESS control system are the reference powers calculated by the upper level control system ($P_{a,ref}$, $Q_{a,ref}$). The BESS control algorithm is based on the single-phase instantaneous power theory [106]. Since in the application under study the active and reactive power output of the inverters are controlled for voltage unbalance mitigation, the control system needs to calculate instantaneous power values.

Starting from current and voltage measurement at the BESS terminals (i_{ga} and v_{ga}), an Orthogonal Signal Generator (OSG) based on the second order generalized integrator [109], [110], [111] calculates the orthogonal voltage and current signals - i.e. the "α" and "β" grid voltage and current components in the $\alpha\beta$-stationary reference frame ($v_{g\alpha}$, $v_{g\beta}$, $i_{g\alpha}$, $i_{g\beta}$). From these signals, the instantaneous active and reactive power are calculated as:

$$p_a = (v_{g\alpha} i_{g\alpha} + v_{g\beta} i_{g\beta}) \times 1/2 \tag{3.12}$$

$$q_a = (v_{g\beta} i_{g\alpha} - v_{g\alpha} i_{g\beta}) \times 1/2 \tag{3.13}$$

Since the active and reactive power are dc quantities under sinusoidal and steady-state

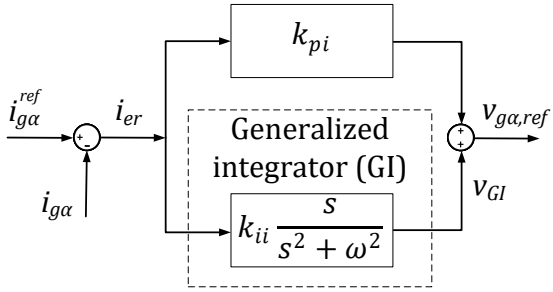

Figure 3.6: Block diagram of the ideal PR controller adopted in this work.

operating conditions, PI controllers are used for power regulation. The current reference in the $\alpha\beta$-stationary reference frame for the single-phase inverter is expressed as [112]:

$$\begin{bmatrix} i_{g\alpha,ref} \\ i_{g\beta,ref} \end{bmatrix} = \frac{1}{v_{g\alpha}^2 + v_{g\beta}^2} \begin{bmatrix} v_{g\alpha} & v_{g\beta} \\ v_{g\beta} & -v_{g\alpha} \end{bmatrix} \begin{bmatrix} G_p(s)(p_a - P_{a,ref}) \\ G_q(s)(q_a - Q_{a,ref}) \end{bmatrix} \tag{3.14}$$

where $P_{a,ref}$, $Q_{a,ref}$ are the active and reactive power references, respectively; $G_p(s)$ and $G_q(s)$ are the transfer functions of the PI controllers for active and reactive power, which are written as:

$$G_p(s) = k_{pp} + \frac{k_{ip}}{s} \tag{3.15}$$

$$G_q(s) = k_{pq} + \frac{k_{iq}}{s} \tag{3.16}$$

where k_{pp}, k_{ip}, k_{pq}, k_{iq} are the proportional and integral gains of the PI controllers for active and reactive power, respectively.

The reference current is regulated by a proportional-resonant (PR) controller: this term introduces an infinite gain to remove the steady–state error at the resonant frequency ω_0, and its transfer function is expressed as [113, 114]:

$$G_i(s) = k_{pi} + k_{ii}\frac{s}{s^2 + \omega_0^2} \tag{3.17}$$

where k_{pi}, k_{ii} the proportional and integral gain of the current controller, respectively. The ideal PR controller was implemented in the case under study, since it presented satisfactory tracking performance with negligible steady state error. The block diagram of this controller is provided in Figure 3.6, which shows that the controller consists of two terms: a proportional gain and a generalized integrator (GI). A more detailed explanation of the function of these terms is provided in the following paragraphs.

Figure 3.7 shows the Bode diagram of the PR controller for three different values of the integral gain, which were chosen such that the trade-off between the obtained magnitude

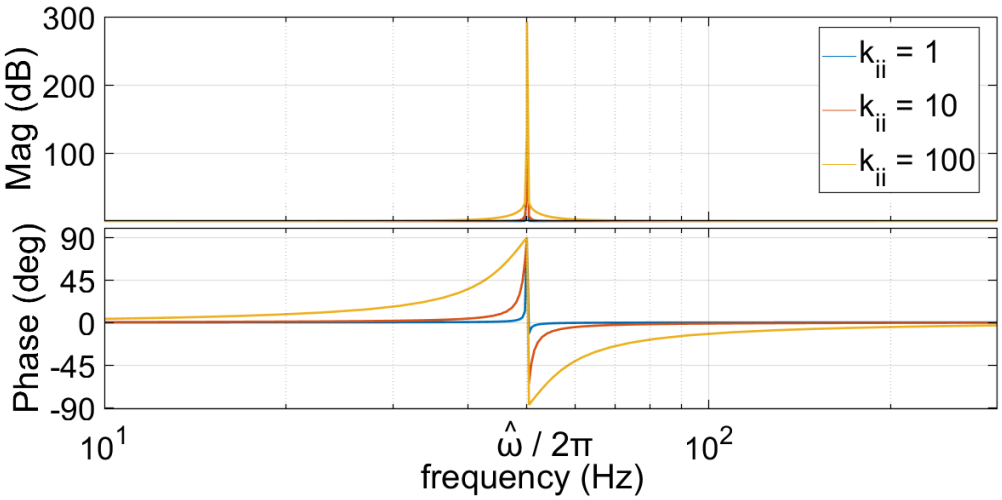

Figure 3.7: Bode plot of the PR controller for varying k_{ii}.

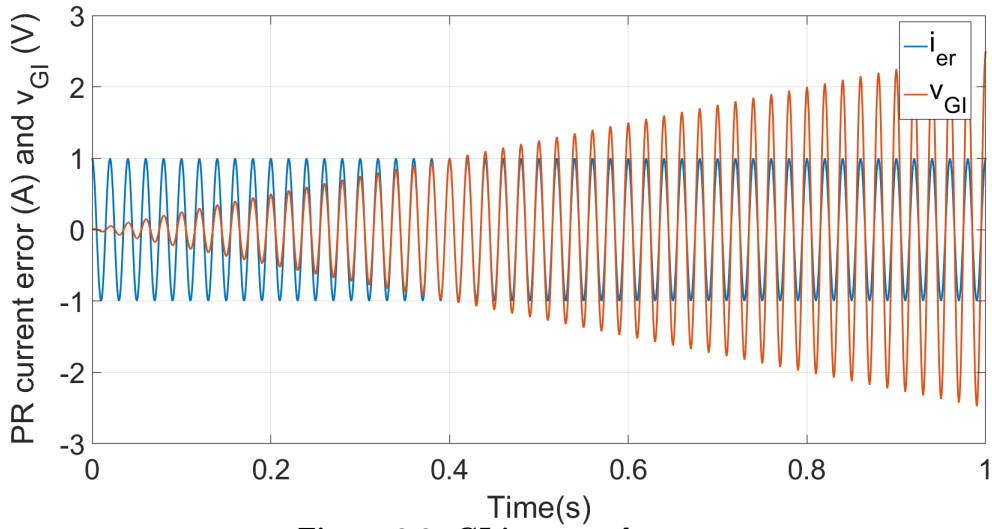

Figure 3.8: GI input and output.

and the width of the frequency band around the resonance frequency can be clearly illustrated. The magnitude plot shows that the PR controller provides a very high gain in a frequency band centered around ω_0, with the width of this band being determined by the value of k_{ii}. More specifically, an increased k_{ii} value results in a wider band. In the case under study, $\omega_0 = 2\pi \cdot 50$ rad/s. Generally, the grid frequency is constant with variations of around 1%, therefore k_{ii} has to be chosen to react to this frequency band.

The second term of the PR controller in Eq. (3.17) is a generalized integrator (GI),

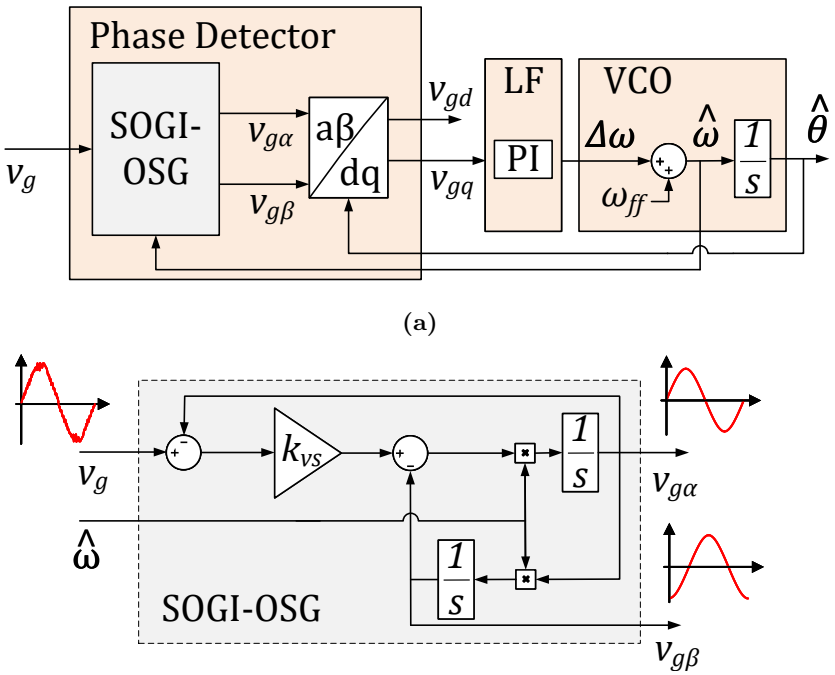

Figure 3.9: (a) General structure of the SOGI–OSG based PLL. (b) Configuration of the SOGI–OSG filter.

which integrates a sinusoidal input with respect to the time. The GI input and output are the current error i_{er} and the voltage term v_{GI}, respectively, as shown in Figure 3.6. These two quantities are plotted in Figure 3.8, which shows that the GI does not introduce any phase delay. Regarding the proportional gain k_{pi}, it is tuned in the same way as for a PI controller. This gain determines the dynamics of the system in terms of bandwidth, phase and gain margin.

To obtain the voltage and current components required for power calculation, a phase–locked loop based on an orthogonal signal generator (OSG) system is used. Typically, the main difference among different PLL methods is in the implementation of the phase detector (PD) and the structure of the orthogonal voltage system generation [109], [110]. Here, the method based on second order generalized integrator (SOGI–OSG) is adopted. Figure 3.9a shows the single–phase PLL: the OSG generates two quadrature sine waves ($v_{g\alpha}$ and $v_{g\beta}$) at the resonant frequency ($\hat{\omega}$), and $v_{g\alpha}$ has the same phase and magnitude as the fundamental component of the input signal (v_g). The voltage-controlled oscillator (VCO) feedbacks $\hat{\omega}$ to the OSG and the estimated phase angle ($\hat{\theta}$) to the Park transform. The output of the phase detector is the phase error v_{gq}, that is passed through a loop

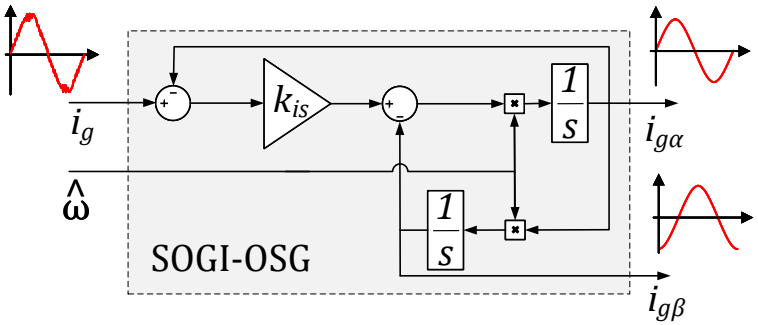

Figure 3.10: Configuration of the SOGI–OSG filter for the current.

filter (LF) to attenuate the high frequency noise before being added to the fundamental frequency ω_{ff} [110], [111]. The addition of signal ω_{ff} decreases the control effort and accelerates the initial lock-in process [110]. As explained in [109], this configuration integrates the benefits of other PLL methods, such as the Hilbert Transformation, the Inverse Park Transformation and the Transport-Delay. More specifically, the SOGI-based PLL structure achieves: orthogonal voltage system generation, filtering without delay and frequency independence.

Figure 3.9b-3.10 show the detailed representation of the adopted SOGI-OSG filter for the voltage and current, respectively. The choice of the gains k_{vs} and k_{is}, commonly referred to as the damping factor, is a trade–off between the desired bandpass frequency and the system's dynamic response [109]. More specifically, lower gain values result in a narrower bandwidth, thereby improving the filtering capability. However, the dynamic response of the system becomes slower, as it will be shown later. The closed-loop transfer functions of the SOGI-OSG block are written as follows [109]:

$$H_\alpha(s) = \frac{v_{g\alpha}(s)}{v_g(s)} = \frac{k_{vs}\hat{\omega}s}{s^2 + k_{vs}\hat{\omega}s + \hat{\omega}^2} \tag{3.18}$$

$$H_\beta(s) = \frac{v_{g\beta}(s)}{v_g(s)} = \frac{k_{vs}\hat{\omega}^2}{s^2 + k_{vs}\hat{\omega}s + \hat{\omega}^2} \tag{3.19}$$

The following analysis is carried out for the SOGI-OSG of the PLL, but it also applies to the current SOGI-OSG. The impact of k_{vs} on the bandwidth and dynamic response of the system is demonstrated in Figure 3.11-3.12, where the Bode plot and the step response of the closed-loop transfer function $H_\alpha(s)$ are plotted for three different values of k_{vs}, respectively. Figure 3.11 shows that the transfer function $H_\alpha(s)$ exhibits a bandpass filtering characteristic with a center frequency $\hat{\omega}$, and its width is dependent on k_{vs} value and independent of $\hat{\omega}$. For low damping factor values, i.e. $k_{vs} = 0.1$ (blue curve), the bandpass of the filter becomes narrower. At the same time, the system presents slower

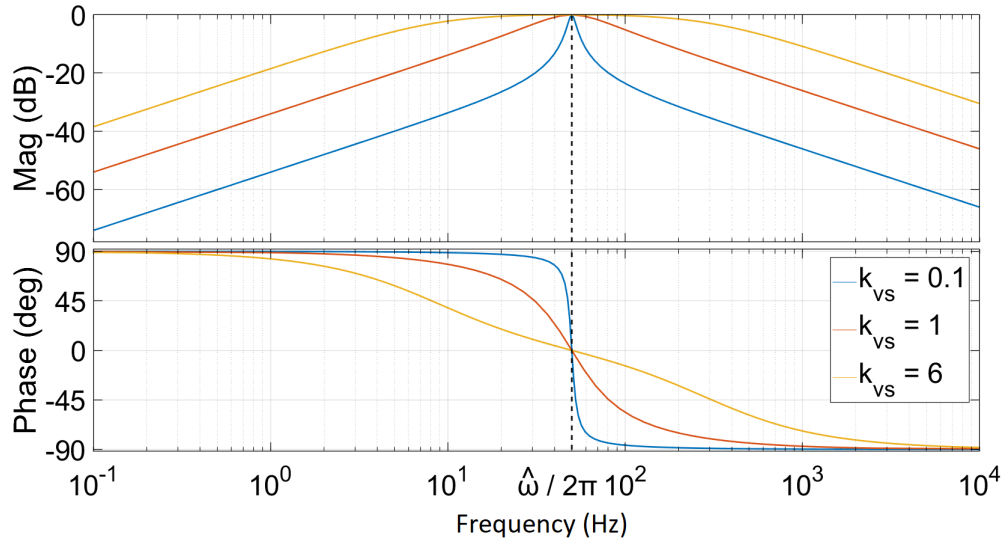

Figure 3.11: Bode plot of the closed-loop transfer function $H_\alpha(s)$ for three different values of the gain parameter: $k_{vs} = 0.1$ (blue line), $k_{vs} = 0.1$ (red line), $k_{vs} = 6$ (yellow line).

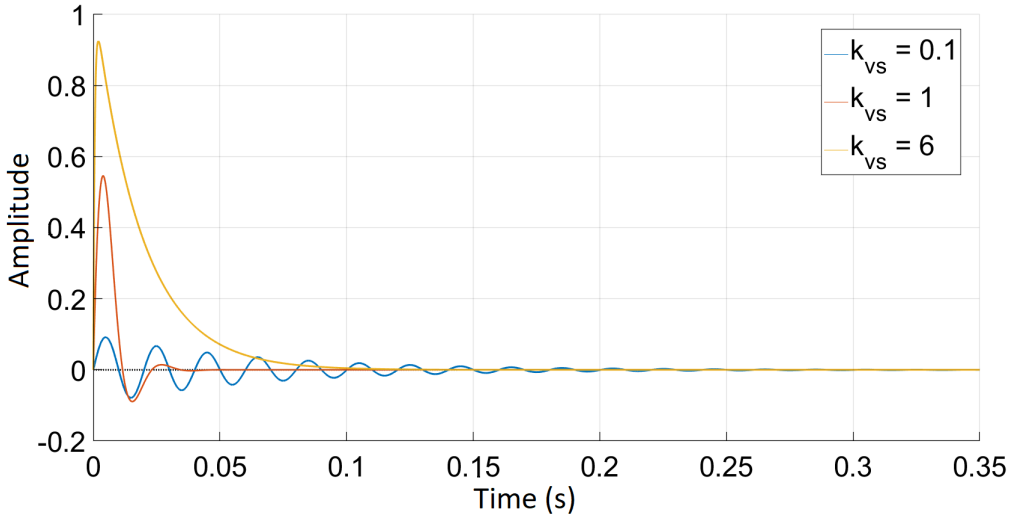

Figure 3.12: Step response of the closed-loop transfer function $H_\alpha(s)$ for three different values of the gain parameter: $k_{vs} = 0.1$ (blue line), $k_{vs} = 0.1$ (red line), $k_{vs} = 6$ (yellow line).

dynamic response, as it can be seen from Figure 3.12. Regarding the transfer function $H_\beta(s)$, Figure 3.13 shows that it exhibits a low-pass filtering characteristic.

By inspection of the Bode magnitude plots of Figure 3.11 and Figure 3.13, it can be

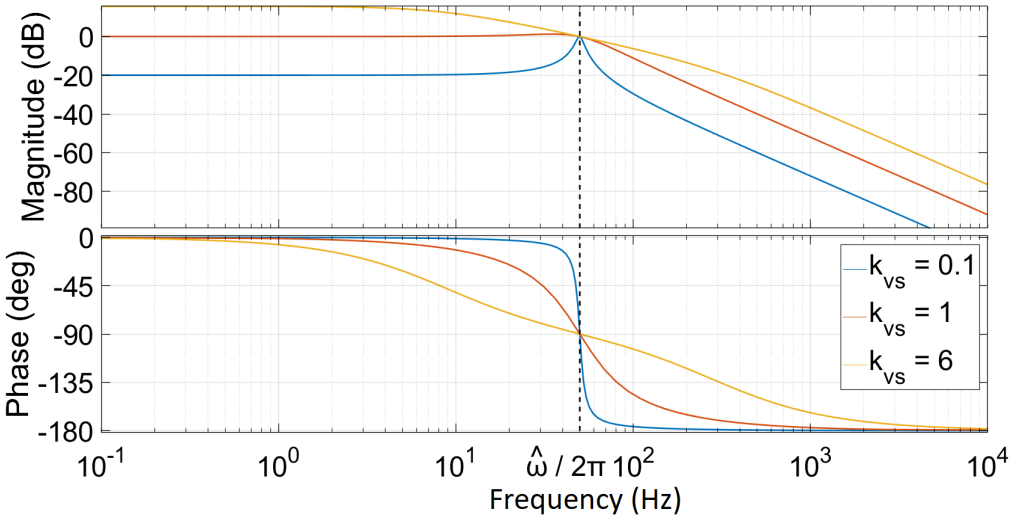

Figure 3.13: Bode plot of the closed-loop transfer function $H_\beta(s)$ for three different values of the gain parameter: $k_{vs} = 0.1$ (blue line), $k_{vs} = 0.1$ (red line), $k_{vs} = 6$ (yellow line).

deduced that $v_{g\alpha}$ and $v_{g\beta}$ will have the same amplitude with the fundamental component of the input voltage v_g, since the magnitude at the fundamental frequency is 0 dB; regarding the Bode phase plots, $v_{g\alpha}$ will be in phase with the fundamental component of v_g, since the phase introduced by $H_\alpha(s)$ at the fundamental frequency is zero, while a phase difference of 90^o exists between $v_{g\beta}$ and v_g. Therefore, $v_{g\alpha}$ and $v_{g\beta}$ are orthogonal.

3.3.1 Equivalent model of the inverter output LC filter

Next the equivalent model of the inverter output LC filter is derived. With reference to Figure 3.5, the system equations in the AC side of the inverter can be expressed in the time domain and the Laplace domain as shown in (3.20) and (3.21), respectively:

$$\frac{di_g(t)}{dt} + \frac{R_f}{L_f} i_g = \frac{v_i(t)}{L_f} - C_f \frac{d^2 v_g(t)}{dt^2} - \frac{R_f C_f}{L_f} \frac{dv_g(t)}{dt} - \frac{v_g(t)}{L} \tag{3.20}$$

$$I_g(s) = \frac{1}{L_f s + R_f} V_i(s) - \frac{L_f C_f s^2 + R_f C_f + 1}{L_f s + R_f} V_g(s) \tag{3.21}$$

The equivalent model of the LC filter in the Laplace domain and the block diagram of the current control loop are provided in Figure 3.14-3.15, respectively. The closed-loop and open-loop transfer functions of the current controller are obtained as follows:

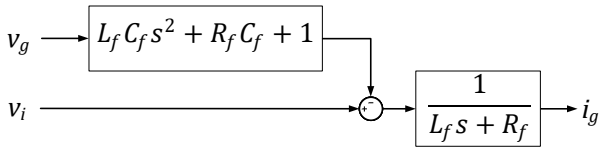

Figure 3.14: Equivalent model of the LC filter in the Laplace domain.

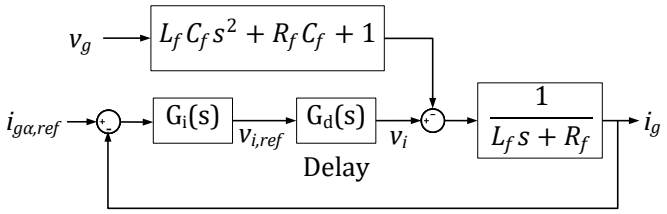

Figure 3.15: Block diagram of the current control loop.

$$G_{cl}(s) = \frac{G_i G_d}{L_f s + R_f + G_i G_d} \tag{3.22}$$

$$G_{ol}(s) = \frac{G_i G_d}{L_f s + R_f} \tag{3.23}$$

where $G_d(s)$ is the transfer function of the processing and PWM delay, which is expressed as a function of the sampling time T_s [115]:

$$G_d(s) = \frac{1}{1 + 1.5 T_s s} \tag{3.24}$$

3.3.2 Discretization of the PLL, PI controllers for active and reactive power and PR controller

The continuous-time domain controllers have to be discretized since a discrete-time solver is used both in offline simulations and in real-time simulations realized in the OPAL-RT device. More specifically, the controllers have to be mapped from the S-domain to the Z-domain. Different discretization methods can be utilized to implement the digital controller. In the case under study, the Forward Euler method was used to discretize the PI controllers of the active and reactive power and the PLL, while the PR controller was discretized using the zero-order hold method [116], [117]. For each case, the disrete transfer functions are provided next.

- PI controllers for active and reactive power: In the forward Euler discretization method,

the variable s is replaced with:

$$s = \frac{z-1}{T_s} \tag{3.25}$$

Replacing (3.25) in (3.15) and (3.16), the transfer functions in the z-domain are obtained as:

$$G_p(z) = k_{pp} + \frac{k_{ip}T_s}{z-1} \tag{3.26}$$

$$G_q(z) = k_{pq} + \frac{k_{iq}T_s}{z-1} \tag{3.27}$$

- PLL: All the integrators of the PLL were discretized using the Forward Euler method, i.e. they were approximated as:

$$\frac{1}{s} = \frac{T_s}{z-1} \tag{3.28}$$

The transfer function of the PI controller of the loop filter in the z-domain is:

$$G_{pll}(z) = k_{pLF} + \frac{k_{iLF}T_s}{z-1} \tag{3.29}$$

- PR current controller: The PR controller was discretized with the zero-order-hold (ZOH) method. The controller transfer function in the z-domain is obtained from the s-domain transfer fuction based on the following formula [116], [117]:

$$G_i(z) = (1-z^{-1})Z\left[L^{-1}\left\{\frac{G_i(s)}{s}\right\}\right] \tag{3.30}$$

which yields:

$$G_i(z) = k_{pi} + \frac{k_{ii}}{\omega_0^2+\omega_c^2}\left(\frac{b_0+b_1z^{-1}+b_2z^{-2}}{1+a_1z^{-1}+a_2z^{-2}}\right) \tag{3.31}$$

where the PR coefficients are calculated as follows:
$b_0 = 0$, $b_1 = \omega_c + \omega_0 e^{-\omega_c T_s} sin(\omega_0 T_s) - \omega_c e^{-\omega_c T_s} cos(\omega_0 T_s)$
$b_2 = \omega_c e^{-2\omega_c T_s} - \omega_c e^{-\omega_c T_s} cos(\omega_0 T_s) - \omega_0 e^{-\omega_c T_s} sin(\omega_0 T_s)$
$a_1 = -2e^{-\omega_c T_s} cos(\omega_0 T_s)$, $a_2 = e^{-2\omega_c T_s}$
For $\omega_c = 0$, the coefficient values of the ideal PR controller are equal to:
$b_0 = 0$, $b_1 = \omega_0 sin(\omega_0 T_s)$, $b_2 = -\omega_0 sin(\omega_0 T_s)$
$a_1 = -2cos(\omega_0 T_s)$, $a_2 = 1$

Table 3.1: Parameters of PI and PR controllers.

Controllers	Values
PI based power controller	$k_{pp} = k_{pq} = 0.1$, $k_{ip} = k_{iq} = 10\ s^{-1}$
PR current controller	$k_{pi} = 20\ \Omega$, $k_{ii} = 150\ \Omega s^{-1}$
SOGI-OSG filters	$k_{vs} = 1$, $k_{is} = 0.1$
PI controller of LF	$k_{pLF} = 0.05$ rad $V^{-1}s^{-1}$, $k_{iLF} = 0.2$ rad $V^{-1}s^{-2}$

3.3.3 Controller design

PI and PR controllers can be designed based on several methods, which are broadly categorized into time-domain and frequency domain methods. In the context of this work, the focus has been placed on examining the impact of the developed control strategy on the voltage unbalance levels across the distribution system, rather than on optimizing the designed controller. Therefore, the PI and PR controllers were designed through trial and error to ensure a stable power and current response at the inverter output, and no specific time-domain or phase-domain performance specifications were set.

Initially, the control system was simulated by considering only the inner (current) loop, and its step response was tested by giving sinusoidal signals of different magnitude as a reference current and observing the inverter output current. The values of the PR gains were modified until a stable and reasonably fast current regulation is achieved. Then, the outer (active and reactive power) loop was added, and it was tuned in a similar way: different step inputs were given as a reference, and the gains were chosen such that the active and reactive power response is stable.

Regarding the gains of the SOGI-OSG for the voltage, PI controller of the Loop Filter and SOGI-OSG for the current, these were determined by operating the inverter in open-loop, i.e. the outer and inner control loops were not connected, and a constant reference voltage was given to the inverter; the obtained orthogonal voltage and current components were monitored, and the gains of the above structures were selected through trial and error, considering the trade-off between the bandwidth and the system dynamic response when choosing the proper k_{vs}, k_{is}, as discussed in Section 3.3.

The selected gains are summarized in Table 3.1. These parameters were used through the simulations of both distribution networks introduced in Chapter 4 and Chapter 5. The parameters were modified in the real-time experiments, as it will be explained in Chapter 6.

Figure 3.16-3.19 show the performance of the BESS control system when the three BESS inverters are controlled to compensate the voltage unbalance caused by an unbalanced three-phase load. The load active and reactive power at each phase is equal to $P_{fa} = 100$ kW, $P_{fb} = 90$ kW, $P_{fc} = 80$ kW and $Q_{fa} = 10$ kvar, $Q_{fb} = 7$ kvar, $Q_{fc} = 5$

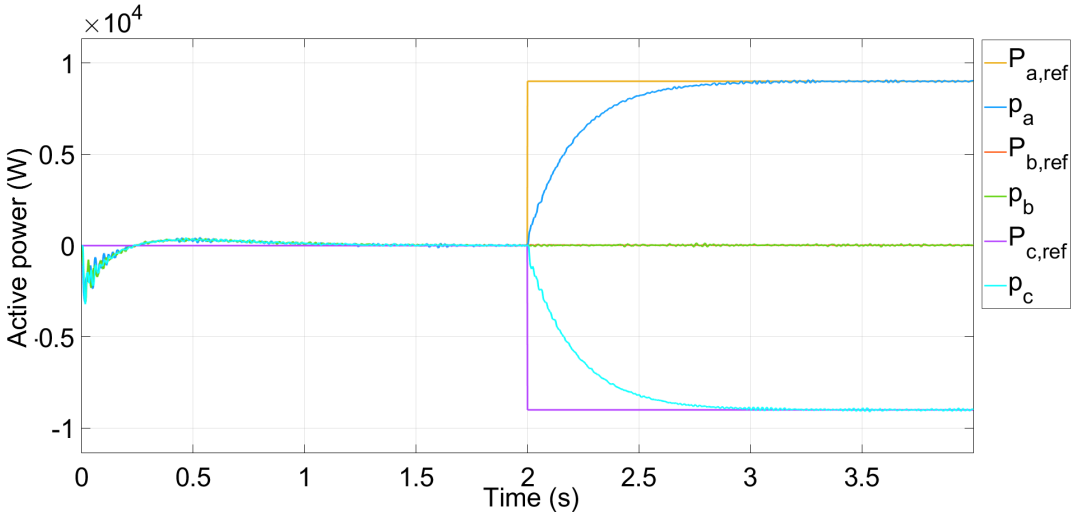

Figure 3.16: Reference and measured inverter active and reactive power.

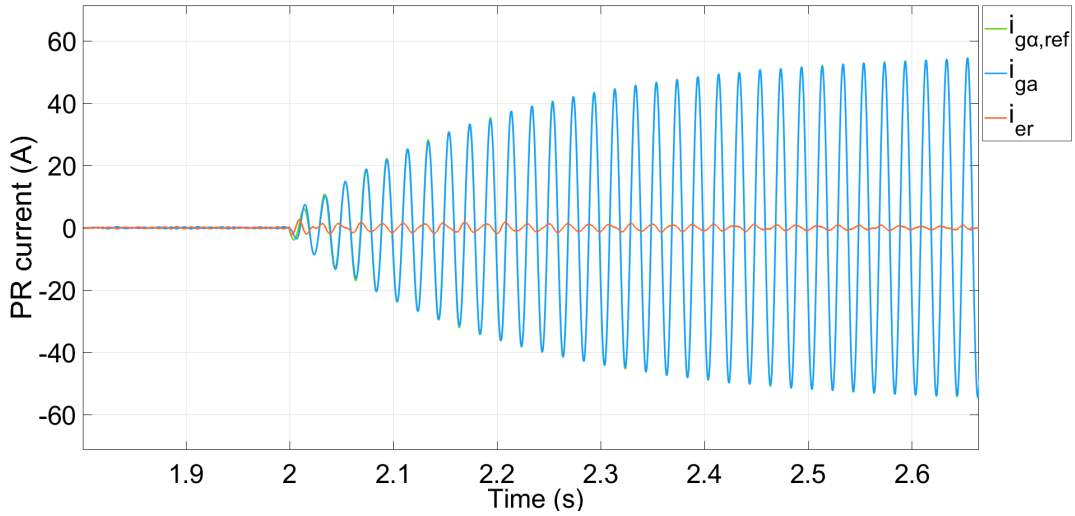

Figure 3.17: Reference and measured inverter current and PR controller error.

kvar, respectively. At $t = 2$ s, the control system is activated, and the BESS inverters mitigate voltage unbalance by injecting and absorbing active and reactive power. Figure 3.16 shows that with the designed PI controller, the active power tracks the reference power in 1 s, while Figure 3.17 shows that with the designed PR controller, phase-a inverter current tracks the reference current within milliseconds and with negligible steady state error.

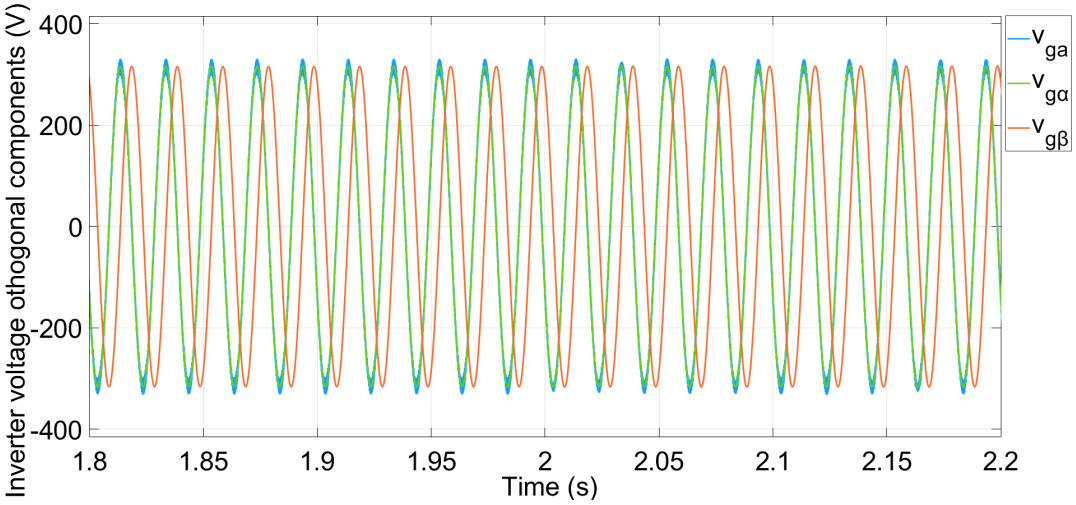

Figure 3.18: SOGI-OSG for phase-a inverter voltage.

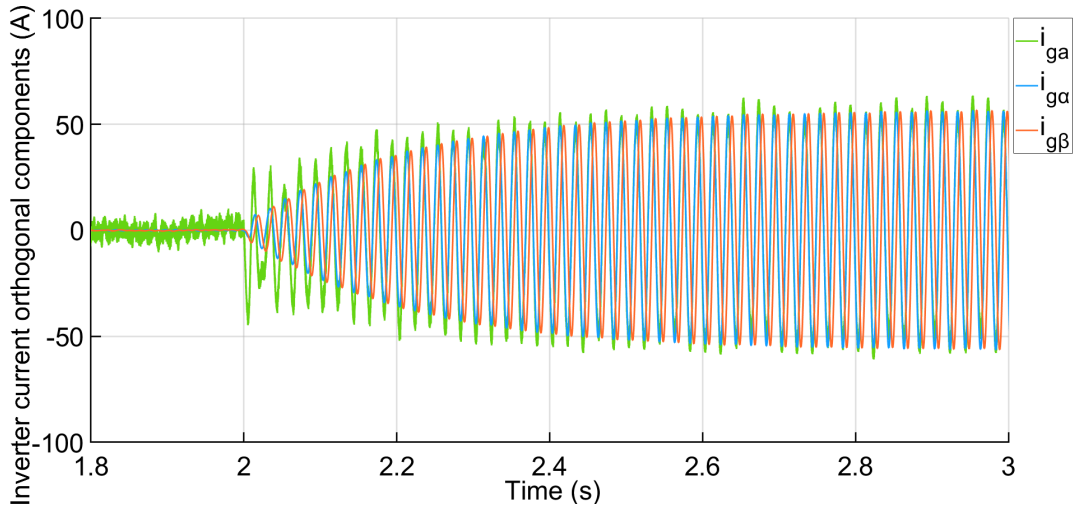

Figure 3.19: SOGI-OSG for phase-a inverter current.

Finally, Figure 3.18-3.19 show that the designed SOGI-OSG systems can extract the orthogonal components of the fundamental voltage and current, respectively.

Furthermore, the stability of the designed PR controller was assessed based on the Bode plot of the open-loop transfer function G_{ol} (given in (3.23)), which is plotted in Figure 3.20 with its discretized transfer function $G_{ol,d}$. It can be seen that for the chosen values of $k_{pi} = 20$ and $k_{ii} = 150$, the system is stable, with infinite gain margin and phase margin equal to PM = 87.5 deg at 883 Hz. The phase margin can be affected by different system conditions, i.e. in case of a weak grid (large value of grid inductance), it can be

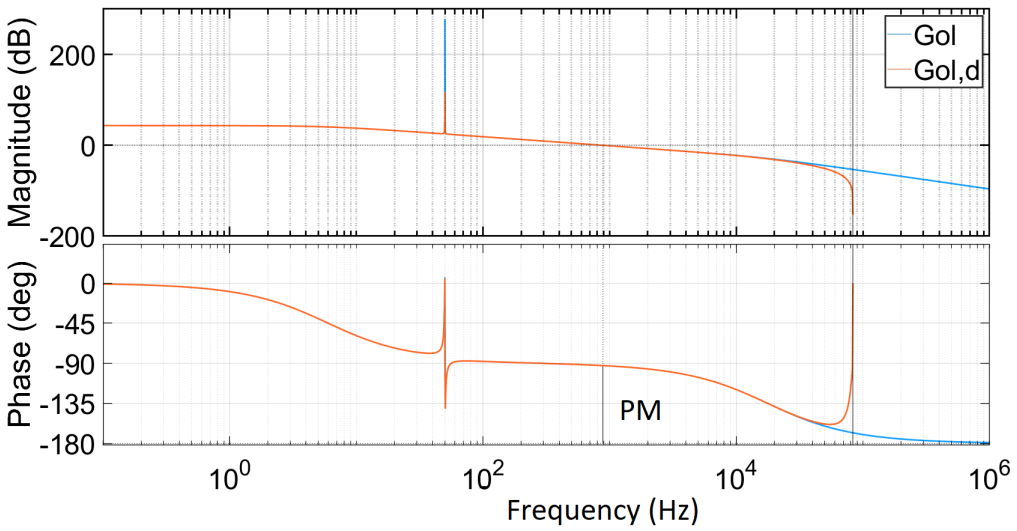

Figure 3.20: Bode plot of the open-loop transfer function $G_{ol}(s)$ and its discretized version.

reduced significantly leading to instability. For the distribution networks under study (Chapter 4-6), a stable inverter and system operation was obtained for all the simulated scenarios.

3.4 Conclusions

In this chapter, the proposed voltage unbalance mitigation strategy was introduced and discussed in detail. The development of the BESS control system was presented, and the function of each component of the control system was analysed. The controller design was demonstrated. The developed control scheme will be validated in Chapter 4 and Chapter 5 by means of simulations, while Chapter 6 will provide the experimental validation.

Chapter 4

Deterministic Validation of Voltage Unbalance Mitigation Strategy in a Rural Distribution System Model

4.1 Introduction

The aim of this chapter is to validate the developed voltage unbalance mitigation strategy. In the first part of the chapter, a single distribution feeder is modelled, and different distributions of static three-phase load demands are considered, with the aim to test the proposed control functionality by controlling either a single or all three single-phase BESS inverters. In the second part of the chapter, a realistic distribution system model based on typical German rural networks is developed, and the single-phase BESS units are controlled to mitigate voltage unbalance caused by single-phase load demands, which are modelled using real data. The impact of the proposed control system is assessed considering realistic operating conditions based on measurements of load demand with a 1-minute resolution. A sensitivity analysis is carried out to investigate the impact of installing the BESS at different locations in the distribution system, in terms of the voltage unbalance factor, transformer zero-sequence current component and BESS size parameters[1].

[1] This chapter is based on the work published in [118].

4.2 Validation of voltage unbalance mitigation strategy using a single feeder

4.2.1 Single feeder model

For the purpose of performing an initial evaluation of the voltage unbalance mitigation functionality provided by the BESS inverters, the model presented in Figure 4.1 was used. Four three-phase static loads (L_{A1}-L_{A4}) were created in Simulink, as described in Appendix C, and they were connected at buses A1-A4. The overhead line consists of four segments of length $\ell_1 = 200$ m, with resistance and reactive inductance equal to 0.358 Ω and 0.252 Ω, respectively. The short circuit level of the network is $\frac{X_s}{R_s} = 12$. A feeder circuit of 3 km, $Z_f = 0.216$+j0.207 Ω was connected between the MV network and the high–voltage side of the distribution transformer. The impedance of the MV source is given by Eq. (4.1), while its angle, resistance and inductance are calculated by (4.2)-(4.3):

$$Z_s = R_s + j\omega L_s \tag{4.1}$$

$$\phi_z = \tan^{-1}\left(\frac{X_s}{R_s}\right) \tag{4.2}$$

$$R_s = \frac{V_n^2}{S_k}\cos(\phi_z), L_s = \frac{V_n^2}{\omega S_k}\sin(\phi_z) \tag{4.3}$$

The upstream grid and distribution transformer parameters are provided in Table 4.1. The BESS units were connected at busbar LV to provide voltage unbalance mitigation, and k_{v2} was measured at busbar LV. Both cases of deploying a single and all three BESS inverters for mitigating voltage unbalance were examined. The BESS nominal apparent power was chosen equal to $S_{gn} = 9$ kVA, as discussed in Section 2.6.

The voltage unbalance compensation algorithm was tested considering four cases of load distribution, for $k = 1, 2, 3, 4$. For each case, different subcases were created by modifying (i) the load type and (ii) the control mode of the BESS inverters. More specifically, the examined load cases and BESS control modes are symbolized as follows:

- $\mathbf{C_{kp}}$: Case k with pure resistive load (P in kW)
- $\mathbf{C_{kq}}$: Case k with pure inductive load (Q in kvar)
- $\mathbf{C_{ks}}$: Case k with combined resistive–inductive load (S in kVA)
- **p–mode**: the inverter is controlled to inject/absorb active power.
- **q–mode**: the inverter is controlled to inject/absorb reactive power.
- **pq–mode**: both active and reactive power are injected/absorbed by the inverter.

Throughout the simulations it is assumed that the load is balanced from $t_1 = 0$ s to $t_2 = 1$

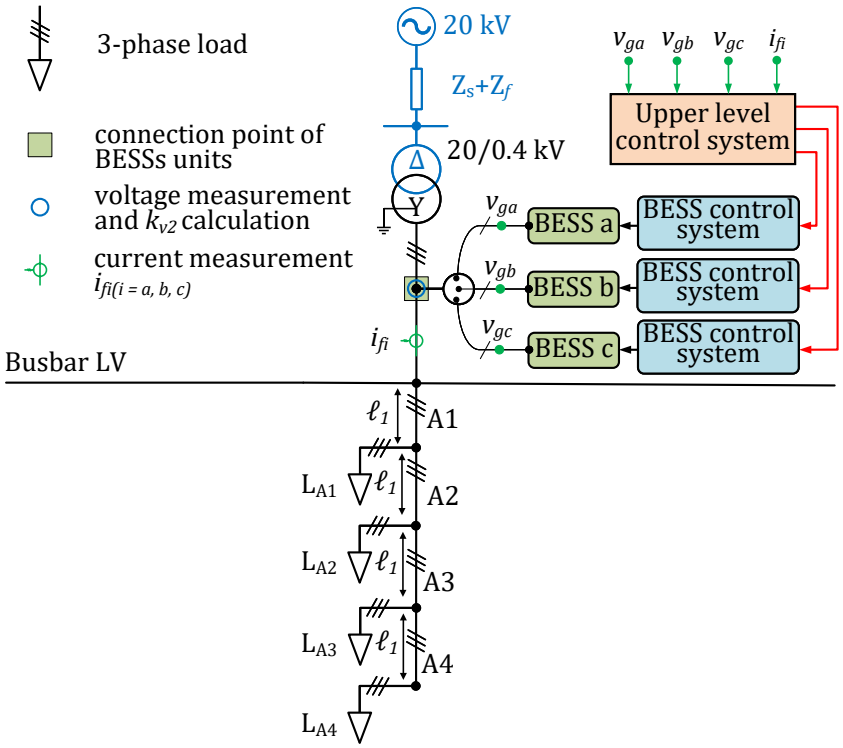

Figure 4.1: Distribution network layout with four static three-phase loads.

Table 4.1: Upstream grid and distribution transformer parameters.

Parameters	Values
Upstream grid	
Short–circuit power	$S_k = 150$ MVA
Nominal voltage	$V_n = 20$ kV
Distribution transformer	
Nominal power	$S_{tr,n} = 250$ kVA
Winding configuration	Dyn5
Short-circuit voltage	$u_k = 6$ %

s, i.e. $P_{L_{Aa,j}} = P_{L_{Ab,j}} = P_{L_{Ac,j}} = 1.33$ kW and $Q_{L_{Aa,j}} = Q_{L_{Ab,j}} = Q_{L_{Ac,j}} = 1$ kvar, for $j = 1, 2, 3, 4$. The load becomes unbalanced at $t_2 = 1$ s, and the compensation signals are sent to the inverter at $t_3 = 2$ s. Table 4.2 presents the unbalanced load distributions among the three phases for the studied cases. In case 1 the unbalance is at phase-a, while a three–phase unbalance is introduced in cases 2 and 3, with phase-b having the lowest and largest load, respectively. In case 4 all the load is allocated at phase-a. The maximum active and reactive power of each three–phase load is 4 kW and 3 kvar, respectively.

Table 4.2: Load distribution for Cases 1-4.

Case	A1	A2	A3	A4	Total load	Units
Case 1						
$\mathbf{C_{1p}}$	[3 0.5 0.5]	[3 0.5 0.5]	[3 0.5 0.5]	[3 0.5 0.5]	[12 2 2]	kW
$\mathbf{C_{1q}}$	[2 0.5 0.5]	[2 0.5 0.5]	[2 0.5 0.5]	[2 0.5 0.5]	[8 2 2]	kvar
$\mathbf{C_{1s}}$	[3.6 0.7 0.7]	[3.6 0.7 0.7]	[3.6 0.7 0.7]	[3.6 0.7 0.7]	[14.4 2.8 2.8]	kVA
Case 2						
$\mathbf{C_{2p}}$	[2 0 2]	[1.5 0.5 2]	[2.5 0.5 1]	[0.5 0.5 3]	[6.5 1.5 8]	kW
$\mathbf{C_{2q}}$	[1.25 0.5 1.25]	[2 0 1]	[1.5 0.25 1.25]	[0.75 1 1.25]	[5.5 1.75 4.75]	kvar
$\mathbf{C_{2s}}$	[2.36 0.5 2.36]	[2.5 0.5 2.24]	[2.9 0.56 1.6]	[0.9 1.12 3.25]	[8.66 2.68 9.45]	kVA
Case 3						
$\mathbf{C_{3p}}$	[1 3 0]	[0.5 2.5 1]	[1 2 1]	[2 2 0]	[4.5 9.5 2]	kW
$\mathbf{C_{3q}}$	[1 1.5 0.5]	[0.5 2 0.5]	[1.5 1 0.5]	[0.5 1.5 1]	[3.5 6 2.5]	kvar
$\mathbf{C_{3s}}$	[1.41 3.36 0.5]	[0.71 3.2 1.12]	[1.8 2.24 1.12]	[2.06 2.5 1]	[6 11.3 3.74]	kVA
Case 4						
$\mathbf{C_{4p}}$	[4 0 0]	[4 0 0]	[4 0 0]	[4 0 0]	[16 0 0]	kW
$\mathbf{C_{4q}}$	[3 0 0]	[3 0 0]	[3 0 0]	[3 0 0]	[12 0 0]	kvar
$\mathbf{C_{4s}}$	[5 0 0]	[5 0 0]	[5 0 0]	[5 0 0]	[20 0 0]	kVA

For all cases, only the plots for operation of the three inverters in pq–mode are provided. A list of the plotted electrical quantities and the points of measurements are provided next (for $i = a, b, c$, while $j = 1, 2, 0$ is used to represent the positive-, negative- and zero-sequence component of the measured quantity, respectively).

1. Active, reactive and apparent power:
   - Terminal of each inverter (p_{gi}, q_{gi}) and sum of powers ($p_{g,tot}$, $q_{g,tot}$).
   - Busbar LV: power per phase (p_{LVi}, q_{LVi}), sum of powers ($p_{LV,tot}$, $q_{LV,tot}$, $s_{LV,tot}$).
   - Beginning of feeder A: power per phase (p_{fi}, q_{fi}), sum of powers ($p_{f,tot}$, $q_{f,tot}$).
2. root-mean-square (rms) current values:
   - Terminal of each inverter ($i_{gi,rms}$).
   - Busbar LV ($i_{LVi,rms}$, neutral current $i_{LVn,rms}$ and $i_{LVa,j,rms}$).
3. Instantaneous current values:
   - Terminal of each inverter (i_{gi}).
   - Busbar LV (i_{LVi}).
   - Beginning of feeder A (i_{fi}).
4. Magnitudes of inverter current symmetrical components ($|i_{ga,j}|$).
5. Sum of instantaneous current values:
   - Busbar LV ($\sum i_{LVi}$).
   - Terminals of the three inverters ($\sum i_{gi}$).

Table 4.3: Voltage unbalance factor for Cases 1-4.

Load cases	$k_{v2}(\%)$			
	Base case	pq–mode	p–mode	q–mode
$\mathbf{C_{1p}}$	2.25	0.15	0.15	2.25
$\mathbf{C_{1q}}$	1.4	0.11	1.4	0.11
$\mathbf{C_{1s}}$	2.5	0.13	1.35	2.25
$\mathbf{C_{2p}}$	1.4	0.15	0.15	1.4
$\mathbf{C_{2q}}$	0.8	0.14	0.8	0.14
$\mathbf{C_{2s}}$	1.8	0.14	0.8	1.4
$\mathbf{C_{3p}}$	1.5	0.15	0.15	1.5
$\mathbf{C_{3q}}$	0.75	0.1	0.75	0.1
$\mathbf{C_{3s}}$	1.7	0.15	0.75	1.5
$\mathbf{C_{4p}}$	3.5	0.23	0.23	3.5
$\mathbf{C_{4q}}$	2.75	0.2	2.75	0.2
$\mathbf{C_{4s}}$	4.15	1	2.5	3.4

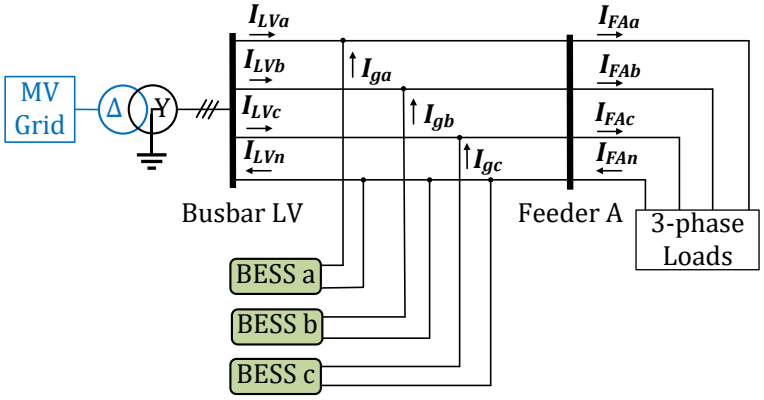

Figure 4.2: Three-phase representation of Figure 4.1.

The simulation results obtained for Case 1 are presented in detail, while the results for Cases 2-4 are described in Appendix F. Table 4.3 contains the aggregated results of k_{v2} for Cases 1-4, without (base case) and with BESS compensation.

Figure 4.2 is a three-phase representation of the distribution network layout of Figure 4.1, and it presents the currents measured at busbar LV, inverter terminals and beginning of feeder A. These quantities are plotted for the cases under study.

4.2.2 Simulation results

The simulation results of this section are organized as follows: Sections 4.2.2.1, 4.2.2.3 and 4.2.2.4 present the results obtained for pure resistive, pure inductive and combined

resistive-inductive load, respectively. In these cases, all three inverters are controlled to compensate voltage unbalance by operating in pq-mode. At the end of each section, the results for inverter operation in p-mode and q-mode are briefly summarized.

Additionally, Section 4.2.2.2 presents the results when only phase-a inverter is controlled to mitigate voltage unbalance caused by a purely resistive load with the aim to show that the proposed functionality can be provided independently by a single BESS unit. This case could arise when the desired operation cannot be achieved by the three BESSs simultaneously (because of maintenance or unavailability of charge from the battery, for example). In addition, depending on the unbalance profile of the system under consideration, e.g. for a three-phase feeder with the heavy loading in one phase, it may be unnecessary to deploy the proposed functionality in the three units at the same time.

4.2.2.1 Case C_{1p} (pq–mode): [12 2 2] kW

A pure resistive load is considered, and the unbalance is at phase-a. The load is balanced from $t_1 = 0$ s to $t_2 = 1$ s, when it becomes unbalanced causing asymmetrical power flows at busbar LV, and thereby introducing voltage unbalance at that point, with $k_{v2} = 2.25\%$. Since the reference power signals are sent to the inverters at $t_3 = 2$ s, the active and reactive power measured at the terminal of each inverter are zero from $t_1 = 0$ s to $t_3 = 2$ s, as can be seen in Figure 4.3(a)-(c).

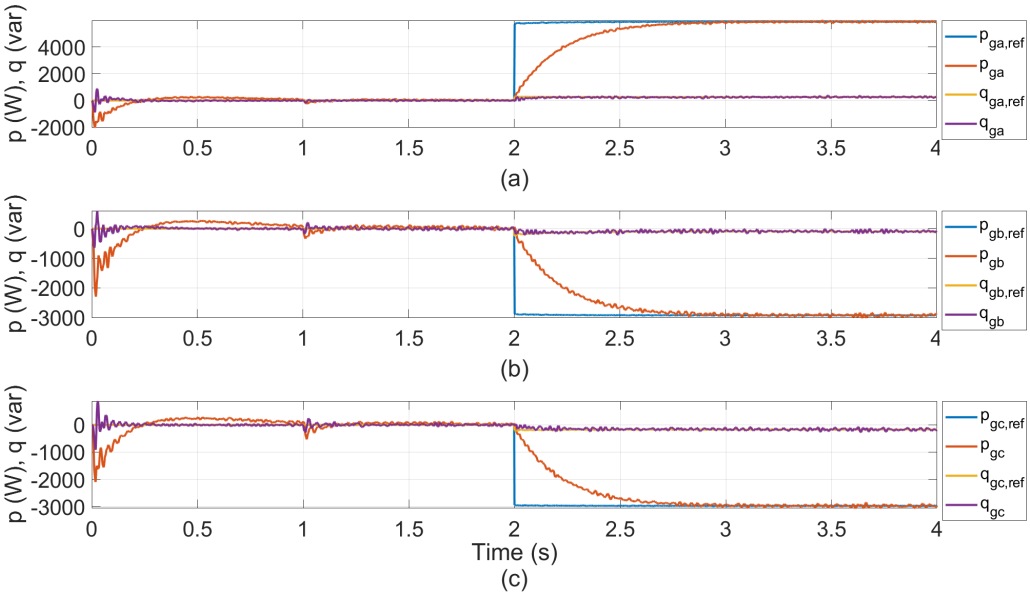

Figure 4.3: Reference and measured active and reactive power at the terminal of each inverter: (a) phase-a, (b) phase-b and (c) phase-c.

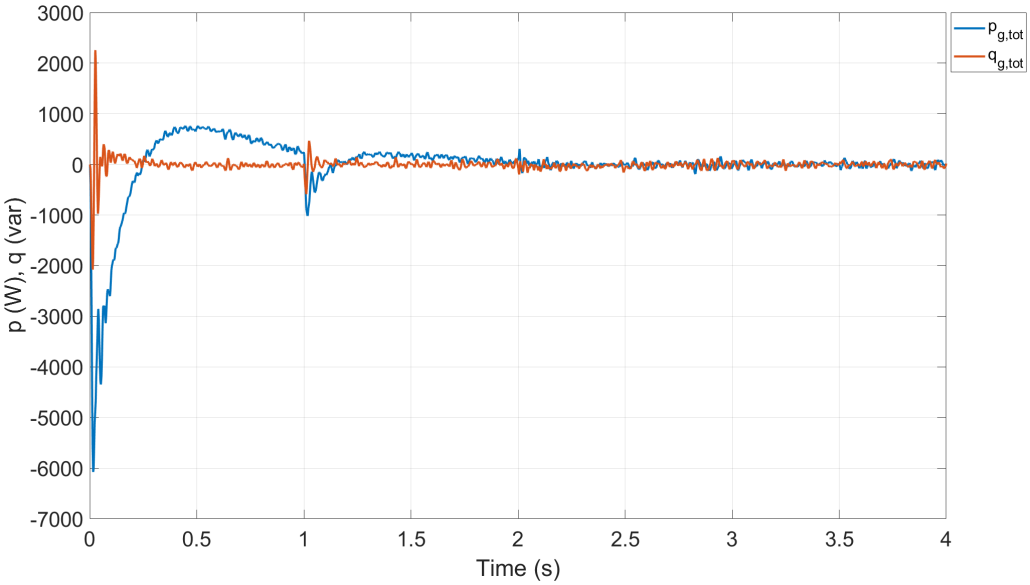

Figure 4.4: Sum of active and reactive power measured at the terminals of the three inverters.

When the compensating mechanism is activated at $t_3 = 2$ s, the three BESS units start to compensate the unbalance by injecting and absorbing active power. Figure 4.3(a)-(c) show that the three BESS units regulate their active power output to the reference value within 1 s, which was shown to be the response time of the designed PI controller presented in Subsection 3.3.3. More specifically, phase-a BESS unit discharges $p_{ga} = 5.9$ kW to the load, while phase-b and phase-c BESS units charge $p_{gb} = -2.92$ kW and $p_{gc} = -2.97$ kW from the grid, respectively. As a result, the active power flows converge at busbar LV, i.e. phase-a active power is decreasing, while phase-b and phase-c active power are increasing at that point, thereby leading to a reduction in the voltage unbalance levels, with $k_{v2} = 0.15\%$. Note that since voltage unbalance is introduced due to load active power mismatch, the reactive power measured in the output of the BESS units is negligible, i.e. phase-a BESS unit injects $q_{ga} = 265$ var, while phase-b and phase-c BESS units absorb $q_{gb} = -98$ var and $q_{gc} = -175$ var, respectively. It is worth mentioning that both active and reactive power values are well below the BESS inverter ratings.

The charging and discharging pattern observed above for the three BESS units is the expected one, since when the unbalance is at one phase, the BESS units connected at the other two phases contribute to voltage unbalance mitigation with the same amount of power (as proved in Section F.10 of Appendix F analytically). At the same time, based on (3.9), it has been shown that the total power exchanged between the three BESSs

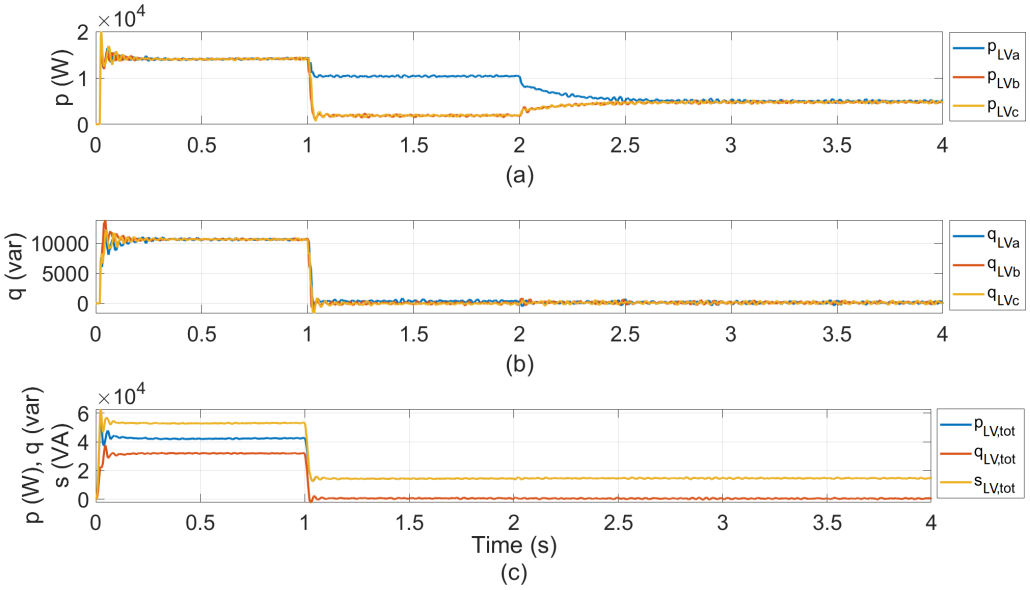

Figure 4.5: (a) Active and (b) reactive power at each phase, and (c) total active, reactive and apparent power measured at bus LV.

and the system is zero. This is depicted in Figure 4.4, where the sum of the active and reactive power measured at the terminals of the three inverters are plotted. Therefore, for the case under study, phase-a inverter active power is twice the active power charged by phase-b and phase-c inverter units.

Figure 4.5 shows the active and reactive power flows at the secondary side of the transformer (busbar LV). From $t_1 = 0$ s to $t_2 = 1$ s, the active and reactive power flows are symmetrical and equal to 14 kW and 10.7 kvar, respectively, due to the presence of balanced load. From $t_2 = 1$ s to $t_3 = 2$ s, the load becomes unbalanced, therefore most of the load power flows through phase-a, i.e. $p_{LVa} = 10.3$ kW and $q_{LVa} = 400$ var (not visible from the graph, due to the scale used), while $p_{LVb} = p_{LVc} = 2$ kW and $q_{LVb} = q_{LVc} = 0$ var. At $t_3 = 2$ s, the compensating action from the inverters leads to a gradual decrease in phase-a active power, since phase-a BESS unit is discharging, while phase-b and phase-c BESS units are charging, drawing active power from phase-b and phase-c of the transformer, based on the discussion carried out in the preceding paragraph. As a result, the active power flows converge to 5 kW, as shown in Figure 4.5(a).

Similarly, Figure 4.5(b) demonstrates that convergence of the reactive power flows is achieved: phase-a reactive power flow is slightly reduced, while phase-b and phase-c reactive power flows are slightly increased due to the reactive power injected and absorbed

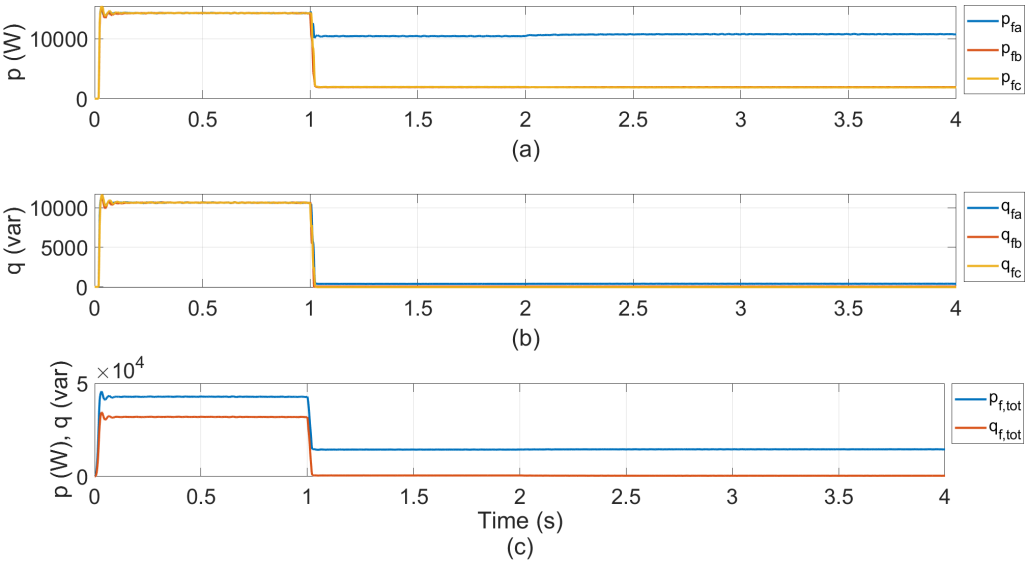

Figure 4.6: (a) Active and (b) reactive power at each phase, and (c) total active and reactive power measured at the feeder.

from the inverters in these phases, respectively.

Figure 4.5(c) presents the total active, reactive and apparent power flow at the secondary of the transformer. Focusing in the time period from $t_1 = 1$ s to $t_3 = 4$ s, the total apparent power remains the same before and after the compensation from the BESS units. This is the expected result. More specifically, the sum of the apparent power dissipated by the feeder loads at the three phases remains unchanged during this period (as shown in Figure 4.6(c)), the only difference being that the zero- and negative-sequence load current components are provided by the BESSs after the compensation, while before the compensation these two components were fed by the grid (i.e. busbar LV). Considering that the sum of the apparent power measured at the terminals of the three BESSs is zero (as shown in Figure 4.4), it can be deduced that the total apparent power flow at busbar LV is not altered.

The phase and total active and reactive power flows through the feeder are presented in Figure 4.6(a)-(c). While the active and reactive power flows are symmetrical from $t_1 = 0$ s to $t_2 = 1$ s, the introduction of the unbalanced load at $t_2 = 1$ s causes unsymmetrical power flows, with $p_{fa} = 10.4$ kW, $p_{fb} = 1.91$ kW, $p_{fc} = 1.96$ kW, while $q_{fa} = 375$ var, $q_{fb} = 36$ var, $q_{fc} = -43$ var, as demonstrated in Figure 4.6(a) and Figure 4.6(b), respectively. The load active power consumed at each phase is lower than the nominal load power, i.e. [12 2 2] kW, due to the voltage drop across the feeder. Comparing the total active and reactive power flows before and after the compensation, it

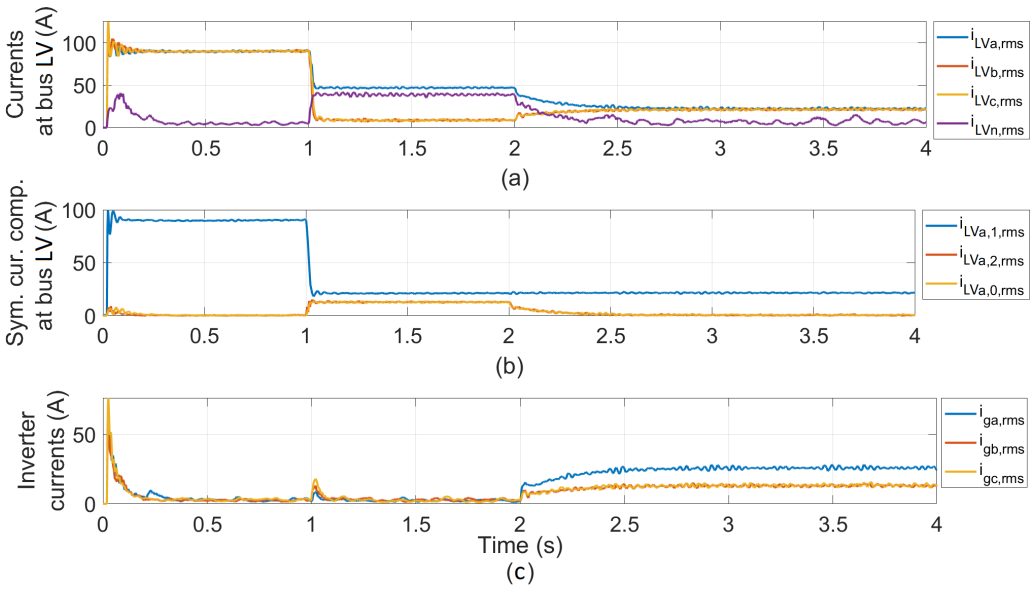

Figure 4.7: rms values of (a) phase and neutral currents at bus LV (b) symmetrical current components at bus LV, and (c) inverter currents.

can be observed that they slightly change from $p_{f,tot} = 14.4$ kW to 14.6 kW and from $q_{f,tot} = 527$ var to 386 var, respectively. As discussed above, the values of these quantities remain almost unchanged after the compensating action from the BESS units.

Throughout the following paragraphs, the curves of the currents measured at busbar LV, inverter terminals and beginning of feeder A (see Figure 4.2) are examined and discussed in detail.

Figure 4.7(a)-(c) present the rms values of the phase and neutral currents at busbar LV, symmetrical components at the same bus and inverter currents. Figure 4.7(a) shows that from $t_1 = 0$ s to $t_2 = 1$ s, i.e. under balanced conditions, the rms values of the phase currents measured at the secondary of the transformer are equal to 90 A, and the current flowing through the neutral conductor of the transformer is close to zero. During this period, only the positive–sequence current component flows through the transformer, with its value being equal to 90 A, as can be seen in Figure 4.7(b). From $t_2 = 1$ s to $t_3 = 2$ s, i.e. under unbalanced conditions, most of the current flows through phase-a, with $i_{LVa,rms} = 47$ A and $i_{LVb,rms} = i_{LVc,rms} = 9$ A, therefore giving rise to the neutral current value. As demonstrated in Figure 4.7(b), a considerable amount of negative- and zero currents are flowing through the transformer, with $i_{LVa,2,rms} = i_{LVa,0,rms} = 13$ A, while the positive-sequence current component is equal to $i_{LVa,1,rms} = 21$ A.

The compensating action from the BESS units starts at $t_3 = 2$ s, causing the currents

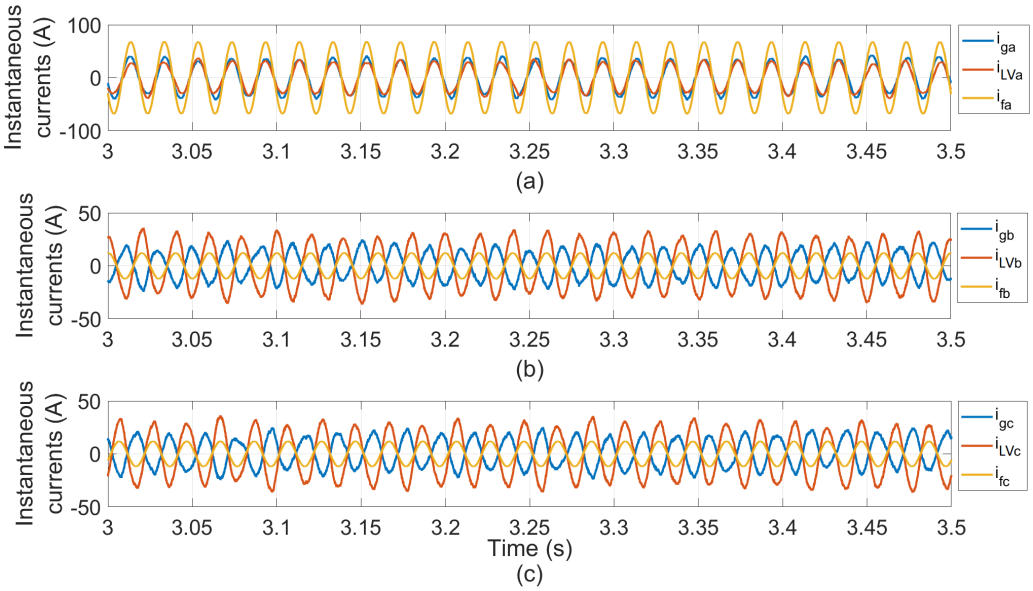

Figure 4.8: Instantaneous values of currents measured at bus LV, inverter terminal and feeder A for (a) phase a, (b) phase b and (c) phase c.

to converge at 21 A and achieving mitigation of the neutral current. From $t_3 = 2$ s onwards, the negative– and zero–sequence current components gradually decrease to zero, since the three BESS inverters provide the negative– and zero–sequence components of the load current, therefore only the positive–sequence component flows through the transformer. Figure 4.7(c) shows that the rms values measured at the inverter terminals are equal to $i_{ga,rms} = 27$ A and $i_{gb,rms} = i_{gc,rms} = 14$ A.

The compensation mechanism is further explained with the use of Figure 4.8(a)-(c), which shows the instantaneous current values measured at the inverter terminals, bus LV and feeder A. The three currents are plotted over 0.5 s, when the steady-state condition has been reached and the three BESS units are providing voltage unbalance compensation. The currents of the same phase are coplotted. Figure 4.8(a) shows that phase-a feeder current is provided by both the transformer and the inverter: the transformer provides the positive-sequence component, while the inverter provides the negative- and zero-sequence components of the load current. Both phase-b and phase-c inverter and transformer currents are in anti–phase, since the inverters draw current from the grid in these two phases to equalize the power flows at bus LV, as Figure 4.8(b)-(c) show.

The instantaneous inverter currents are plotted together in Figure 4.9(a) for a period of 0.5 s, when the steady-state condition has been reached. Based on the observed phase sequence, it can be easily deduced that the three BESS inverters inject an unsymmetrical

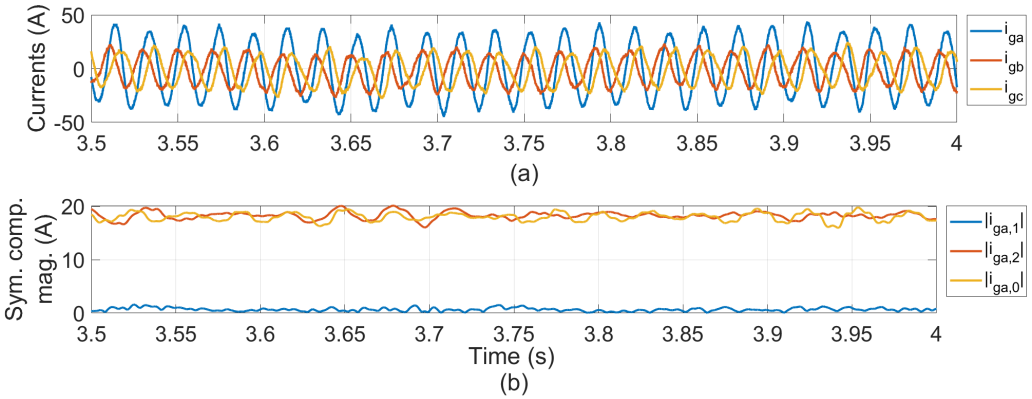

Figure 4.9: Currents measured at inverter terminal (a) instantaneous values and (b) magnitudes of their symmetrical components.

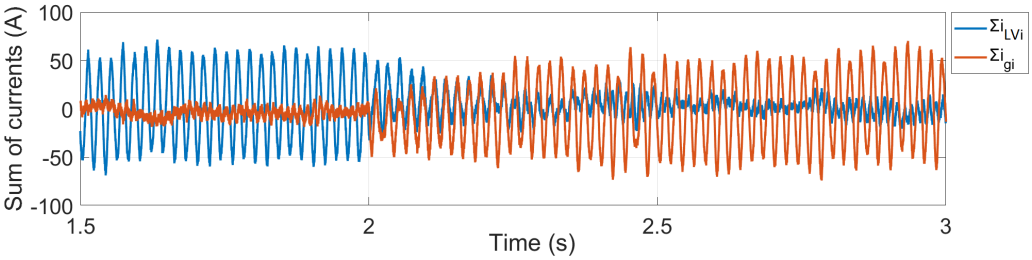

Figure 4.10: Sum of instantaneous phase currents at bus LV and inverter terminals.

current triplet, which includes the negative- and zero-sequence component of the load. The magnitudes of the inverter symmetrical components are provided in Figure 4.9(b), which shows that the magnitudes of the negative– and zero–sequence current components are equal to $|i_{ga,2}| = |i_{ga,0}| = 19$ A, i.e. their rms values are equal to $i_{ga,2,rms} = i_{ga,0,rms} = 13.4$ A. Notably, these values coincide with those observed in Figure 4.7(b) in the time period between $t_1 = 1$ s and $t_2 = 2$. In others words, during that period the negative– and the zero–sequence components of the load were provided by the transformer, while after $t_2 = 2$ these two current components are provided by the BESS inverters.

The sums of the phase currents at the transformer secondary side (blue curve) and at the inverter terminals (red curve) are plotted in Figure 4.10, and they can be expressed as follows:

$$i_{LVn} = \sum_{i=a}^{c} i_{LVi} = i_{LVa} + i_{LVb} + i_{LVc} \tag{4.4}$$

$$\sum_{i=a}^{c} i_{gi} = i_{ga} + i_{gb} + i_{gc} \tag{4.5}$$

where i_{LVn} is the transformer neutral current. Before $t_3 = 2$ s, the load is unbalanced, and the BESS inverters are not providing any unbalance compensation. The load current is provided solely by the transformer, and the feeder neutral current flows through the transformer neutral conductor. At $t_3 = 2$ s, the inverters start to compensate the voltage unbalance by injecting the negative– and zero–sequence load current components. As a result, the feeder neutral current is gradually flowing through the inverters, therefore resulting in a significant reduction of the transformer neutral current.

The above results demonstrate the positive impact of the proposed control strategy on reducing the transformer neutral current. Since in a four-wire, three-phase system, the neutral current is three-times the zero sequence current component, the BESS units are able to mitigate the current flowing to the transformer neutral conductor by providing the zero-sequence load current component.

Finally, the results obtained for inverter operation in p-mode and q-mode are summarized below:

- **p-mode**: The inverters are controlled to inject/absorb only active power, while the reference reactive power is kept to zero. Since the voltage unbalance arises from the active power mismatch of the load, it is expected that the unbalance levels will not be affected if no reactive power is injected/absorbed by the inverters. Indeed, for this operation mode, $k_{v2} = 0.15\%$ is obtained, similar to the value of k_{v2} calculated for inverter operation in pq-mode, which was examined throughout this section.
- **q-mode**: The inverters are controlled to inject/absorb only reactive power, while the reference active power is kept to zero. Based on Figure 4.5, there is a very low reactive power unbalance due to the positive phase-a reactive power flow. Therefore, phase-a inverter injects reactive power, while phase-b and phase-c inverters absorb reactive power to equalize the reactive power flows at busbar LV. However, the effect of this compensation on k_{v2} is negligible. Since a purely resistive load has been considered, the main source of unbalance in the system is active power unbalance, therefore active power injection/absorption is needed to eliminate it, as it has already been discussed.

4.2.2.2 Case C_{1p} (pq–mode) – one BESS inverter in service

In this case, only phase-a inverter is connected to the network with the aim to examine its impact on mitigating voltage unbalance. Since only phase-a negative- and zero-sequence components of the load current are compensated, the unbalance cannot be fully mitigated. However, the proposed strategy still has positive impact on reducing voltage unbalance, but it is less effective. In particular, the voltage unbalance factor is reduced to $k_{v2} = 0.8\%$.

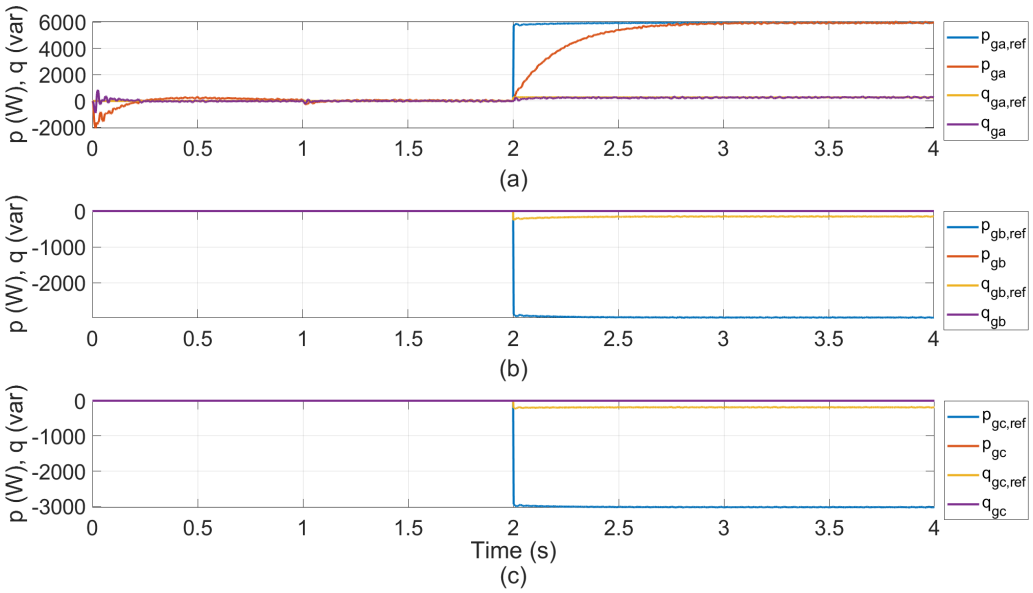

Figure 4.11: Reference and measured active and reactive power at the terminal of each inverter: (a) phase-a, (b) phase-b and (c) phase-c.

Figure 4.11 shows the reference active and reactive power of each inverter as calculated by the voltage unbalance correction algorithm. Although the reference power values are calculated for phase-b and phase-c inverters, they are not used. Only phase-a BESS unit is in service, discharging active power equal to 5.9 kW and injecting reactive power of 265 var. By comparison of Figure 4.11(a) to Figure 4.3(a), it can be observed that both active and reactive power values coincide with those measured at the terminal of phase-a inverter for the case where all three BESS inverters were controlled for voltage unbalance mitigation.

In contrast to the case when all three BESS inverters are in service, the sum of the active and reactive power of the inverters is not zero when a single inverter is controlled to mitigate voltage unbalance. More specifically, Figure 4.12 shows that the total power values will be positive. As a result, only the phase-a active and reactive power of the transformer are affected, i.e., both power values are reduced, as demonstrated in Figure 4.13(a)-(b). However, since the phase-b and phase-c active and reactive power values remain unchanged, voltage unbalance is only partially mitigated.

Additionally, the total active, reactive and apparent power are reduced, as depicted in Figure 4.13(c). This case demonstrates that apart from the reduction in the voltage unbalance levels, the control of the BESS unit may also have a positive impact on the distribution system by reducing the power losses in the transformer.

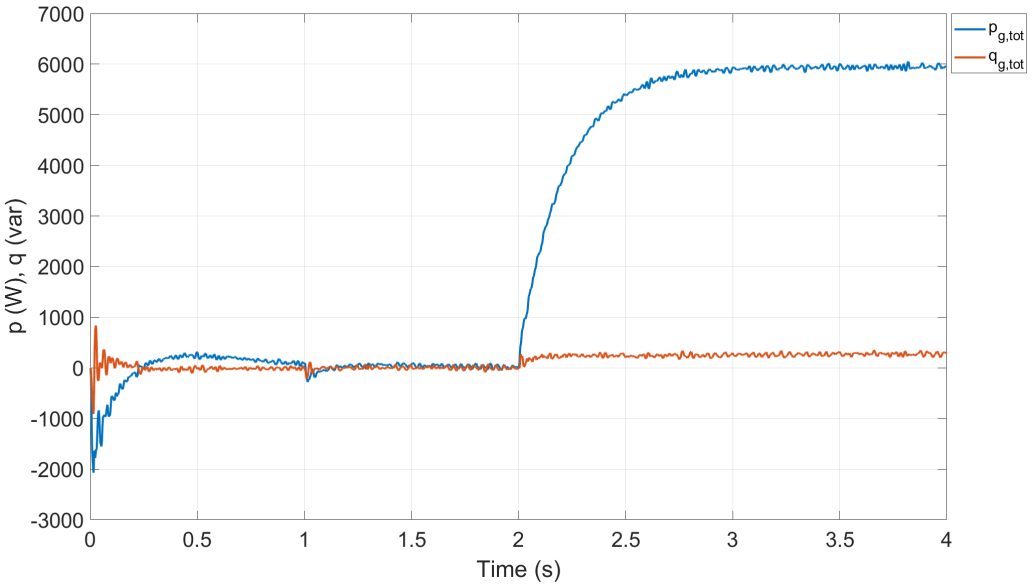

Figure 4.12: Sum of active and reactive power measured at the terminals of the three inverters.

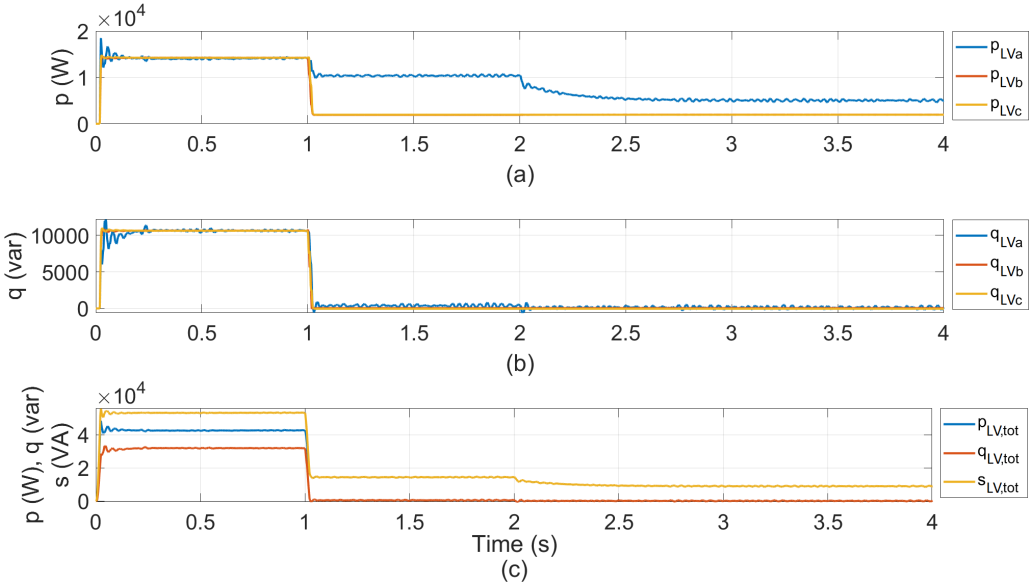

Figure 4.13: Power measured at bus LV: (a) Active power at each phase, (b) reactive power at each phase, (c) total active, reactive and apparent power.

Similar to the observations made for the active and reactive power flow at busbar LV, Figure 4.14(a) demonstrates that the compensation of voltage unbalance by phase-

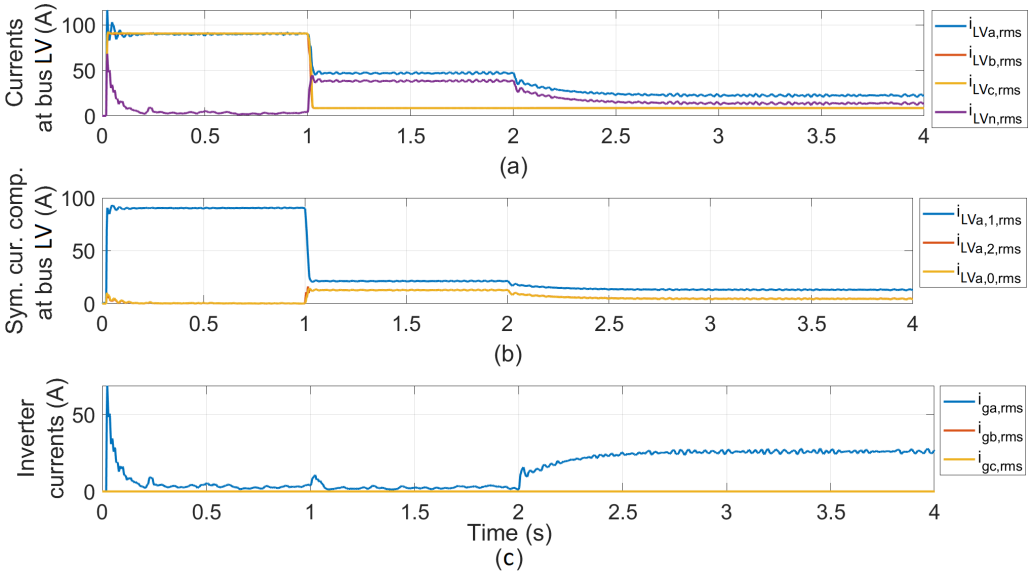

Figure 4.14: Current measurements: (a) bus LV rms, (b) bus LV symmetrical current components and (c) inverter rms.

a BESS unit causes a decrease in phase-a transformer current, since phase-a inverter injects current at this phase. As a result, Figure 4.14(b) shows that the negative– and zero–sequence components of the transformer current are partially reduced and not fully mitigated, as in the case where all three inverters were controlled to mitigate voltage unbalance.

Notably, in contrast to the case when the three inverters were utilized for unbalance compensation, in this case the positive–sequence transformer current component is also affected, i.e. it is reduced, since phase-a BESS unit is not solely injecting the negative- and zero-sequence current components, but also the positive-sequence current component. More specifically, Figure 4.15(b) demonstrates that when phase-a BESS inverter is controlled to provide voltage unbalance mitigation, the positive-, negative- and zero-sequence current components injected by the inverter are equal, i.e. $|i_{ga,1}| = |i_{ga,2}| = |i_{ga,0}| = 12.3$.

Finally, Figure 4.16 shows that when only phase-a inverter is in service, only part of the feeder neutral current flows through the inverter, thus the current flowing through the transformer neutral is higher compared to the case when all three inverters are utilized for voltage unbalance compensation (compare with Figure 4.10, where the neutral current represented by the blue curve is driven to zero).

Based on the obtained results, it can be deduced that a single BESS inverter can reduce voltage unbalance partially, while all three inverters are needed to fully mitigate

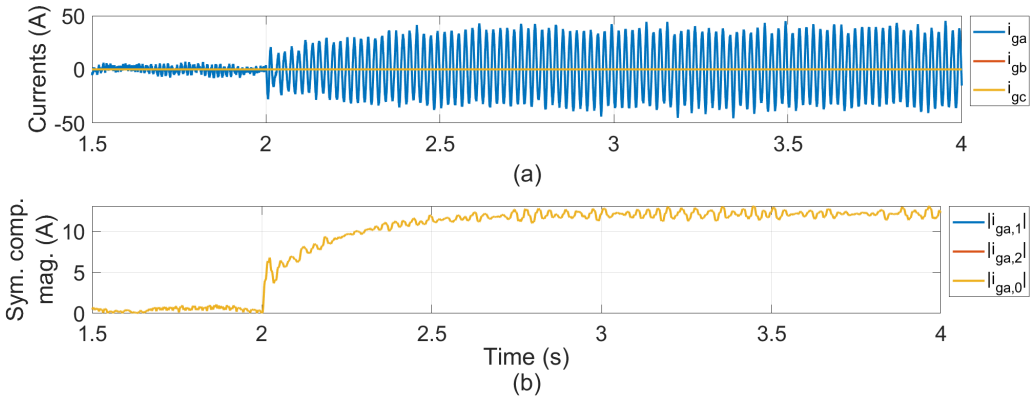

Figure 4.15: Currents measured at inverter terminal (a) instantaneous values and (b) magnitudes of their symmetrical components.

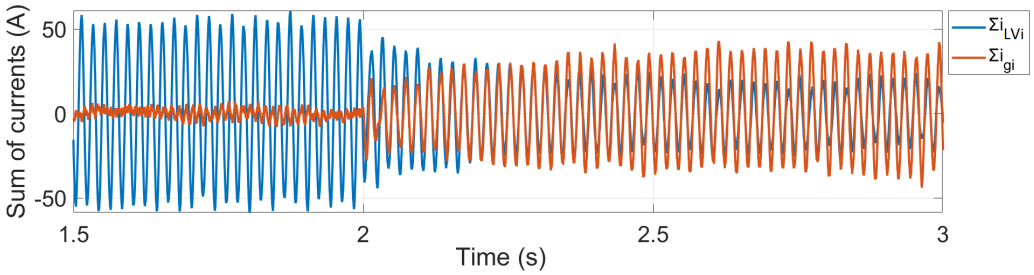

Figure 4.16: Sum of the instantaneous phase currents at bus LV and inverter terminal.

voltage unbalance. This is due to the fact that a single inverter can compensate only the negative– and zero–sequence current components of the phase to which it is connected, while the simultaneous control of all inverters leads to compensation of the negative– and zero–sequence current components of all three phases.

4.2.2.3 Case C_{1q} (pq–mode): [8 2 2] kvar

A purely inductive load is modelled. The compensating action from the BESS inveters reduces the voltage unbalance factor from $k_{v2} = 1.4\%$ to 0.11%. Since the largest reactive power load is located at phase-a, phase-a inverter injects reactive power equal to $q_{ga} = 3.7$ kvar, while phase-b and phase-c inverters absorb reactive power equal to $q_{gb} = -1.87$ kvar and $q_{gc} = -1.82$ kvar to equalize the reactive power flows at busbar LV, as depicted in Figure 4.17. The amount of active power injected and absorbed is negligible. The sum of active and reactive power of the inverters is zero; for brevity, the corresponding plot is omitted here and for the rest of the presented cases.

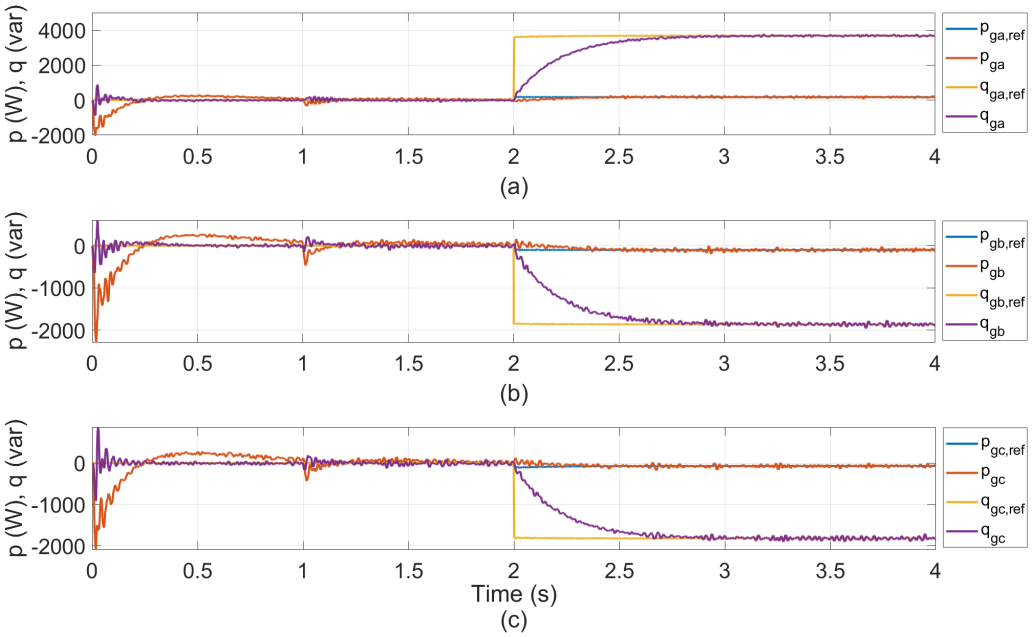

Figure 4.17: Reference and measured active and reactive power at the terminal of each inverter: (a) phase-a, (b) phase-b and (c) phase-c.

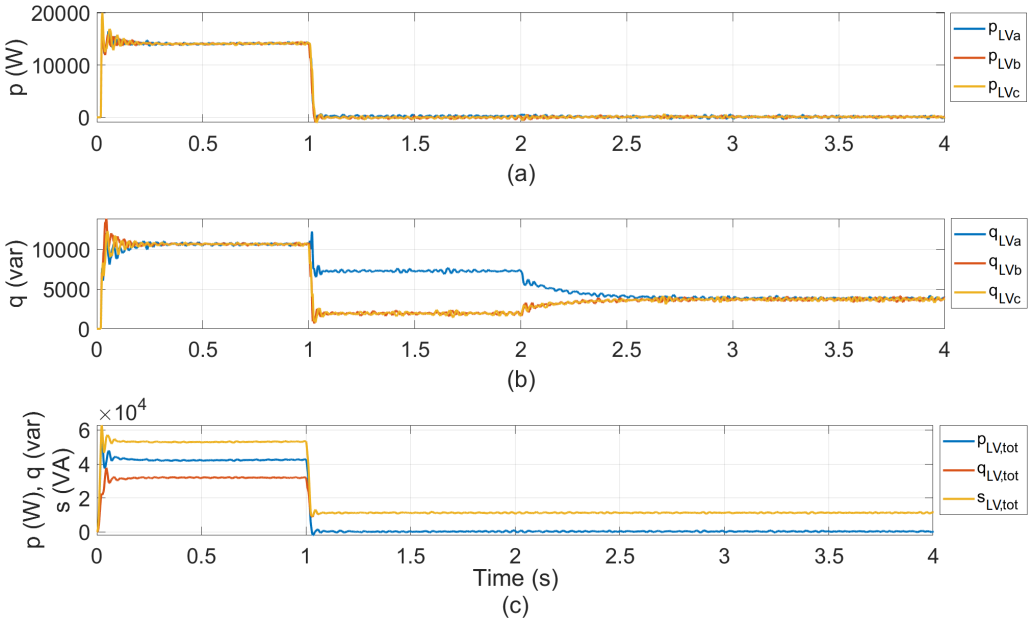

Figure 4.18: (a) Active and (b) reactive power at each phase, and (c) total active, reactive and apparent power measured at busbar LV.

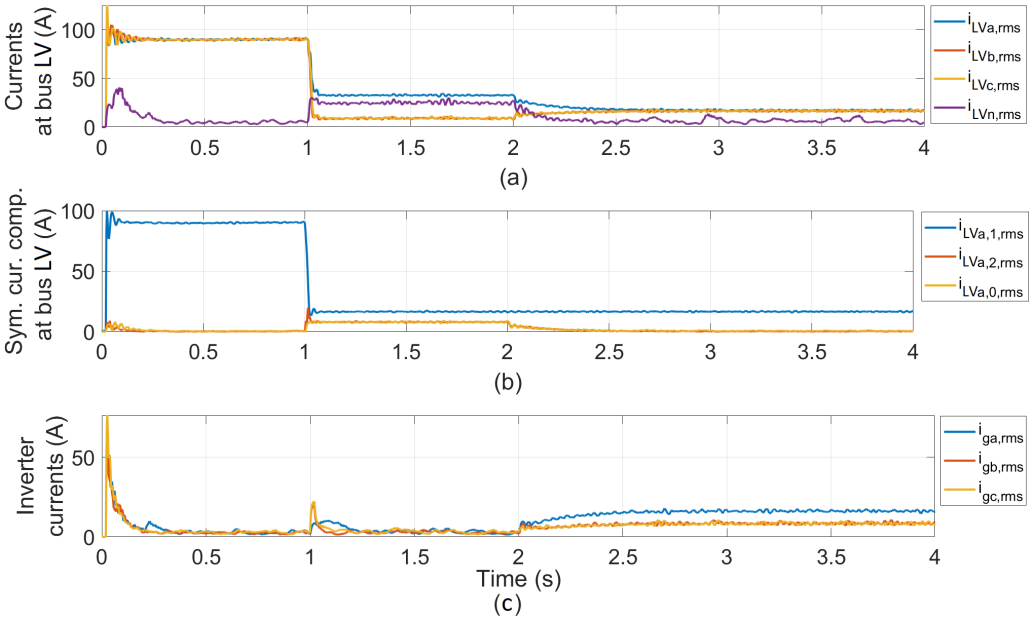

Figure 4.19: rms values of (a) phase and neutral currents at bus LV (b) symmetrical current components busbar LV, and (c) inverter currents.

Figure 4.18(a) shows that a small amount of active power starts flowing at phase-a at $t_2 = 1$ s due to the presence of reactive power unbalance. The active and reactive power unbalance at busbar LV are compensated by the inverters, as shown in Figure 4.18(a)-(b), since the power values start converging after $t_3 = 2$ s.

Similar to the case of the purely resistive load, Figure 4.19(a)-(b) show that the compensating action of the inverters mitigates the neutral current, the zero- and negative-sequence current components at the transformer by injecting asymmetrical currents, as shown in Figure 4.19(c).

Finally, the magnitudes of the zero- and negative-sequence inverter current components are plotted in Figure 4.20, which shows that these two components have the same magnitude, while there is not any positive-sequence current component injection from the BESS units.

Next, the results obtained for inverter operation in p-mode and q-mode are briefly summarized:

- **p-mode**: Since the voltage unbalance arises due to the reactive power load mismatch, the voltage unbalance factor is not affected for inverter operation in p–mode, i.e. $k_{v2} = 1.4\%$.
- **q-mode**: When the inverter is operated to inject only reactive power, the obtained

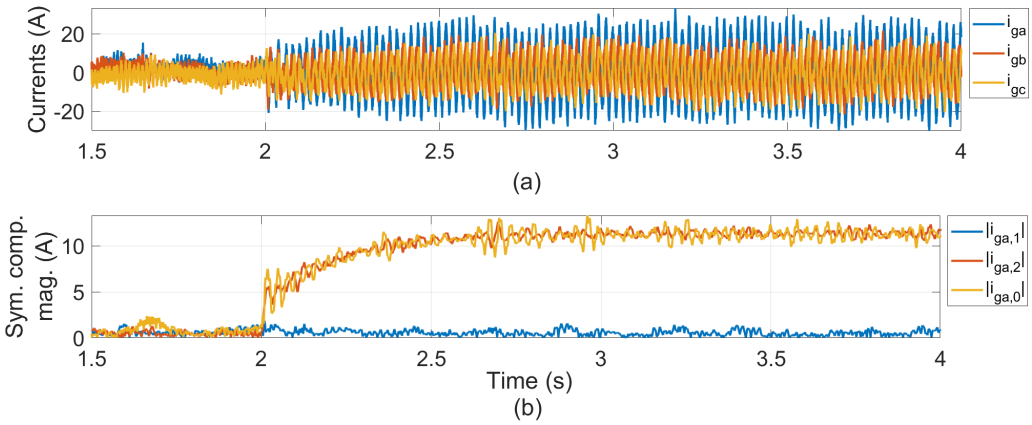

Figure 4.20: Currents measured at inverter terminal (a) instantaneous values and (b) magnitudes of their symmetrical components.

results for k_{v2} are similar to the ones found for inverter operation in pq-mode, i.e. $k_{v2} = 0.11\%$.

4.2.2.4 Case C_{1s} (pq–mode): [14.4 2.8 2.8] kVA

A mixed resistive–inductive load is modelled. The injection of both active and reactive power by the BESS inverters reduces the voltage unbalance factor from $k_{v2} = 2.5\%$ to 0.13%.

Based on Figure 4.21, the active power flows are $p_{ga} = 5.5$ kW, $p_{gb} = -2.8$ kW and $p_{gc} = -2.7$ kW, while the reactive power flows are $q_{ga} = 3.3$ kvar, $q_{gb} = -1.6$ kvar and $q_{gc} = -1.7$ kvar. The total inverter power is zero.

Figure 4.22(a)-(b) show that between $t_2 = 1$ s and $t_3 = 2$ s, the unbalanced active and reactive power flows are $p_{LVa} = 9.6$ kW, $p_{LVb} = p_{LVc} = 2$ kW and $q_{LVa} = 6.5$ kvar, $q_{LVb} = q_{LVc} = 2$ kvar, respectively. After the compensation, the active and reactive power values converge at 4.4 kW and 3.6 kvar, respectively. Similar to the previous cases studied for the three BESS inverters, the total active, reactive and apparent power at busbar LV remains unchanged, as shown in 4.22(c).

Figure 4.23-4.25 present the curves of the currents measured at the same points as in the previous cases, i.e.: busbar LV, terminals of the three inverters and beginning of feeder A. Similar to the case of purely active and purely reactive load, it can be observed that the inverters fully compensate the voltage unbalance by injecting the negative- and zero-sequence load current components, which are equal to 20 A. Additionally, the compensation of the zero-sequence load current component results in the mitigation of the transformer neutral current.

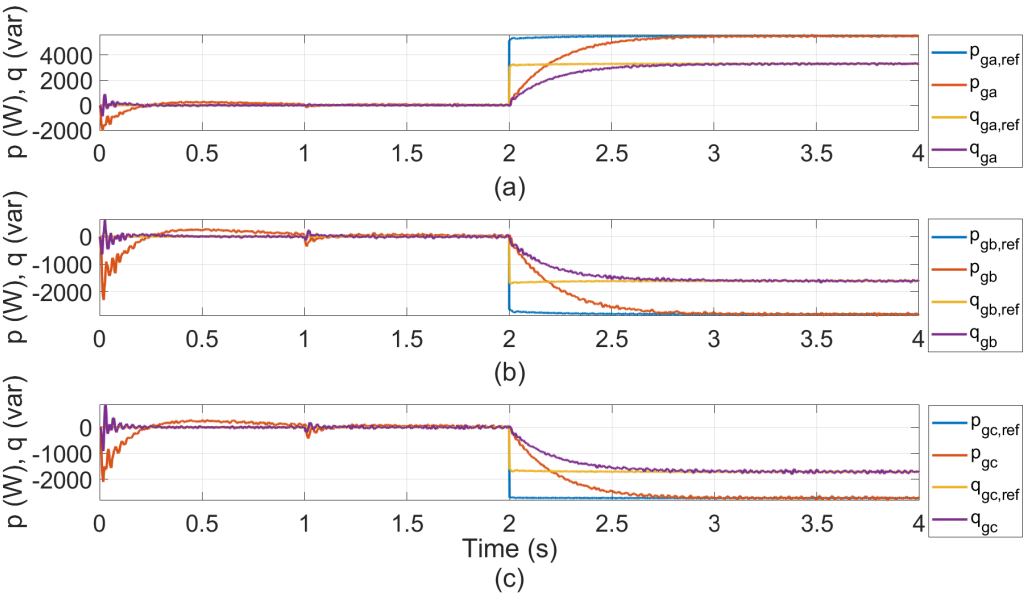

Figure 4.21: Reference and measured active and reactive power at the terminal of each inverter: (a) phase-a, (b) phase-b and (c) phase-c.

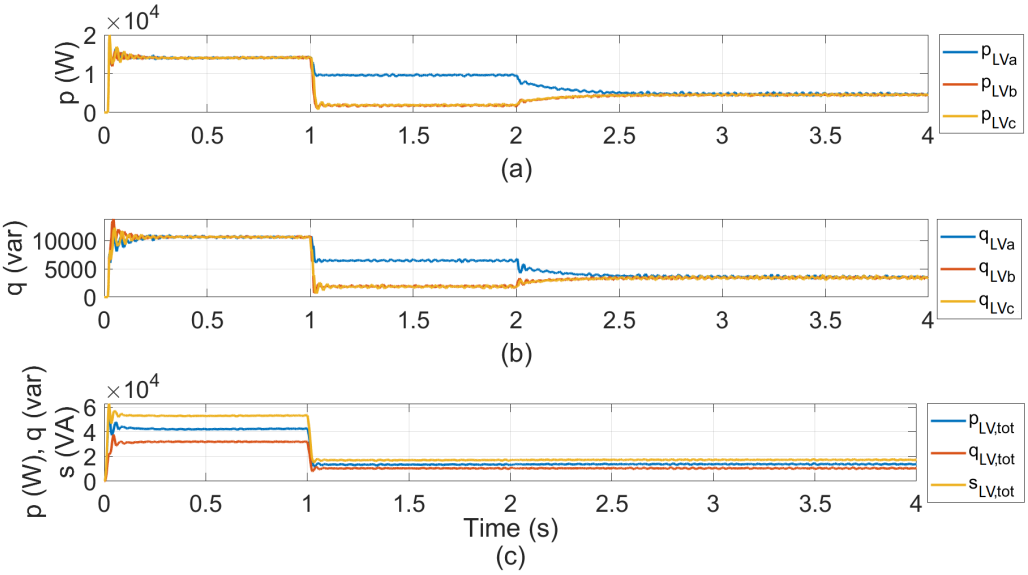

Figure 4.22: (a) Active and (b) reactive power at each phase, and (c) total active, reactive and apparent power measured at busbar LV.

A summary of the results for inverter operation in p-mode and q-mode is provided below:

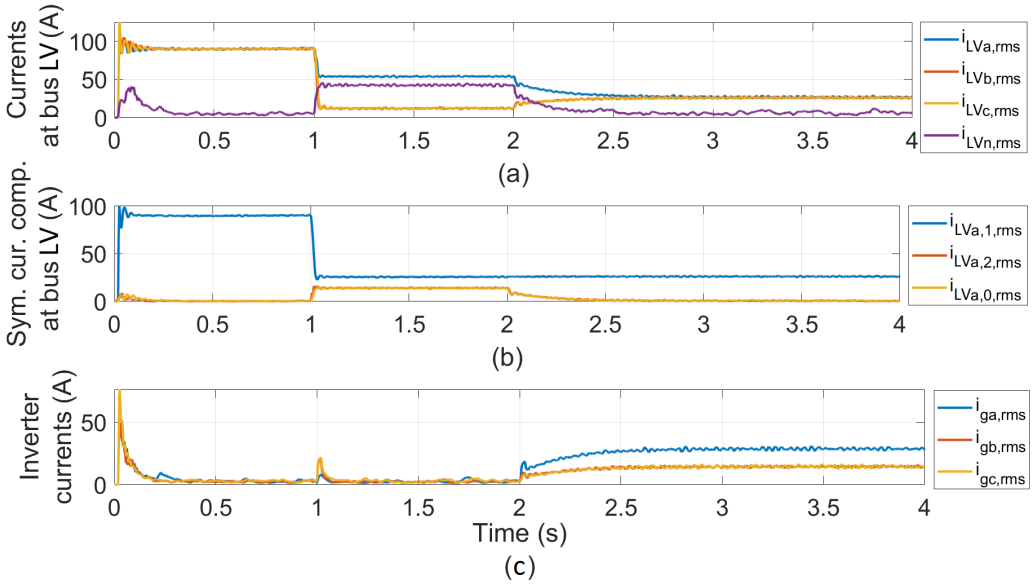

Figure 4.23: rms values of (a) phase and neutral currents and (b) symmetrical current components measured at busbar LV, and (c) output currents of inverters A, B and C.

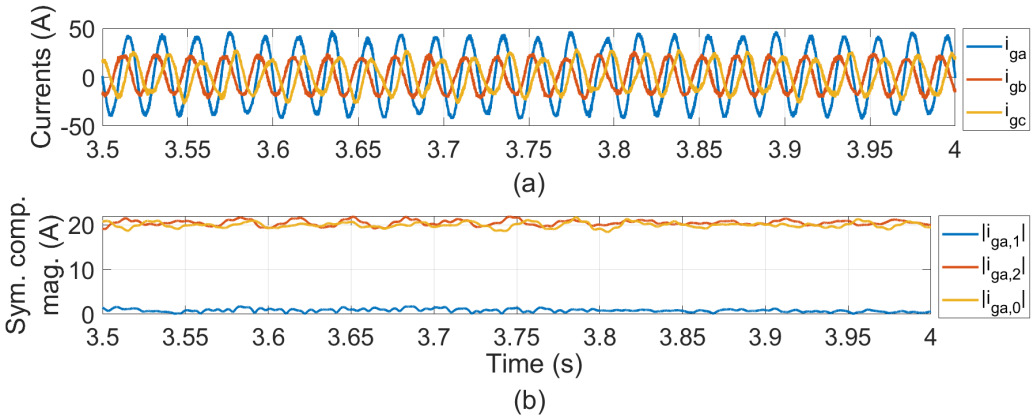

Figure 4.24: Instantaneous values of currents at busbar LV, inverter and feeder at (a) phase a, (b) phase b and (c) phase c.

- **p-mode**: In this case, only the active power unbalance is compensated by the inverters, while the reactive power unbalance remains unaffected. The voltage unbalance factor is reduced to $k_{v2} = 1.35\%$. As expected, this value is very similar to the value of k_{v2} for the uncompensated system of Case C_{1q}, where only reactive power unbalance was considered.
- **q-mode**: In this case, only the reactive power unbalance is compensated by the invert-

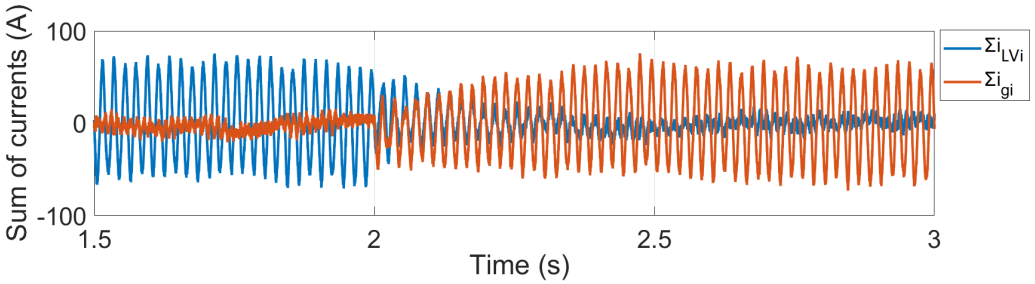

Figure 4.25: (a) Sum of the instantaneous phase currents at busbar LV and inverter, and (b) neutral current of feeder FA, busbar LV, and ground current

ers, while the active power unbalance remains unaffected. The voltage unbalance factor is reduced to $k_{v2} = 2.25\%$, which is equal to the value of k_{v2} for the uncompensated system of Case C_{1p}, where only active power unbalance was considered.

4.2.3 Conclusions

This section summarizes the main conclusions drawn from the simulation results of the cases presented in the previous sections and in Appendix F. These cases provide an initial validation of the proposed research strategy for a simple feeder configuration, and static loads.

When all three single–phase BESS inverters are in service, the following observations were made:

- For the cases when the BESS inverter rating is sufficient to fully compensate the load unbalance, the inverters are controlled to inject or absorb active and reactive power at each phase such that the power flows at the transformer secondary side converge and the voltage unbalance factor value is driven to zero.
- For the cases when the unbalance levels are high due to unbalance at one phase or at all three phases and the BESS inverter rating is not sufficient to eliminate voltage unbalance, the voltage unbalance factor is partially reduced, while full mitigation could be achieved by installing BESS units of larger rating. However, the latter may not be necessary if the voltage unbalance factor is already regulated well below the established limits.
- The voltage unbalance compensation strategy decreases the negative- and zero–sequence current components flowing at the transformer secondary side, thereby reducing the transformer neutral current, which is proportional to the zero–sequence component.
- For the cases when the unbalance is at one phase or at all three phases and the

BESS inverter rating is sufficient to fully compensate the load unbalance, the total active and reactive power of the three inverters is equal to zero, therefore the total power through the transformer stays unaffected after the compensation. On the contrary, for the cases when the unbalance levels are high due to unbalance at one phase or at all three phases and the BESS inverter rating is not sufficient to eliminate voltage unbalance, the active and reactive power of one or more inverters will saturate, thereby leading to non-zero total power flow at the transformer after the compensation. More specifically, this condition was observed for Case 4, where the sum of the powers at the terminals of the inverters becomes negative, i.e. the power absorbed by the inverters is higher that the power injected by them, thus leading to increased total power flow at the transformer. To avoid this operating condition, the control system could be modified such that one of the BESSs stops charging and/or absorbing reactive power or reduces its active and/or reactive power dissipation, if the sum of the powers at the terminals of the inverters becomes negative. Although this would result in sacrificing the voltage unbalance mitigating performance, it may be possible that the provision of voltage unbalance compensation by the other two BESS units is sufficient to regulate the voltage unbalance factor value well below the established limits.

When a single BESS inverter is in service, the following observations were made:

- The effectiveness of the proposed strategy on unbalance mitigation is reduced, since the inverter compensates only the negative- and zero–sequence current components of the phase to which it is connected. As a result, the negative- and zero–sequence current components for the other two phases are transferred to the transformer.
- The total power flow at the transformer is increased if the power measured at the inverter terminal is negative, i.e. the inverter absorbs power, while it is reduced if the power measured at the inverter terminal is positive, i.e. the inverter injects power.

4.3 Validation of voltage unbalance mitigation strategy using a rural distribution system and time-varying loads

In this section, the validation of the voltage unbalance mitigation algorithm is carried out on a more complex distribution network, which consists of time-varying loads.

4.3.1 Rural distribution system model

Figure 4.26 presents the single–line diagram of the distribution system under study, which is based on a German rural network that has been previously used to carry out unbalance studies [119]. The network consists of 24 customers connected via cables and overhead lines to the distribution transformer (busbar LV), and it distinguishes three-phase farm and single-phase household (HH) loads. Both load types were modelled as described in Appendix C. The maximum apparent power for HH and farm loads is 4.5 kVA and 12.3 kVA, respectively [120]. In this study, k_{v2} is monitored at five buses (marked with blue circles in Figure 4.26): the secondary side of the distribution transformer (busbar LV) and the end of feeders A-D (buses A4-D4). The calculation of k_{v2} is based on the phase-to-neutral voltages measured at these buses. The parameters of the medium-voltage

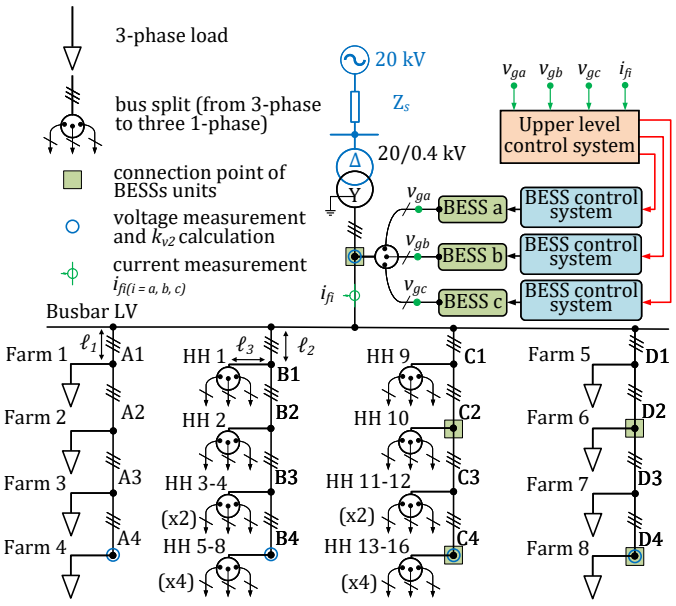

Figure 4.26: Layout of the rural network with 24 customers.

Table 4.4: Overhead line (OHL) and cables parameters.

Parameters	**OHL ℓ_1**	**Cable ℓ_2**	**Cable ℓ_3**
Resistance per km	0.358 Ω	0.153 Ω	0.524 Ω
Inductive reactance per km	0.252 Ω	0.067 Ω	0.073 Ω
Section length	200 m	200 m	15 m

Table 4.5: Location of the BESSs for the cases studied.

Case a	Case b	Case c	Case d	Case e	Case f
-	LV	C2	C4	D2	D4

(MV) upstream grid and distribution transformer are the same with the ones provided in Table 4.1, while the parameters of the overhead lines (ℓ_1) and cables (ℓ_2, ℓ_3) are given in Table 4.4.

Various locations (marked with green squares) were considered for the single-phase BESS units: busbar LV, C2, D2, C4 and D4. The simulation studies performed to validate the proposed control scheme for realistic load demands are given in Section 4.3.

The scope of the simulations presented in this section is to evaluate the effectiveness of the voltage unbalance mitigation strategy provided by the BESS inverters. The impact of the proposed control system is assessed considering operating conditions based on measurements of load demand with a 1-minute resolution. The BESS units are modelled in detail including the main electrical components and the control system. The power and energy rating for each BESS were chosen equal to 9 kvar and 90kWh, respectively, as has been discussed in Section 2.6. The voltage unbalance in the distribution system originates both from the unbalanced load and the background unbalance of the upstream grid, which is $k_{v2,MV} = 0.505\%$.

A 24-hour simulation without BESS is carried out to identify the hour with the highest voltage unbalance levels. Next, a stochastic load model is derived for the worst-case hour: the load changes are randomized around the switching time (i.e. the time instant when a change in the load value occurs) obtained from the measurement data, as the exact time of load change is not known. This approach makes the model more realistic and allows testing the robustness of the proposed control. The effectiveness of the control algorithm on mitigating the voltage unbalance is evaluated for the 'worst case' hour for various BESS locations. Initially, the BESS is located at busbar LV. Then, various BESS locations along the feeders are tested to carry out a sensitivity analysis and examine the impact of varying location on the voltage unbalance factor, transformer neutral current and BESS size. Table 3 lists the location of the BESS for cases a-f. Case a is the reference case, when no BESS is connected to the distribution system, whereas from case b-f the

BESS units are allocated at five different buses across the system.

4.3.2 Simulation results

4.3.2.1 System without BESS

The model was simulated without BESS, and the highest voltage unbalance values are found between 18:30 and 19:30 h, due to the amount of single-phase loads in service and their levels. In the previous section, the plots of the voltage unbalance factor were not shown because k_{v2} was not changing in time, while in this section the k_{v2} value varies due to the time-varying loads. The profiles of k_{v2} at each bus are plotted in Figure 4.27. The simulation results are presented as 10-min aggregated values (based on IEC 61000-4-30 [77]) of k_{v2}. This graph shows that the highest value occurs at bus D4 at 19:15 h with $k_{v2.D4} = 1.75\%$. The increase of voltage unbalance is also reflected in the rise of the transformer zero-sequence fundamental current component. Figure 4.28 shows that the peak value of this current is 55.4 A at 19:15 h. The impact of the stochastic load for this hour was minimal since few load changes take place.

4.3.2.2 BESS at busbar LV

Three BESS units were connected at busbar LV. Figure 4.29 gives the voltage unbalance factor time characteristics at each bus. Note that this graph is more noisy than

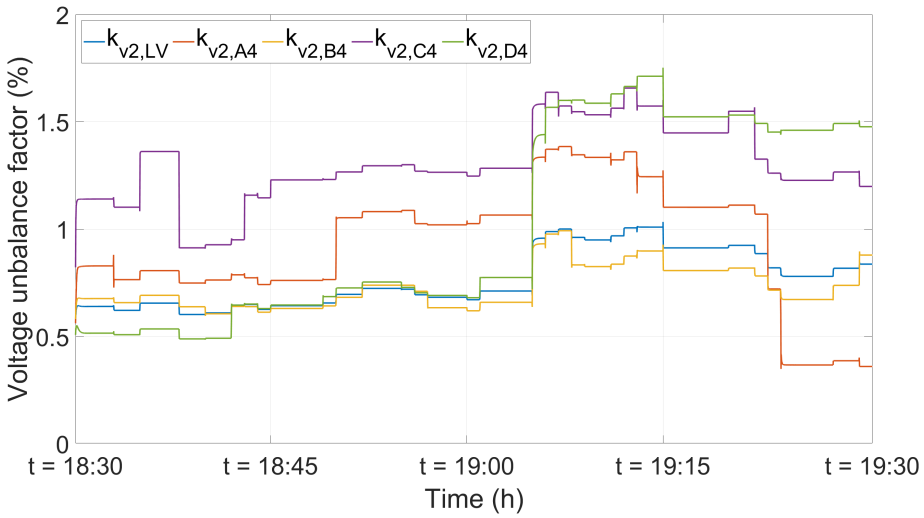

Figure 4.27: Voltage unbalance factor for case a.

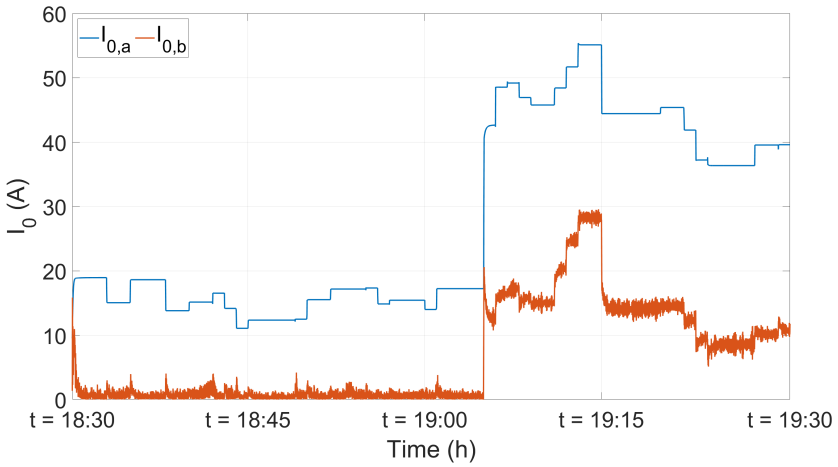

Figure 4.28: Transformer zero-sequence current amplitude for case a (blue) and case b (orange).

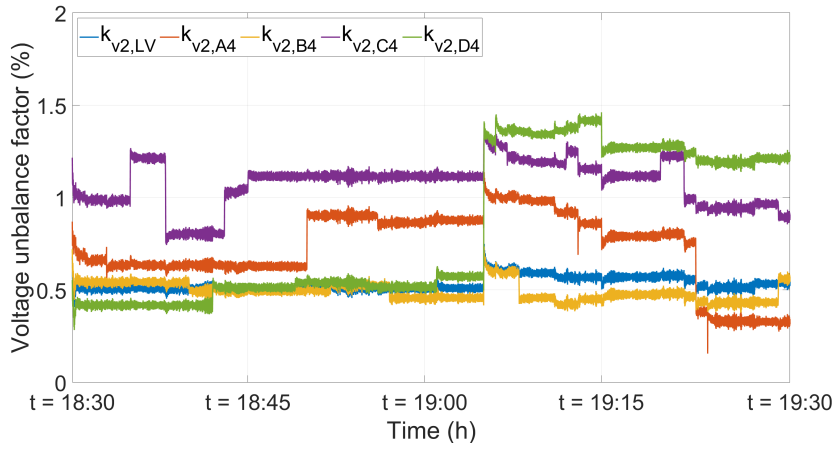

Figure 4.29: Voltage unbalance factor at five buses for case b.

Figure 4.27 because of the BESS switching operation. The peak values at buses LV and A4-D4 are reduced to 72.8%, 77.4%, 65.8%, 84.9% and 82.2% of the reference case (case a) values (Figure 4.27), respectively. Although the BESSs have an overall positive impact on k_{v2} reduction, they cannot eliminate the voltage unbalance at the busbar LV due to the presence of background unbalance of the upstream grid ($k_{v2,MV} = 0.505\%$). Figure 4.28 shows that the transformer zero-sequence current component is also reduced.

The peak value of the zero-sequence current amplitude for case b is 29.5 A at 19:15 h.

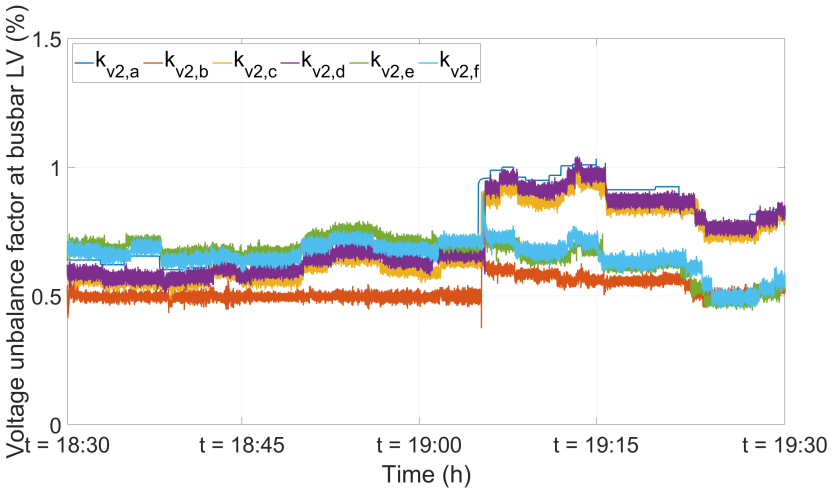

Figure 4.30: Voltage unbalance factor at busbar LV for cases a-f.

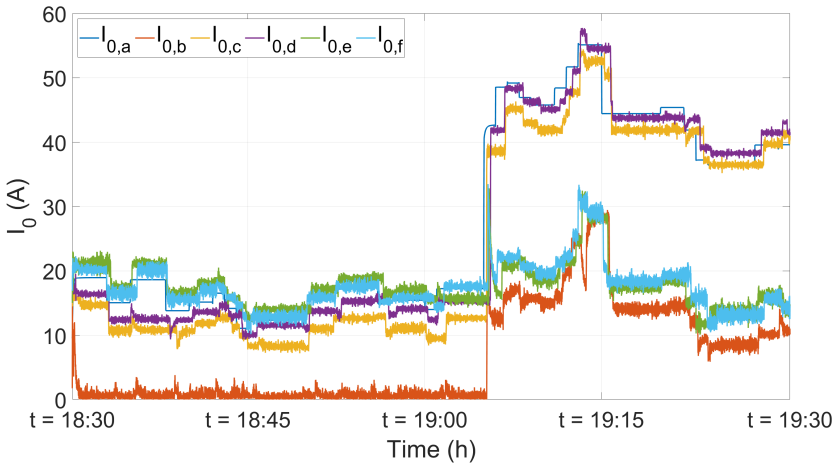

Figure 4.31: Transformer zero-sequence current amplitude for the low voltage windings for cases a-f.

4.3.2.3 Sensitivity analysis

A sensitivity analysis was carried out to investigate the impact of installing the BESS at different locations (cases c-f) in the distribution system. The impact was assessed on the same parameters studied above: voltage unbalance factor at five buses and magnitude of the transformer zero-sequence current component. In addition, the impact on the BESS size was also evaluated.

Table 4.6: Peak values of k_{v2} and transformer zero-sequence current for cases a-f. The cases leading to higher reduction are highlighted in blue.

%	a -	b LV	c C2	d C4	e D2	f D4
$k_{v2,LV}$	1.03	0.75	1	1.04	0.9	0.89
$k_{v2,A4}$	1.38	1.14	1.37	1.4	1.3	1.28
$k_{v2,B4}$	0.99	0.74	0.94	1	0.87	0.86
$k_{v2,C4}$	1.66	1.41	1.42	1.47	1.52	1.15
$k_{v2,D4}$	1.75	1.44	1.75	1.8	1.26	1.15
$\|\boldsymbol{I_0}\|$	55.4	29.5	54.6	57.7	32.8	33.5

Table 4.7: Average values of k_{v2} and transformer zero-sequence current for cases a-f. The cases leading to higher reduction are highlighted in blue.

%	a -	b LV	c C2	d C4	e D2	f D4
$k_{v2,LV}$	0.77	0.52	0.69	0.72	0.66	0.66
$k_{v2,A4}$	0.93	0.72	0.91	0.95	0.88	0.87
$k_{v2,B4}$	0.73	0.48	0.65	0.68	0.62	0.62
$k_{v2,C4}$	1.3	1.05	0.94	0.8	1.17	1.18
$k_{v2,D4}$	1.02	0.81	0.96	0.99	0.73	0.66
$\|\boldsymbol{I_0}\|$	27.8	6.64	24.3	26.5	17.7	17.5

Figure 4.30 shows k_{v2} time characteristics at busbar LV for all cases (the voltage unbalance factor at other feeders is not shown for clarity). When the BESSs are connected at busbar LV (case b), k_{v2} is minimised. The impact from BESS allocation at feeder C (cases c, d) is negligible, while the BESS allocation at feeder D (cases e, f) improves k_{v2} from 19:05-19:30 h.

Figure 4.31 presents the zero-sequence current in the transformer for cases a-f. Overall, BESS placement at busbar LV has the highest impact on this quantity. From 19:05-19:30 h, the zero-sequence current is reduced when the BESS is placed at feeder D, while allocation at feeder C has a small effect, since the negative-sequence current component flowing to feeder C is a small portion of the one flowing to feeder D.

Table 4.6-Table 4.7 summarize the peak and average (calculated over 1-hour) values of k_{v2} and zero-sequence current of cases a-f. Table 4.6 shows that the peak is minimized for case b at all locations, except for bus D4.

Table 4.7 shows that in average unbalance mitigation at each bus is maximized when the BESS is connected at the same bus, i.e. $k_{v2,LV} = 0.52$ % (case b), $k_{v2,C4} = 0.8$ % (case d) and $k_{v2,D4} = 0.66$ % (case f).

Regarding the mitigation at feeders A and B, BESS connection upstream in the dis-

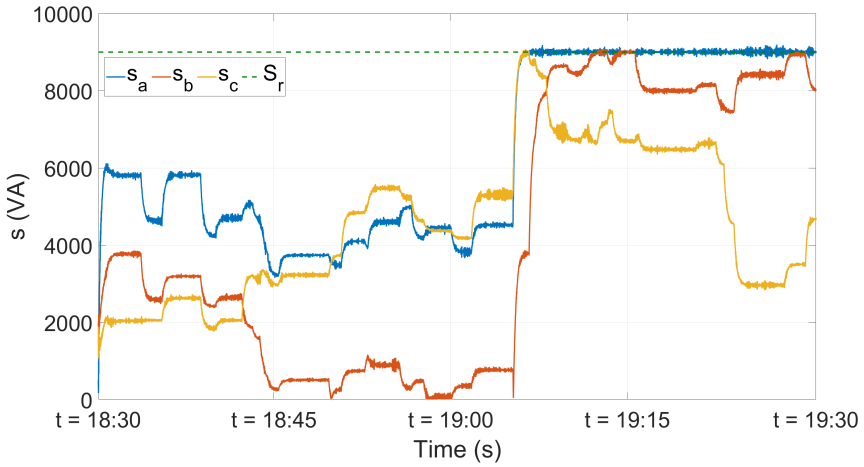

Figure 4.32: Apparent power of single-phase BESS inverters for case b.

tribution system (busbar LV) provides higher compensation compared to the other cases, i.e. $k_{v2,A4} = 0.72$ % and $k_{v2,B4} = 0.48$ % for case b. For feeders C and D, the BESS was connected in two locations, in the middle and at the end of the feeder. Comparing these locations, it is observed that BESS allocation at bus C2 has a higher impact on mitigating the unbalance at all buses, except for bus C4. The unbalance reduction caused by the BESSs allocated at buses D2 and D4 is very similar.

In terms of the zero-sequence current component minimization, busbar LV is the optimal location, resulting in an average value of 6.64 A.

Figure 4.32-Figure 4.34 present the inverter apparent power for cases b, c and e. The results for cases d and f are omitted since they are very close to those obtained from cases c and e, respectively. Figure 4.32 shows that the apparent power for BESS placed at busbar LV is saturated at all three phases at 9 kVA: while phase-a is saturated continuously from 19:10 h, saturation is intermittent on the other phases. At 19:05 h, a large increase of phase-a load at bus D4 causes phase-a BESS to discharge active power to mitigate the unbalance, while the other two BESSs charge. Therefore, the full installed rating is used when the BESS is connected at this location. Connecting largest BESSs at this location would lead to further voltage unbalance compensation.

Figure 4.33 shows that the apparent power is significantly lower for location at bus C2. The BESS output is reduced since the load power flowing downstream of bus C2 is lower compared to that flowing downstream of busbar LV. Therefore, a BESS of lower size can be installed at feeder C without impacting the effect on unbalance compensation. Figure 4.34 shows that for allocation at bus D2, phase-a apparent power is close to the

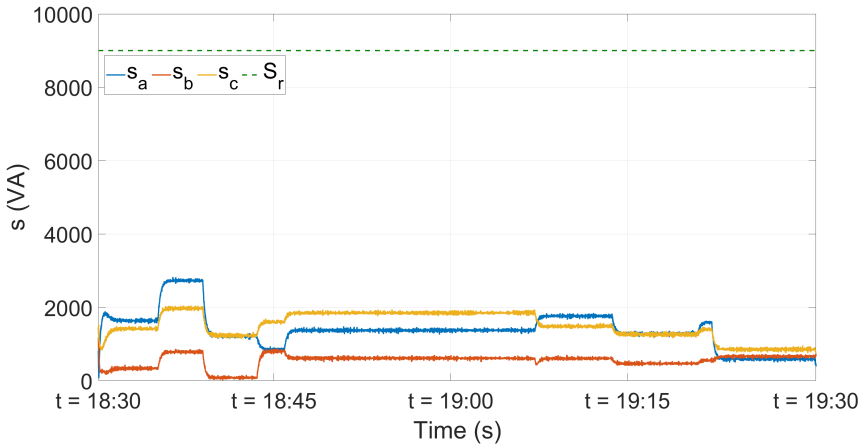

Figure 4.33: Apparent power of single-phase BESS inverters for case c.

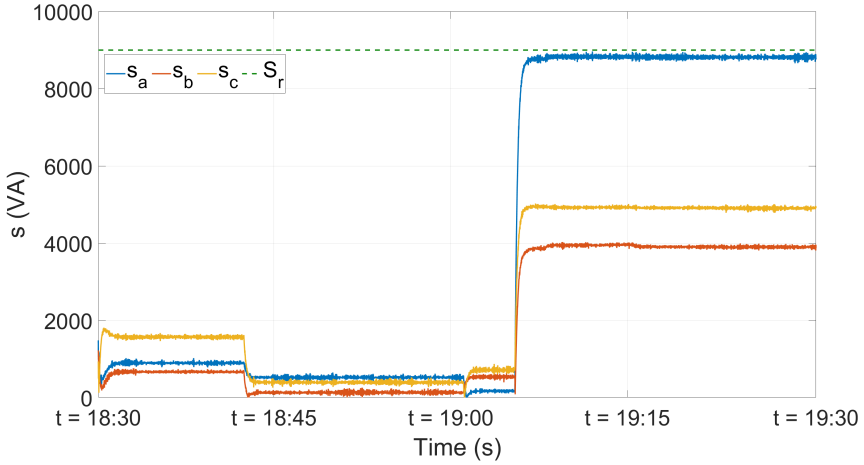

Figure 4.34: Apparent power of single-phase BESS inverters for case e.

saturation limits. In addition, the apparent power values of the inverters are constant from 19:05 – 19:30 h, since the load at the three phases is constant during this period. Based on the above results, it is possible to conclude that smaller batteries can be used on the feeders without affecting the algorithm performance.

4.3.3 Conclusions

In this section, the effectiveness of single-phase BESS units on performing voltage unbalance compensation within a realistic distribution network was assessed. Three single-

phase BESS units were allocated at different buses of the distribution system and they were controlled to reduce the voltage unbalance factor at the busbar they were connected to. A sensitivity analysis with the aim to test the impact of the proposed control strategy on voltage unbalance factor, transformer zero-sequence current and battery loading.

The tests carried out showed that the largest impact on both voltage unbalance factor peak and zero-sequence current amplitude is achieved when the BESS is installed at busbar LV, while the most visible impact on the average values is obtained for BESS installed at the same location as the measurement point. It is also shown that with increasing distance between the substation and the BESS location, the size of the inverter and battery can be reduced without compromising the effectiveness of the proposed algorithm.

4.4 Overall conclusions

In this chapter, the proposed voltage unbalance mitigation strategy was validated for two types of distribution networks.

Initially, a simple feeder configuration and static loads were modelled. Based on the obtained results, the following conclusions can be made: Overall, it is concluded that single–phase BESS inverters connected at the three phases are able to completely eliminate voltage unbalance if they are adequately sized. However, larger BESS size results in increased cost, and reducing k_{v2} to zero may not be necessary in the majority of the cases, since the standards generally require k_{v2} to be below a certain threshold (2% for IEC 61000-4-30). In a practical application, the battery rating will be chosen as a compromise between performance, cost, ancillary services provided and their remuneration. In all four cases under study, the negative– and zero–sequence current components in the secondary side of the transformer are reduced, thereby decreasing the neutral current of the transformer. Therefore, the voltage unbalance compensation strategy leads to the reduction of the voltage unbalance factor independently of the number of the inverters in service. However, the proposed compensation scheme can potentially increase the power flow through the transformer if the total output power from the inverters becomes negative. More specifically, this condition is the result of unbalanced inverter operation and can arise in the following cases: (i) saturation of the output power of one or more of the three inverters, (ii) two inverters in service, with both absorbing power from the grid or one inverter absorbing power from the grid and the other injecting power to the grid, (iii) a single inverter in service absorbing power from the grid.

Next, a rural network and dynamic loads with a 1-minute resolution were modelled. It was concluded that BESS placement at busbar LV affects the highest number of busbars in terms of voltage unbalance factor mitigation, while it also leads to the minimization of the

zero-sequence current component flowing to the neutral conductor. For BESS placement along the feeder, the unbalance can be mitigated effectively even by using lower BESS size.

In this study, each BESS acts as unbalance mitigating device only. However, the proposed control functionality can be combined with load balancing. To avoid overloading of the units, the inverter control system can be modified such that it can switch between load balancing and unbalance mitigation. The priority of each control function can be determined according to grid conditions but also to the remuneration for each service provided.

The results demonstrate that single-phase BESS units can effectively mitigate voltage unbalance in residential distribution networks. The next step of this analysis will consist in assessing the effectiveness of the proposed method in mitigating unbalance caused by PVs and EVs. Such operating conditions are simulated in the next chapter.

Chapter 5

Deterministic Validation of Voltage Unbalance Mitigation Strategy in a Distribution System Model with varying levels of PVs and EVs

5.1 Introduction

The aim of this chapter is twofold: first, to evaluate the impact of varying penetration levels of PVs and EVs within a distribution system on voltage unbalance; second, to validate the proposed voltage unbalance mitigation strategy on an unbalanced distribution system with high penetration of PVs and EVs. To this end, a model of a distribution system that is commonly adopted in the UK is built. The network consists of single-phase residential customers, PVs and EVs, with the demand and generation profiles retrieved from a public database [121]. This data source has been chosen since the profiles represent typical winter and summer operating conditions in the UK[1].

[1] This chapter is based on the work published in [2].

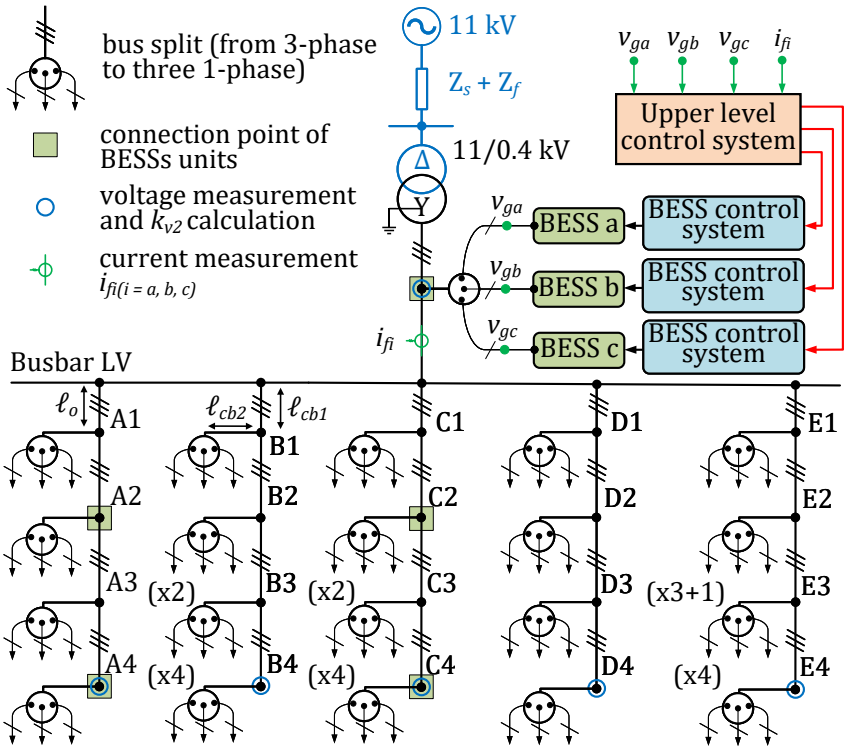

Figure 5.1: Single-line diagram of the UK distribution network. Feeders A and C consist of overhead lines with segment length ℓ_o. Feeders B, D and E consist of cables with segment length ℓ_{cb1}, while service cables with length ℓ_{cb2} are used to connect each single-phase customer to its bus. The green squares indicate five different locations where the three BESSs are connected. The blue circles indicate the buses where voltage measurements are taken to calculate the voltage unbalance factor k_{v2}. Each arrow represents one single-phase load.

5.2 Distribution network configuration

The single-line diagram of the system under consideration is shown in Figure 5.1. The system parameters (equivalent impedance, transformer, line impedance) are summarized in Table 5.1. These values were retrieved from [122], where typical arrangements and equipment deployed in UK distribution systems are described. The upstream voltage source is considered to be balanced, while the main BESS parameters are the same as those used in the previous chapter, and summarised in Table 2.6 and Table 3.1.

The network includes five three-phase feeders and 20 buses, labelled $\mathrm{A_k}$, $\mathrm{B_k}$, $\mathrm{C_k}$, $\mathrm{D_k}$, $\mathrm{E_k}$, with $k = 1, 2, 3, 4$. The network supplies 100 single-phase loads, and in the rest of

Table 5.1: Upstream grid and distribution system parameters.

Parameters	Values
Short–circuit power	S_k = 141 MVA, $X/R = 12$
Nominal voltage and frequency	V_n = 11 kV (primary); 230 V (secondary); 50 Hz
Source impedance	$\boldsymbol{Z_s}$ = 0.069 + j0.825 Ω
11 kV feeder impedance	$\boldsymbol{Z_f}$ = 0.784 + j0.75 Ω
Transformer rated power and winding impedance	$S_{tr,n}$ = 200 kVA $\boldsymbol{z_{tr1}} = \boldsymbol{z_{tr2}}$ = 0.0075+j0.0225 pu
Impedance of overhead lines and cables	$\boldsymbol{Z_o}$ = 0.0716+j0.0504 Ω, ℓ_o = 200 m $\boldsymbol{Z_{cb1}}$ = 0.0287+j0.0140 Ω, ℓ_{cb1} = 200 m $\boldsymbol{Z_{cb2}}$ = 0.0236+j0.0020 Ω, ℓ_{cb2} = 30 m

the thesis they will be referred to simply as 'loads' since no three-phase customers are connected. The great majority of the buses supplies three loads, except for buses B4, C4 and E4 (twelve loads each), buses B3 and C3 (six loads each), and bus E3 (ten loads). The residential demand, PV and EV profiles have been retrieved from a public database [123], [124]. This data source has been chosen since the profiles represent typical winter and summer operating conditions in the UK and allows other researchers to carry out comparative studies. Each load varies independently, and the minihmum and maximum load ratings are 1.2 and 12.3 kW, respectively. The power factor of all loads is equal to 0.98 lagging.

A realistic mix of PV power sources, based on statistics presented in [123], is used: the PV nominal powers adopted in this study are rated 1.5, 2.0, 2.5, 3.0, 3.5 and 4.0 kW. These ratings apply to 7, 11, 16, 20, 13 and 33% of the PV panels, respectively. As explained in [123], the data was obtained from a meteorological observatory, with the 30 sunniest days being chosen from solar irradiance curves to capture the most challenging scenarios. The data is translated into single-phase PV generation profiles, assuming efficiencies 15% and 95% for the energy conversion process and the inverter, respectively. As reported in [125], the EV profiles have been created based on data from an one-year field trial in Dublin. One charge at home per day is assumed for each EV. Given that UK residential loads are single–phase, EV users are initially expected to mostly adopt slow charging modes at home. Therefore, all EVs are assumed to have a battery rated 3 kW, 24 kWh.

Similarly to the loads, EVs and PVs are single-phase units - however, their connection is not indicated in the single-line diagram because various locations were considered in this work. More specifically, varying penetration levels, i.e. percentage of buses with either PVs, EVs, or both, were examined with the aim to evaluate the impact of these

two technologies on voltage unbalance.

The effectiveness of the proposed control methodology was evaluated for five different BESS locations (buses LV, A2, A4, C2 and C4 indicated with green squares in Figure 5.1). For illustrative purpose, Figure 5.1 shows the case when three BESS units are connected to busbar LV. In this case, the phase voltages (v_{gi} for i = a, b, c) correspond to the busbar LV voltage, and the feeder currents (i_{fi}) are measured at the secondary side of the distribution transformer. For other BESS locations, the voltage and current measurements are taken at the terminal where the BESSs are connected. For example, when the BESSs are connected at bus A2, the upper level control system receives voltage measurements at bus A2 and feeder current measurements taken downstream of that bus. Section 5.3 will present simulation results for the considered BESS locations. In the case under study, k_{v2} is monitored at busbar LV and at the end of the feeders (buses A4-E4). These locations are marked with blue circles in Figure 5.1.

5.3 Simulation results

The distribution system shown in Figure 5.1 was modelled in MATLAB/Simulink. Two sets of simulations were carried out: the first set was intended to assess voltage unbalance levels due to increasing penetration of single-phase PVs and EVs, with no BESSs in service. These simulations will be presented in Subsection 5.3.1 and Subsection 5.3.2, respectively.

The second set of simulations aimed at evaluating the effectiveness of the control strategy proposed in Section 3.2 for operating conditions corresponding to high voltage unbalance levels. To this end, three single-phase BESSs were connected at various locations, and their impact on both average and peak k_{v2} was evaluated. Subsection 5.4 will illustrate the positive impact of the proposed strategy for a scenario including both PVs and EVs.

To make the EMT simulation time manageable, the time scale was compressed such that 5 minutes in real time (the data resolution available from [123]) correspond to 0.5 seconds in the simulation.

5.3.1 Effect of varying PV penetration on voltage unbalance

Five different PV penetration levels were examined, i.e. from 20% to 100% with steps of 20%, while no EVs (and no BESSs) were connected to the network. The observation time was from 08:00 h to 16:00 h: this 8-hour period was chosen because PV power generation occurs mostly during this time frame, as shown in Figure 5.2, where the 24-h PV profiles are plotted. As has been described in Section 5.2, six different PV ratings

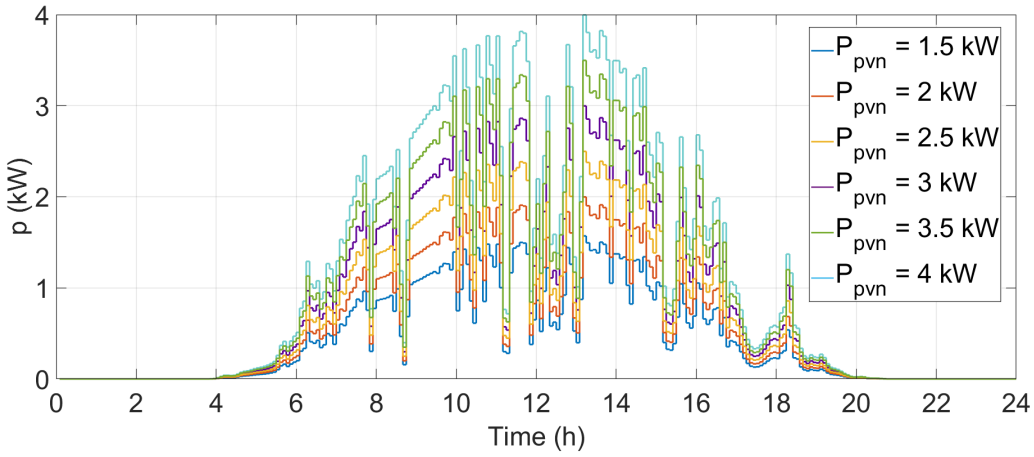

Figure 5.2: 24-h profiles of PVs in the summer.

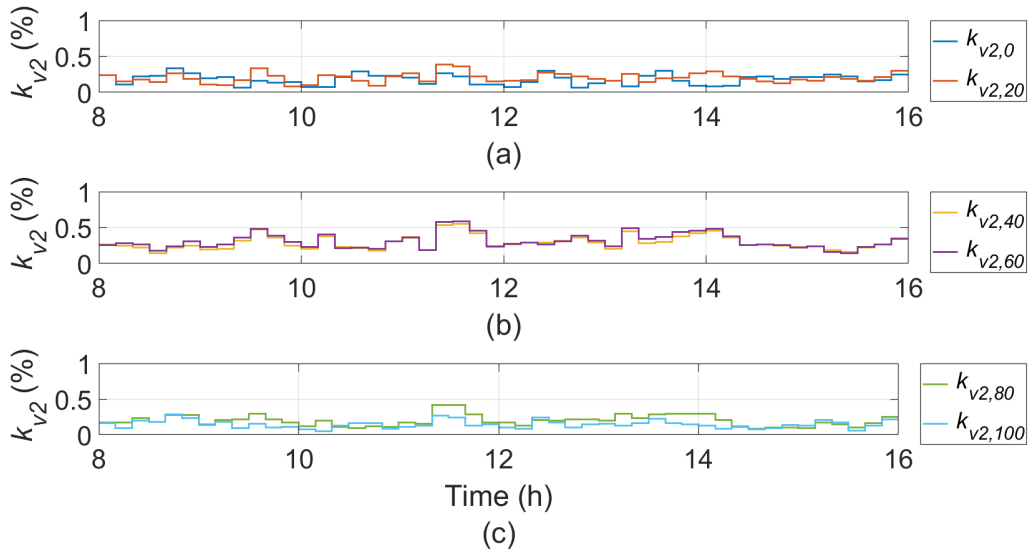

Figure 5.3: Voltage unbalance factor at busbar LV without and with PVs.

varying from 1.5 to 4 kW are considered. In addition, it is assumed that the profiles of the PVs with the same rating coincide, therefore only six curves are plotted in Figure 5.2. The impact on voltage unbalance is expected to be the maximum during this 8-hour period.

Figure 5.3 presents the voltage unbalance factor profiles for busbar LV without and with PV for the five penetration levels. The simulation results are presented as 10-min aggregated values (based on IEC 61000-4-30 [126]) of k_{v2}. Figure 5.3(a)-(b) show that a

Table 5.2: peak values of k_{v2} for varying PV penetration levels.

Bus	$\boldsymbol{k_{v2}}$**(%)**	**PV penetration level (%)**					
		0	**20**	**40**	**60**	**80**	**100**
LV	$k_{v2,LV}$	0.42	0.39	0.60	0.64	0.46	0.34
A4	$k_{v2,A4}$	2.14	1.99	1.95	1.89	1.74	1.85
B4	$k_{v2,B4}$	0.96	0.96	1.05	1.00	0.86	0.81
C4	$k_{v2,C4}$	2.27	2.22	2.15	2.01	1.85	1.67
D4	$k_{v2,D4}$	0.72	0.63	0.90	0.90	0.58	0.61
E4	$k_{v2,E4}$	0.71	0.91	1.13	1.18	1.25	0.74

Table 5.3: average values of k_{v2} for varying PV penetration levels.

Bus	$\boldsymbol{k_{v2}}$**(%)**	**PV penetration level (%)**					
		0	**20**	**40**	**60**	**80**	**100**
LV	$k_{v2,LV}$	0.17	0.20	0.30	0.32	0.20	0.14
A4	$k_{v2,A4}$	0.36	0.58	0.68	0.68	0.49	0.30
B4	$k_{v2,B4}$	0.28	0.35	0.44	0.46	0.33	0.25
C4	$k_{v2,C4}$	0.93	0.92	1.02	1.02	0.72	0.62
D4	$k_{v2,D4}$	0.26	0.26	0.46	0.46	0.27	0.22
E4	$k_{v2,E4}$	0.30	0.31	0.38	0.44	0.51	0.27

20% PV penetration results in an increased value of k_{v2} during most of the simulation period compared to the case when no PVs are connected, while voltage unbalance is increasing for 40% and 60% PV penetration levels. As shown in Figure 5.3(c), k_{v2} starts decreasing for higher PV penetration levels.

The results for busbar LV and the end of the feeders are summarised in Table 5.2 and Table 5.3. Table 5.3 shows the average values of k_{v2} calculated at each bus and for different PV penetration levels. During the 8-hour period, k_{v2} shows an increasing trend for penetration levels up to 60%. The voltage unbalance increase is more prominent when PV penetration increases from 0% to 20% and from 20% to 40%. For penetration levels above 60%, the additional PVs have a smoothing effect, thus the value of k_{v2} decreases: this can be clearly observed by comparing the k_{v2} trend for 80% and 100% PV penetration in Figure 5.3. For 100% PV penetration, k_{v2} is lower then the case when no PVs are connected. Notably, these observations apply to all buses shown in Table 5.3.

Table 5.2 shows that peak values of k_{v2} do not follow a clear pattern, as in the case of the average values. However, at most of the buses, peak values tend to decrease for penetration levels above 80%.

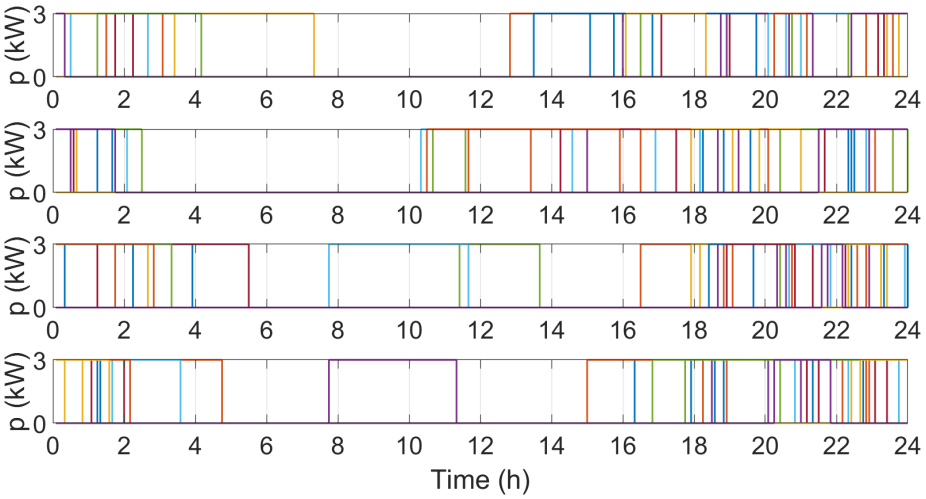

Figure 5.4: 24-h charging periods of EVs in the winter.

5.3.2 Effect of varying EV penetration on voltage unbalance

As for the PV assessment described above, five EV penetration levels were examined, i.e. from 20% to 100% with steps of 20%, while no PVs (and no BESSs) were connected to the network. The profiles are studied from 16:00 h to 4:00 h, since most of the EVs charge within this 12-hour period, as shown in Figure 5.4(a)-(d), where the 100 24-h EV profiles are plotted in groups of 25.

The time-series of the voltage unbalance factor for busbar LV without and with EVs are plotted in Figure 5.5. Similarly to the results above, when the EV penetration level is increasing from 0% to 60%, the voltage unbalance rises. However, for higher penetration levels, k_{v2} does not change significantly. This phenomenon is illustrated more clearly in Table 5.4. For example, at the LV busbar, the average value of k_{v2} increases until 60% penetration level, where $k_{v2,LV} = 0.3\%$. Above this penetration level, k_{v2} stabilizes around 0.3%. Regarding the remaining buses, the average value of k_{v2} follows an increasing trend with higher EV penetration levels across the system except for the end of feeder D (bus D4), where a reduction of the average value is recorded for penetration levels above 60%. Table 5.5 shows that the peak values of k_{v2} follow a similar trend as the average values.

Overall, by comparing the effect of PVs and EVs on voltage unbalance, it can be inferred that while increasing the number of PVs installed causes a rise in voltage unbalance up to a certain penetration level (i.e. 60%), the penetration of EVs generally results in higher voltage unbalance with increasing penetration levels. This is due mostly to the high rating of the EVs (3 kW), and the fact that the EVs act as loads, therefore increas-

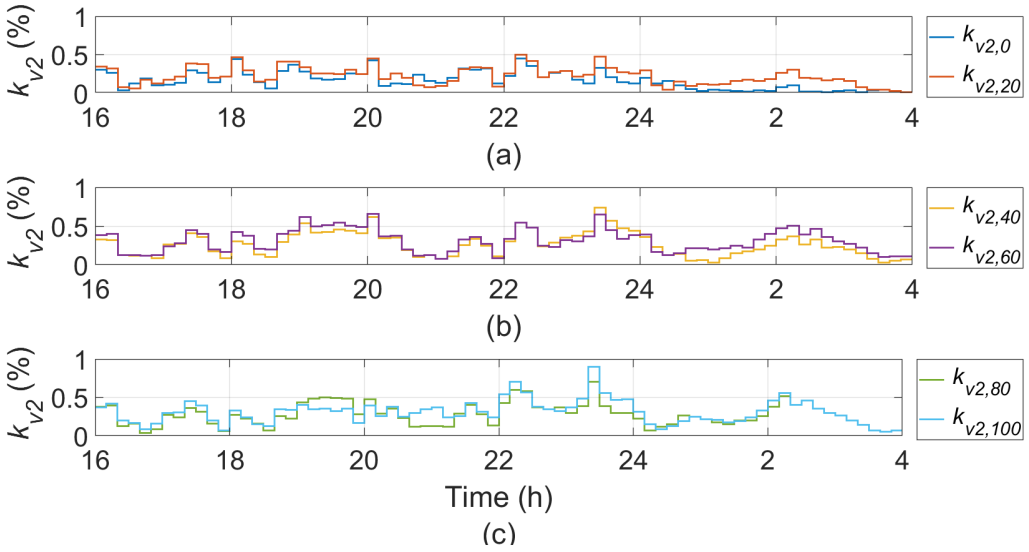

Figure 5.5: Voltage unbalance factor at busbar LV without and with EVs.

Table 5.4: Average values of k_{v2} for varying EV penetration level.

Bus	$\boldsymbol{k_{v2}}$**(%)**	**EV penetration level (%)**					
		0	**20**	**40**	**60**	**80**	**100**
LV	$k_{v2,LV}$	0.16	0.21	0.26	0.30	0.27	0.30
A4	$k_{v2,A4}$	0.34	0.79	0.80	0.88	0.97	1.11
B4	$k_{v2,B4}$	0.28	0.43	0.46	0.52	0.51	0.63
C4	$k_{v2,C4}$	0.64	0.67	1.24	1.28	1.35	1.46
D4	$k_{v2,D4}$	0.22	0.28	0.41	0.47	0.43	0.43
E4	$k_{v2,E4}$	0.27	0.31	0.35	0.48	0.50	0.53

Table 5.5: Peak values of k_{v2} for varying EV penetration level.

Bus	$\boldsymbol{k_{v2}}$**(%)**	**EV penetration level (%)**					
		0	**20**	**40**	**60**	**80**	**100**
LV	$k_{v2,LV}$	0.54	0.57	0.78	0.74	0.87	1.09
A4	$k_{v2,A4}$	1.43	2.24	2.3	2.33	2.33	2.98
B4	$k_{v2,B4}$	1.07	1.2	1.25	1.27	1.23	1.70
C4	$k_{v2,C4}$	3.47	3.56	4.81	4.84	7.41	7.57
D4	$k_{v2,D4}$	0.93	0.95	1.36	1.45	1.25	1.00
E4	$k_{v2,E4}$	0.94	1.06	1.06	1.24	1.37	1.71

ing the unbalance levels when they are connected to the system. On the other hand, PV ratings are generally smaller (with ratings provided in Section 5.2) and they act as generators, thus contributing to supply the local loads as their penetration increases, and therefore resulting in a reduction of voltage unbalance.

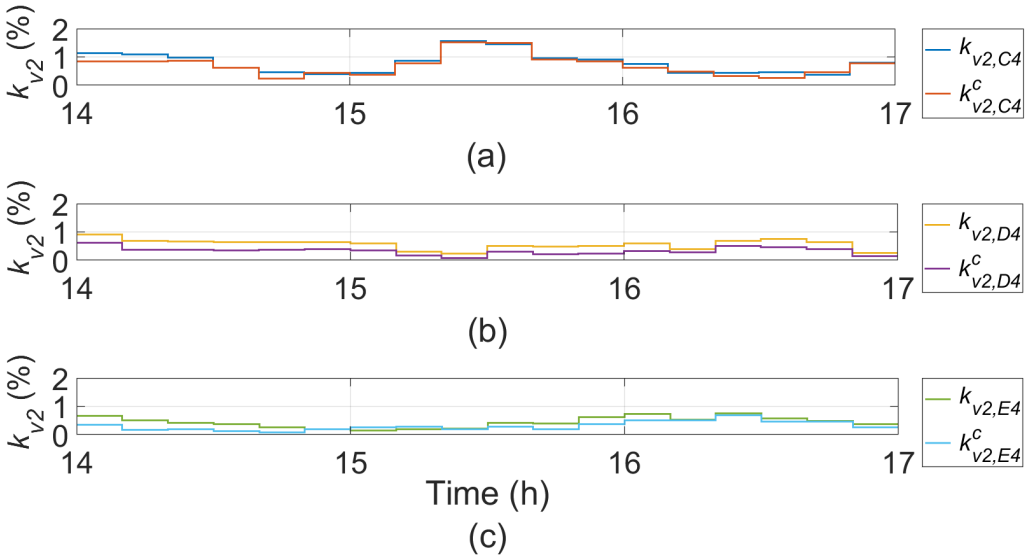

Figure 5.6: k_{v2} **at bus (a) C4 (b) D4 (c) E4, with and without BESS installed at busbar LV (the superscipt 'c' is used for the system with BESS).**

5.4 Deployment of BESS for voltage unbalance mitigation

The proposed control strategy was tested for an operating condition with 60% PV and 20% EV penetration level. This scenario was chosen because it resulted in high voltage unbalance during certain times of the day. Various BESS locations were tested, specifically: LV, A2, A4, C2 and C4. These busbars are highlighted in Figure 5.1 with green squares. They were chosen based on two criteria: LV is the low voltage side of the transformer, and the highest unbalance originates from feeder A and feeder C. Therefore, it is expected that the BESS units will have more prominent effect on voltage unbalance mitigation if they are placed either at the secondary side of the distribution transformer or close to the main origin of voltage unbalance, which is caused by the aforementioned feeders.

The results are shown for the time between 14:00 h and 17:00 h to capture the effect of both PVs and EVs on voltage unbalance. Figure 5.6 presents the simulation results of k_{v2} for a summer day. For buses C4, D4, E4, the results are plotted without and with the BESSs placed at busbar LV in order to observe the impact of the BESS control on mitigating the unbalance. The graphs for buses LV, A4, B4 have been omitted for brevity. The superscript 'c' in k_{v2} denotes the voltage unbalance factor of the compensated system.

Table 5.6 and Table 5.7 show the average and peak values of k_{v2} calculated over

Table 5.6: Average values of k_{v2} per bus for varying BESS location.

k_{v2}(%)	BESS location					
	–	**LV**	**A2**	**A4**	**C2**	**C4**
$k_{v2,LV}$	0.31	0.05	0.27	0.33	0.31	0.33
$k_{v2,A4}$	0.92	0.80	0.55	0.74	0.94	0.96
$k_{v2,B4}$	0.51	0.32	0.47	0.52	0.52	0.53
$k_{v2,C4}$	0.76	0.67	0.78	0.81	0.50	0.42
$k_{v2,D4}$	0.56	0.32	0.51	0.57	0.56	0.58
$k_{v2,E4}$	0.43	0.30	0.44	0.48	0.44	0.45

Table 5.7: Peak values of k_{v2} per bus for varying BESS location.

k_{v2}(%)	BESS location					
	–	**LV**	**A2**	**A4**	**C2**	**C4**
$k_{v2,LV}$	0.97	0.72	0.99	1.05	1.00	1.06
$k_{v2,A4}$	1.67	1.62	1.53	2.00	1.84	1.85
$k_{v2,B4}$	1.21	1.03	1.24	1.3	1.27	1.31
$k_{v2,C4}$	2.14	2.01	2.22	2.3	2.03	2.00
$k_{v2,D4}$	1.40	1.16	1.42	1.50	1.46	1.51
$k_{v2,E4}$	1.20	0.96	1.22	1.30	1.25	1.31

the 3-hour period, respectively. In the table, blue highlights are used to indicate the minimum value for each busbar. Table 5.6 shows that the BESS placement at busbar LV leads to the minimization of the voltage unbalance factor at buses LV, B4, D4 and E4. This result means that in general, the more upstream the BESS is connected, the highest is its mitigating effect on voltage unbalance in the downstream buses. The maximum reduction of k_{v2} at bus A4 and bus C4 is achieved for BESS location in the middle of feeder A (bus A2) and in the end of feeder C (bus C4), respectively. This result can be explained by the high unbalance originated at these feeders, that require installation of BESS in close proximity to the loads. Table 5.7 shows similar results in terms of peak value. In particular, the peak unbalance at bus C4 is reduced below the standard limits. It is worth noticing that in this model the voltage source is considered symmetrical, while in the practice voltage unbalance levels may be higher thus making the proposed control more attractive to mitigate voltage unbalance locally.

Based on Figure 5.6, one can observe that the BESS control reduces the voltage unbalance factor throughout the simulation period, except a few time periods during which k_{v2} increases. For instance, Figure 5.6(c) shows that with the BESS connected to the LV busbar, the unbalance levels at the end of feeder E (bus E4) rise between 15:00-15:20 h. These times coincide with high PV generation at phase-b and phase-c at bus E4 during this period, and more investigation was carried out to interpret this result.

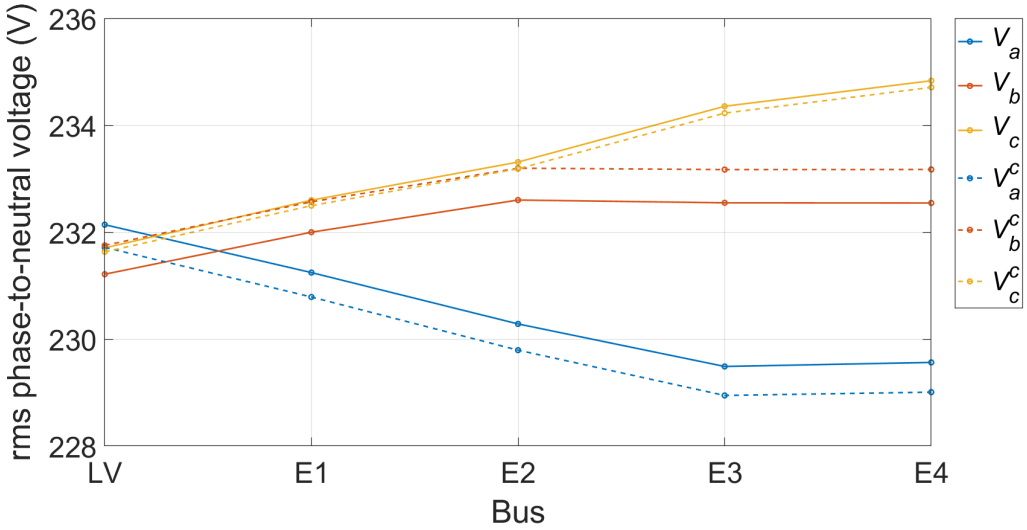

Figure 5.7: rms phase-to-neutral voltage across feeder E for the compensated system (dashed line) and the uncompensated system (continuous line).

More specifically, Figure 5.7 shows the rms voltage values recorded at 15:08 h across feeder E, for the case without compensation and for the case when the BESS units are installed at busbar LV. For the uncompensated system, phase-b voltage (V_b) and phase-c voltage (V_c) values (red and yellow continuous line) increase across the feeder due to the presence of PVs in these two phases. For the compensated system, the contribution of BESSs causes the three rms voltage values (dashed line) to converge at busbar LV ($V_a^c = V_b^c = V_c^c$), i.e. phase-a and phase-c voltage decrease, while phase-b voltage increases. This is the expected result from the proposed control system algorithm. As a result, in the compensated system, phase-a and phase-c voltages are translated downward, while phase-b voltages are translated upward across the system, thus resulting in an increased deviation between the voltages at bus E4 and, as a result, an increased voltage unbalance factor value. This result highlights the importance of monitoring the impact of the proposed strategy across the system to identify the best location.

Figure 5.8 shows the active and reactive power exchange of the BESS units installed at busbar LV for a time frame where high level of unbalance is observed. The active power of phase-a BESS inverter is negative throughout the simulation period, meaning that phase-a BESS unit charges, while phase–b and phase-c BESS units discharge throughout most of the simulation period to mitigate the unbalance. The amount of reactive power absorbed or injected by the BESS units is significantly lower than the active power, since the system unbalance is mostly due to active power unbalance. Figure 5.8 shows that there are time intervals during which phase-a BESS active power is saturated to the limit

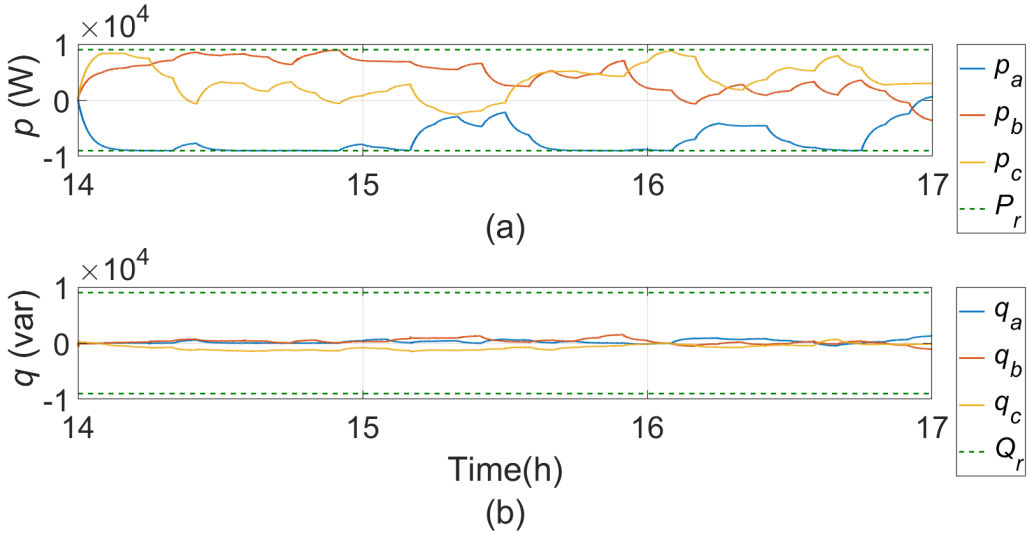

Figure 5.8: (a) Active and (b) reactive power of the BESS inverters connected at busbar LV.

of 9 kVA. As a result of output saturation, the voltage unbalance is not fully eliminated at busbar LV, i.e. $k_{v2,LV} = 0.05$ %, as shown in Table 5.6. Voltage unbalance could be further reduced if BESSs of larger size were installed at this location. However, this may not be necessary as voltage unbalance levels are mitigated to acceptable values.

For BESS located at other busbars, the power exchange with the system is significantly lower and no saturation is observed. For example, it was found that the maximum power exchange between the BESS and the grid is 3 kW and 4 kW for BESS placement at feeder A and C, respectively. These results are in agreement with the ones obtained in [118], where it was shown that the BESS power exchange is reduced when BESSs are placed downstream due to lower load demand at these locations. As a result, a BESS with lower rating may be installed at feeders A and C without compromising the effectiveness of unbalance compensation. In this work, the same battery size was considered at all locations for simplicity, but in a practical application the battery rating will be chosen as a compromise between performance, cost, ancillary services provided and their remuneration [118].

Figure 5.9(a)-(b) show the active power flows at busbar LV without ($p_{i,LV}$) and with ($p^c_{i,LV}$) the proposed control strategy for BESS units connected at busbar LV, respectively. The compensating action performed by the three BESS units results in balanced power flows at the substation, therefore more effective utilization of the distribution line and transformer capacity can be achieved. This is demonstrated by the fact that a peak of -52 kW maximum capacity is required for the feeder in Figure 5.9(a) compared to the

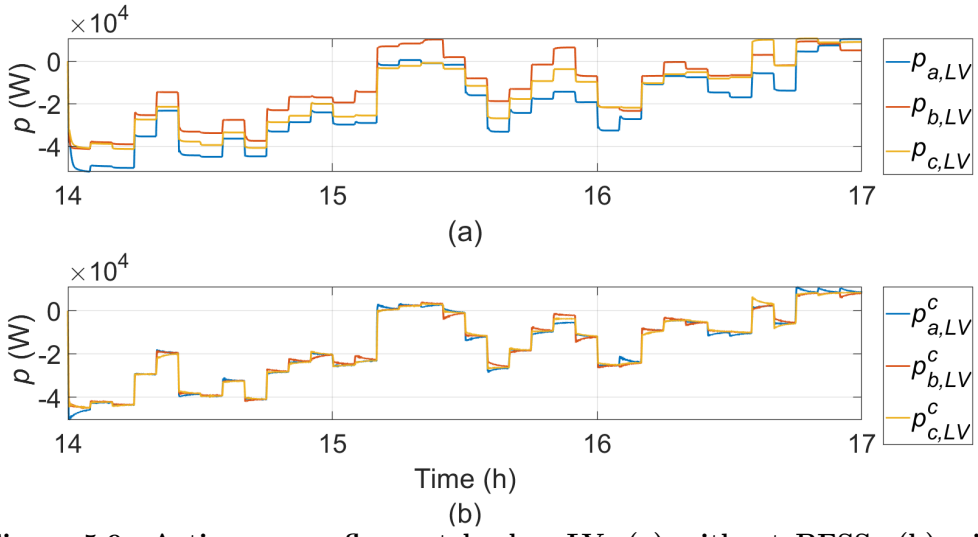

Figure 5.9: Active power flows at busbar LV: (a) without BESSs (b) with BESSs connected.

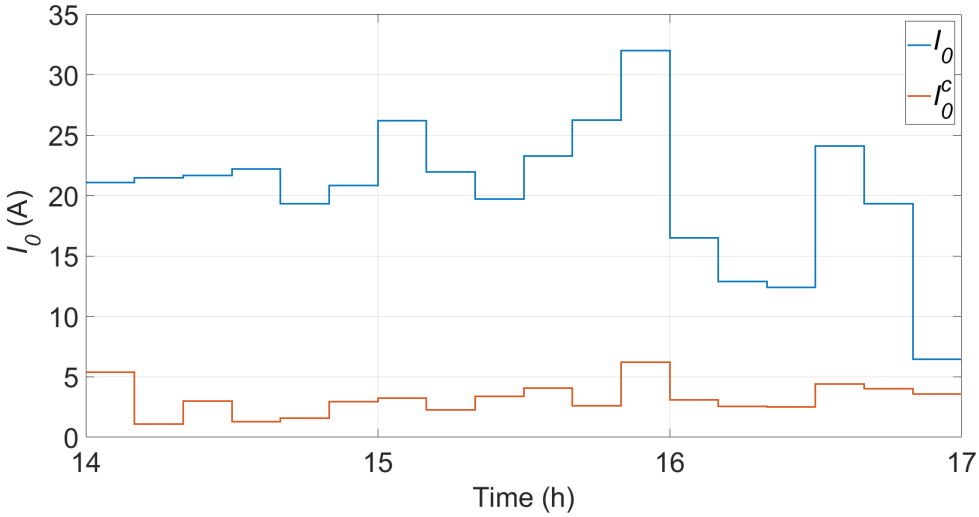

Figure 5.10: Zero-sequence current component at busbar LV without (blue) and with (orange) compensation.

-45 kW peak capacity required in Figure 5.9(b). Similar results were obtained for the reactive power profiles, which are omitted here for brevity.

The 10-min aggregated values of the zero-sequence current component of the transformer are plotted in Figure 5.10: these results show that the proposed control strategy can alleviate the current flowing in the neutral conductor.

Based on the positive results obtained in the simulation environment, the next step consisted in experimental validation that will be described in Chapter 6.

5.5 Conclusions

In this chapter, the proposed voltage unbalance compensation strategy was validated for a typical UK distribution network consisting of realistic profiles of residential demand, PVs and EVs. Initially, the effect of varying penetration of PVs and EVs on voltage unbalance was examined, showing that these two technologies may have a different impact on the system unbalance.

The effectiveness of the unbalance compensation scheme was demonstrated for a simulation scenario in which both PVs and EVs were connected to the distribution system. The results have shown that the BESS units have the capability to provide an overall reduction in the unbalance levels, decrease the neutral current and equalize the power flows at the substation, thereby enabling a more effective utilization of the feeder and transformer capacity.

In Chapter 7, probabilistic simulations will be carried out to reinforce the conclusions of this chapter, in which a deterministic approach was adopted.

Chapter 6

Experimental Validation of Voltage Unbalance Mitigation Strategy

6.1 Introduction

In this chapter, the experimental verification of the developed voltage unbalance mitigation strategy is carried out. Hardware-In-The-Loop simulations are realized using MATLAB/Simulink software, OPAL-RT device and an ARM-based microcontroller[1].

6.2 Experimental Setup

To validate the control strategy experimentally, Hardware-In-The-Loop (HIL) tests were carried out. Figure 6.1 shows the laboratory setup: an OP5600 real-time simulator was used to run the grid, load and inverter models in real-time [2]. As a first step, a series of edits were made to the Simulink model using RT-LAB, which is the software platform of OPAL-RT. This step was necessary in order to enable the model to run in real time. Then, the model was loaded in the simulator and it was executed in real time. These steps are described in Appendix E in detail. The communication between the computer and the OPAL-RT was established via an Ethernet cable. The PELab-3PHHPLC is a power electronics development system consisting of a configurable inverter and an embedded controller based on ARM Cortex M7/M4 dual-core microcontroller, which is programmed

[1] This chapter is based on the work published in [2].

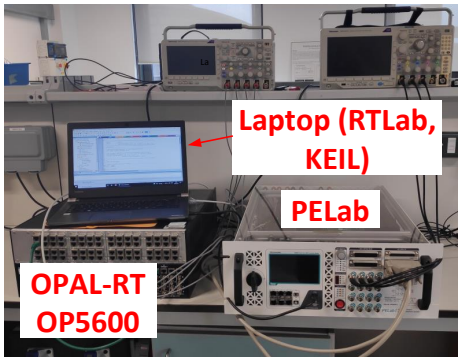

Figure 6.1: Laboratory setup including the PELab-3PHHPLC and OPAL-RT simulator managed by the RT-LAB and Keil software respectively.

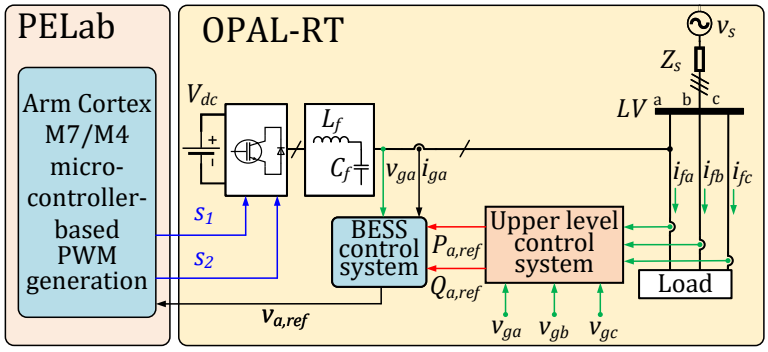

Figure 6.2: Real time simulation model and overview of the control scheme and signals [2].

with the use of Keil software. More details regarding the microcontroller programming are provided in Appendix E. PELab exchanges analogue and digital signals with OPAL-RT by means of DB37 connector cables.

In this work, the control algorithm was implemented in OPAL-RT, with the microcontroller being responsible for generating the PWM signals. More specifically, as shown in Figure 6.2, the closed-loop controller calculates and sends the reference voltage $v_{a,ref}$ to the microcontroller, which generates the switching signals (s_1, s_2) for the single-phase inverter connected at phase-a. In this work, only single-phase inverter operation is carried out due to equipment limitations. However, it is worth emphasizing that this approach is still valid to test the proposed control strategy. The experimental setup corresponds to simulation cases where one inverter is in service (see Section 4.2.2.2). As Figure 6.2 shows, phase-a voltage and current (v_{ga}, i_{ga}) are measured at the inverter terminal to be used in the BESS control system, while phase-a voltage and the three phase feeder

Table 6.1: Experimental parameters.

Parameters	Values
rms grid voltage	$V_s = 230$ V
Source impedance	$\boldsymbol{Z_s} = 0.0716 + j0.0504\ \Omega$
Switching and sampling frequency	$f_{sw} = f_s = 5$ kHz
PI power controller	$k_{pp} = 0.1$, $k_{pq} = 0.1$ $k_{ip} = 10\ \text{s}^{-1}$, $k_{iq} = 10\ \text{s}^{-1}$
PR current controller	$k_{pi} = 5\ \Omega$, $k_{ii} = 70\ \Omega\text{s}^{-1}$
Three-phase Load 1 (L1)	$P_{L1i} = 100$ kW, $Q_{L1i} = 5$ kvar, i = a,b,c
Three-phase Load 2 (L2)	$P_{L2a} = 15$ kW, $Q_{L2a} = 2$ kvar, $P_{L2b} = 6$ kW, $Q_{L2b} = 1$ kvar, $P_{L2c} = 2$ kW, $Q_{L2c} = 0.5$ kvar
Single-phase Load 3 (L3)	$P_{L3a} = 5$ kW, $Q_{L3a} = 1$ kvar

currents' readings (v_{ga} and i_{fi} for i = a, b, c) are needed for the upper level control system to calculate phase-a reference power based on the formula provided in Eq. (3.3).

The circuit modelled in OPAL-RT consists of three symmetrical voltage sources connected to an unbalanced load via impedances. The BESS was modelled using a constant DC voltage source. The PR controller gains were modified compared to the values used in the offline simulations to obtain a stable response. Additionally, the switching frequency was reduced to 5 kHz from the value of 10 kHz that was used in the offline simulations. This modification was made to satisfy OPAL-RT platform requirements [127]. Based on [128], the accuracy of the simulation results is increased if the ratio of the simulator's sampling frequency over the inverter's switching frequency is kept above ten, i.e. $\frac{f_{s,op}}{f_{sw}} > 10$. In addition, the sampling time of the OPAL-RT simulator should satisfy the requirement $T_{s,op} \geq 20$ us or $f_{s,op} \leq 50$ kHz, since lower sampling time values generally lead to overruns and inaccurate results [127]. Given the above limitations, the simulator's sampling frequency and the inverter's switching frequency were chosen as $f_{s,op} = 50$ kHz and $f_{sw} = 5$ kHz, respectively. The sampling frequency of the microcontroller (f_s) was chosen equal to the switching frequency. Table 6.1 summarizes the experimental parameters.

6.3 Experimental Results

To validate the developed control strategy experimentally, a single BESS unit connected at phase-a was controlled to mitigate the unbalance caused by three-phase and single-phase loads. Initially, a balanced load L1 was connected to the system. At $t = 2$ s, an unbalanced load L2 was added in parallel, and at $t^{'} = 4$ s the unbalance at phase-a

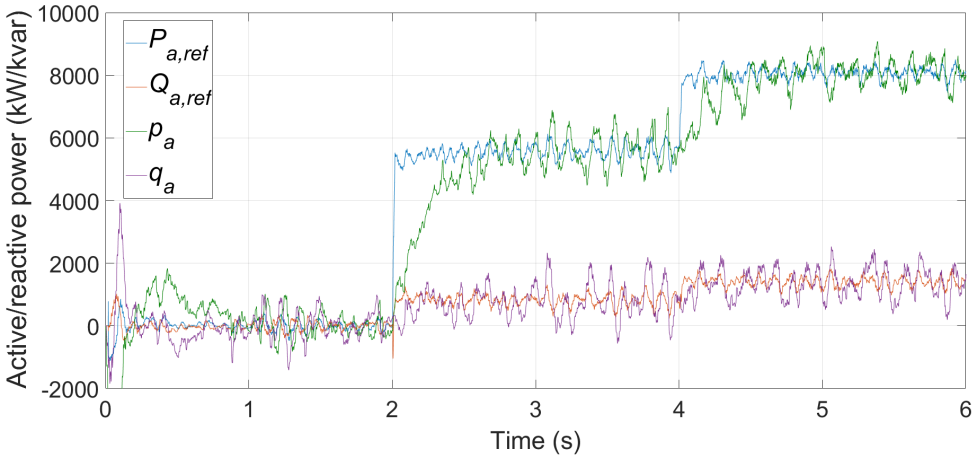

Figure 6.3: Active and reactive power injected by phase-a inverter [2].

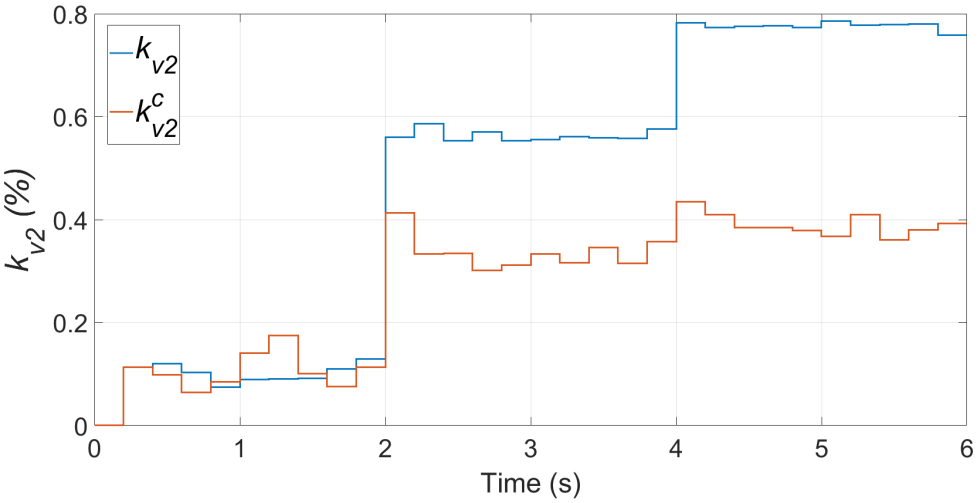

Figure 6.4: Voltage unbalance factor at busbar LV, without (blue) and with (orange) compensation [2].

was further increased by adding the load L3 at the same phase. The loads' active and reactive powers are provided in Table 6.1.

The active and reactive power injections from phase-a inverter are shown in Figure 6.3 [2]. Figure 6.4 shows the voltage unbalance factor profiles without BESS (k_{v2}) and with BESS connected (k^c_{v2}) aggregated over 200 ms for a simulation period of 6 s [2]. The aggregation window in this case is different from the one used in simulation, as shorter times are monitored. However, both aggregation windows are used in practical applications, as described in IEC 61000-2-2 [77]. Between $t = 0$ s and $t = 2$ s, the

unbalance is close to zero since the load is balanced. At $t = 2$ s, the unbalanced load is introduced and $k_{v2} = 0.57\%$ for the uncompensated system. For the compensated system, the BESS inverter injects active and reactive power equal to $p_a = 5.5$ kW and $q_a = 0.8$ kvar. As a result, the phase-a power flow through busbar LV is reduced and a more balanced power flow is obtained, leading to a lower voltage unbalance factor value, i.e. $k_{v2}^c = 0.33\%$. At $t^{'} = 4$ s, k_{v2} increases to 0.77% due to the additional load connected at phase-a. Therefore, the controller responds by further increasing the injection of active and reactive power to $p_a = 8$ kW and $q_a = 1.4$ kvar, respectively.

As it can be observed from Figure 6.3, both curves of active and reactive power of phase-a inverter contain high frequency noise. This is due to hardware limitations. More specifically, as described in Section 6.2, the maximum possible sampling frequency of the OPAL-RT simulator is $f_{s,op,max} = 50$ kHz. At the same time, the inverter's switching frequency is equal to $f_{sw} = 5$ kHz. Even though the condition $\frac{f_{s,op}}{f_{sw}} > 10$ is marginally satisfied, the obtained results demonstrate that the value of the sampling frequency used to simulate the inverter model should be further increased in order to improve the accuracy of the obtained results.

Alternatively, the PWM generation scheme can be implemented inside OPAL-RT, i.e. the TSB-RD inverter model can be used in conjuction with the blocks from the RT-EVENTS library to generate the PWM pulses instead of using the microcontroller. The benefit of this approach is that these blocks are implemented based on interpolation techniques, which allow for improved accuracy of the PWM pulses without having to increase the value of $f_{s,op}$ significantly. This will be shown in the next subsection, where the accuracy of the obtained results is significantly improved since it is possible to compensate for the sampling effect of the simulator.

6.3.1 Experimental Results for PWM generation in OPAL-RT

In this case, the PWM pulses are generated in OPAL-RT instead of using the microcontroller. Figure 6.5 presents the circuit built in Simulink to produce the switching pulses for phase-a inverter. As can be seen from this graph, PWM with unipolar voltage switching is implemented. Note that bipolar voltage switching can be also used without having any significant impact on the results, since the focus is on k_{v2}, which is calculated based on the fundamental components of the phase voltages. The PWM scheme is briefly described next: phase-a reference voltage signal is scaled between -1 and +1 by dividing it with the inverter DC voltage (V_{dc}), and it is compared to the carrier signal v_{car}, which

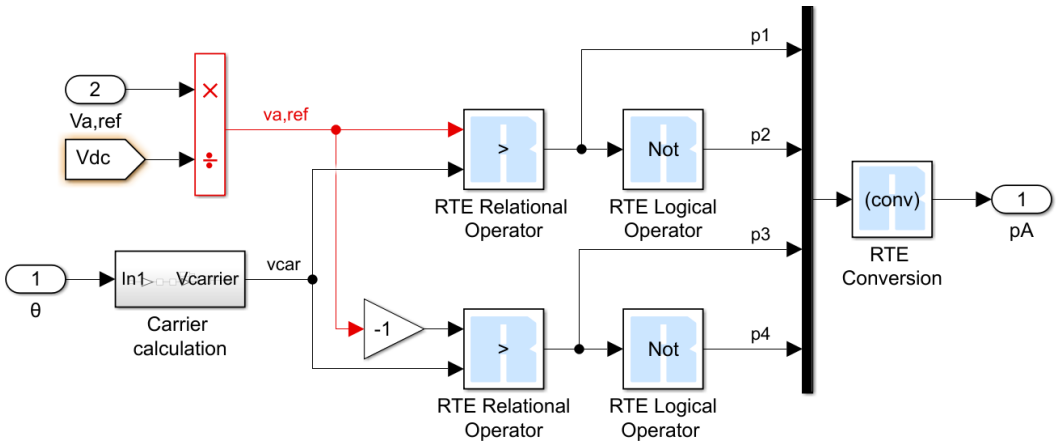

Figure 6.5: PWM generation scheme using OPAL-RT blocks.

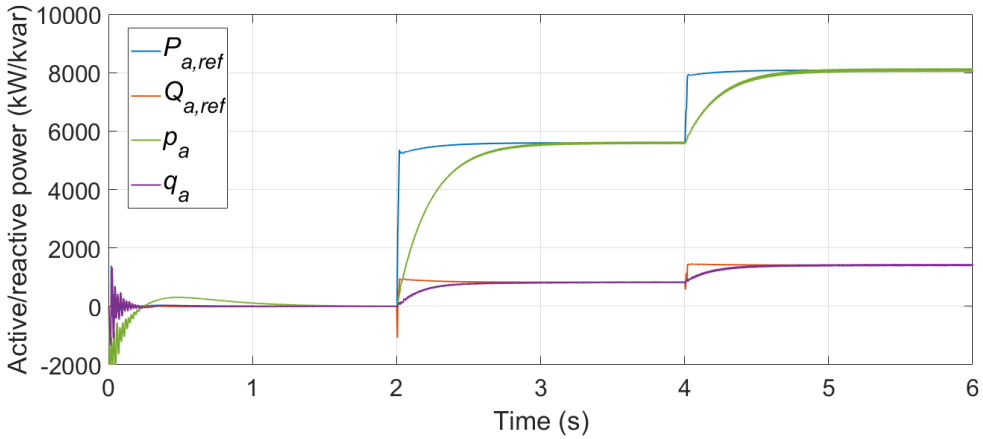

Figure 6.6: Active and reactive power injected by phase-a inverter.

receives the PLL estimated angle θ as an input, and it is calculated as follows:

$$v_{car} = 2\pi sin^{-1}(sin(\theta m_f)) \tag{6.1}$$

where $m_f = \frac{f_{sw}}{f_1}$ is the frequency modulation ratio, for $f_{sw} = 5$ kHz and $f_1 = 50$ Hz. The signals $v_{a,ref}$ and $-v_{a,ref}$ are compared with v_{car} in order to produce the pulses for the single-phase full-bridge inverter (p1-p4). The data type is converted from 'Boolean' to 'Double' so that the pulses can be fed to the inverter's gate.

The real-time simulation results obtained for the active and reactive power of phase-a inverter when the PWM pulses are generated based on the circuit described above can be seen in Figure 6.6. By comparison of this graph with Figure 6.3, it can be observed that

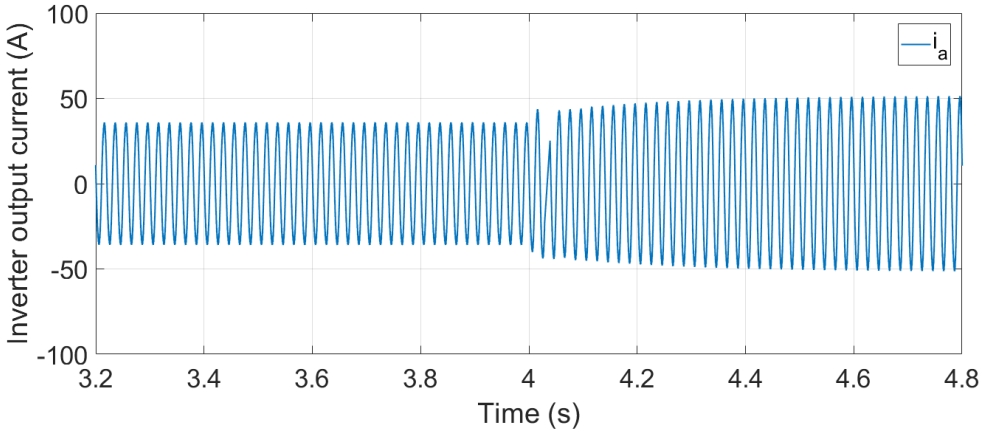

Figure 6.7: Current measured at phase-a inverter's terminal.

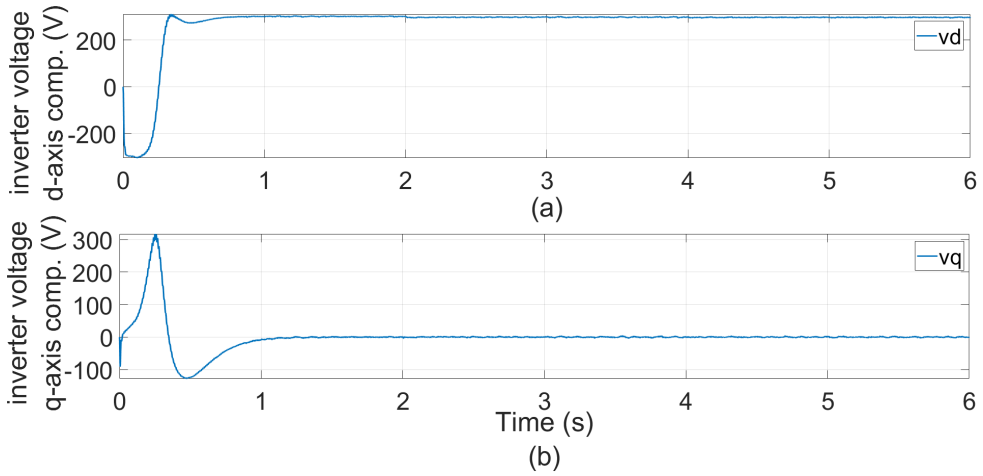

Figure 6.8: dq-components of phase-a inverter voltage.

the steady state values of active and reactive power injected by phase-a inverter are very similar for the two cases. As a result, the voltage unbalance factor value is very similar to the one shown in Figure 6.4, therefore the corresponding curve is omitted here.

Figure 6.7 shows the current injected by the inverter to compensate voltage unbalance. Between $t = 2$ s and $t^{'} = 4$ s, the peak value of the inverter current is measured equal to $i_{a,peak} = 36$ A, while this value is increased to $i_{a,peak} = 51$ A after $t^{'} = 4$ s, since the levels of voltage unbalance are increased due to the addition of load at phase-a.

Finally, Figure 6.8 presents the curves of the dq-components of phase-a voltage, demonstrating that the PLL can track its frequency and phase angle. More specifically, once the initial transients fade out, the q-axis component (v_q) is forced to zero, while the

d-axis component (v_d) becomes equal to the peak voltage of phase-a voltage.

6.4 Conclusions

The experimental work presented in this chapter demonstrates that the developed control strategy can effectively mitigate voltage unbalance for the case when an individual BESS is connected. Further reduction or full unbalance mitigation will require providing zero- and negative-sequence load current component at phase-b and phase-c by the other two inverters. This operating condition was not examined in the context of this thesis due to time and hardware limitations. More specifically, the availability of a single CPU core in the OPAL-RT platform used in this work renders the real-time simulation of three BESS inverters challenging and the obtained results prone to errors due to limited computational resources. Furthermore, as discussed in this chapter, another limitation of the platform is related to the minimum possible sampling rate, which was shown to have an impact on the accuracy of the obtained results. This issue could be solved by using up-to-date versions of the OPAL-RT platform, and it can be the topic of future research.

Chapter 7

Probabilistic Assessment of the Impact of PVs and EVs on Voltage Unbalance without and with Voltage Unbalance Mitigation Provided by BESS

7.1 Introduction

In Chapter 5, deterministic simulations were carried out to examine the impact of varying PV and EV penetration levels on voltage unbalance and to evaluate the effectiveness of the BESS control strategy on mitigating the unbalance. The location and size of the loads, PVs and EVs were fixed, and a single simulation was executed for each penetration level. This chapter presents a statistical analysis, which is performed to account for varying loading conditions, PV and EV penetration levels. Probabilistic simulations are realized by randomizing the location and size of the loads, PVs and EVs for each simulated day with the aim to represent the statistical variations of voltage unbalance levels in the distribution system under varying loading and generating conditions. For the purpose of performing the probabilistic simulations, a simplified model is derived from the detailed Inverted-based model presented in the previous chapters.

7.2 Development of the Current Source-based model

Probabilistic simulation studies generally involve a large number of simulations, which is typically in the range of thousands. The detailed BESS Inverted-based model developed in Chapter 2-3 is not suitable for this type of studies due to its complexity, which results in long computational times for values of the sample time (T_s) in the range of μs. The computational time can be decreased by applying lower sample frequency values. However, this approach introduces significant delays in the control system, which adversely affect its stability and eventually lead to control system misoperation. Therefore, an equivalent simplified model - referred to as Current Source–based model - was derived from the Inverter-based model by replacing the BESS units with current sources controlled to inject the negative– and zero–sequence fundamental current components into the power system. This model allows for the use of higher sample time values and therefore decreases the required computational time, while concurrently providing accurate results in close agreement with those obtained from the original model. The value of T_s was chosen considering the trade-off between the computational time and the accuracy of the results.

The Current Source-based model is presented in Figure 7.1. Compared to Figure 3.5, it can be observed that the detailed inverter control system is not modelled, and the same upper level control system is deployed to calculate the reference current signals, except that the control system does not receive the phase voltage measurements at the BESS terminals, since for the purpose of this model the current references are calculated instead of power references. Once the reference current phasors [$\boldsymbol{I_{a,ref}}$, $\boldsymbol{I_{b,ref}}$, $\boldsymbol{I_{c,ref}}$] have been calculated, they are converted to the time domain and they are fed to the controlled current sources of each phase. The time domain expressions of the reference currents are given below:

$$i_{a,ref} = I_{a,ref} sin(\omega t + \phi_a) \tag{7.1}$$

$$i_{b,ref} = I_{b,ref} sin(\omega t + \phi_b) \tag{7.2}$$

$$i_{c,ref} = I_{c,ref} sin(\omega t + \phi_c) \tag{7.3}$$

where $\omega = 100\pi$ rad/s the fundamental angular frequency, while $I_{i,ref}$ and ϕ_i are the magnitude and phase angle of phase-i current controlled source, for $i = a, b, c$. A saturator block is added to ensure that the current magnitudes do not exceed the nominal current, and its value is set equal to $\frac{\sqrt{2}S_n}{V_{LNn}}$.

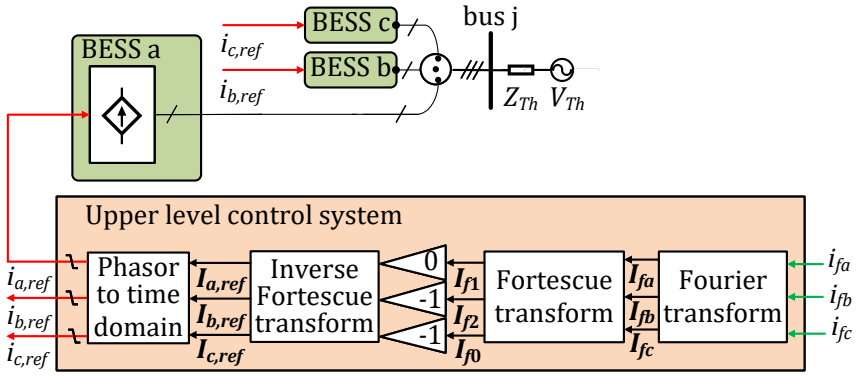

Figure 7.1: Phase-a controlled current source and upper level control system.

7.2.1 Simulation framework for the validation of the Current Source-based model

To verify the validity of the developed model, the same network model as in Chapter 5 was used and comparative simulations were performed between the Current Source–based model and the Inverter–based model under two different power system operating conditions: (i) 100 Loads and no PVs (ii) 100 Loads and 60 PVs connected to the distribution system. In both cases, no EVs were connected. The Inverter-based model was simulated using the step size of $T_{s1} = 6$ μs. To determine the step size used for the Current Source-based model, various sample time values in the range of 50 μs-5 ms were tested, leading to the choice of $T_{s2} = 0.5$ ms. This value was chosen since the results of the two models were shown to present a satisfactory match with negligible error for the operating conditions described above, while at the same time allowing to run the probabilistic cases within a manageable time frame. In the next section, the comparative results between the two models for $T_{s2} = 0.5$ ms are plotted.

The loads and EVs were modelled as static loads, in contrast to the approach adopted in Chapter 5. The reason for this choice is that the use of static load models decreases the simulation time. The PVs were modelled based on the approach followed in Chapter 5. However, it was observed that the use of $T_{s2} = 0.5$ ms introduces a phase shift in the phase angle of the PV current, therefore this phase shift was compensated inside the block to make the PVs operate at unity power factor.

Simulations were realized for the two models for the time period 15:00-15:30 h, and the following quantities were plotted comparatively: voltage unbalance factor (k_{v2}) on six busbars, reference current ($i_{i,ref}$), active power (p_i) and reactive power (q_i) of phase-i compensating unit, where $i = a, b, c$. Note that depending on the model under study,

the term compensating unit is used to describe either phase-i inverter (Inverter-based model) or phase-i current source (Current-Source based model). Five 10-min simulations were run for each of the two power system operating conditions described above. At each simulation, a step change was introduced in the load power for case (i), while a step change was applied to both the load and PV power for case (ii). The load and PV step changes were applied at the following time instants: 15:05 h, 15:10 h, 15:15 h, 15:20 h and 15:25 h. While other time periods can be chosen to perform the comparison between the two models, this time period was selected due to the presence of considerable voltage unbalance.

The time scale was compressed such that 5 min correspond to 2 s, instead of 0.5 s that has been used in the simulations presented in the previous chapters. This choice was made to allow the outputs of the Inverter-based model enter in steady state, and therefore to enable the comparison of the results between the two models. In the following figures, the subscripts 's1' and 's2' refer to the Inverted-based model and Current source-based model, respectively.

7.2.2 Validation of the Current Source-based model for the case with 100 loads

Figure 7.2 presents the simulation results of k_{v2} at the six buses for the time period 15:00-15:10 h. Between 15:00-15:05 h, the graph shows that the curves of k_{v2} coincide for the two models. More specifically, it was found that the k_{v2} values obtained from the simulation of the Current Source-based model are equal to the k_{v2} values of the Inverter-based model averaged over this 5-minute period. A load step change is introduced at 15:05 h, and the voltage unbalance factor at bus C4 (purple line) is reduced to half, while a slight change is observed in the corresponding values in the other buses. Again, it can be observed that the k_{v2} curves concur.

From the same figure, it can be observed that the k_{v2} values of the Current Source-based model change instantaneously, while the k_{v2} values of the inverter-based model present some transient both in the beginning of the simulation and at the instant of the load step change, at 15:05 h. These transients arise from the detailed inverter control system, which cannot regulate the inverter active and reactive power output to their reference values instantaneously. However, the transients fade after a few milliseconds, demonstrating that under steady state conditions the two curves coincide and the modelled controlled current source can approximate the inverter model accurately.

Figure 7.3-7.6 shows the k_{v2} results obtained for the rest of the simulated cases. It can be observed that the k_{v2} values of the two models closely match for these cases as well,

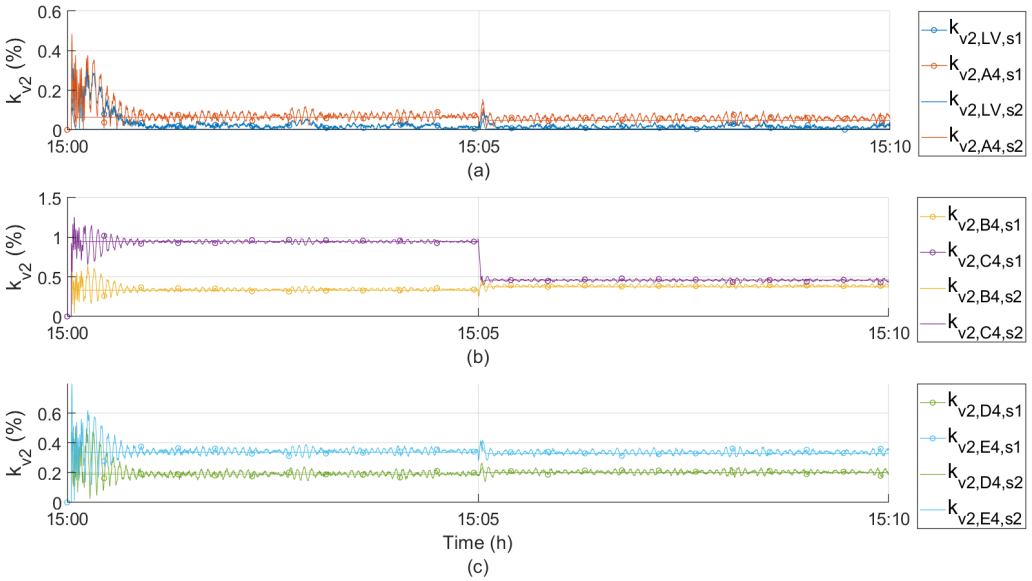

Figure 7.2: Voltage unbalance factor values between 15:00–15:10 h ('s1': inverted-based model, 's2': current source-based model).

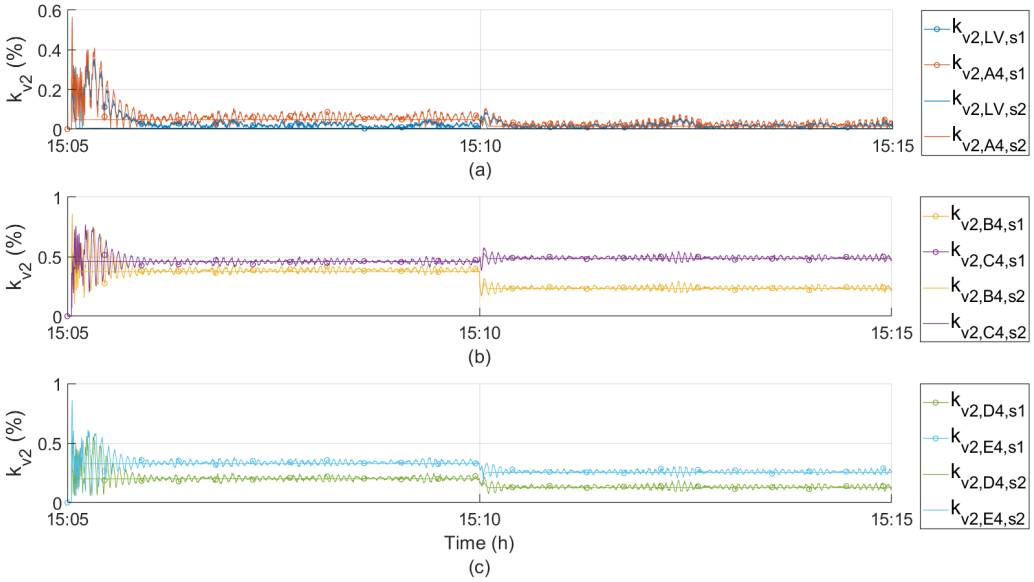

Figure 7.3: Voltage unbalance factor values between 15:05–15:15 h ('s1': inverted-based model, 's2': current source-based model).

therefore verifying that the Current Source-based model can accurately approximate the Inverter-based model when a sample time of $T_{s2} = 0.5$ ms is used.

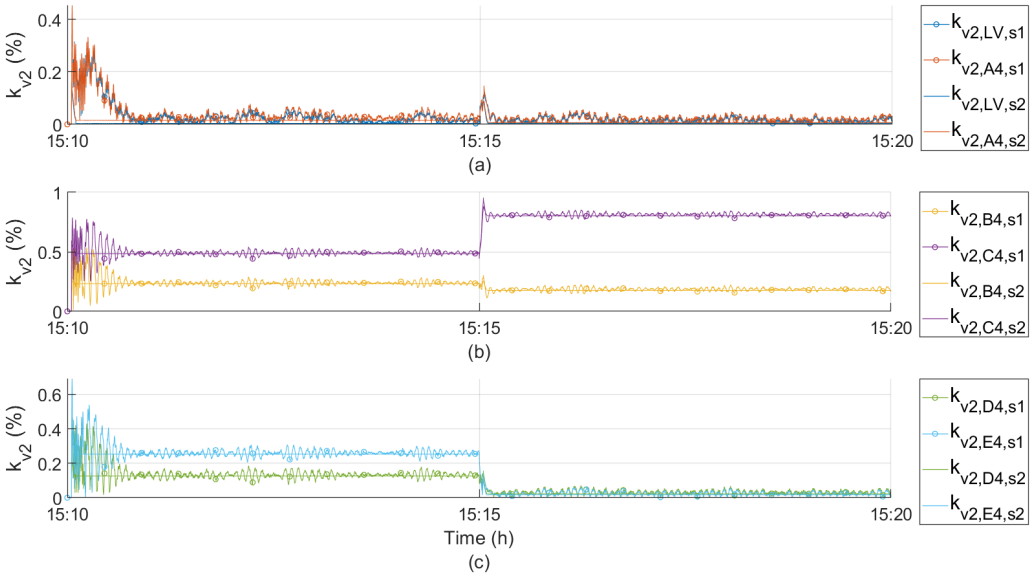

Figure 7.4: Voltage unbalance factor values between 15:10–15:20 h ('s1': inverted-based model, 's2': current source-based model).

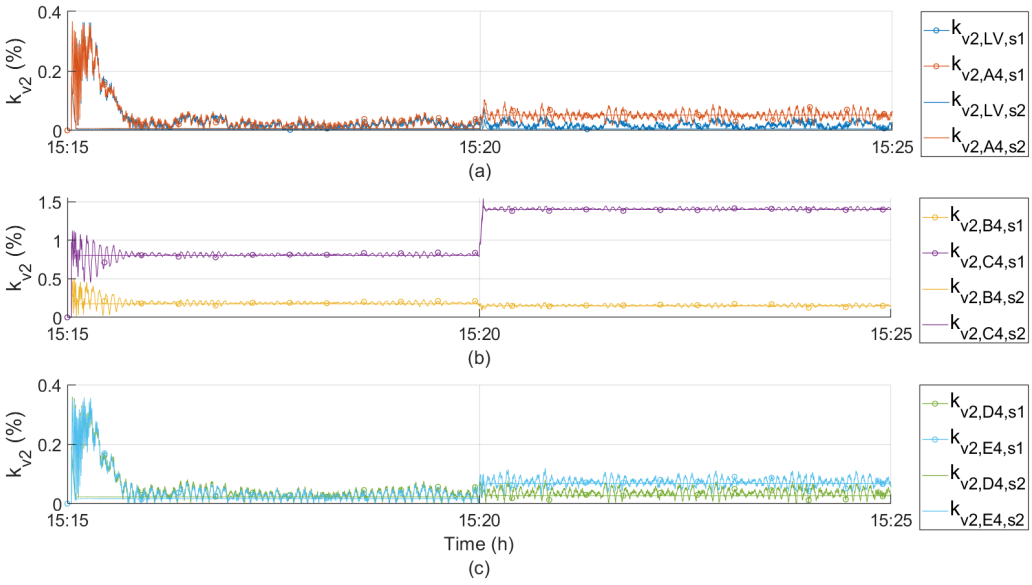

Figure 7.5: Voltage unbalance factor values between 15:15–15:25 h ('s1': inverted-based model, 's2': current source-based model).

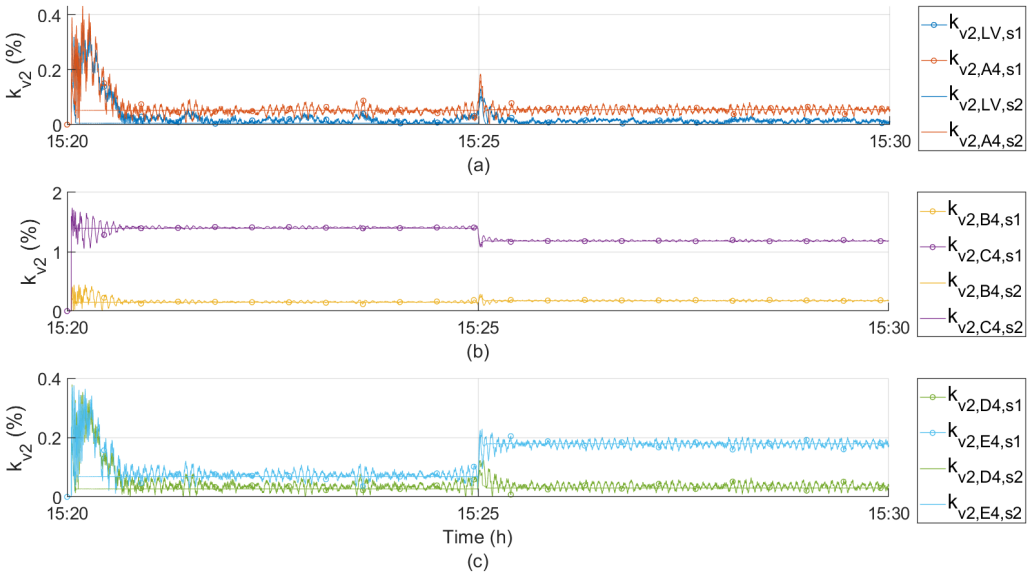

Figure 7.6: Voltage unbalance factor values between 15:20–15:30 h ('s1': inverted-based model, 's2': current source-based model).

The k_{v2} curves obtained from the inverter-based model's simulations exhibit noise since the k_{v2} values are calculated in Simulink using an aggregation window of 1 cycle. The presence of small steady-state errors in the current control may introduce small oscillations in the voltage and, consequently, in the k_{v2} curves. Alternatively, 5-min aggregated values could have been plotted. However, the current approach is sufficient for the purpose of comparing the k_{v2} values with the ones obtained from the current source-based model, and thus validate the latter.

Figure 7.7(a)-(c) present the simulation results obtained for the reference current of the three compensating units $i_{i,ref}$, for $i = a, b, c$. Similar to the plots of k_{v2}, it can be seen that the reference currents of the Current Source-based model (red curves) change instantaneously, while the inverter control system introduces transients in the reference currents of the inverter-based model (blue curves). However, the two curves coincide under steady state conditions demonstrating that the controlled current source constitutes an accurate approximation of the inverter model. The above conclusion is reinforced by the results obtained from the rest of the simulated cases, as shown in Figure 7.8-7.11. For some of these figures, the initial load condition results in a longer duration of these transients, since the inverter needs more time to regulate the current to its reference value.

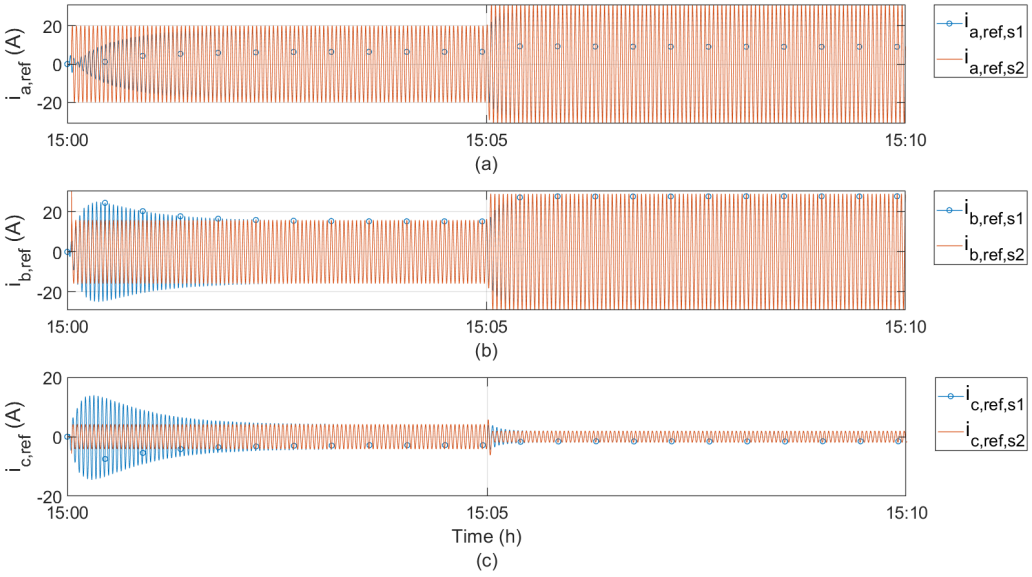

Figure 7.7: Reference current of (a) phase-a (b) phase-b (c) phase-c compensating unit between 15:00–15:10 h ('s1': inverted-based model, 's2': current source-based model).

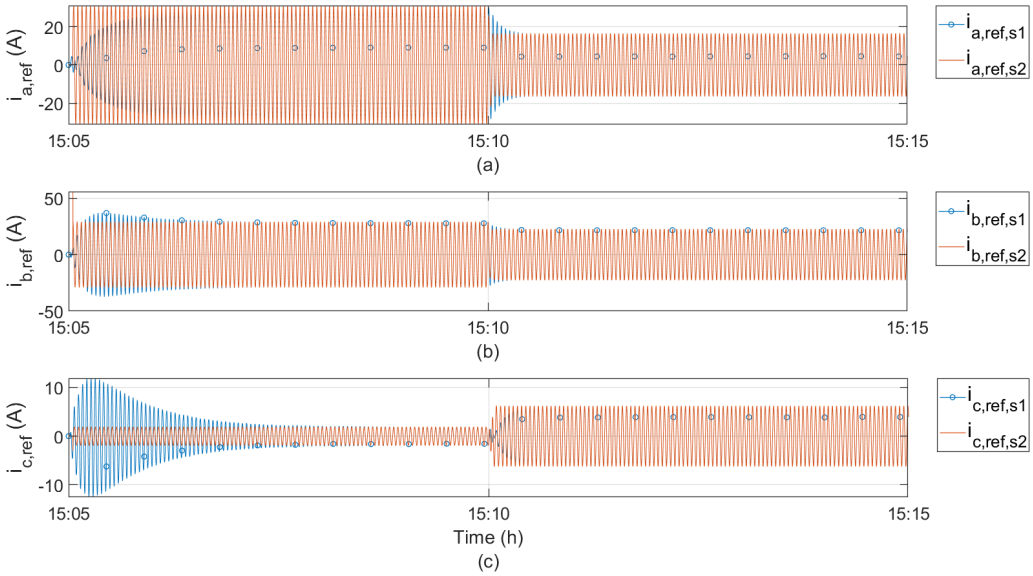

Figure 7.8: Reference current of (a) phase-a (b) phase-b (c) phase-c compensating unit between 15:05–15:15 h ('s1': inverted-based model, 's2': current source-based model).

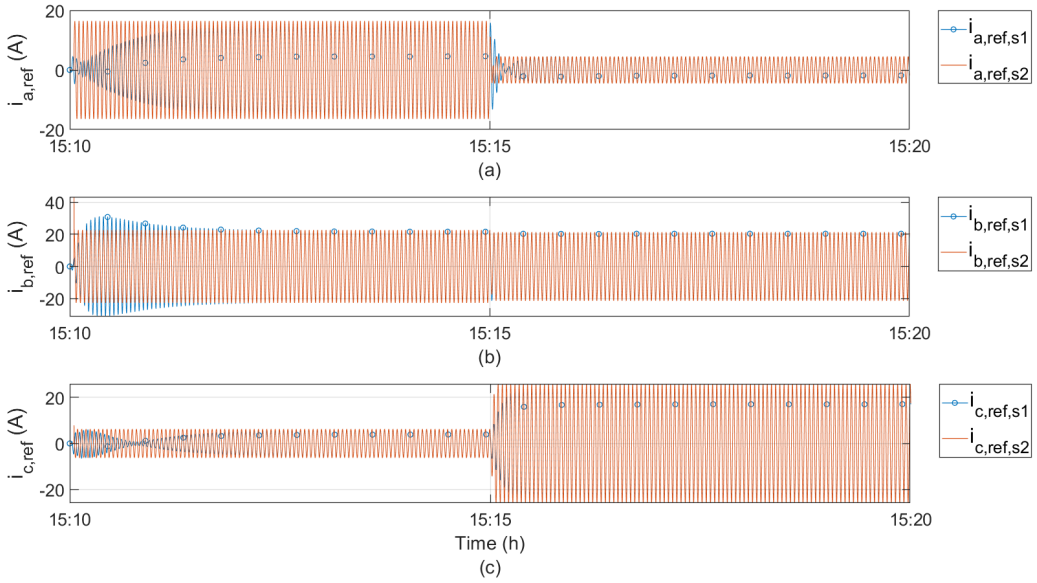

Figure 7.9: Reference current of (a) phase-a (b) phase-b (c) phase-c compensating unit between 15:10–15:20 h ('s1': inverted-based model, 's2': current source-based model).

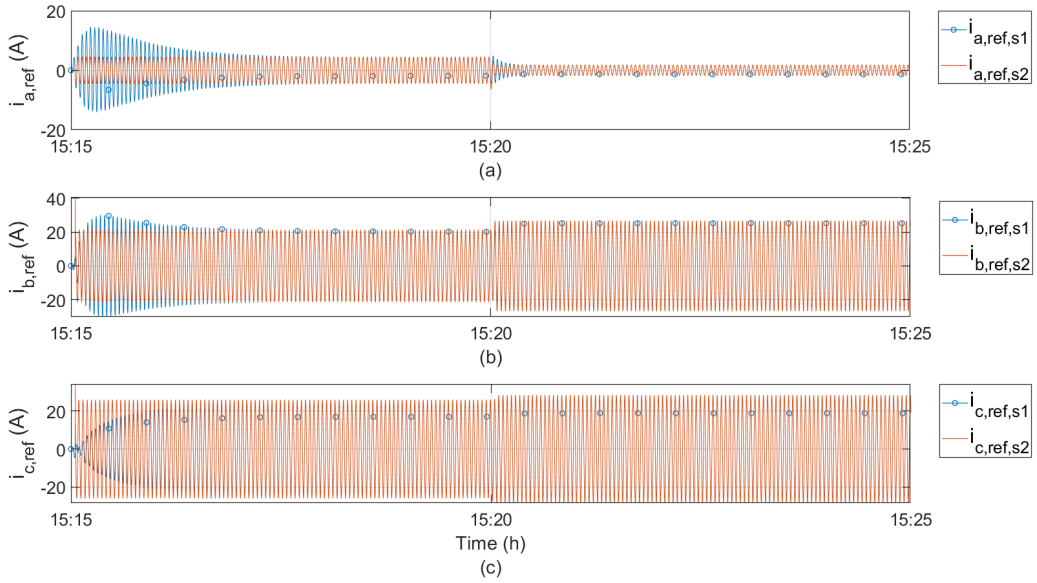

Figure 7.10: Reference current of (a) phase-a (b) phase-b (c) phase-c compensating unit between 15:15–15:25 h ('s1': inverted-based model, 's2': current source-based model).

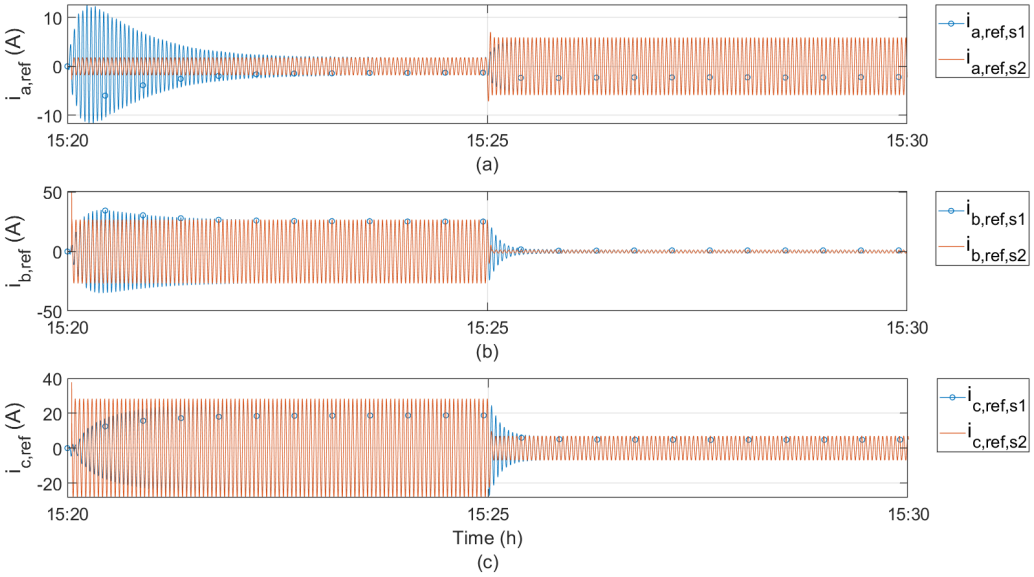

Figure 7.11: Reference current of (a) phase-a (b) phase-b (c) phase-c compensating unit between 15:20–15:30 h ('s1': inverted-based model, 's2': current source-based model).

Figures 7.12-7.16 present the simulation results of the measured active and reactive power (p_i and q_i) in the output of the compensating units for the two models. Similarly to the figures of k_{v2} and reference current, it can be observed that the active and reactive power injected and absorbed by the inverter units and the current sources coincide; negligible variations in the measured power may occur due to the fact that the inverter output filter was not included in the Current Source-based model.

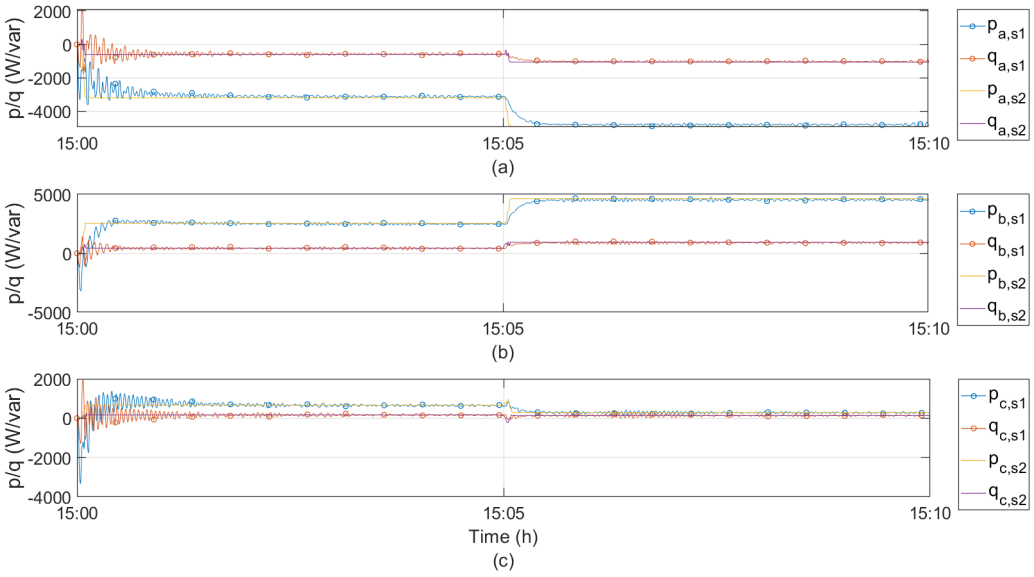

Figure 7.12: Measured active and reactive power of (a) phase-a (b) phase-b (c) phase-c compensating unit between 15:00–15:10 h ('s1': inverted-based model, 's2': current source-based model).

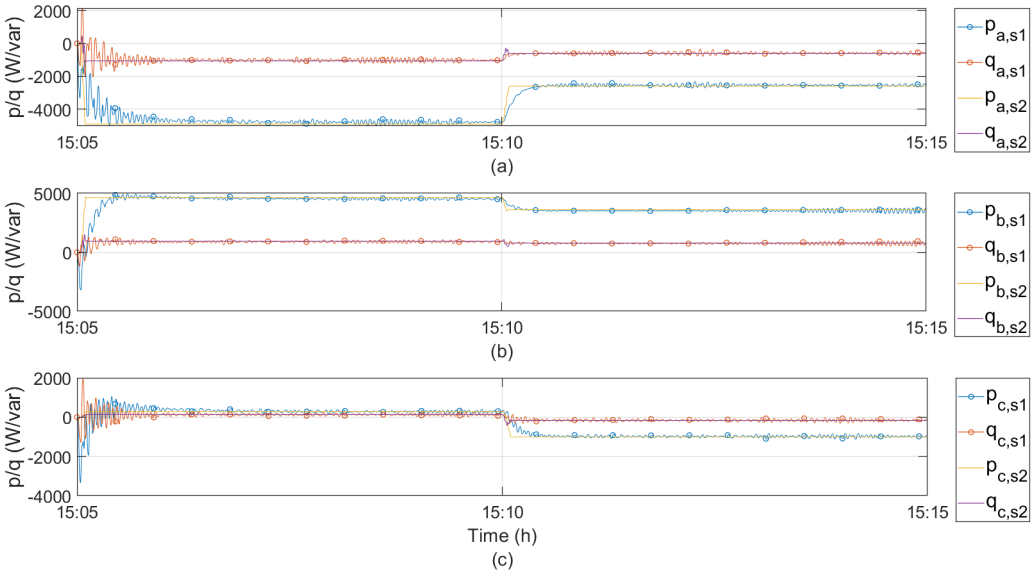

Figure 7.13: Measured active and reactive power of (a) phase-a (b) phase-b (c) phase-c between 15:05–15:15 h ('s1': inverted-based model, 's2': current source-based model).

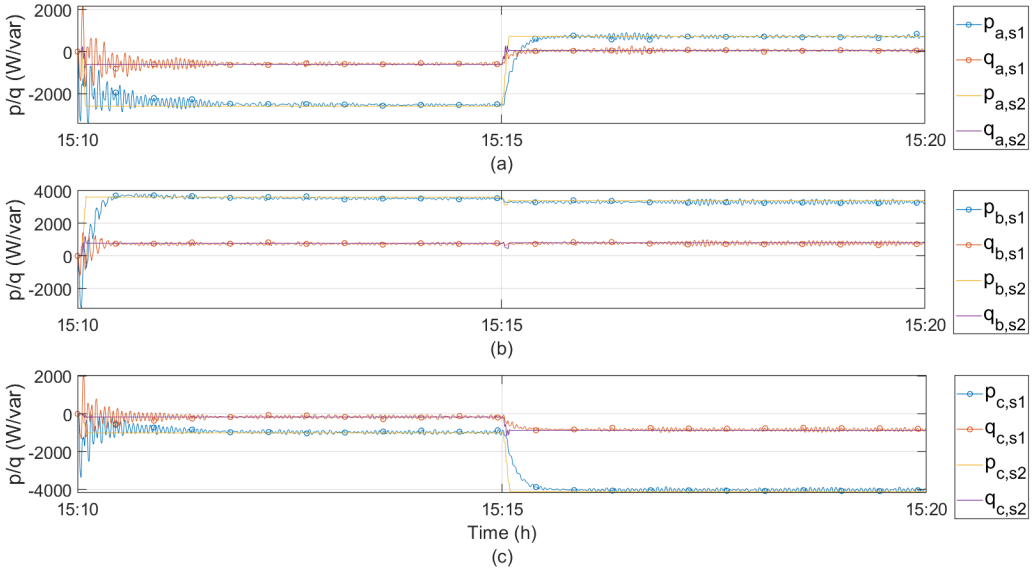

Figure 7.14: Measured active and reactive power of (a) phase-a (b) phase-b (c) phase-c between 15:10–15:20 h ('s1': inverted-based model, 's2': current source-based model).

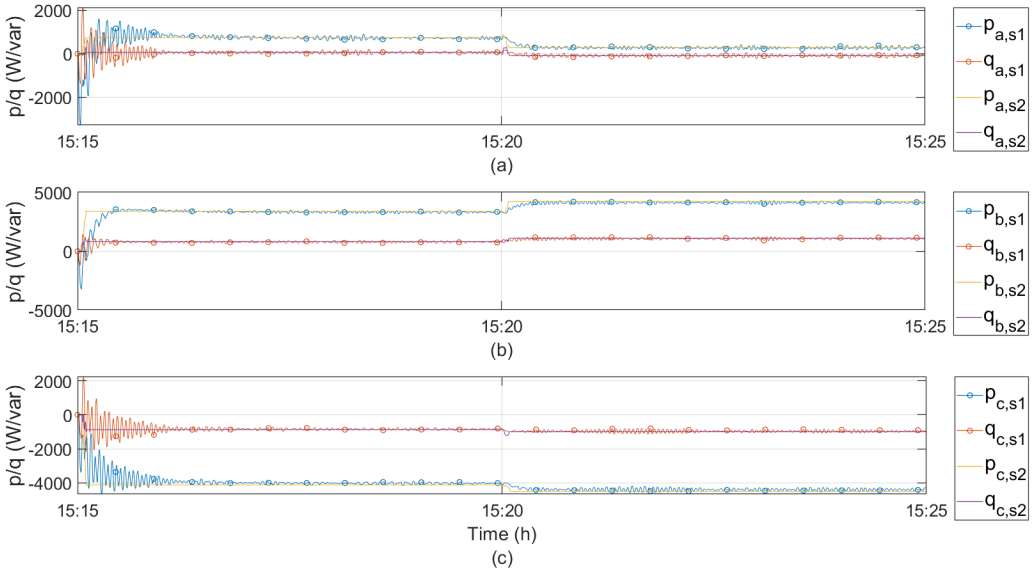

Figure 7.15: Measured active and reactive power of (a) phase-a (b) phase-b (c) phase-c between 15:15–15:25 h ('s1': inverted-based model, 's2': current source-based model).

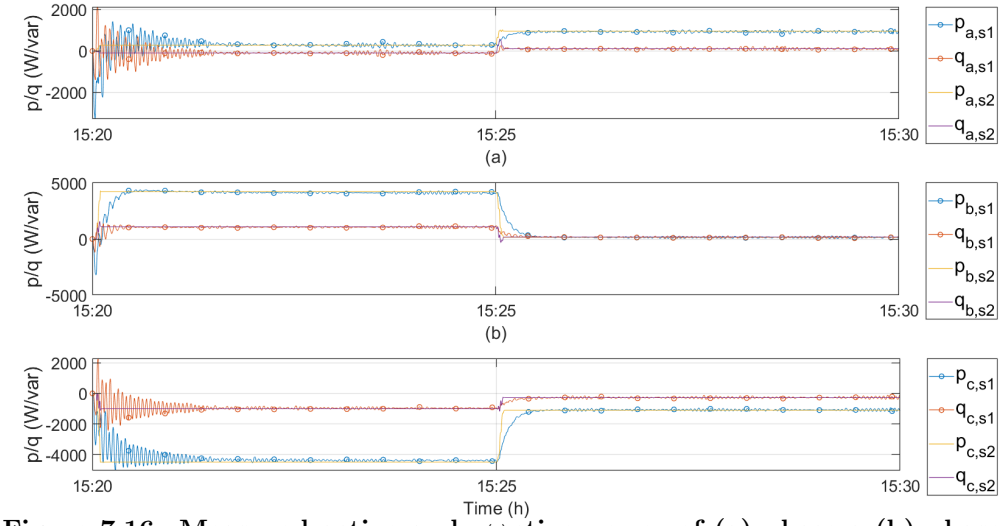

Figure 7.16: Measured active and reactive power of (a) phase-a (b) phase-b (c) phase-c between 15:20–15:30 h ('s1': inverted-based model, 's2': current source-based model).

7.2.3 Validation of the Current Source-based model for the case with 100 loads and 60% PV penetration level

The Current Source-based model was further validated for a case in which 60 PVs are connected in the distribution system. Again, 5 different 10-min simulations were realized. The corresponding figures are presented in Section D.1 of Appendix D, which shows that there is a close match between the results obtained from the two models under this operating condition. As a result, the developed Current-Source Based model was used for realizing the probabilistic simulations, which are introduced in the next section.

7.3 Probabilistic simulations

7.3.1 Simulation framework

Probabilistic simulations were carried out to cater for the uncertainties related to the PVs and EVs in terms of their location and size. Two types of cases were considered depending on the low-carbon technology (LCT) connected to the distribution system: PV cases and EV cases. To capture the seasonality of the impacts that different LCTs may have on the distribution system, the summer load profiles were simulated together with the PV profiles, while the winter load profiles were used for the EV cases. The load, PV and EV profiles were obtained from the public database mentioned in Chapter 5, and

Table 7.1: Cases considered for the statistical analysis.

Category	Simulated profiles	Time period [h]	Penetration level	No. of days per pen. level
PV	summer load summer PV	8:00-16:00	0%, 20%, 60%, 100%	30
EV	winter load winter EV	16:00-4:00	0%, 20%, 60%, 100%	30

they have a 5-min resolution. To make the simulation time manageable, the time scale was compressed such that 5 minutes in real time (the data resolution available from [121]) correspond to 0.5 seconds in the simulation. This time scale is different from that used in Subsections 7.2.2-7.2.3, where it was assumed that 5 min correspond to 2 s to facilitate the comparison between the inverter-based and the current-source based model.

Similar to the deterministic simulations presented in Chapter 5, the observation time for the PV cases was from 08:00 h to 16:00 h, while the EV profiles were studied from 16:00 h to 4:00 h. Different PV and EV penetration levels varying from 0 to 100% were investigated. For each penetration level, 30 days were simulated, and for each day, the size and location of the PVs/EVs were randomized using the MATLAB built-in functions 'randperm' and 'rand', which are based on a uniform pseudorandom number generator [129]. It should be highlighted that only a cursory study was carried due to time limitation; given the number of loads connected in the distribution system, i.e. 100 single-phase loads, a much larger set of simulations would be required to identify the probability distribution more accurately. Table 7.1 summarizes the cases under study. In total, 480 cases are run for the 8 PV and EV penetration levels under study.

The Distribution Fitter App of the Statistics and Machine Learning Toolbox in MATLAB was used to fit probability distributions to the simulation data of k_{v2} at six busbars. More details on the choice of the suitable probability distribution for each bus and penetration level are provided in Appendix D. In the case under study, the Weibull distribution was used for all cases. Once the probability distribution was chosen, the probability distribution object was exported to MATLAB workspace in order to plot the cumulative distribution functions (CDFs) presented in the next sections.

7.3.2 Simulation results for varying PV penetration levels, with and without the BESSs in service

The CDFs of k_{v2} at busbar LV for varying PV penetration levels, without and with the BESSs in service, are provided in this subsection. For brevity, the CDFs of k_{v2} at the other busbars are provided in Section D.3 of Appendix D.

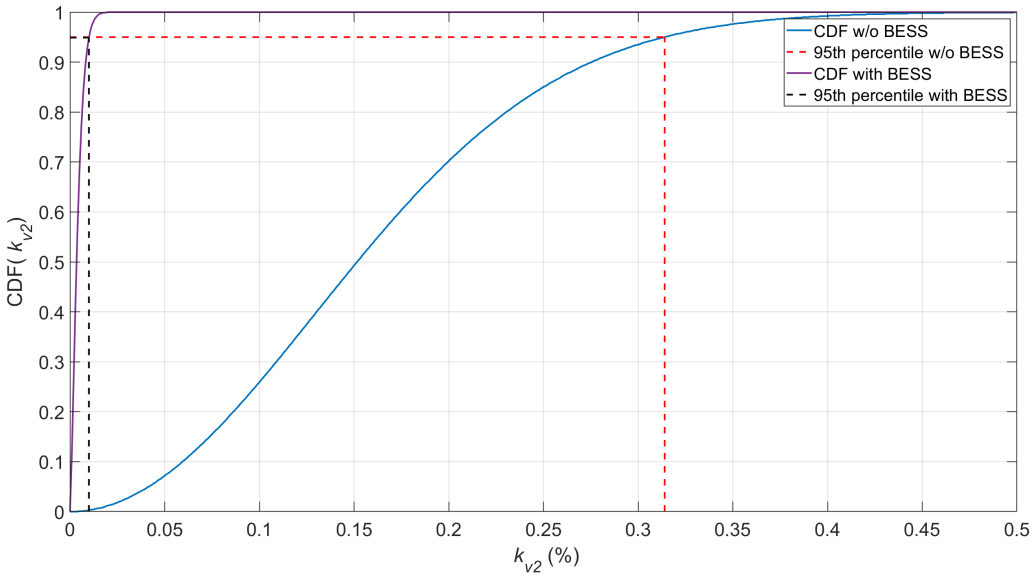

Figure 7.17: Cumulative distribution function of k_{v2} at busbar LV for 0% PV penetration level, with and without the BESSs in service.

Figure 7.17 presents the CDF of k_{v2} at busbar LV for 0% PV penetration level, with and without the BESSs in service. By inspection of this graph and Figure D.22-D.26, which refer to busbars A4-E4, the following observations can be made: the 95^{th} percentile value is well below the limit of 2% for all busbars, with and without the BESSs in service. In addition, the BESS units fully mitigate voltage unbalance at busbar LV, while the unbalance is reduced at the rest of the buses. The highest voltage unbalance levels occur at busbar C4 due to the combination of high line impedance and load ratings at this feeder. However, the control of the BESSs can still improve voltage unbalance, since k_{v2} decreases from 1.35 to 1.2%.

Similar to the 0% PV penetration level, the voltage unbalance factor value stays below 2% when 20 PVs are added to the distribution network, as demonstrated in Figure 7.18 and Figure D.27-D.31. In this case, the 95^{th} percentile value increases, while the control of the BESSs has a mitigating effect on k_{v2} at all buses.

Figure 7.19 and Figure D.32-D.36 show that for 60% PV penetration level, the voltage unbalance factor values are lower compared to those obtained for 20% PV penetration level, showing that the additional PVs have a smoothing effect, thus leading to decreased VU levels. These results are in agreement with the ones obtained from the deterministic analysis in Chapter 5, where a gradual descrease in voltage unbalance levels was observed when more than 60 PVs were connected to the distribution network.

When 100 PVs are connected to the distribution system, the voltage unbalance levels

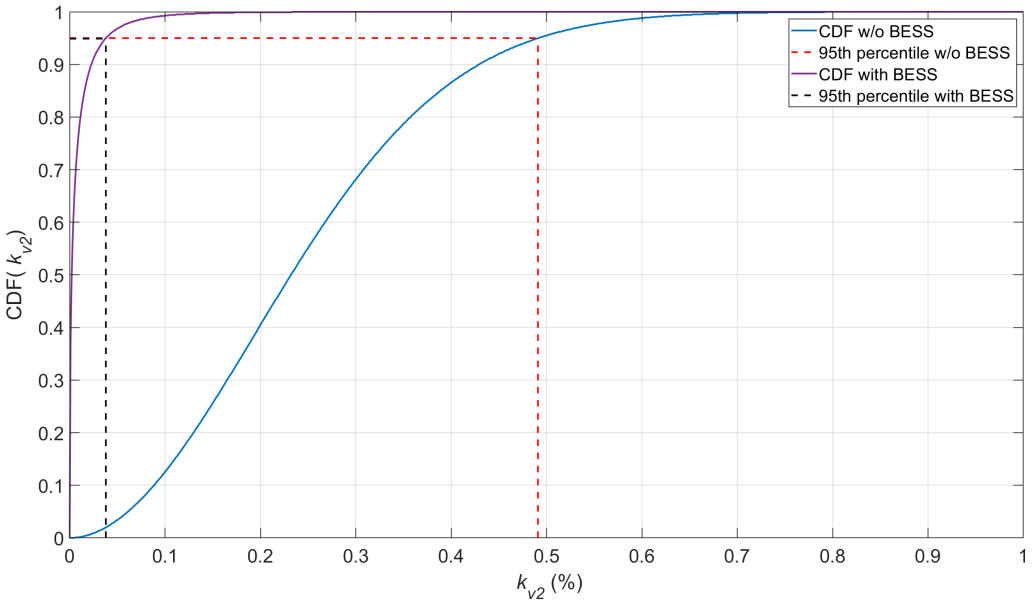

Figure 7.18: Cumulative distribution function of k_{v2} at busbar LV for 20% PV penetration level, with and without the BESSs in service.

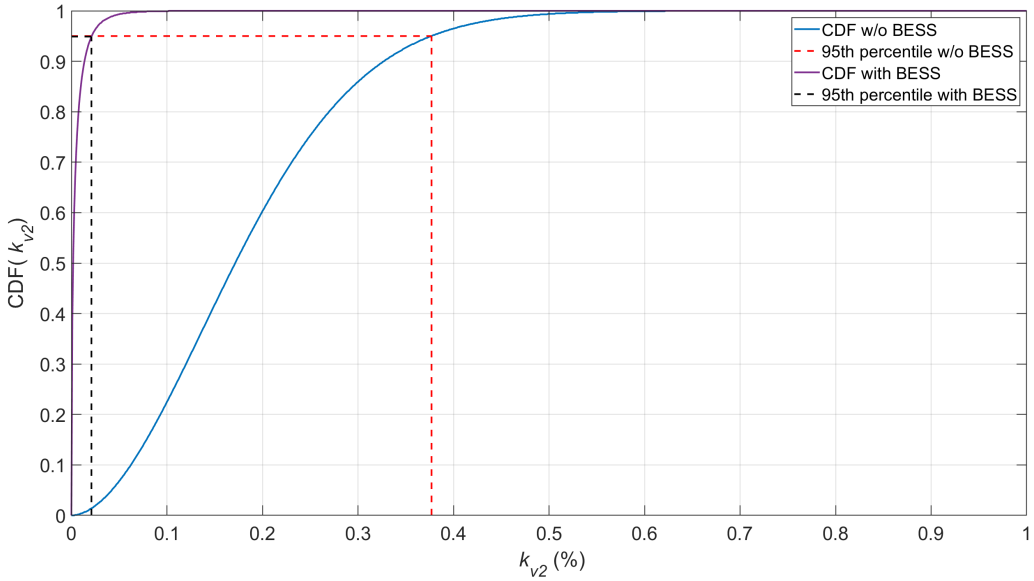

Figure 7.19: Cumulative distribution function of k_{v2} at busbar LV for 60% PV penetration level, with and without the BESSs in service.

are decreased compared to those for 60% penetration level due to the smoothing effect, as it can be deduced from Figure 7.20 and Figure D.37-D.41.

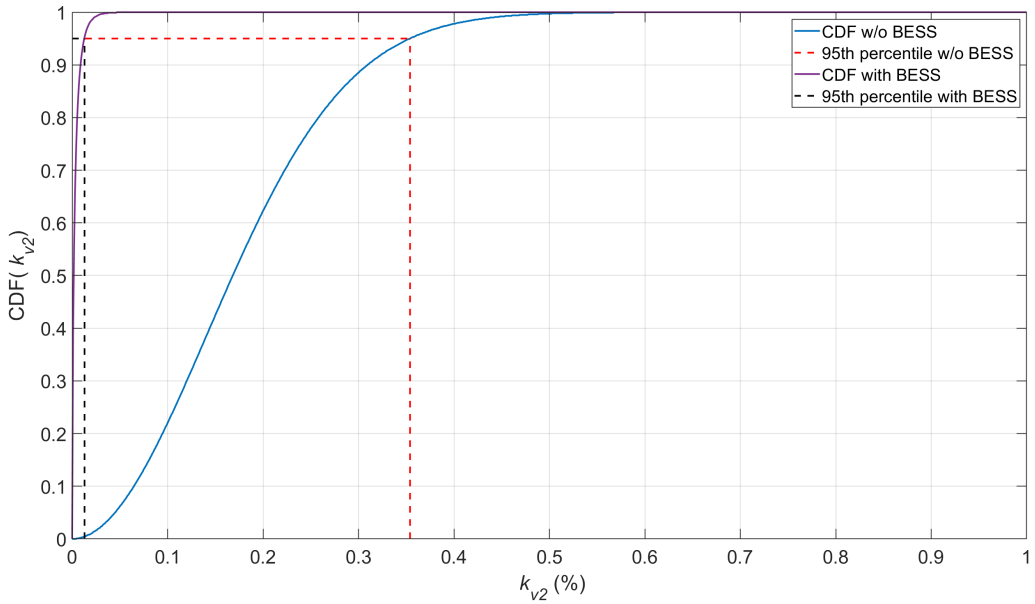

Figure 7.20: Cumulative distribution function of k_{v2} at busbar LV for 100% PV penetration level, with and without the BESSs in service.

7.3.3 Simulation results for varying EV penetration levels, with and without the BESSs in service

The CDFs of k_{v2} at busbar LV for varying EV penetration levels, without and with the BESSs in service, are provided in this subsection. Similar to the PV cases, the CDFs of k_{v2} at the other busbars are provided in Section D.3 of Appendix D for brevity.

Figure 7.21 and Figure D.42-D.46 show that when no EVs are connected to the distribution network, the voltage unbalance levels caused by the single-phase winter loads are very similar to those caused by the summer loads (Figure 7.17 and Figure D.22-D.26). Again, the highest voltage unbalance factor value is measured at bus C4 with $k_{v2} = 1.4\%$, with the k_{v2} values not exceeding the limit of 2% even without any compensation. The BESS units reduce the voltage unbalance at all buses.

The addition of 20 EVs increases the voltage unbalance levels at all buses, as can be seen in Figure 7.22 and Figure D.47-D.51. In particular, Figure D.49 shows that the value of the voltage unbalance factor at bus C4 exceeds the prescribed limits, with $k_{v2} = 2.25\%$. However, the compensating action from the three BESS units reduces this value to 1.95%.

Figure 7.23 and Figure D.52-D.56 show the results obtained for 60% EV penetration level. Comparing these results with those obtained for 20% EV penetration level, it can

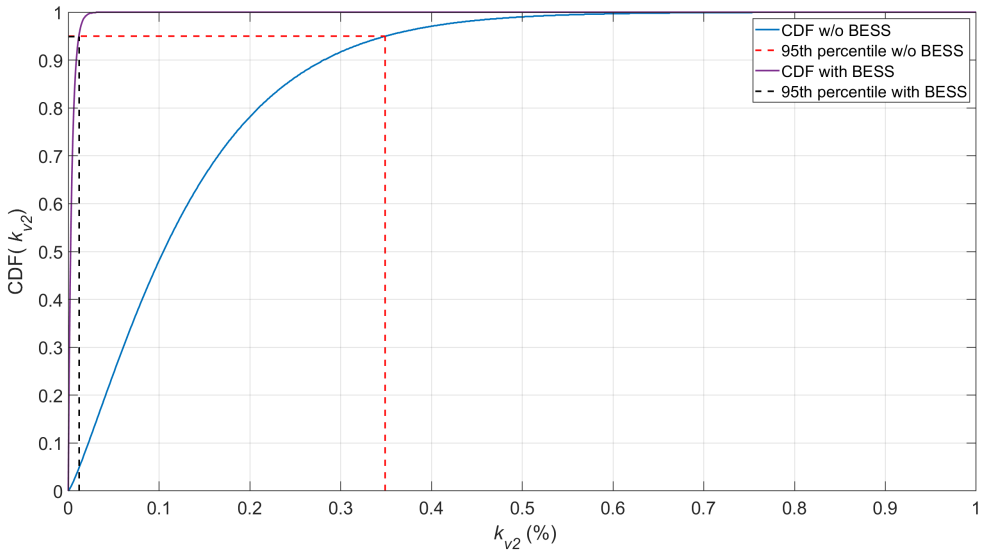

Figure 7.21: Cumulative distribution function of k_{v2} at busbar LV for 0% EV penetration level, with and without the BESSs in service.

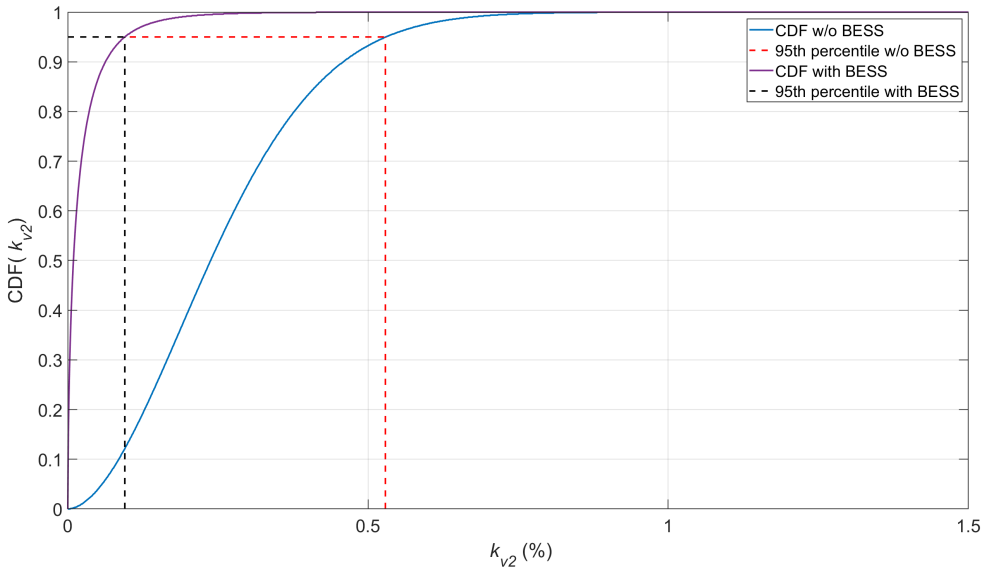

Figure 7.22: Cumulative distribution function of k_{v2} at busbar LV for 20% EV penetration level, with and without the BESSs in service.

be deduced that there is a slight increase in the voltage unbalance levels, which is however lower compared to the increase caused from the addition of 20 EVs to the distribution network. Again, the voltage unbalance factor at bus C4 exceeds the prescribed limits, and even with BESS compensation, $k_{v2} = 2.1\%$.

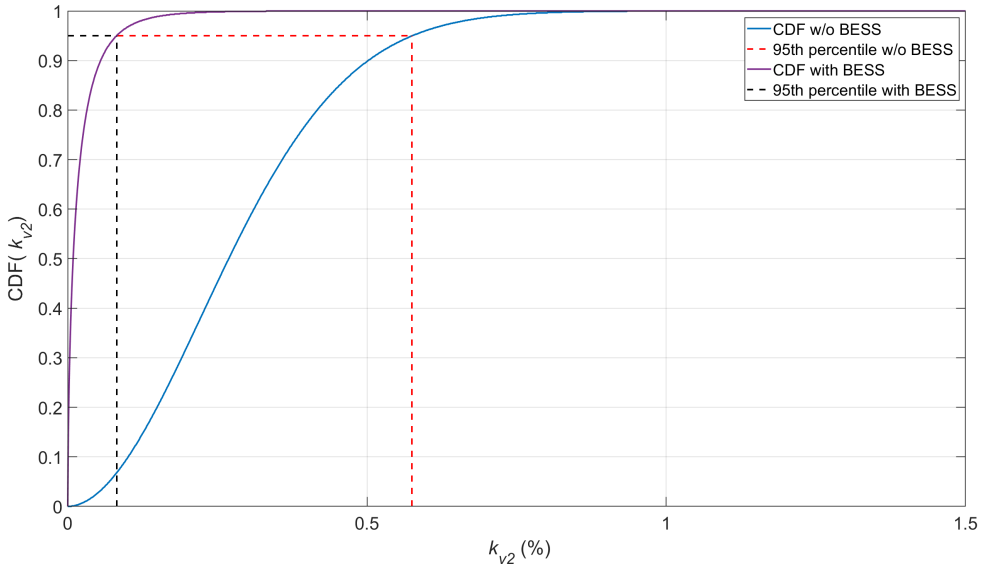

Figure 7.23: Cumulative distribution function of k_{v2} at busbar LV for 60% EV penetration level, with and without the BESSs in service.

Figure 7.24 and Figure D.57-D.61 show that for 100 EVs connected to the distribution network, the obtained values of k_{v2} are very similar to the case when 60 EVs are connected in the network. This shows that the voltage unbalance levels saturate above a certain EV penetration level, which was also observed in the deterministic simulations realized in Chapter 5.

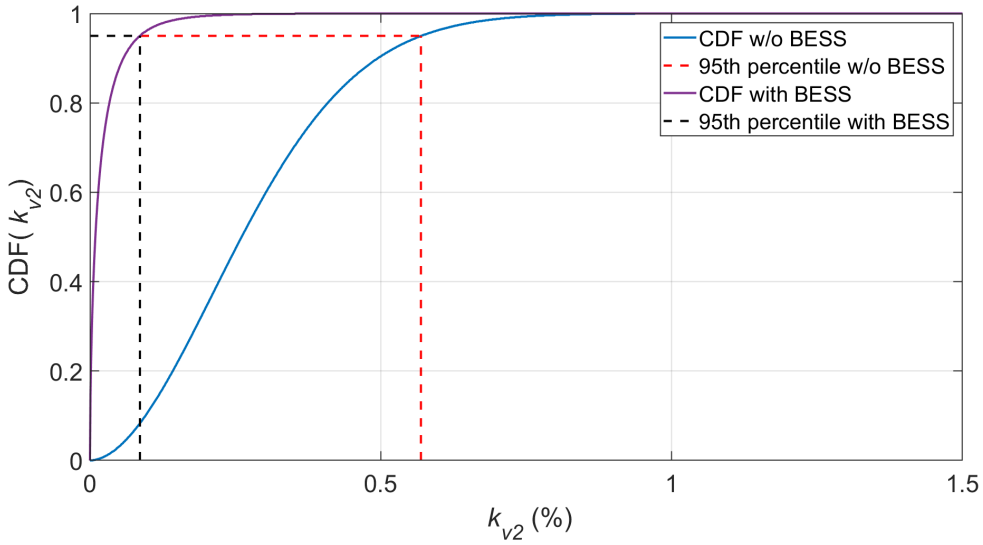

Figure 7.24: Cumulative distribution function of k_{v2} at busbar LV for 100% EV penetration level, with and without the BESSs in service.

7.4 Conclusions

This chapter introduced the Current Source-based model, which was developed with the aim to realize probabilistic simulations and evaluate the effect of varying PV and EV penetration levels on voltage unbalance within the distribution system, without and with the BESS controlled to mitigate the unbalance. Initially, the model validation was carried out, followed by the description of the probabilistic simulation framework and the presentation of the simulation results for different PV and EV penetration levels. It was observed that the simulation results of this cursory probabilistic study reinforced the ones obtained from the deterministic simulations carried out in Chapter 5. In particular, it was shown that increasing PV penetration led to higher voltage unbalance levels, which showed a steady decline above 60 % penetration. The control of the BESS units was shown to mitigate the unbalance, and the 95^{th} percentile was below the limit of 2 % for all busbars, even without compensation.

Regarding the behaviour of the EVs, it was shown that increasing EV penetration levels increase the voltage unbalance; for 60 % penetration level, k_{v2} is above the limit even with the BESS controlled to mitigate voltage unbalance. Similar to the deterministic simulation results, a saturation of k_{v2} was observed for higher penetration levels. The high rating of the EVs and the fact that the EVs act as loads lead to increased voltage unbalance levels, while the PVs have lower ratings and they act as generators that supply the local loads as their penetration increases, thus reducing the voltage unbalance levels.

Chapter 8

Conclusions and Recommendations for Future Work

8.1 Conclusions

This thesis has investigated the application of single-phase BESS units for voltage unbalance mitigation in power distribution systems with varying PV and EV penetration. The main contributions and achievements of this research are summarised below:

1. **The literature review performed on the applications of BESSs on power grids has allowed identifying the emerging applications for the UK electricity network;** the most widely deployed ancillary services in the UK have been identified through a systematic recording of the main BESS projects being deployed both at the transmission and distribution level and being under operational status; the notation used for the ancillary services has been harmonised, a robust classification of the ancillary services currently offered by BESSs has been carried out, and a classification suitable for the UK electricity system has been identified.

2. **A novel voltage unbalance mitigation strategy has been developed.** The control strategy is based on the coordination of three single-phase BESS inverters, and it allows to independently control both their active and reactive power with the aim to mitigate voltage unbalance caused by loads and disruptive single-phase loads and generating units, such as PVs and EVs, connected to the distribution

system. The proposed control scheme can be implemented as ancillary service, and it has been demonstrated that it can cause a significant reduction of voltage unbalance levels under the regulatory limits, therefore enhancing the power quality and facilitating the penetration of LCTs at the distribution system level.

3. **The developed voltage unbalance mitigation strategy has been numerically validated in the simulation environment.** To this purpose, two realistic distribution system models have been built by using real data for the network configuration, parameters, loads and LCTs, similar to those found in distribution networks in Germany and in the UK. The positive impact of the proposed BESS functionaly in the distribution system has been demonstrated under load and generation operating conditions that lead to high voltage unbalance levels. In particular, the results have shown that the BESS units have the capability to provide an overall reduction in the unbalance levels, decrease the neutral current and equalize the power flows at the substation, thereby enabling a more effective utilization of the feeder and transformer capacity. Additionally, various BESS locations along the feeders were tested to carry out a sensitivity analysis, therefore allowing to identify the impact of varying location on the voltage unbalance factor, transformer neutral current and BESS size. It was shown that BESS placement at the substation level generally results in a larger rating, affects a higher number of nodes in terms of voltage unbalance factor reduction and has the largest impact on the transformer neutral current reduction.

4. **The proposed voltage unbalance mitigation strategy has been experimentally validated via HIL experiments.** An individual BESS was controlled to mitigate voltage unbalance introduced by single-phase and three-phase loads, showing that the developed control strategy can effectively mitigate voltage unbalance. Further reduction or full unbalance mitigation will require providing zero- and negative-sequence load current component at the corresponding phases by the other two inverters.

5. **The impact of increasing penetration of realistic PV and EV profiles on voltage unbalance has been assessed for typical UK distribution systems by means of simulations based on both a deterministic and a probabilistic approach, which caters for the uncertainties related to the location and size of the PVs and EVs.** A model based on controlled current sources has been developed with the aim to run the probabilistic simulation scenarios, which calculate the voltage unbalance levels at each bus and for each PV and EV penetration

level, without and with the BESSs controlled to compensate the unbalance. Both simulation approaches have demonstrated that while increasing PV penetration levels generally tend to have a smoothing effect and reduce voltage unbalance, the unbalance may increase to unacceptable levels as the penetration of EVs grows in the distribution system. In the latter case, BESS units of larger size may need to be deployed to reduce voltage unbalance under the regulatory limit. In a practical application, the battery rating will be chosen as a compromise between performance, cost, ancillary services provided and their remuneration.

8.2 Recommendations for future work

The following topics have been identified for further research on the subject of voltage unbalance mitigation by single-phase BESS units:

- While the proposed control system has been shown to be capable of effectively mitigating voltage unbalance, the impact on the battery lifetime will need to be assessed. The control system can be modified such that the reference power calculation in the upper level controller is based on a compromise between the battery lifetime and voltage unbalance mitigation performance. The calculated power values could be the outcome of an optimization problem solved in the upper level controller with the aim to minimize the number of charge and discharge cycles of the batteries.

- The integration of the proposed strategy with other control features can be addressed, both in stand-alone batteries and in other devices, including EVs. While this research has focused on the coordinated control of BESS units connected at the same bus, alternative configurations can be examined, including the coordination of BESS units and EV batteries dispersed in the distribution system for voltage unbalance mitigation. In this case, the power and energy rating of the BESS units will be affected by the type and number of services deployed.

- The statistical analysis of the voltage unbalance levels in the distribution system can be carried out by realizing a much larger set of simulations that would allow identifying the probability distribution of the voltage unbalance factor more accurately and establishing the relationship between the BESS power and the voltage unbalance factor for each PV and EV penetration level. The results of this analysis could provide useful insights for DSOs and BESS developers on evaluating the impact of varying PV and EV penetration levels on their networks and make more informed decisions regarding the sizing and the necessity of deploying BESSs for

voltage unbalance mitigation for each case study.

- The provision of unbalance compensation adds additional rating requirements, and therefore adequate remuneration for the BESS owners should be associated with this service. At the same time, this solution may be attractive for the DNOs as it allows mitigating voltage unbalance without the installation of additional equipment. Economic considerations can be the subject of future work.

- In this research, the proposed configuration for performing voltage unbalance compensation is based on the co-location of the BESS control system and the upper level control system, with the latter receiving voltage and current measurements at the BESS terminals. The examination of alternative configurations can be part of future work, where these two control systems are deployed far from each other, e.g. the upper level controller is deployed in the secondary of the distribution transformer and receives voltage and current measurements at the same point, while the BESS units are connected across the distribution system.

Bibliography

[1] I. Mexis and G. Todeschini, "Battery Energy Storage Systems in the United Kingdom: A Review of Current State-of-the-Art and Future Applications," *Energies*, vol. 13, no. 14, 2020.

[2] I. Mexis, G. Todeschini, and Z. Zhou, "Coordinated control of three single–phase bess inverters using local measurements to mitigate voltage unbalance," *IEEE Transactions on Energy Conversion*, vol. 37, no. 4, pp. 2941–2951, 2022.

[3] M. Molina, "Energy storage and power electronics technologies: A strong combination to empower the transformation to the smart grid," *Proceedings of the IEEE*, vol. PP, pp. 1–29, 09 2017.

[4] M. J. Alexander, P. James, and N. Richardson, "Energy storage against interconnection as a balancing mechanism for a 100% renewable uk electricity grid," *IET Renewable Power Generation*, vol. 9, no. 2, pp. 131–141, 2015.

[5] C. A. Hill, M. C. Such, D. Chen, J. Gonzalez, and W. M. Grady, "Battery energy storage for enabling integration of distributed solar power generation," *IEEE Transactions on Smart Grid*, vol. 3, no. 2, pp. 850–857, June 2012.

[6] J. Hu, Z. Li, J. Zhu, and J. M. Guerrero, "Voltage stabilization: A critical step toward high photovoltaic penetration," *IEEE Industrial Electronics Magazine*, vol. 13, no. 2, pp. 17–30, June 2019.

[7] J. C. Perez Campion, E. O. Oregi, and C. Foote, "Active harmonic filtering in statcoms for enhanced renewable energy integration," in *IEEE ECCE Conference, Baltimore MD*, Oct 2019.

[8] G. Todeschini, "Control and derating of a pv inverter for harmonic compensation in a smart distribution system," in *2017 IEEE Power Energy Society General Meeting*, July 2017, pp. 1–5.

[9] L. Toma, M. Sanduleac, S. A. Baltac, F. Arrigo, A. Mazza, E. Bompard, A. Musa, and A. Monti, "On the virtual inertia provision by bess in low inertia power systems," in *2018 IEEE International Energy Conference (ENERGYCON)*, June 2018,

pp. 1–6.

[10] E. Telaretti and L. Dusonchet, "Stationary battery systems in the main world markets: Part 1: Overview of the state-of-the-art," in *2017 IEEE International Conference on Environment and Electrical Engineering and 2017 IEEE Industrial and Commercial Power Systems Europe (EEEIC / I CPS Europe)*, June 2017, pp. 1–5.

[11] M. Kocer, C. Cengiz, M. Gezer, D. Gunes, M. Cinar, B. Alboyaci, and A. Onen, "Assessment of battery storage technologies for a turkish power network," *Sustainability*, vol. 11, p. 3669, 07 2019.

[12] X. Luo, J. Wang, M. Dooner, and J. Clarke, "Overview of current development in electrical energy storage technologies and the application potential in power system operation," *Applied Energy*, vol. 137, pp. 511 – 536, 2015. [Online]. Available: http://www.sciencedirect.com/science/article/pii/S0306261914010290

[13] O. Palizban and K. Kauhaniemi, "Energy storage systems in modern grids—matrix of technologies and applications," *Journal of Energy Storage*, vol. 6, pp. 248 – 259, 2016. [Online]. Available: http://www.sciencedirect.com/science/article/pii/S2352152X1630010X

[14] F. Alsokhiry, G. P. Adam, and K. L. Lo, "Contribution of distributed generation to ancillary services," in *2012 47th International Universities Power Engineering Conference (UPEC)*, Sep. 2012, pp. 1–5.

[15] J. Eyer and G. Corey, "Energy storage for the electricity grid: Benefits and market potential assessment guide," pp. 1–232, 01 2011.

[16] A. Saez-de-Ibarra, A. Milo, H. Gaztañaga, I. Etxeberria-Otadui, P. Rodríguez, S. Bacha, and V. Debusschere, "Analysis and comparison of battery energy storage technologies for grid applications," in *2013 IEEE Grenoble Conference*, June 2013, pp. 1–6.

[17] Xiu-Hua Guo, Che-Wei Chang, and Le-Ren Chang-Chien, "An automatic voltage compensation technique for three-phase stand-alone inverter to serve unbalanced or nonlinear load," in *2015 IEEE 2nd International Future Energy Electronics Conference (IFEEC)*, Nov 2015, pp. 1–6.

[18] S. M. Alhejaj and F. M. Gonzalez-Longatt, "Impact of inertia emulation control of grid-scale bess on power system frequency response," in *2016 International Conference for Students on Applied Engineering (ICSAE)*, Oct 2016, pp. 254–258.

[19] N. G. plc, "Future energy scenarions," 2019.

[20] R. E. Association, "Energy storage in the uk - an overview," 2015.

[21] DOE, "Global Energy Storage Database," https://www.sandia.gov/ess-ssl/global-energy-storage-database-home/, [Online; accessed 1-July-2019].

[22] Western Power Distribution, "Western power distribution's: Distribution system

operability framework," 2018.

[23] A. S. Sidhu, M. G. Pollitt, and K. L. Anaya, "A social cost benefit analysis of grid-scale electrical energy storage projects: A case study," *Applied Energy*, vol. 212, pp. 881 – 894, 2018. [Online]. Available: http://www.sciencedirect.com/science/article/pii/S0306261917318068

[24] D. M. Padraig Lyons, Phil Taylor, "Overview of network flexibility trial design for clnr," 2014.

[25] N. Powergrid, "Operational guidance and training requirements: Electrical energy storage systems," 2014.

[26] "Toshiba to supply lithium-titanate battery for 2mw energy storage system project in uk led by the university of sheffield," https://www.businesswire.com/news/home/20140624005760/en/Toshiba-Supply-Lithium-Titanate-Battery-2MW-Energy-Storage#.U6l2S_ldWQA, [Online; accessed 24-October-2019].

[27] "Uk's fastest energy storage system connects to grid," https://www.edie.net/news/6/Universities-unite-to-connect-UK-s-fastest-energy-storage-system-to-the-grid/, [Online; accessed 24-October-2019].

[28] D. M. Andrew Urquhart, "Lcnf tier 1 close-down report - orkney energy storage park," 2017.

[29] R. Currie, G. Ault, and J. Mcdonald, "Initial design and specification of a scheme to actively manage the orkney distribution network," 07 2005, pp. 1 – 5.

[30] http://analysis.newenergyupdate.com, [Online; accessed 22-October-2019].

[31] Western Power Distribution, "Solar storage: Final report," 2019.

[32] ——, "Project falcon: Final report," 2015.

[33] ——, "Project falcon - meshed networks," 2015.

[34] D. M. Alistair Steele, "Lcnf tier 1 closedown report," 2014.

[35] L. Breen, "Modelling, optimisation and the lessons learned of a renewable based electrical network – the isle of eigg," 2015.

[36] Z. Chmiel and S. C. Bhattacharyya, "Analysis of off-grid electricity system at isle of eigg (scotland): Lessons for developing countries," *Renewable Energy*, vol. 81, pp. 578 – 588, 2015. [Online]. Available: http://www.sciencedirect.com/science/article/pii/S0960148115002438

[37] W. . Sun, http://www.windandsun.co.uk/case-studies/islands-mini-grids.

[38] A. UK and Ireland, "Aes uk and ireland 2014 sustainability report," 2014.

[39] S. Koohi-Kamali, V. Tyagi, N. Rahim, N. Panwar, and H. Mokhlis, "Emergence of energy storage technologies as the solution for reliable operation of smart power systems: A review," *Renewable and Sustainable*

Energy Reviews, vol. 25, pp. 135 – 165, 2013. [Online]. Available: http://www.sciencedirect.com/science/article/pii/S1364032113002153

[40] M. Beaudin, H. Zareipour, A. Schellenberglabe, and W. Rosehart, "Energy storage for mitigating the variability of renewable electricity sources: An updated review," *Energy for Sustainable Development*, vol. 14, no. 4, pp. 302 – 314, 2010. [Online]. Available: http://www.sciencedirect.com/science/article/pii/S0973082610000566

[41] N. Miller, D. Manz, J. Roedel, P. Marken, and E. Kronbeck, "Utility scale battery energy storage systems," in *IEEE PES General Meeting*, July 2010, pp. 1–7.

[42] X. Tan, Q. Li, and H. Wang, "Advances and trends of energy storage technology in microgrid," *International Journal of Electrical Power and Energy Systems*, vol. 44, no. 1, pp. 179 – 191, 2013. [Online]. Available: http://www.sciencedirect.com/science/article/pii/S0142061512003754

[43] R. Hidalgo-León, D. Siguenza, C. Sanchez, J. León, P. Jácome-Ruiz, J. Wu, and D. Ortiz, "A survey of battery energy storage system (bess), applications and environmental impacts in power systems," in *2017 IEEE Second Ecuador Technical Chapters Meeting (ETCM)*, Oct 2017, pp. 1–6.

[44] "Chapter 2 - technologies of energy storage systems," in *Grid-scale Energy Storage Systems and Applications*, F.-B. Wu, B. Yang, and J.-L. Ye, Eds. Academic Press, 2019, pp. 17 – 56. [Online]. Available: http://www.sciencedirect.com/science/article/pii/B9780128152928000022

[45] http://ease-storage.eu/energy-storage/technologies/.

[46] S. Sabihuddin, A. E. Kiprakis, and M. Mueller, "A numerical and graphical review of energy storage technologies," *Energies*, vol. 8, no. 1, pp. 172–216, 2015. [Online]. Available: https://www.mdpi.com/1996-1073/8/1/172

[47] P. J. Hall and E. J. Bain, "Energy-storage technologies and electricity generation," *Energy Policy*, vol. 36, no. 12, pp. 4352 – 4355, 2008, foresight Sustainable Energy Management and the Built Environment Project. [Online]. Available: http://www.sciencedirect.com/science/article/pii/S0301421508004497

[48] A. Gallo, J. Simões-Moreira, H. Costa, M. Santos, and E. M. dos Santos, "Energy storage in the energy transition context: A technology review," *Renewable and Sustainable Energy Reviews*, vol. 65, pp. 800 – 822, 2016. [Online]. Available: http://www.sciencedirect.com/science/article/pii/S1364032116303562

[49] V. A. Boicea, "Energy storage technologies: The past and the present," *Proceedings of the IEEE*, vol. 102, pp. 1777–1794, 11 2014.

[50] H. L. Ferreira, R. Garde, G. Fulli, W. Kling, and J. P. Lopes, "Characterisation of electrical energy storage technologies," *Energy*, vol. 53, pp. 288 – 298, 2013. [Online]. Available: http://www.sciencedirect.com/science/article/pii/S0360544213001515

[51] T. Mahlia, T. Saktisahdan, A. Jannifar, M. Hasan, and H. Matseelar, "A review of available methods and development on energy storage; technology update," *Renewable and Sustainable Energy Reviews*, vol. 33, pp. 532 – 545, 2014. [Online]. Available: http://www.sciencedirect.com/science/article/pii/S1364032114000902

[52] M. Aneke and M. Wang, "Energy storage technologies and real life applications – a state of the art review," *Applied Energy*, vol. 179, pp. 350 – 377, 2016. [Online]. Available: http://www.sciencedirect.com/science/article/pii/S0306261916308728

[53] D. Rastler, "Electricity energy storage technology options: A white paper primer on applications, costs, and benefits," pp. 1–170, 12 2010.

[54] K. Divya and J. Østergaard, "Battery energy storage technology for power systems—an overview," *Electric Power Systems Research*, vol. 79, no. 4, pp. 511 – 520, 2009. [Online]. Available: http://www.sciencedirect.com/science/article/pii/S0378779608002642

[55] P. Medina, A. W. Bizuayehu, J. P. S. Catalão, E. M. G. Rodrigues, and J. Contreras, "Electrical energy storage systems: Technologies' state-of-the-art, techno-economic benefits and applications analysis," in *2014 47th Hawaii International Conference on System Sciences*, Jan 2014, pp. 2295–2304.

[56] S. O. Amrouche, D. Rekioua, T. Rekioua, and S. Bacha, "Overview of energy storage in renewable energy systems," *International Journal of Hydrogen Energy*, vol. 41, no. 45, pp. 20 914 – 20 927, 2016. [Online]. Available: http://www.sciencedirect.com/science/article/pii/S0360319916309478

[57] W. Shi, J. Jiang, S. Li, S. Lin, P. Lin, and F. Wen, "Applications of battery energy storage system (bess) for energy conversion base in expo 2010," in *The 2nd International Symposium on Power Electronics for Distributed Generation Systems*, June 2010, pp. 918–923.

[58] R. Benato, S. Dambone Sessa, G. Crugnola, M. Todeschini, A. Turconi, N. Zanon, and S. Zin, "Sodium-nickel chloride (na-nicl2) battery safety tests for stationary electrochemical energy storage," in *2016 AEIT International Annual Conference (AEIT)*, Oct 2016, pp. 1–5.

[59] G. Zhao, L. Shi, B. Feng, Y. Sun, and Y. Su, "Development status and comprehensive evaluation method of battery energy storage technology in power system," in *2019 IEEE 3rd Information Technology, Networking, Electronic and Automation Control Conference (ITNEC)*, March 2019, pp. 2080–2083.

[60] E. O. Ogunniyi and H. Pienaar, "Overview of battery energy storage system advancement for renewable (photovoltaic) energy applications," in *2017 International Conference on the Domestic Use of Energy (DUE)*, April 2017, pp. 233–239.

[61] H. C. Hesse, M. Schimpe, D. Kucevic, and A. Jossen, "Lithium-ion battery storage

for the grid—a review of stationary battery storage system design tailored for applications in modern power grids," *Energies*, vol. 10, no. 12, 2017. [Online]. Available: https://www.mdpi.com/1996-1073/10/12/2107

[62] A. Poullikkas, "A comparative overview of large-scale battery systems for electricity storage," *Renewable and Sustainable Energy Reviews*, vol. 27, pp. 778 – 788, 2013. [Online]. Available: http://www.sciencedirect.com/science/article/pii/S1364032113004620

[63] B. Roberts, "Capturing grid power," *IEEE Power and Energy Magazine*, vol. 7, no. 4, pp. 32–41, July 2009.

[64] J. G. Paul Komor, "Electricity storage and renewables for island power," 2012.

[65] B. Dunn, H. Kamath, and J.-M. Tarascon, "Electrical energy storage for the grid: A battery of choices," *Science*, vol. 334, no. 6058, pp. 928–935, 2011. [Online]. Available: https://science.sciencemag.org/content/334/6058/928

[66] H. E. O. Farias and L. N. C. Canha, "Battery energy storage systems (bess) overview of key market technologies," in *2018 IEEE PES Transmission Distribution Conference and Exhibition - Latin America (T D-LA)*, Sep. 2018, pp. 1–5.

[67] B. Battke, T. S. Schmidt, D. Grosspietsch, and V. H. Hoffmann, "A review and probabilistic model of lifecycle costs of stationary batteries in multiple applications," *Renewable and Sustainable Energy Reviews*, vol. 25, pp. 240 – 250, 2013. [Online]. Available: http://www.sciencedirect.com/science/article/pii/S136403211300275X

[68] M. Farhadi and O. Mohammed, "Energy storage technologies for high-power applications," *IEEE Transactions on Industry Applications*, vol. 52, no. 3, pp. 1953–1961, May 2016.

[69] A. Malhotra, B. Battke, M. Beuse, A. Stephan, and T. Schmidt, "Use cases for stationary battery technologies: A review of the literature and existing projects," *Renewable and Sustainable Energy Reviews*, vol. 56, pp. 705 – 721, 2016. [Online]. Available: http://www.sciencedirect.com/science/article/pii/S1364032115013520

[70] M. S. Guney and Y. Tepe, "Classification and assessment of energy storage systems," *Renewable and Sustainable Energy Reviews*, vol. 75, pp. 1187 – 1197, 2017. [Online]. Available: http://www.sciencedirect.com/science/article/pii/S1364032116308218

[71] D. Manz, J. Keller, and N. Miller, "Value propositions for utility-scale energy storage," in *2011 IEEE/PES Power Systems Conference and Exposition*, March 2011, pp. 1–10.

[72] A. Nourai and C. Schafer, "Changing the electricity game," *IEEE Power and Energy Magazine*, vol. 7, no. 4, pp. 42–47, July 2009.

[73] B. Battke and T. S. Schmidt, "Cost-efficient demand-pull policies for

multi-purpose technologies – the case of stationary electricity storage," *Applied Energy*, vol. 155, pp. 334 – 348, 2015. [Online]. Available: http://www.sciencedirect.com/science/article/pii/S0306261915007680

[74] C. I. Ciontea and F. Iov, "A study of load imbalance influence on power quality assessment for distribution networks," *Electricity*, vol. 2, no. 1, pp. 77–90, 2021. [Online]. Available: https://www.mdpi.com/2673-4826/2/1/5

[75] "Definitions of voltage unbalance," *IEEE Power Engineering Review*, vol. 21, no. 5, pp. 49–51, 2001.

[76] "IEEE Recommended Practice for Monitoring Electric Power Quality," *IEEE Std 1159-2009 (Revision of IEEE Std 1159-1995)*, pp. 1–94, 2009.

[77] IEC-International Electrotechnical Commission and others, "IEC 61000-2-2," 2002.

[78] V. Rigoni, L. F. Ochoa, G. Chicco, A. Navarro-Espinosa, and T. Gozel, "Representative residential lv feeders: A case study for the north west of england," *IEEE Transactions on Power Systems*, vol. 31, no. 1, pp. 348–360, 2016.

[79] K. Ma, L. Fang, and W. Kong, "Review of Distribution Network Phase Unbalance: Scale, Causes, Consequences, Solutions, and Future Research Directions," *CSEE Journal of Power and Energy Systems*, vol. 6, no. 3, pp. 479–488, 2020.

[80] P. Lico, M. Marinelli, K. Knezović, and S. Grillo, "Phase balancing by means of electric vehicles single-phase connection shifting in a low voltage danish grid," in *2015 50th International Universities Power Engineering Conference (UPEC)*, 2015, pp. 1–5.

[81] M. T. Bina and A. Kashefi, "Three-phase unbalance of distribution systems: Complementary analysis and experimental case study," *International Journal of Electrical Power & Energy Systems*, vol. 33, no. 4, pp. 817–826, 2011. [Online]. Available: https://www.sciencedirect.com/science/article/pii/S014206151000205X

[82] K. Ma, F. Li, and R. Aggarwal, "Quantification of additional reinforcement cost driven by voltage constraint under three-phase imbalance," *IEEE Transactions on Power Systems*, vol. 31, no. 6, pp. 5126–5134, 2016.

[83] K. Ma, R. Li, and F. Li, "Utility-scale estimation of additional reinforcement cost from three-phase imbalance considering thermal constraints," *IEEE Transactions on Power Systems*, vol. 32, no. 5, pp. 3912–3923, 2017.

[84] Ma, Kang and Li, Ran and Li, Furong, "Quantification of additional asset reinforcement cost from 3-phase imbalance," *IEEE Transactions on Power Systems*, vol. 31, no. 4, pp. 2885–2891, 2016.

[85] L. J. Thomas, "Connection imbalance in low voltage distribution networks," 2015.

[86] F. Shahnia, R. Majumder, A. Ghosh, G. Ledwich, and F. Zare, "Voltage imbalance analysis in residential low voltage distribution networks with rooftop pvs," *Electric*

Power Systems Research, vol. 81, no. 9, pp. 1805–1814, 2011. [Online]. Available: https://www.sciencedirect.com/science/article/pii/S0378779611001040

[87] F. Nejabatkhah, Y. W. Li, and B. Wu, "Control strategies of three-phase distributed generation inverters for grid unbalanced voltage compensation," *IEEE Transactions on Power Electronics*, vol. 31, no. 7, pp. 5228–5241, July 2016.

[88] P. J. Douglass, I. Trintis, and S. Munk-Nielsen, "Voltage unbalance compensation with smart three-phase loads," in *2016 Power Systems Computation Conference (PSCC)*, June 2016, pp. 1–7.

[89] J. M. Guerrero, P. C. Loh, T.-L. Lee, and M. Chandorkar, "Advanced Control Architectures for Intelligent Microgrids—Part II: Power Quality, Energy Storage, and AC/DC Microgrids," *IEEE Transactions on Industrial Electronics*, vol. 60, no. 4, pp. 1263–1270, 2013.

[90] M. Castilla, J. Miret, A. Camacho, J. Matas, and L. García de Vicuña, "Voltage Support Control Strategies for Static Synchronous Compensators Under Unbalanced Voltage Sags," *IEEE Transactions on Industrial Electronics*, vol. 61, no. 2, pp. 808–820, 2014.

[91] F. Nejabatkhah, Y. Li, and B. Wu, "Control Strategies of Three-phase Distributed Generation Inverters for Grid Unbalanced Voltage Compensation," in *2015 IEEE Energy Conversion Congress and Exposition (ECCE)*, 2015, pp. 6467–6474.

[92] F. Nejabatkhah and Y. W. Li, "Flexible Unbalanced Compensation of Three-Phase Distribution System Using Single-Phase Distributed Generation Inverters," *IEEE Transactions on Smart Grid*, vol. 10, no. 2, pp. 1845–1857, March 2019.

[93] F. Nejabatkhah, Y. W. Li, and H. Tian, "Power Quality Control of Smart Hybrid AC/DC Microgrids: An Overview," *IEEE Access*, vol. 7, pp. 52 295–52 318, 2019.

[94] R. Caldon, M. Coppo, and R. Turri, "Distributed voltage control strategy for LV networks with inverter-interfaced generators," *Electric Power Systems Research*, vol. 107, pp. 85 – 92, 2014.

[95] M. Yao, I. A. Hiskens, and J. L. Mathieu, "Mitigating Voltage Unbalance Using Distributed Solar Photovoltaic Inverters," *IEEE Transactions on Power Systems*, vol. 36, no. 3, pp. 2642–2651, 2021.

[96] L. Hadjidemetriou, A. Charalambous, and E. Kyriakides, "Control Scheme for Phase Balancing of Low-Voltage Distribution Grids," in *2019 International Conference on Smart Energy Systems and Technologies (SEST)*, 2019, pp. 1–6.

[97] M. J. E. Alam, K. M. Muttaqi, and D. Sutanto, "Community Energy Storage for Neutral Voltage Rise Mitigation in Four-Wire Multigrounded LV Feeders With Unbalanced Solar PV Allocation," *IEEE Transactions on Smart Grid*, vol. 6, no. 6, pp. 2845–2855, 2015.

[98] J. Fernandez, S. Bacha, D. Riu, H. Turker, and M. Paupert, "Current Unbalance Reduction in Three-phase Systems Using Single Phase PHEV Chargers," in *2013 IEEE International Conference on Industrial Technology (ICIT)*, Feb 2013, pp. 1940–1945.

[99] K. H. Chua, Y. S. Lim, P. Taylor, S. Morris, and J. Wong, "Energy Storage System for Mitigating Voltage Unbalance on Low-Voltage Networks With Photovoltaic Systems," *IEEE Transactions on Power Delivery*, vol. 27, no. 4, pp. 1783–1790, 2012.

[100] W. Pinthurat and B. Hredzak, "Distributed Control Strategy of Single-Phase Battery Systems for Compensation of Unbalanced Active Powers in a Three-Phase Four-Wire Microgrid," *Energies*, vol. 14, no. 24, 2021.

[101] M. J. E. Alam, K. M. Muttaqi, and D. Sutanto, "Alleviation of Neutral-to-Ground Potential Rise Under Unbalanced Allocation of Rooftop PV Using Distributed Energy Storage," *IEEE Transactions on Sustainable Energy*, vol. 6, no. 3, pp. 889–898, 2015.

[102] Y. Zhang, Y. Xu, H. Yang, Z. Y. Dong, and R. Zhang, "Optimal whole-life-cycle planning of battery energy storage for multi-functional services in power systems," *IEEE Transactions on Sustainable Energy*, pp. 1–1, 2019.

[103] MathWorks, "Battery-generic battery model," https://www.mathworks.com/help/sps/powersys/ref/battery.html;jsessionid=ad191ef9842f29c776601fefaf6b, accessed October 12, 2022.

[104] N. Mohan, T. M. Undeland, and W. P. Robbins, "Power electronics: Converters, applications and design," 1989.

[105] MathWorks, "Universal bridge," https://www.mathworks.com/help/sps/powersys/ref/universalbridge.html, accessed Oct 26, 2022.

[106] I. Mexis and G. Todeschini, "Voltage Unbalance Mitigation by Novel Control of BESS Single–phase Inverters," in *2020 IEEE PES Innovative Smart Grid Technologies Europe (ISGT-Europe)*, 2020, pp. 146–150.

[107] P. Santos Valois, C. Vieira Tahan, N. Kagan, and H. Arango, "Voltage unbalance in low voltage distribution networks," in *16th International Conference and Exhibition on Electricity Distribution, 2001. Part 1: Contributions. CIRED. (IEE Conf. Publ No. 482)*, vol. 2, 2001, pp. 5 pp. vol.2–.

[108] P. Tenti, D. Trombetti, E. Tedeschi, and P. Mattavelli, "Compensation of Load Unbalance, Reactive Power and Harmonic Distortion by Cooperative Operation of Distributed Compensators," in *2009 13th European Conference on Power Electronics and Applications*, 2009, pp. 1–10.

[109] M. Ciobotaru, R. Teodorescu, and F. Blaabjerg, "A New Single-phase PLL Struc-

ture Based on Second Order Generalized Integrator," in *2006 37th IEEE Power Electronics Specialists Conference*, June 2006, pp. 1–6.

[110] S. Golestan, M. Monfared, F. D. Freijedo, and J. M. Guerrero, "Dynamics Assessment of Advanced Single-Phase PLL Structures," *IEEE Trans. on Industrial Electronics*, vol. 60, no. 6, pp. 2167–2177, 2013.

[111] A. Nagliero, R. A. Mastromauro, M. Liserre, and A. Dell'Aquila, "Monitoring and Synchronization Techniques for Single-phase PV Systems," in *SPEEDAM 2010*, June 2010, pp. 1404–1409.

[112] Y. Yang, F. Blaabjerg, and Z. Zou, "Benchmarking of Grid Fault Modes in Single-Phase Grid-Connected Photovoltaic Systems," *IEEE Transactions on Industry Applications*, vol. 49, no. 5, pp. 2167–2176, 2013.

[113] R. Teodorescu, F. Blaabjerg, M. Liserre, and P. C. Loh, "Proportional-resonant Controllers and Filters for Grid-connected Voltage-source Converters," *IEE Proceedings-El. P. Ap.*, vol. 153, no. 5, pp. 750–762, 2006.

[114] C. Yanarates and Z. Zhou, "Symmetrical Pole Placement Method-Based Unity Proportional Gain Resonant and Gain Scheduled Proportional (PR-P) Controller With Harmonic Compensator for Single Phase Grid-Connected PV Inverters," *IEEE Access*, vol. 9, pp. 93 165–93 181, 2021.

[115] Y. Yang and F. Blaabjerg, "Low-voltage ride-through capability of a single-stage single-phase photovoltaic system connected to the low-voltage grid," *International Journal of Photoenergy*, vol. 2013, pp. 1–9, 2013.

[116] A. G. Yepes, F. D. Freijedo, J. Doval-Gandoy, O. Lopez, J. Malvar, and P. Fernandez-Comesaña, "On the discrete-time implementation of resonant controllers for active power filters," in *2009 35th Annual Conference of IEEE Industrial Electronics*, 2009, pp. 3686–3691.

[117] D. Sera, T. Kerekes, M. Lungeanu, P. Nakhost, R. Teodorescu, G. Andersen, and M. Liserre, "Low-cost digital implementation of proportional-resonant current controllers for pv inverter applications using delta operator," in *31st Annual Conference of IEEE Industrial Electronics Society, 2005. IECON 2005.*, 2005, pp. 6 pp.–.

[118] I. Mexis, G. Todeschini, F. Möller, and J. Meyer, "Mitigation of Voltage Unbalance in Rural Low Voltage Networks Using Single-phase BESS Inverters," in *CIRED 2021 - The 26th International Conference and Exhibition on Electricity Distribution*, vol. 2021, 2021, pp. 789–794.

[119] S. Mueller, F. Moeller, M. Klatt, J. Meyer, and P. Schegner, "Impact of large-scale integration of e-mobility and photovoltaics on power quality in low voltage networks," in *International ETG Congress 2017*, 2017, pp. 1–6.

[120] F. Möller and J. Meyer, "Probabilistic household load model for unbalance studies

based on measurements," in *2016 Electric Power Quality and Supply Reliability (PQ)*, 2016, pp. 107–112.

[121] A. Navarro-Espinosa and L. F. Ochoa, "Probabilistic impact assessment of low carbon technologies in lv distribution systems," *IEEE Transactions on Power Systems*, vol. 31, no. 3, pp. 2192–2203, 2016.

[122] I. Hernando-Gil, H. Shi, F. Li, S. Djokic, and M. Lehtonen, "Evaluation of Fault Levels and Power Supply Network Impedances in 230/400 V 50 Hz Generic Distribution Systems," *IEEE Transactions on Power Delivery*, vol. 32, no. 2, pp. 768–777, 2017.

[123] A. Navarro-Espinosa and L. F. Ochoa, "Probabilistic Impact Assessment of Low Carbon Technologies in LV Distribution Systems," *IEEE Transactions on Power Systems*, vol. 31, no. 3, pp. 2192–2203, 2016.

[124] Electricity North West, "Low Voltage Network Solutions (LVNS) - Project literature," https://www.enwl.co.uk/lvns, [Online; accessed 14-April-2022].

[125] P. Richardson, M. Moran, J. Taylor, A. Maitra, and A. Keane, "Impact of electric vehicle charging on residential distribution networks: An irish demonstration initiative," in *22nd International Conference and Exhibition on Electricity Distribution (CIRED 2013)*, 2013, pp. 1–4.

[126] IEC-Internat. Electrot. Commis. and others, "IEC 61000-4-30," 2015.

[127] OPAL-RT, "RT-LAB Software home page," https://www.opal-rt.com, [Online; accessed 13-April-2022].

[128] "3-level npc, t-type and flying capacitor inverters using tsb-rd models," https://wiki.opal-rt.com/display/Artemis/3-level+NPC%2C+T-type+and+Flying+Capacitor+Inverters+Using+TSB-RD+Models, [Online; accessed 5-October-2022].

[129] MathWorks, "rand," https://uk.mathworks.com/help/matlab/ref/rand.htmll, accessed April 13, 2023.

[130] ——, "Fourier," https://www.mathworks.com/help/sps/powersys/ref/fourier.html, accessed September 26, 2022.

[131] C. L. Fortescue, "Method of symmetrical co-ordinates applied to the solution of polyphase networks," *Transactions of the American Institute of Electrical Engineers*, vol. XXXVII, no. 2, pp. 1027–1140, 1918.

[132] J. Das, *Understanding Symmetrical Components for Power System Modeling*, ser. IEEE Press Series on Power and Energy Systems. Wiley, 2017. [Online]. Available: https://books.google.co.uk/books?id=huqoDQAAQBAJ

[133] J. Blackburn, *Symmetrical Components for Power Systems Engineering*, ser. Electrical and Computer Engineering. CRC Press, 2017. [Online]. Available:

https://books.google.co.uk/books?id=YkIPEAAAQBAJ

[134] G. Chicco and A. Mazza, "100 years of symmetrical components," *Energies*, vol. 12, no. 3, p. 450, 2019.

[135] L. Dr. Bill McNeese, BPI Consulting, "Distribution fitting," https://www.spcforexcel.com/knowledge/basic-statistics/distribution-fitting, 2016 (accessed May 5, 2022).

[136] MathWorks, "Anderson-darling test," https://uk.mathworks.com/help/stats/adtest.html#btq5df8_sep_shared-Alpha, accessed May 5, 2022.

Appendix A

Validation of the BESS Inverter Rating

This appendix presents the procedure followed to validate the chosen apparent power rating of $S_{inv} = 9$ kVA for the single-phase BESS inverter, i.e. test that the inverter power output is stable when the reference power changes from 0 to 9 kVA. With reference to the distribution network of Figure 4.1, a load distribution equal to $P_{L_{A1}} = P_{L_{A2}} = [2, 1, 1]$ kW and $P_{L_{A3}} = P_{L_{A4}} = [1, 2, 2]$ kW is considered[1]. Only phase-a inverter is connected, and its reference reactive power is kept to zero. The validation is performed by setting the reference active power equal to a ramp function and a stepwise function. Both these two types of functions are adopted, since they represent different load operating conditions that can occur during the power system operation.

- Ramp reference active power: Initially, the ramp reference active power of phase-a inverter is set to equal to 10 kW/s. The curves of the reference and measured active and reactive power at the inverter terminal are plotted in Figure A.1, which shows that the inverter active power starts to oscillate when it reaches the value of 15 kW. The curves of both the instantaneous and rms values of the voltage and current at the inverter terminal are plotted in Figure A.2, where it can be seen that the inverter current oscillations start at 70 A.

- Stepwise reference active power: Next, a stepwise reference active power is given to the inverter. Figure A.3-A.4 demonstrate that the active power and the rms current at the inverter terminal start to oscillate at 12 kW and 40 A, respectively.

[1] The values inside the square brackets correspond to phase-a, phase-b and phase-c active power of the load connected at the corresponding bus.

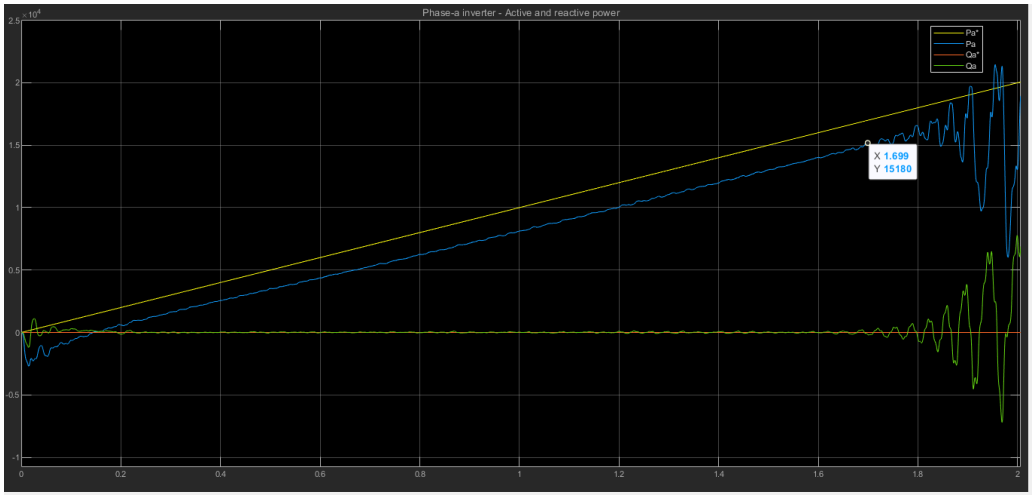

Figure A.1: Ramp reference active power and measured active and reactive power at phase-a inverter terminal.

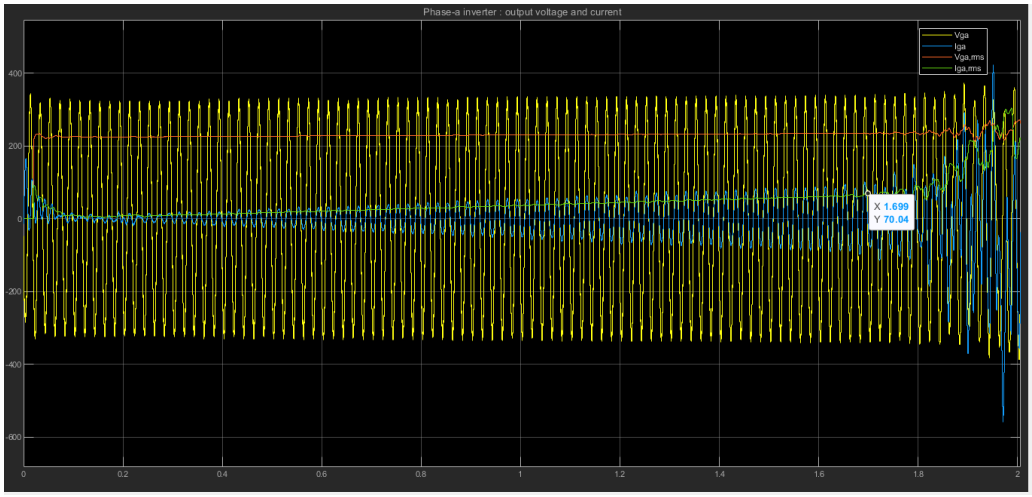

Figure A.2: Measured voltage and current at phase-a inverter terminal for a ramp reference active power.

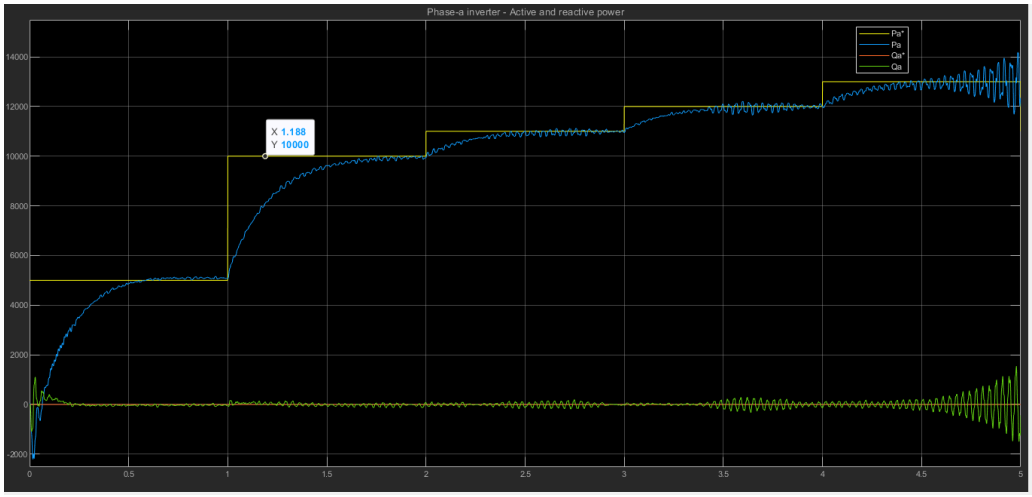

Figure A.3: Stepwise reference active power and measured active and reactive power at phase-a inverter terminal.

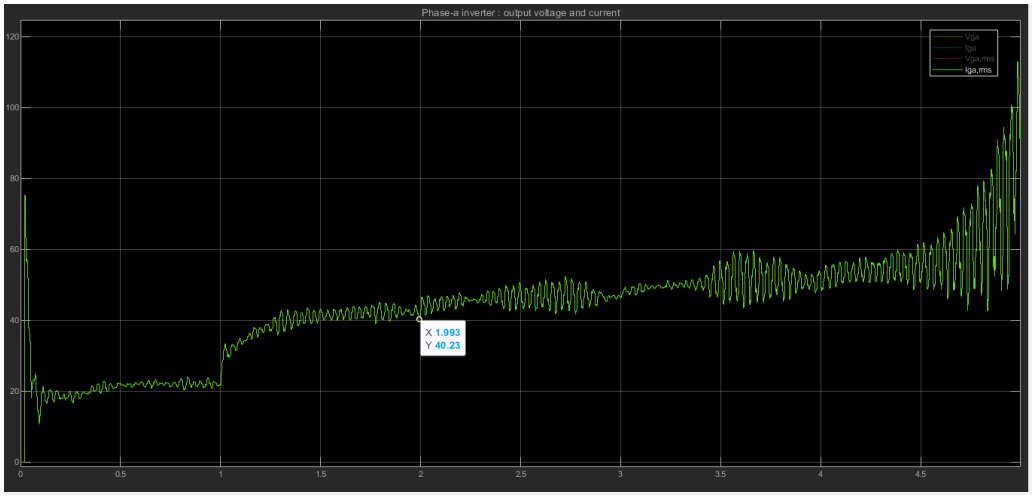

Figure A.4: Measured current at phase-a inverter terminal for a stepwise reference active power.

Based on the above results, it can be concluded that the inverter output power remains stable up to 9 kVA both for ramp and step changes in the load. In addition, Figure A.3 shows that the designed PI controller for the active power can provide a stable response even for large step changes in the load power, such as that occurring at $t = 1s$. More details on the control development are provided in Chapter 3.

Appendix B

Fourier and Fortesque Transformation

B.1 Fourier transformation

The Fourier block is used in Simulink to calculate the Fourier transformation of the input signal. More specifically, this block performs a Fourier analysis of the input signal over a running window of one cycle of the fundamental frequency of the signal. In the case under study, the block is programmed to calculate the magnitude and phase of the fundamental component of the input signal. The input signal f(t) is expressed by a Fourier series of the form [130]:

$$f(t) = \frac{a_0}{2} + \sum_{n=1}^{\infty} [a_n cos(n\omega_1 t) + b_n sin(n\omega_1 t)] \tag{B.1}$$

where n represents the rank of the harmonics and $\omega_1 = 2\pi f_1$, where $f_1 = 50$ Hz is the fundamental frequency. For n = 1, the fundamental component is obtained. The coefficients a_1, b_1 are calculated as:

$$a_1 = \frac{2}{T} \int_{t-T}^{t} f(t) cos(\omega_1 t) dt \tag{B.2}$$

$$b_1 = \frac{2}{T} \int_{t-T}^{t} f(t) sin(\omega_1 t) dt \tag{B.3}$$

The magnitude and phase angle of the fundamental component are calculated as:

$$|H_1| = \sqrt{a_1^2 + b_1^2} \tag{B.4}$$

$$\angle H_1 = atan\left(\frac{a_1}{b_1}\right) \tag{B.5}$$

B.2 Fortescue transformation

The Fortescue transformation is a similarity transformation, which was originally developed for the solution of polyphase networks. More specifically, in [131] it was shown that it is possible to transform any unbalanced set of n phasors into n-1 balanced n-phase systems of different phase sequence and a zero-sequence system, where the n phasors have the same magnitude and they are in phase. This method has been widely used for the study of unbalanced three-phase systems, unsymmetrical short-circuit currents and models of rotating machines, among others [132]. In this section, the Fortescue transformation is presented for the case of three-phase systems. The corresponding equations are provided for current phasors, however they are also applicable to voltage phasors [133].

According to the Fortescue transformation, a set of three unbalanced currents [$\boldsymbol{I_a}$, $\boldsymbol{I_b}$, $\boldsymbol{I_c}$] can be resolved into three balanced systems of phasors [$\boldsymbol{I_{a1}}$, $\boldsymbol{I_{a2}}$, $\boldsymbol{I_{a0}}$], which are calculated based on the following Matrix equation [134]:

$$\begin{bmatrix} \boldsymbol{I_{a0}} \\ \boldsymbol{I_{a1}} \\ \boldsymbol{I_{a2}} \end{bmatrix} = \frac{1}{3} \begin{bmatrix} 1 & 1 & 1 \\ 1 & \boldsymbol{\alpha} & \boldsymbol{\alpha^2} \\ 1 & \boldsymbol{\alpha^2} & \boldsymbol{\alpha} \end{bmatrix} \begin{bmatrix} \boldsymbol{I_a} \\ \boldsymbol{I_b} \\ \boldsymbol{I_c} \end{bmatrix} \tag{B.6}$$

or written in the expanded form:

$$\begin{aligned} \boldsymbol{I_{a0}} &= \frac{1}{3}(\boldsymbol{I_a} + \boldsymbol{I_b} + \boldsymbol{I_c}) \\ \boldsymbol{I_{a1}} &= \frac{1}{3}(\boldsymbol{I_a} + \boldsymbol{\alpha I_b} + \boldsymbol{\alpha^2 I_c}) \\ \boldsymbol{I_{a2}} &= \frac{1}{3}(\boldsymbol{I_a} + \boldsymbol{\alpha^2 I_b} + \boldsymbol{\alpha I_c}) \end{aligned} \tag{B.7}$$

where $\boldsymbol{I_{a1}}$, $\boldsymbol{I_{a2}}$, $\boldsymbol{I_{a0}}$ represent the positive-, negative- and zero-sequence component of phase-a current, respectively, while $\boldsymbol{\alpha} = e^{j\frac{2\pi}{3}}$ is the phasor rotation operator, which rotates a phasor counterclockwise by 120^o. The symmetrical components of phase-b and

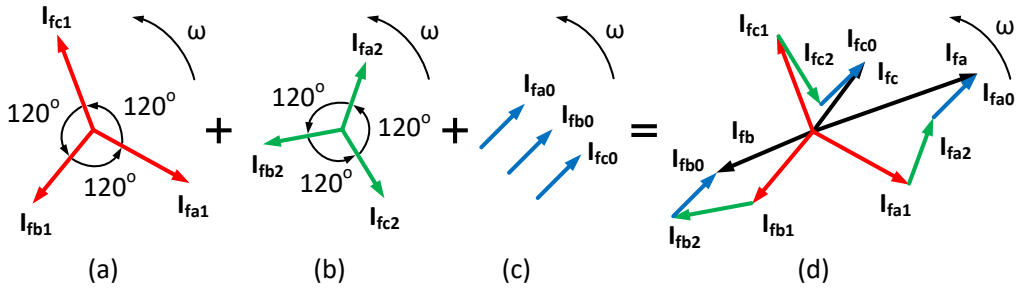

Figure B.1: (d) Decomposition of three unbalanced current phasors into their symmetrical components: (a) positive-sequence (b) negative-sequence (c) zero-sequence

phase-c currents are expressed as a function of phase-a reference phasors:

$$\begin{aligned} \boldsymbol{I_{b0}} &= \boldsymbol{I_{a0}} \\ \boldsymbol{I_{b1}} &= \boldsymbol{\alpha^2 I_{a1}} \\ \boldsymbol{I_{b2}} &= \boldsymbol{\alpha I_{a2}} \end{aligned} \tag{B.8}$$

$$\begin{aligned} \boldsymbol{I_{c0}} &= \boldsymbol{I_{a0}} \\ \boldsymbol{I_{c1}} &= \boldsymbol{\alpha I_{a1}} \\ \boldsymbol{I_{c2}} &= \boldsymbol{\alpha^2 I_{a2}} \end{aligned} \tag{B.9}$$

Conversely, the unbalanced currents can be calculated from their symmetrical components according to the inverse Fortesque transformation:

$$\begin{bmatrix} \boldsymbol{I_a} \\ \boldsymbol{I_b} \\ \boldsymbol{I_c} \end{bmatrix} = \begin{bmatrix} 1 & 1 & 1 \\ 1 & \boldsymbol{\alpha^2} & \boldsymbol{\alpha} \\ 1 & \boldsymbol{\alpha} & \boldsymbol{\alpha^2} \end{bmatrix} \begin{bmatrix} \boldsymbol{I_{a0}} \\ \boldsymbol{I_{a1}} \\ \boldsymbol{I_{a2}} \end{bmatrix} \tag{B.10}$$

or:

$$\begin{aligned} \boldsymbol{I_a} &= \boldsymbol{I_{a0}} + \boldsymbol{I_{a1}} + \boldsymbol{I_{a2}} \\ \boldsymbol{I_b} &= \boldsymbol{I_{a0}} + \boldsymbol{\alpha^2 I_{a1}} + \boldsymbol{\alpha I_{a2}} \\ \boldsymbol{I_c} &= \boldsymbol{I_{a0}} + \boldsymbol{\alpha I_{a1}} + \boldsymbol{\alpha^2 I_{a2}} \end{aligned} \tag{B.11}$$

The phasor diagram of the unbalanced currents and their symmetrical components is presented in Figure B.1, which demonstrates that the three original unbalanced current phasors give rise to nine current phasors. Based on this diagram, it can be observed that

each sequence system consists of phasors of equal magnitude which rotate counterclockwise at the system frequency ω. The zero-sequence phasors are in phase, while the set of the three phasors of both the positive- and the negative-sequence systems are spaced 120^o apart from each other. The positive-sequence components have the same phase sequence as the original unbalanced phasors $(a-b-c)$, while the negative-sequence components have opposite phase sequence to that of the original phasors $(a-c-b)$.

Note that the number of variables between the original unbalanced system and any of the transformed sequence system must remain the same, e.g. the positive-sequence phasors I_{a1}, I_{b1}, I_{c1} cannot exist alone or in pairs but they exist in all three phases [133, 134].

Appendix C

Modelling of Static and Dynamic Loads

C.1 Static load model

The static loads simulated in Chapter 4, 6 and 7 are modelled using the 'Single–Phase Parallel RLC Load' and 'Three–Phase Parallel RLC Load' Simulink blocks. Here, only the 'Three–Phase Parallel RLC Load' block is explained, since the function of these two blocks is very similar. It implements a three-phase load as a parallel combination of RLC elements, which exhibits a constant impedance at the specified frequency. The load active and reactive power values are proportional to the square of the applied voltage.

Figure C.1 presents the three-phase load, which is star connected, and its impedance is calculated based on the following formula:

$$\boldsymbol{Z_i} = R_i + j\omega_n L_i + \frac{1}{j\omega_n C_i} \tag{C.1}$$

where $\omega_n = 2\pi f_n$ is the nominal angular frequency, while R_i, L_i and C_i are the load resistance, inductance and capacitance of phase-i, respectively (for $i = a, b, c$). The following parameters are specified inside the block: nominal phase–to–neutral voltage ($V_{ln} = 230$ V), nominal frequency ($f_n = 50$ Hz), active power (P_i), inductive reactive power (Q_{Li}) and capacitive reactive power (Q_{Ci}) at each phase. The load impedance is determined based on these parameters, as follows:

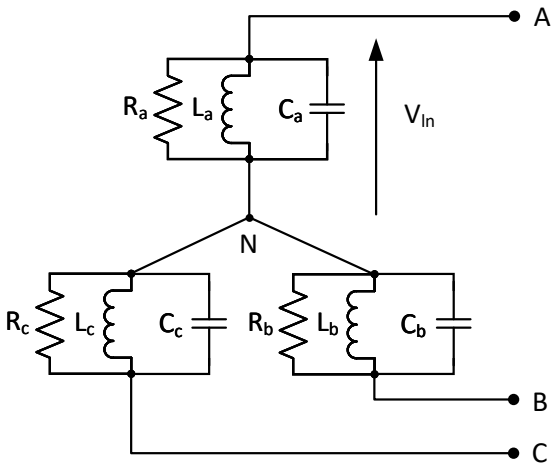

Figure C.1: Configuration of Three-Phase Parallel RLC Load in Simulink.

$$
\begin{aligned}
R_i &= \frac{V_{ln}^2}{\omega_n P_i^2} \\
L_i &= \frac{V_{ln}^2}{\omega_n Q_{Li}^2} \\
C_i &= \frac{V_{ln}^2}{\omega_n Q_{Ci}^2}
\end{aligned}
\tag{C.2}
$$

C.2 Dynamic load model

The 'Single-Phase Dynamic Load' block is used to model the dynamic loads simulated in Chapters 4-5. As Figure C.2 depicts, this model gives a current signal (i) in the output, which is calculated based on the following inputs: the voltage measured at the load terminals, and the active and reactive power profiles, which are provided externally. The current is given as input to a controlled current source, which generates the necessary current to achieve the desired active and reactive power values. It should be highlighted that when modelling loads and EVs, positive active and reactive power values are given in the model, while for PVs the input active power is negative, since the latter are injecting active power into the grid.

Figure C.3 shows the calculations performed inside the 'Model' block with the aim to obtain the positive–sequence component of the voltage in pu ($\boldsymbol{V_1}$) and the complex power

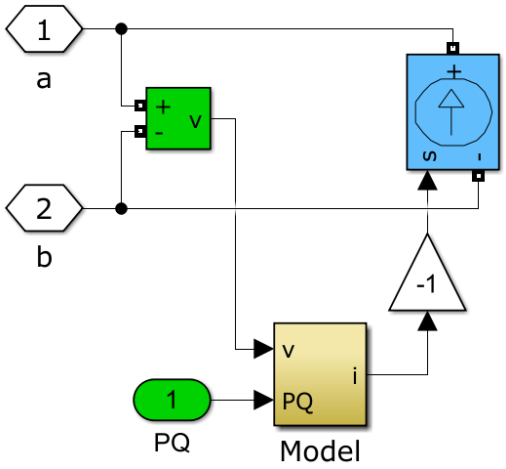

Figure C.2: Model of the single–phase dynamic load.

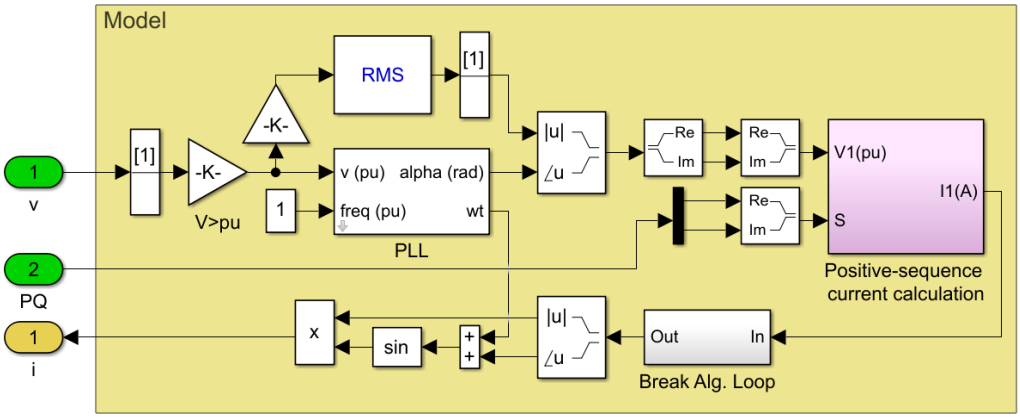

Figure C.3: Calculation of the load current inside the 'model' block.

($\boldsymbol{S}$). These two quantities are given as input to the 'Positive-sequence current calculation' block. The output of this block is the positive–sequence current component in complex form. Then, the magnitude and phase angle of the complex current are calculated, and the voltage phase angle (ωt), which is estimated from the PLL, is added to the current phase angle to obtain the sinusoidal expression of the load current, which is fed to the controlled current source.

Finally, the calculation of the positive-sequence current component of the load inside the 'Positive-sequence current calculation' block is depicted. Figure C.4 shows that the p.u. value of the positive-sequence voltage component is converted to [V], and the load

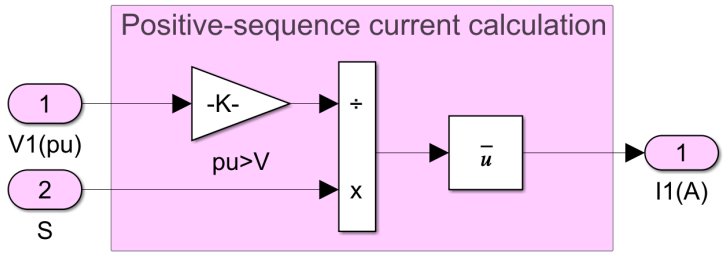

Figure C.4: Calculation of the positive-sequence load current.

current is calculated using the following formula:

$$\boldsymbol{I_1} = \left(\frac{\boldsymbol{S}}{\boldsymbol{V_1}}\right)^* \tag{C.3}$$

Appendix D

Supplementary Results for Chapter 7 and Probability Distribution Fitting

D.1 Validation of the Current Source-based model for the case with 100 loads and 60% PV penetration level

This section presents the validation of the Current Source-based model for the case when 60 PVs are connected in the distribution system. More specifically, Figure D.1-D.5 demonstrate the obtained results of k_{v2}, while the reference current and measured active and reactive power at the output of the compensating units are plotted in Figure D.6-D.10 and Figure D.11-D.15, respectively. Similar comments with the case when only 100 loads are connected in the distribution system (Section 7.2.2) apply for this operating condition, i.e. the results obtained from the simulation of the two models closely match, therefore rendering the developed current-source based model suitable for running the probabilistic simulations presented in Chapter 7.

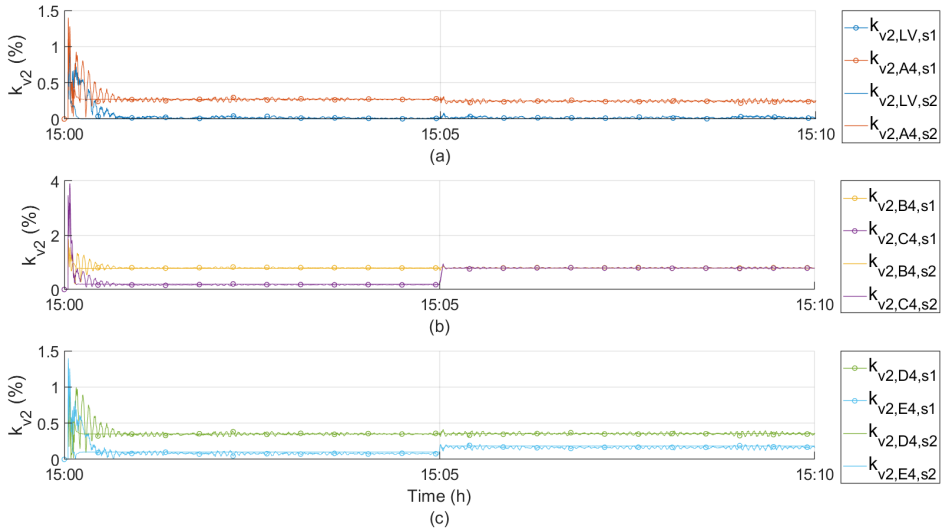

Figure D.1: Voltage unbalance factor values between 15:00–15:10 h.

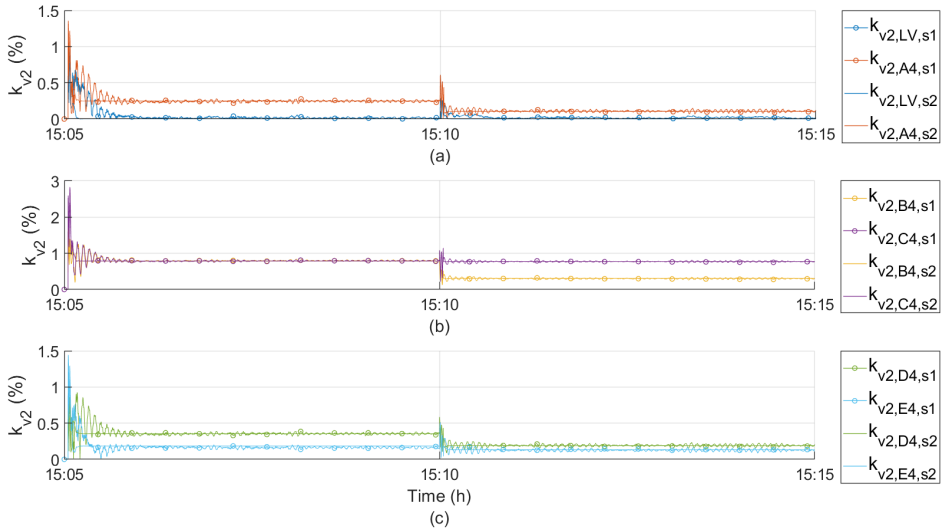

Figure D.2: Voltage unbalance factor values between 15:05–15:15 h.

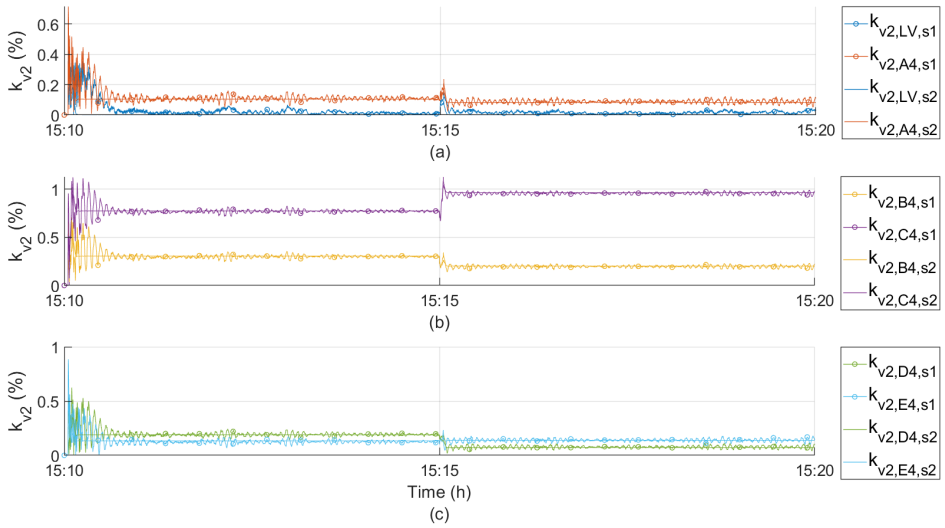

Figure D.3: Voltage unbalance factor values between 15:10–15:20 h.

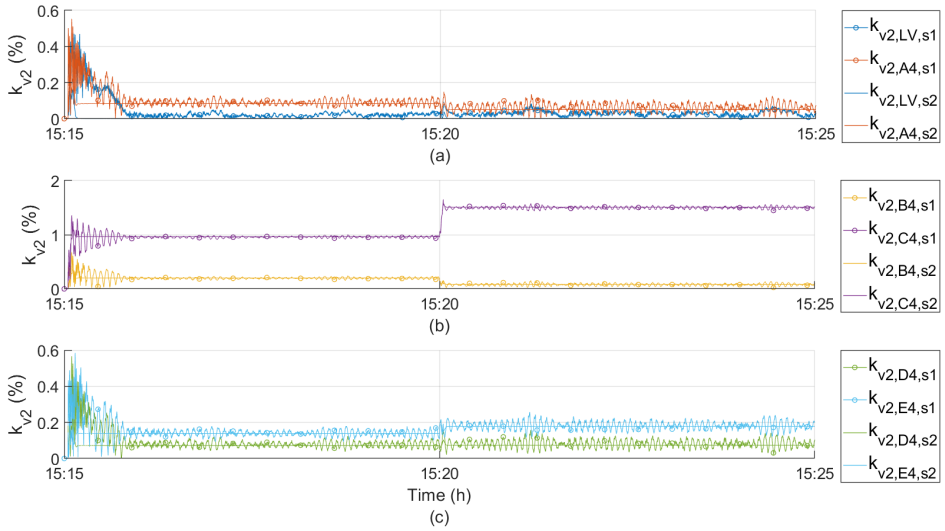

Figure D.4: Voltage unbalance factor values between 15:15–15:25 h.

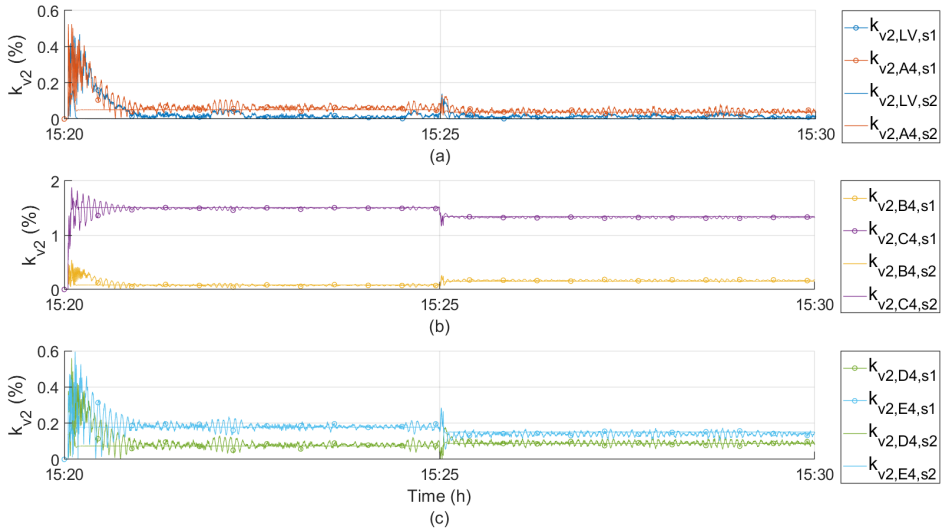

Figure D.5: Voltage unbalance factor values between 15:20–15:30 h.

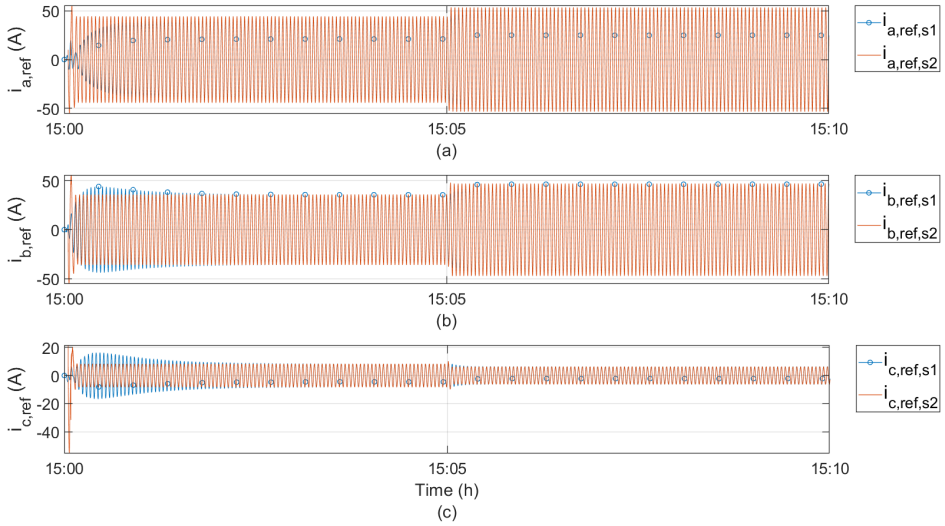

Figure D.6: Reference current of (a) phase-a (b) phase-b (c) phase-c compensating unit between 15:00–15:10 h.

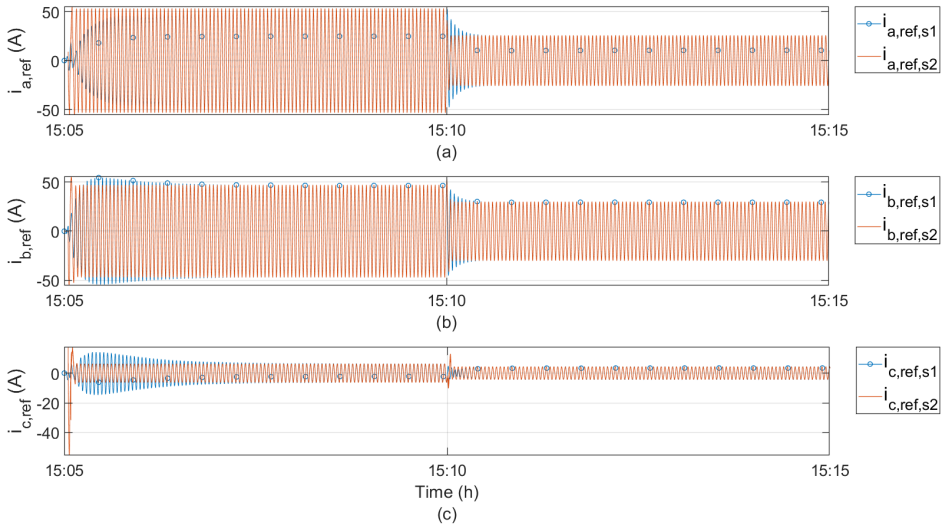

Figure D.7: Reference current of (a) phase-a (b) phase-b (c) phase-c compensating unit between 15:05–15:15 h.

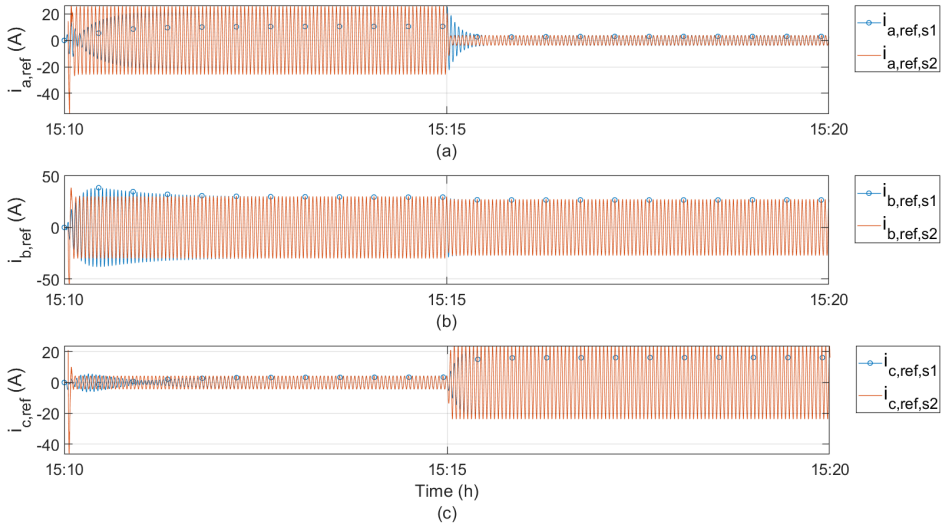

Figure D.8: Reference current of (a) phase-a (b) phase-b (c) phase-c compensating unit between 15:10–15:20 h.

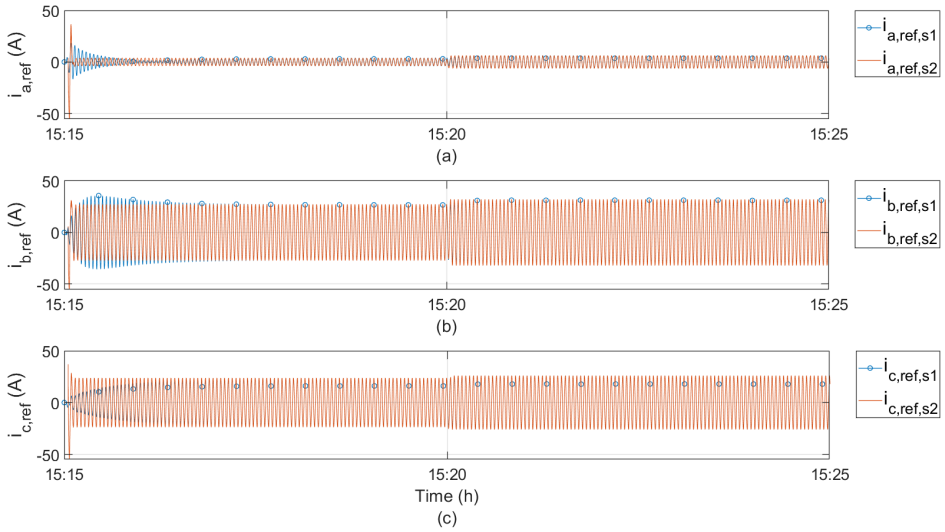

Figure D.9: Reference current of (a) phase-a (b) phase-b (c) phase-c compensating unit between 15:15–15:25 h.

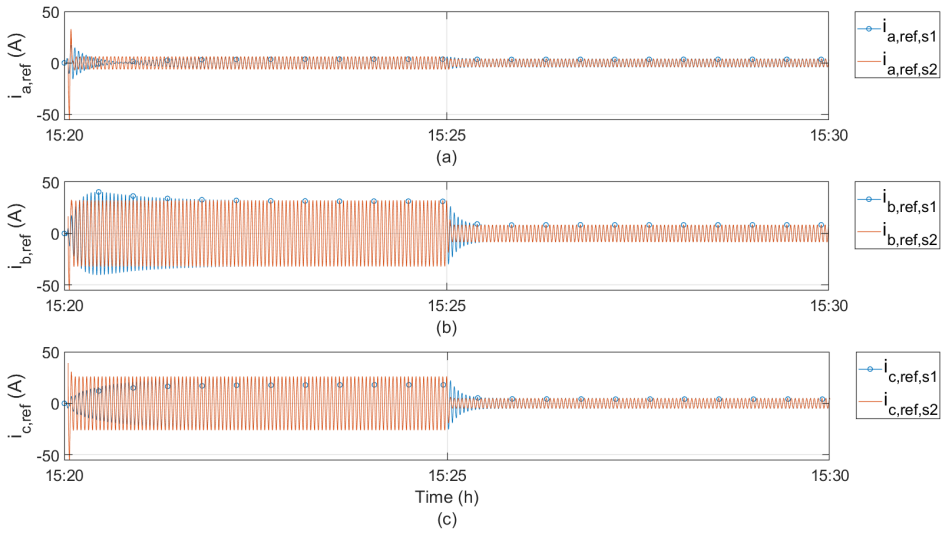

Figure D.10: Reference current of (a) phase-a (b) phase-b (c) phase-c compensating unit between 15:20–15:30 h.

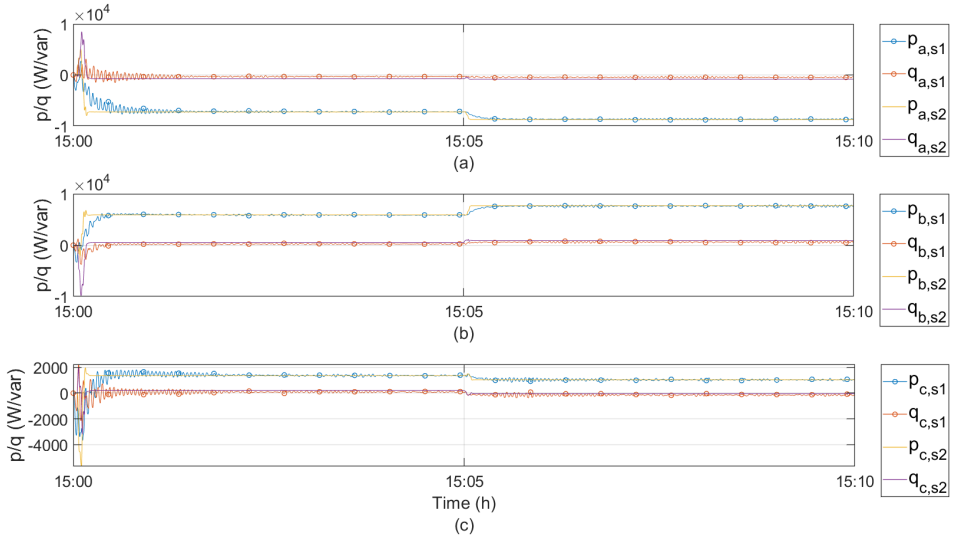

Figure D.11: Measured active and reactive power of (a) phase-a (b) phase-b (c) phase-c compensating unit between 15:00–15:10 h.

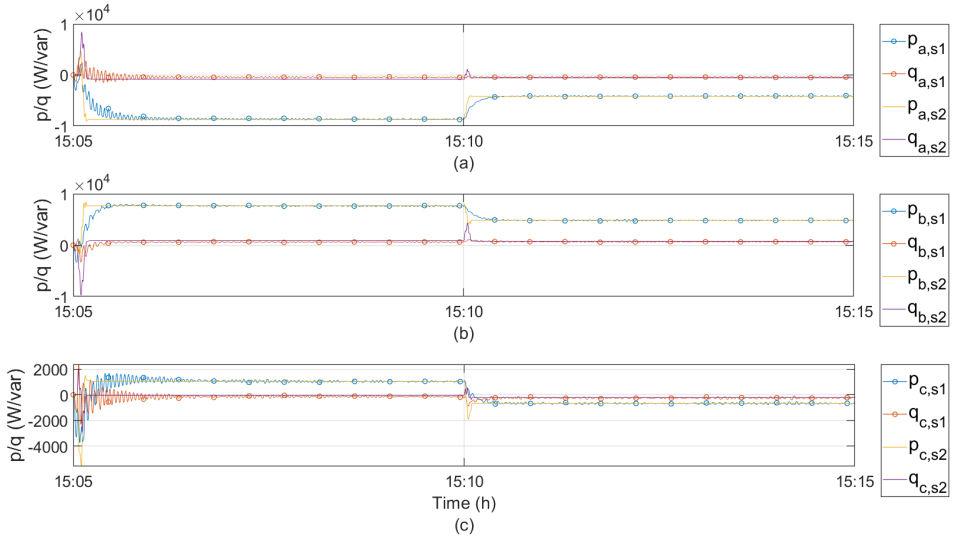

Figure D.12: Measured active and reactive power of (a) phase-a (b) phase-b (c) phase-c between 15:05–15:15 h.

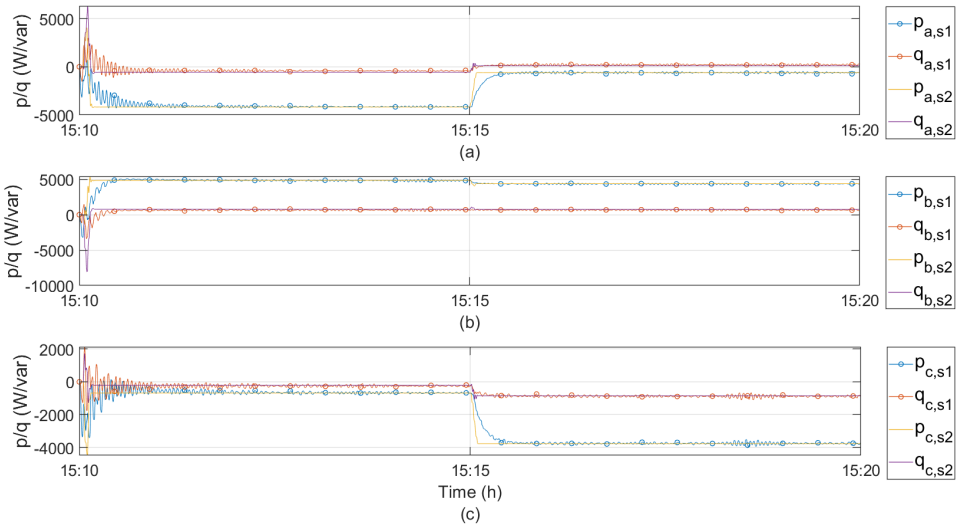

Figure D.13: Measured active and reactive power of (a) phase-a (b) phase-b (c) phase-c between 15:10–15:20 h.

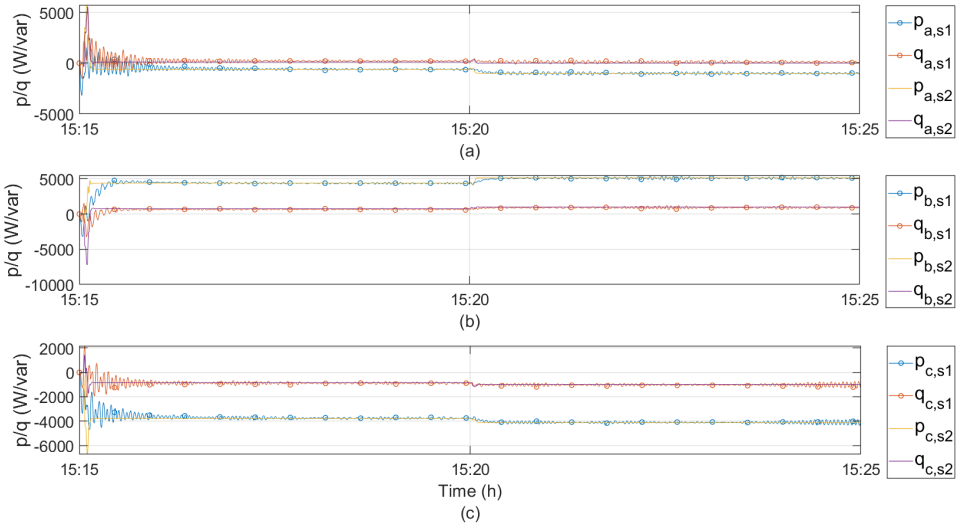

Figure D.14: Measured active and reactive power of (a) phase-a (b) phase-b (c) phase-c between 15:15–15:25 h.

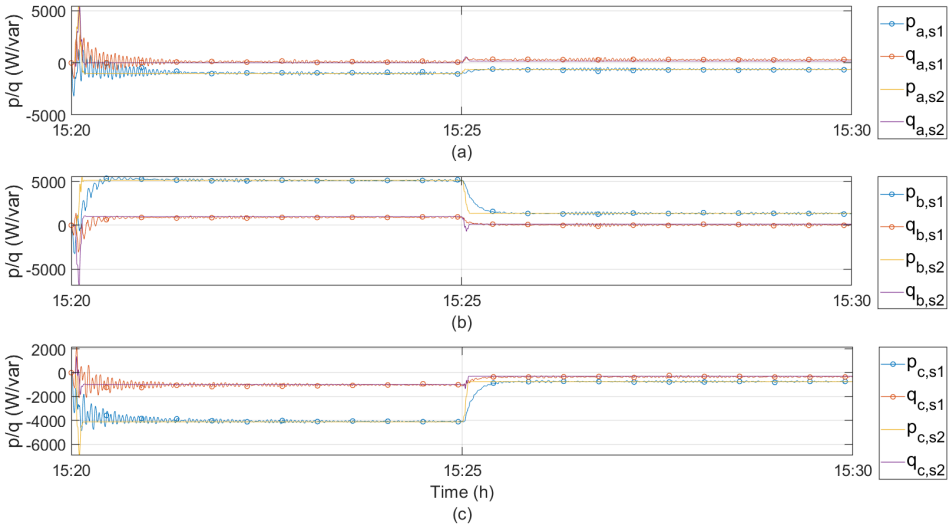

Figure D.15: Measured active and reactive power of (a) phase-a (b) phase-b (c) phase-c between 15:20–15:30 h.

D.2 Distribution fitting

Distribution fitting is the process followed to choose the probability distribution that best fits the sample data. The following techniques can be deployed to identify the best distribution [135]:

- Visual techniques: One visual method is to overlay the chosen probability density function (PDF) for the distribution on the histogram of the data. Another visual method is to construct a probability plot (P-P plot), which plots the empirical cumulative distribution function (CDF) values (based on the data) against the theoretical CDF values (based on the specified distribution).

- Goodness of fit techniques: A very common way for judging goodness of fit is to calculate the Anderson-Darling (AD) statistic and determine the p-value associated with that statistic.

The Distribution Fitter App of MATLAB was used to fit probability distributions to the simulation data of k_{v2} at six busbars. The app allows to interactively fit probability distributions to data imported from the MATLAB workspace, either by choosing between the 22 built-in probability distributions or by creating a custom distribution. To determine if the chosen distribution accurately reflects the data, the following steps were taken for each penetration level and busbar:

- The empirical histogram of the data was plotted in the Distribution Fitter App, and the PDF of the chosen fitted distribution was plotted over the histogram to visually compare the two plots.

- As a complementary step, the AD test was applied to the data to test whether the data comes from the chosen distribution. More details on the AD test are provided in Subsection D.2.1.

D.2.1 Anderson-Darling test

The AD test is commonly used to test whether a data sample comes from a normal distribution. However, it can be used to test for another hypothesized distribution, even if the distribution parameters are not fully specified. Instead, the test estimates any unknown parameters from the data sample. The test statistic belongs to the family of quadratic empirical distribution function statistics, which measure the distance between the hypothesized distribution, $F(x)$ and the empirical cdf, $F_n(x)$ [136].

Table D.1: Hypothesized distribution of the data vector k_{v2}.

Name	**Probability distribution**
norm	Normal
exp	Exponential
ev	Extreme Value
logn	Lognormal
weibull	Weibull

The Anderson-Darling test statistic is:

$$A_n^2 = -n - \sum_{n=1}^{n} \frac{2i-1}{n} [\ln(F(X_i)) + \ln(1 - F(X_{n+1-i}))] \tag{D.1}$$

where $X_1 < ... < X_n$ are the ordered sample data points and n is the number of data points in the sample. The decision to reject or not reject the null hypothesis is based on comparing the p-value for the hypothesis test with the specified significance level, not on comparing the test statistic with the critical value [136]. The syntax of *adtest* is:

$$[h, p] = adtest(k_{v2}, ' Distribution', Name) \tag{D.2}$$

where the parameter *Name* of the hypothesized distribution of the data vector k_{v2} is chosen among the probability distributions of Table D.1. The above command returns a test decision for the null hypothesis that the data in vector k_{v2} is from a population with the chosen distribution. The hypothesis test result, returned as a logical value, is:

- If h = 1, this indicates the rejection of the null hypothesis at the default 5% significance level.
- If h = 0, this indicates a failure to reject the null hypothesis at the default 5% significance level.

The significance level is the probability of the study rejecting the null hypothesis, given that the null hypothesis is true. The test also returns the p-value of the AD test, returned as a scalar value in the range [0,1]. It is defined as the probability of observing a test statistic as extreme as, or more extreme than, the observed value under the null hypothesis. If the hypothesized distribution is specified as a distribution family with unknown parameters (as in the case under study), *adtest* retrieves the critical value from a table and uses inverse interpolation to determine the p-value.

The Anderson-Darling (AD) test was run to determine the type of the probability distribution for k_{v2} of each busbar at each LCT penetration level, with and without the

BESS. Since this test generally does not provide reliable results when the tested sample size is large, the test was run for discrete days, i.e. the vector given as input in (D.2) has a size of 96 k_{v2} values for the PV cases (and 144 k_{v2} values for the EV cases).

D.2.2 Plots of the PDF vs the empirical histogram of the data

The PDF and the empirical histogram of k_{v2} were coplotted for each penetration level and bus. Here, only the results for the case without BESS and 0 PVs are provided for brevity. Based on the histograms of the data shown in Figure D.16-D.21, which were drawn using the Distribution Fitter App, a Weibull distribution was assumed for the k_{v2} data. The Weibull distribution was fitted to the data.

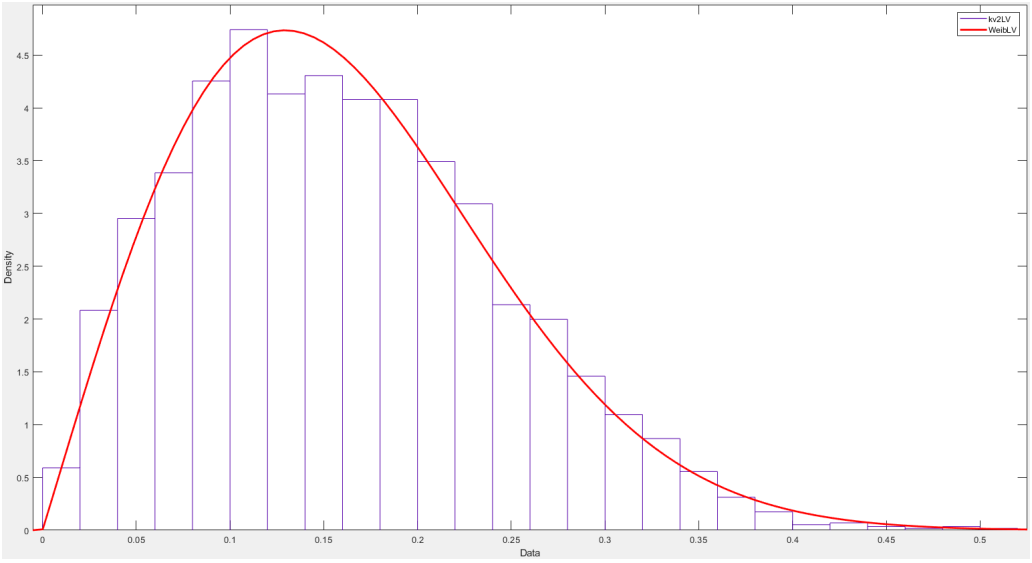

Figure D.16: Probability density function vs empirical histogram of k_{v2} at bus LV.

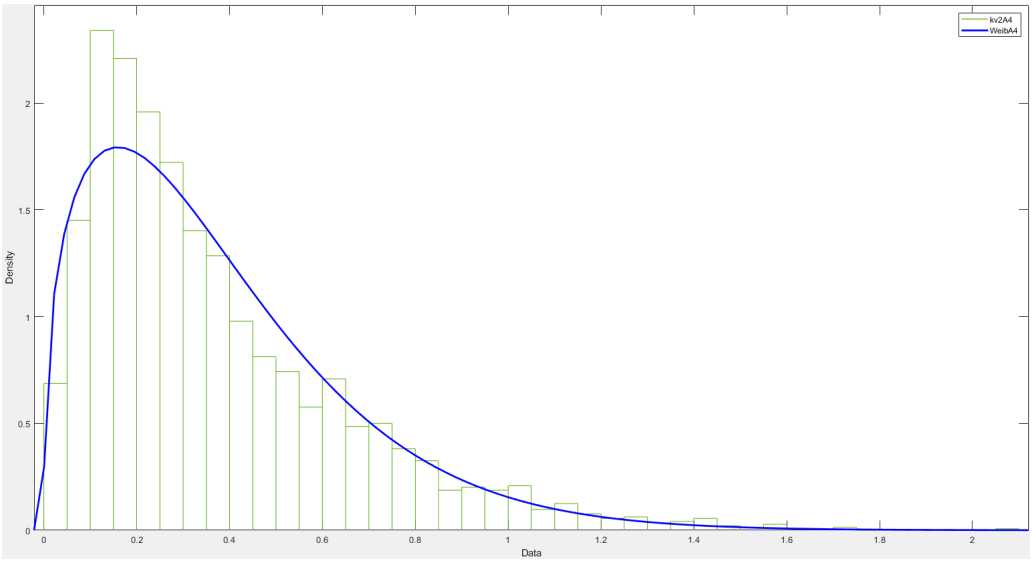

Figure D.17: Probability density function vs empirical histogram of k_{v2} at bus A4.

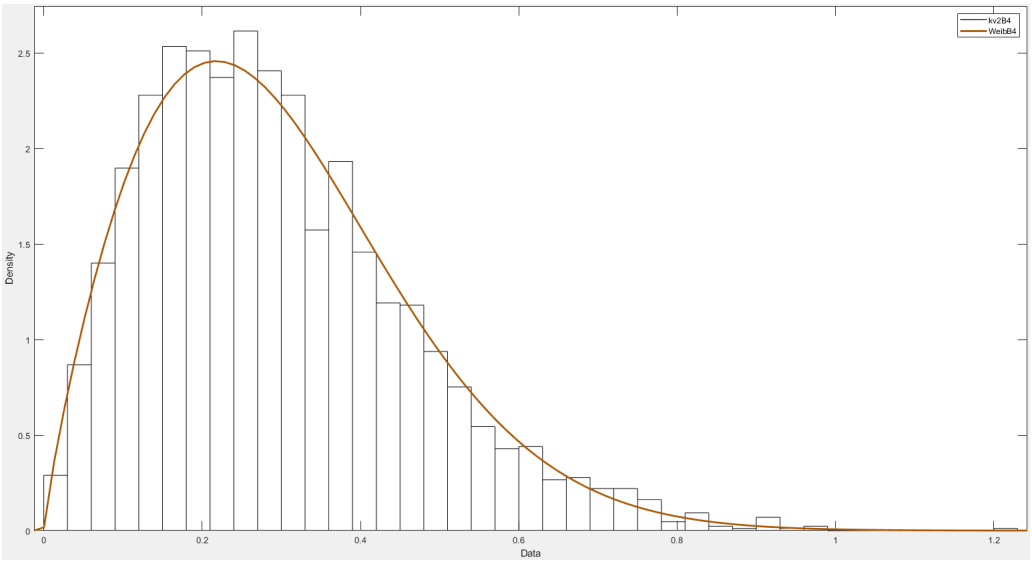

Figure D.18: Probability density function vs empirical histogram of k_{v2} at bus B4.

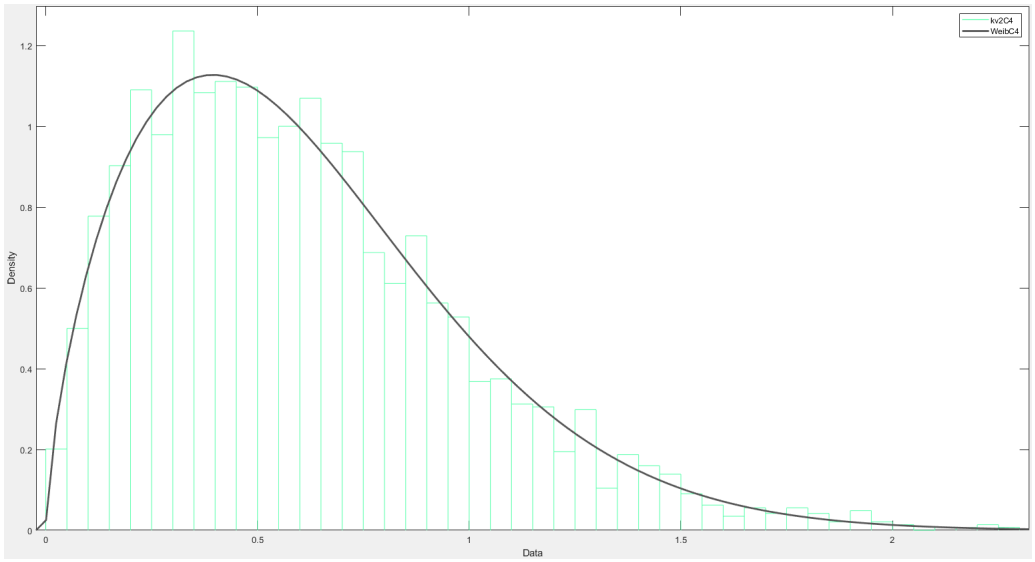

Figure D.19: Probability density function vs empirical histogram of k_{v2} at bus C4.

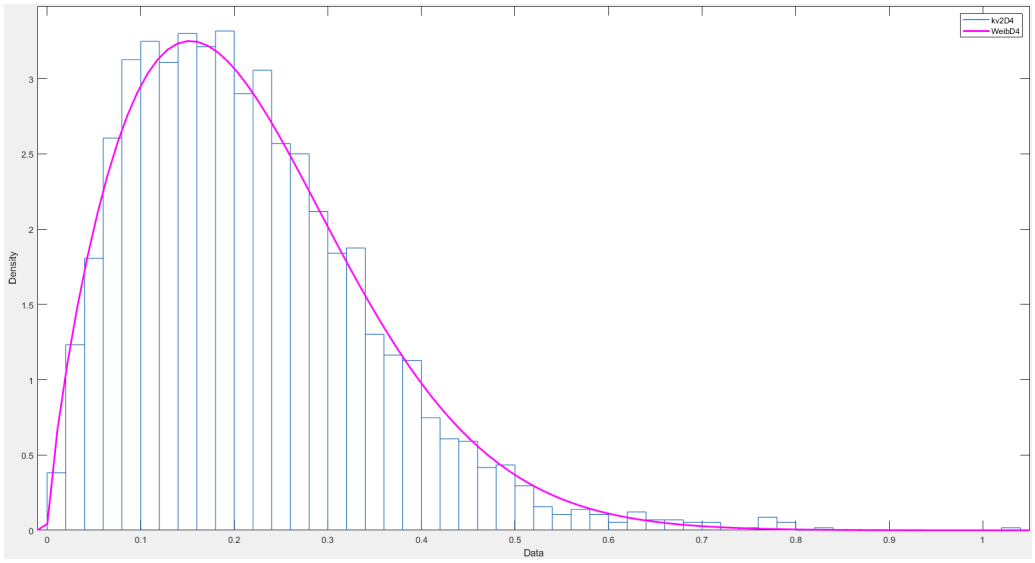

Figure D.20: Probability density function vs empirical histogram of k_{v2} at bus D4.

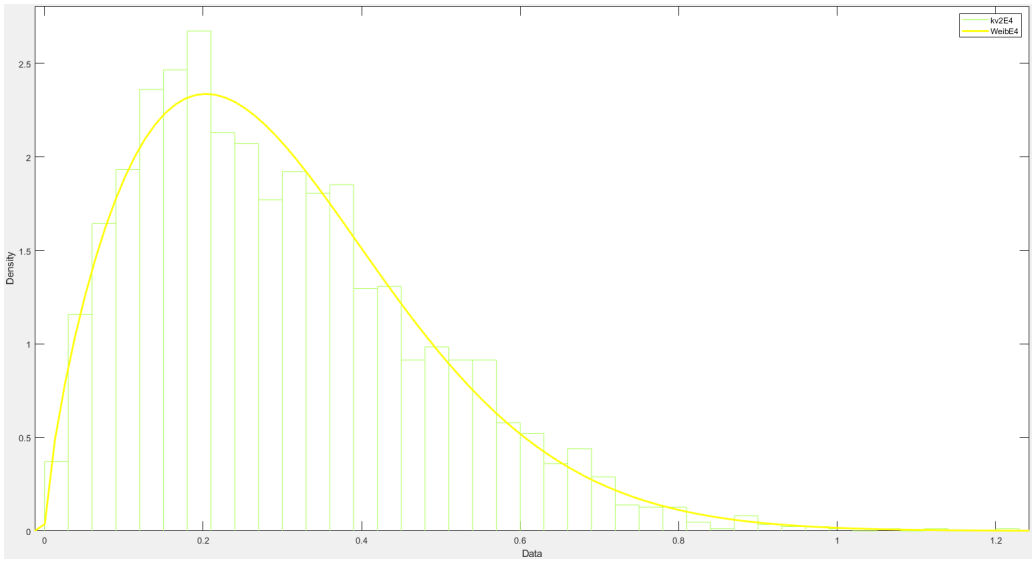

Figure D.21: Probability density function vs empirical histogram of k_{v2} at bus E4.

Table D.2: AD test for each bus for 0 PVs and no BESS.

	LV	**A4**	**B4**	**C4**	**D4**	**E4**
h	0	0	0	0	0	0
p-value	0.556	0.388	0.671	0.198	0.591	0.572

The AD test was used complementarily in order to test whether the data sample comes from a Weibull distribution. Table D.2 shows the obtained results when the 96 k_{v2} values of day 5 are tested. Other days were tested and it was found that the AD test accepts the hypothesis for these days as well, therefore the Weibull distribution was adopted.

For the case with BESS and 0 PVs, the AD test does not give consistent results since it does not accept the Weibull distribution hypothesis for all days and buses. However, since only a cursory statistical analysis was performed in this work, the adoption of the Weibull distribution for all cases was judged as a sufficient approximation to obtain indicative results of the voltage unbalance levels for the various PV and EV penetration levels under study.

D.3 Supplementary simulation results for varying PV penetration levels, with and without the BESSs in service

In this section, the CDFs of k_{v2} at busbars A4-E4 for the examined PV penetration levels of Table 7.1 are provided. The corresponding plots are given in Figure D.22-D.41.

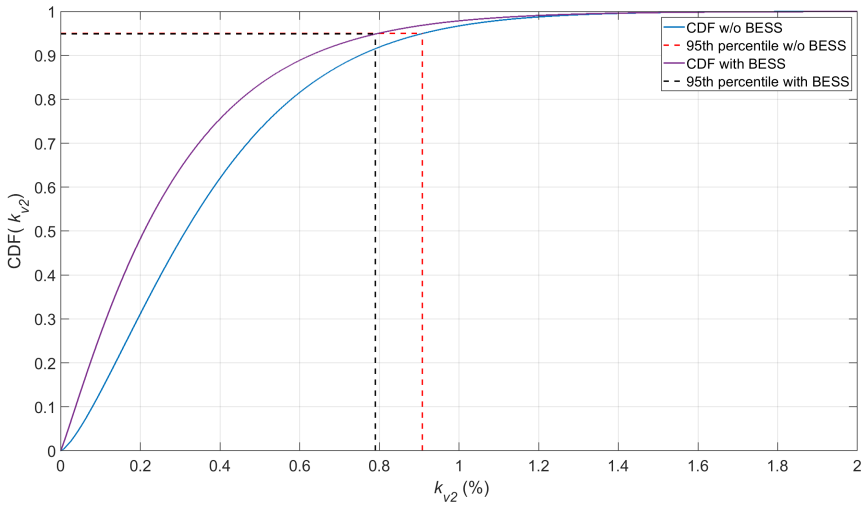

Figure D.22: Cumulative distribution function of k_{v2} at bus A4 for 0% PV penetration level, with and without the BESSs in service.

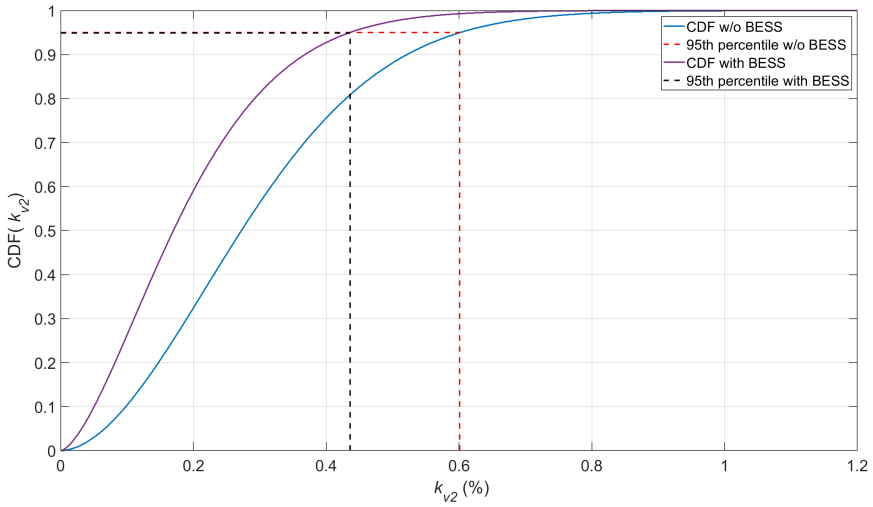

Figure D.23: Cumulative distribution function of k_{v2} at bus B4 for 0% PV penetration level, with and without the BESSs in service.

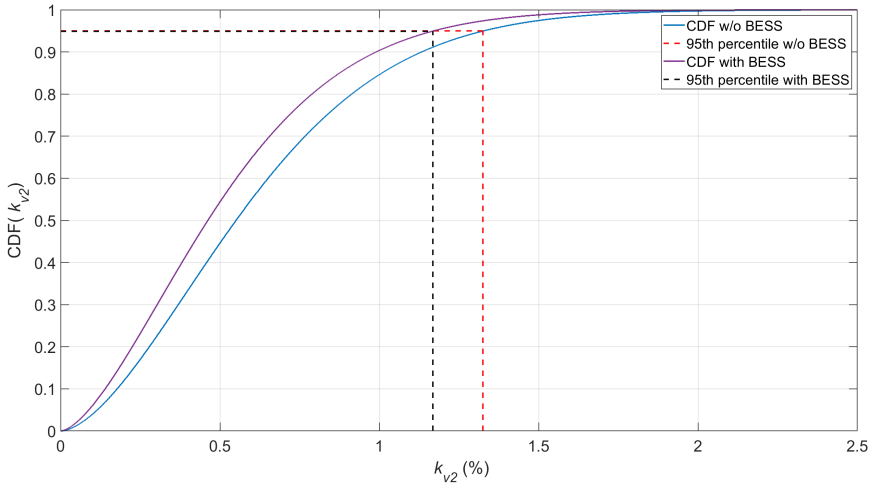

Figure D.24: Cumulative distribution function of k_{v2} at bus C4 for 0% PV penetration level, with and without the BESSs in service.

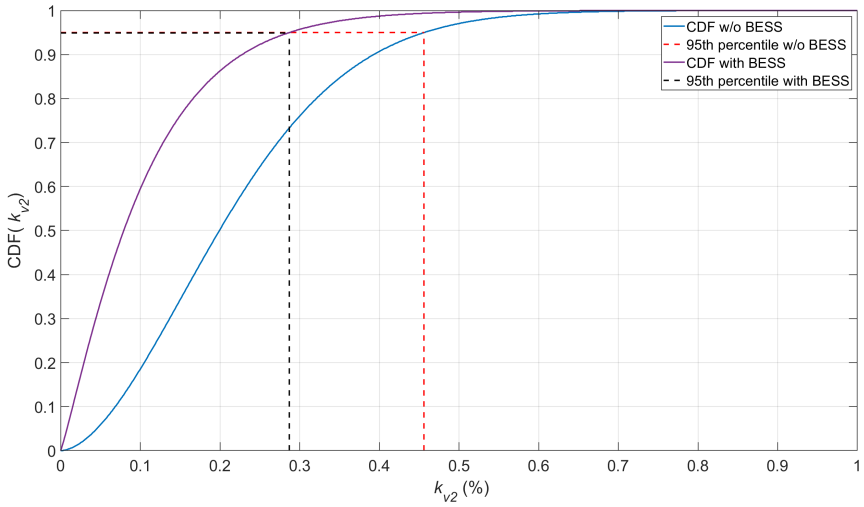

Figure D.25: Cumulative distribution function of k_{v2} at bus D4 for 0% PV penetration level, with and without the BESSs in service.

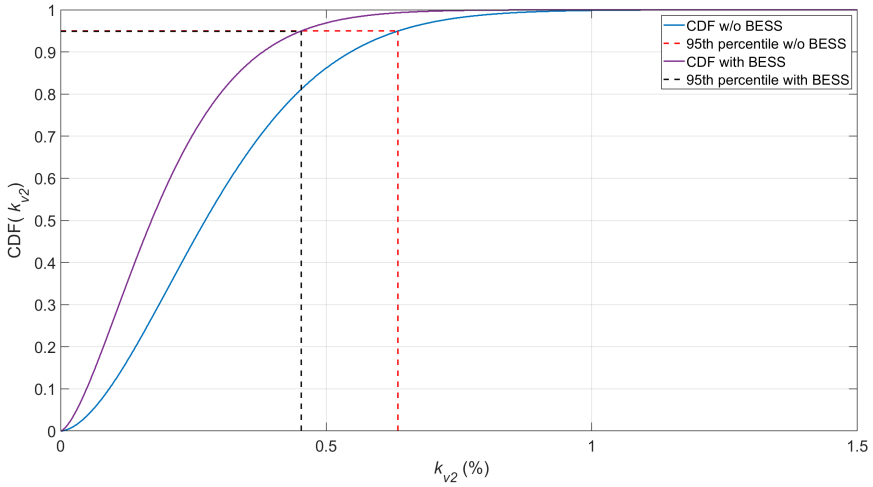

Figure D.26: Cumulative distribution function of k_{v2} at bus E4 for 0% PV penetration level, with and without the BESSs in service.

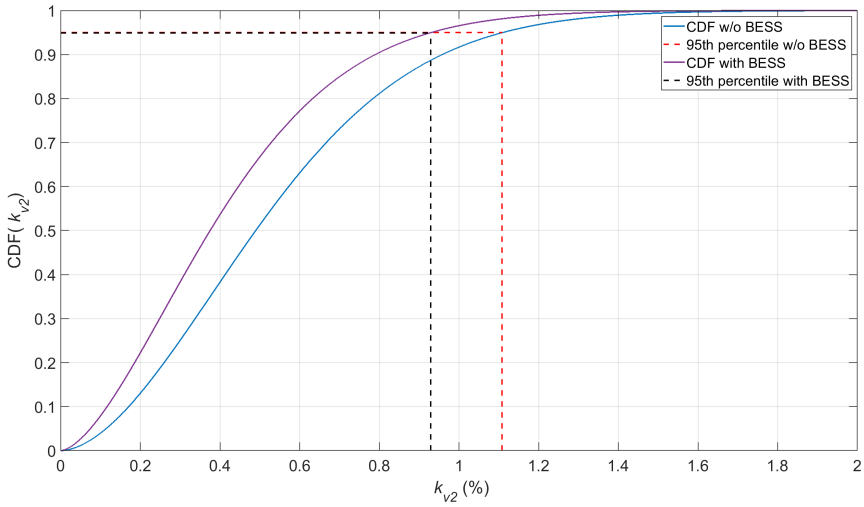

Figure D.27: Cumulative distribution function of k_{v2} at bus A4 for 20% PV penetration level, with and without the BESSs in service.

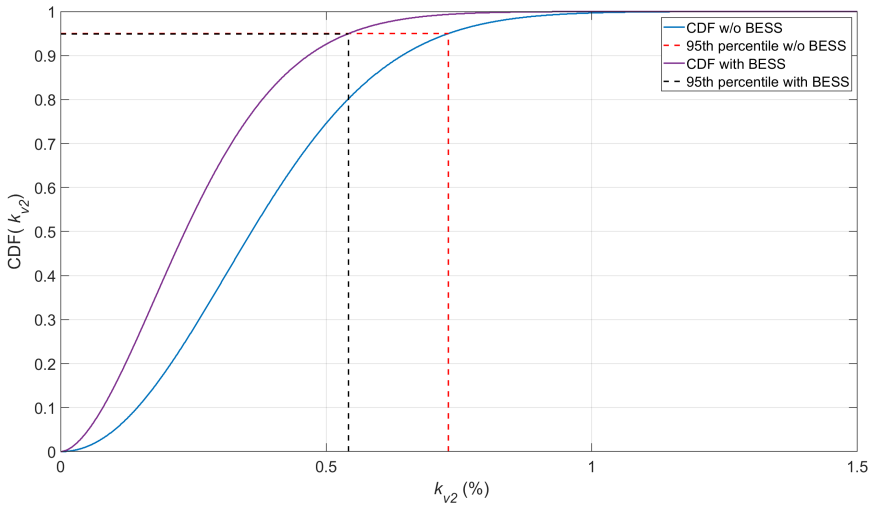

Figure D.28: Cumulative distribution function of k_{v2} at bus B4 for 20% PV penetration level, with and without the BESSs in service.

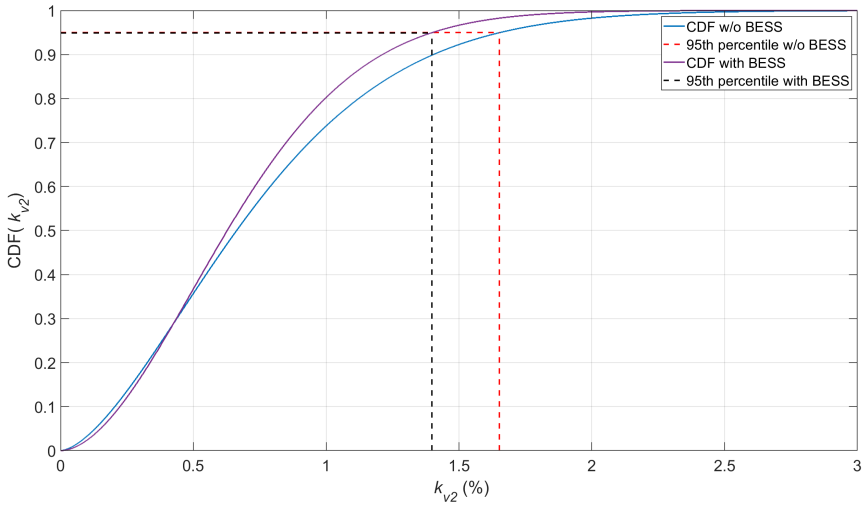

Figure D.29: Cumulative distribution function of k_{v2} at bus C4 for 20% PV penetration level, with and without the BESSs in service.

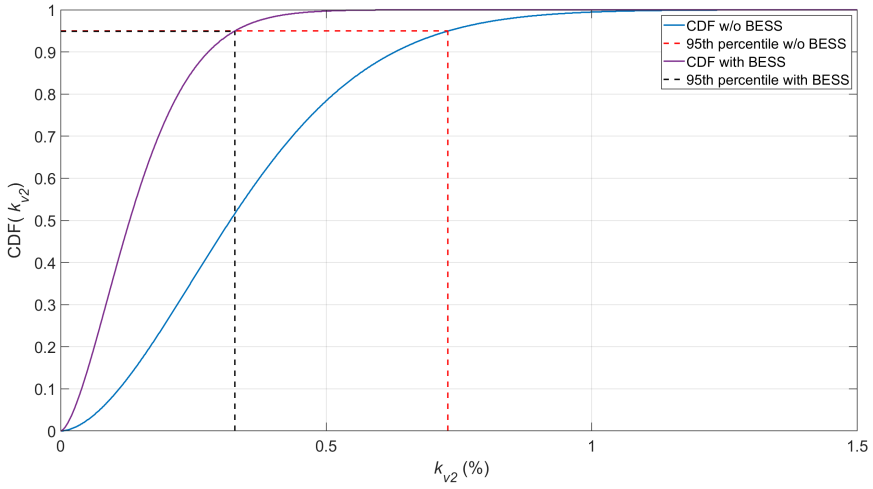

Figure D.30: Cumulative distribution function of k_{v2} at bus D4 for 20% PV penetration level, with and without the BESSs in service.

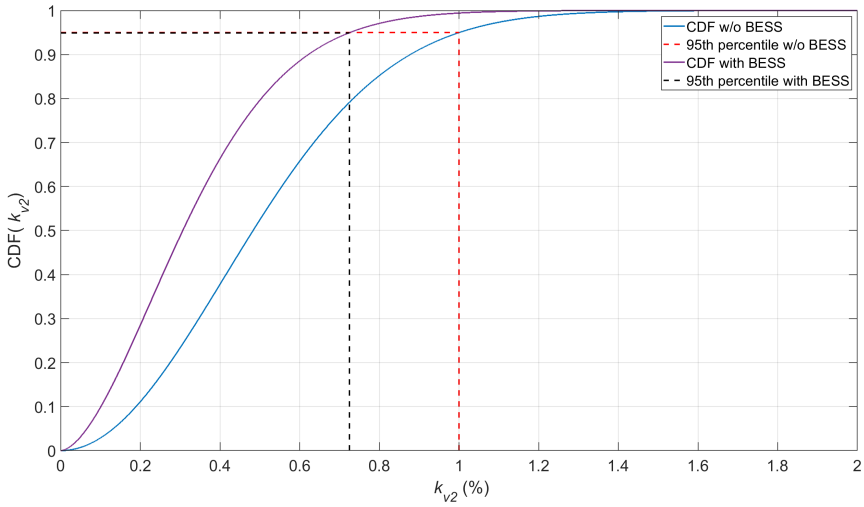

Figure D.31: Cumulative distribution function of k_{v2} at bus E4 for 20% PV penetration level, with and without the BESSs in service.

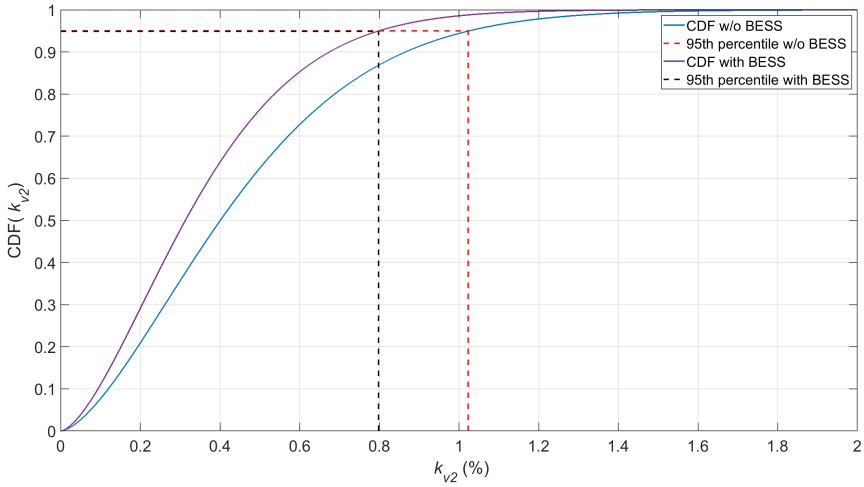

Figure D.32: Cumulative distribution function of k_{v2} at bus A4 for 60% PV penetration level, with and without the BESSs in service.

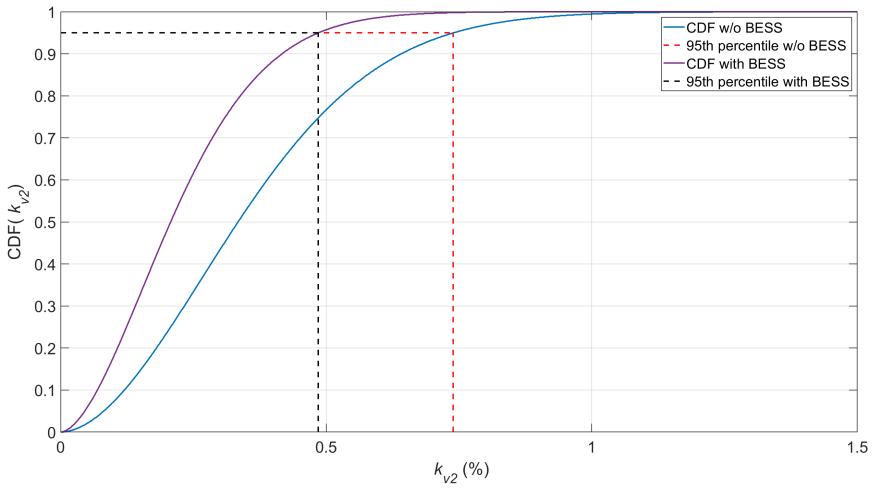

Figure D.33: Cumulative distribution function of k_{v2} at bus B4 for 60% PV penetration level, with and without the BESSs in service.

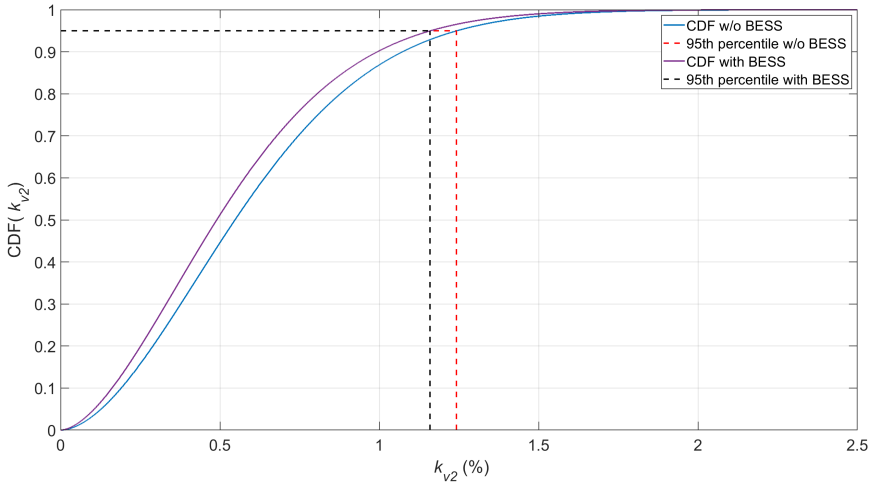

Figure D.34: Cumulative distribution function of k_{v2} at bus C4 for 60% PV penetration level, with and without the BESSs in service.

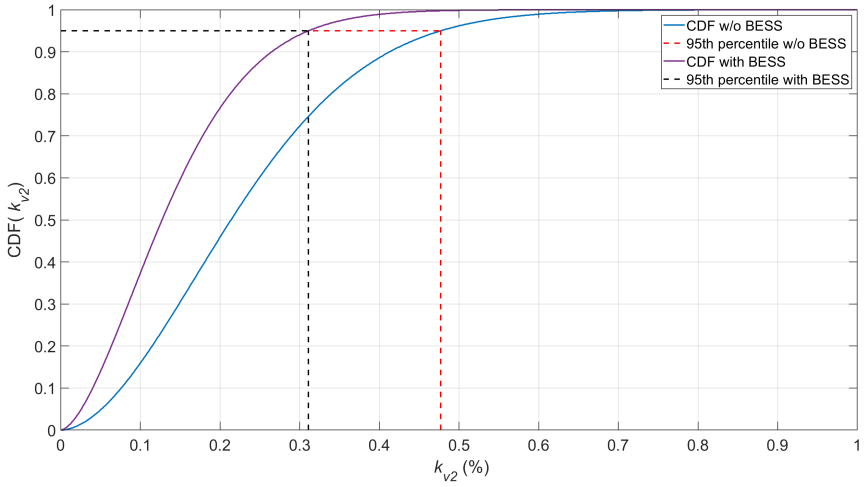

Figure D.35: Cumulative distribution function of k_{v2} at bus D4 for 60% PV penetration level, with and without the BESSs in service.

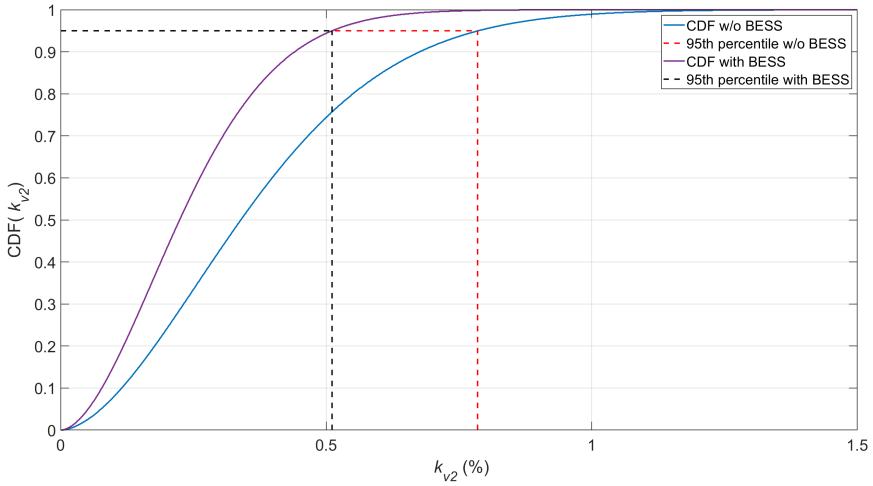

Figure D.36: Cumulative distribution function of k_{v2} at bus E4 for 60% PV penetration level, with and without the BESSs in service.

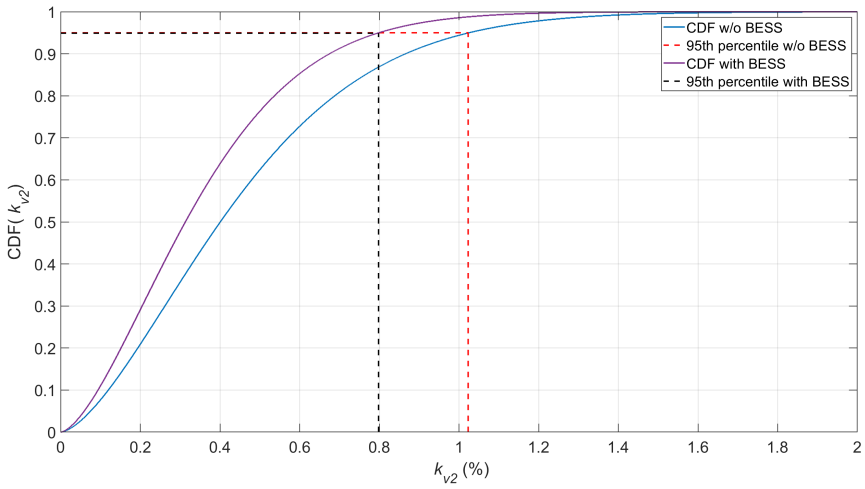

Figure D.37: Cumulative distribution function of k_{v2} at bus A4 for 100% PV penetration level, with and without the BESSs in service.

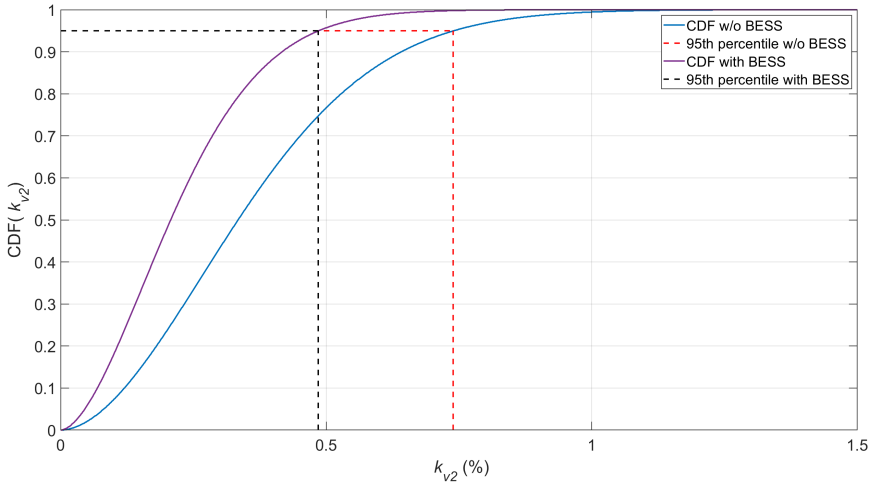

Figure D.38: Cumulative distribution function of k_{v2} at bus B4 for 100% PV penetration level, with and without the BESSs in service.

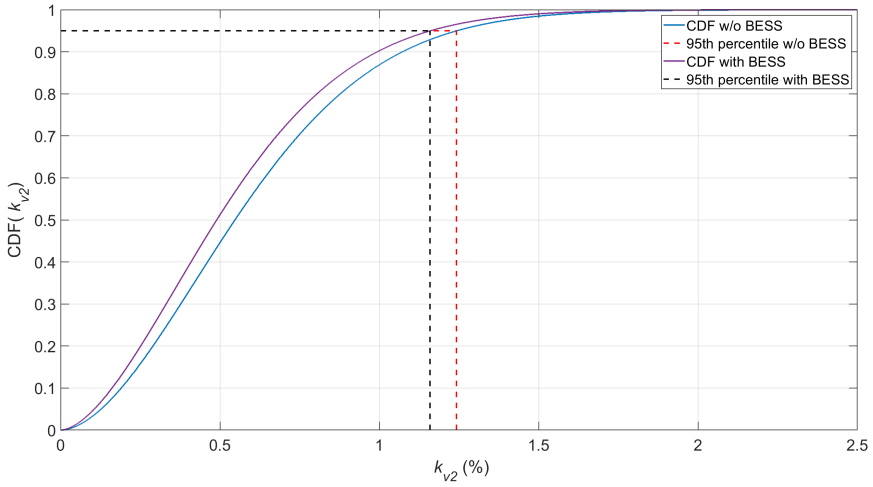

Figure D.39: Cumulative distribution function of k_{v2} at bus C4 for 100% PV penetration level, with and without the BESSs in service.

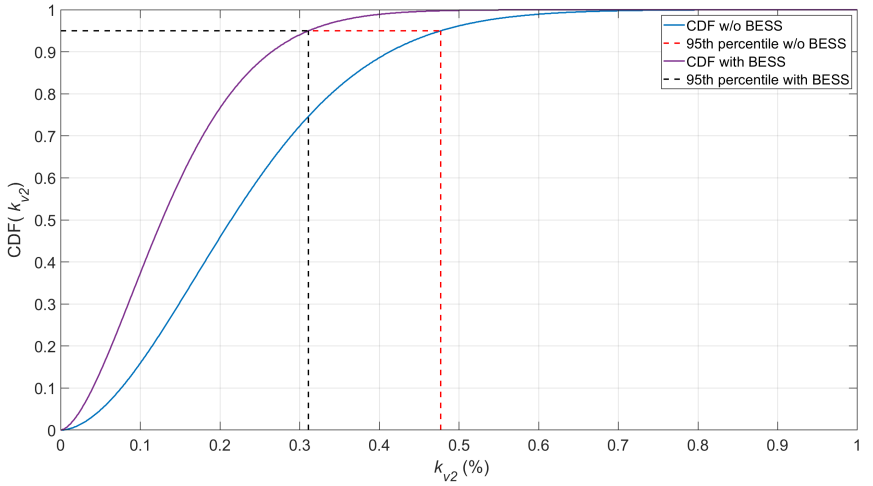

Figure D.40: Cumulative distribution function of k_{v2} at bus D4 for 100% PV penetration level, with and without the BESSs in service.

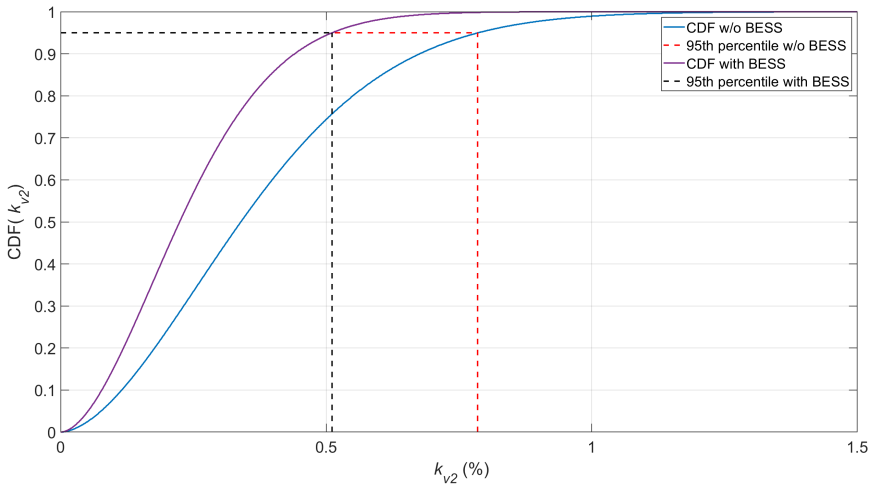

Figure D.41: Cumulative distribution function of k_{v2} at bus E4 for 100% PV penetration level, with and without the BESSs in service.

D.4 Supplementary simulation results for varying EV penetration levels, with and without the BESSs in service

In this section, the CDFs of k_{v2} at busbars A4-E4 for the examined EV penetration levels of Table 7.1 are provided. The corresponding plots are given in Figure D.42-D.61.

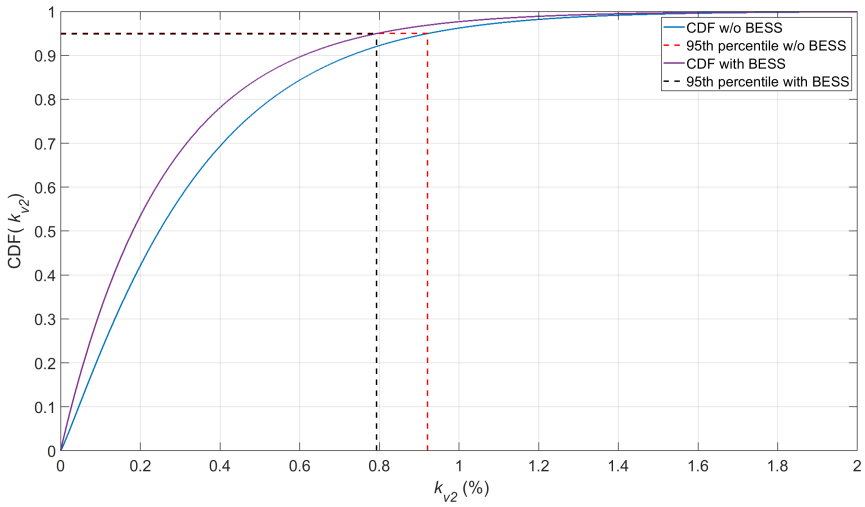

Figure D.42: Cumulative distribution function of k_{v2} at bus A4 for 0% EV penetration level, with and without the BESSs in service.

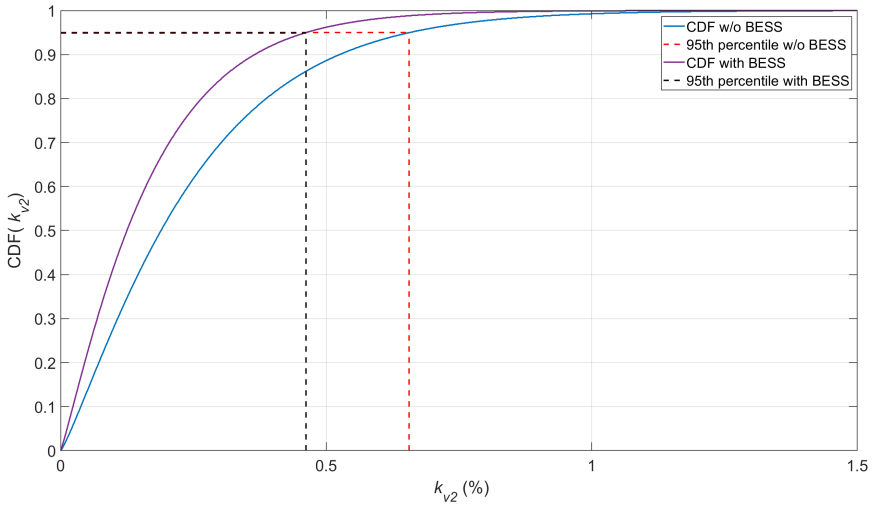

Figure D.43: Cumulative distribution function of k_{v2} at bus B4 for 0% EV penetration level, with and without the BESSs in service.

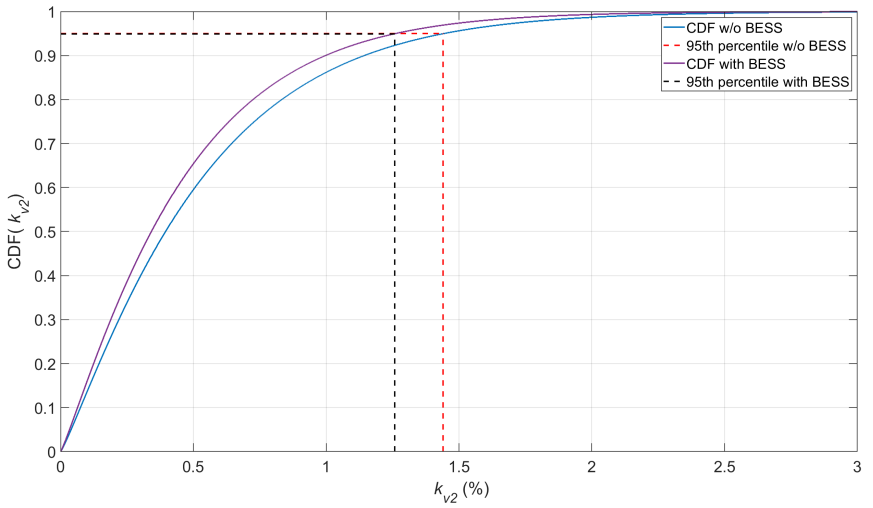

Figure D.44: Cumulative distribution function of k_{v2} at bus C4 for 0% EV penetration level, with and without the BESSs in service.

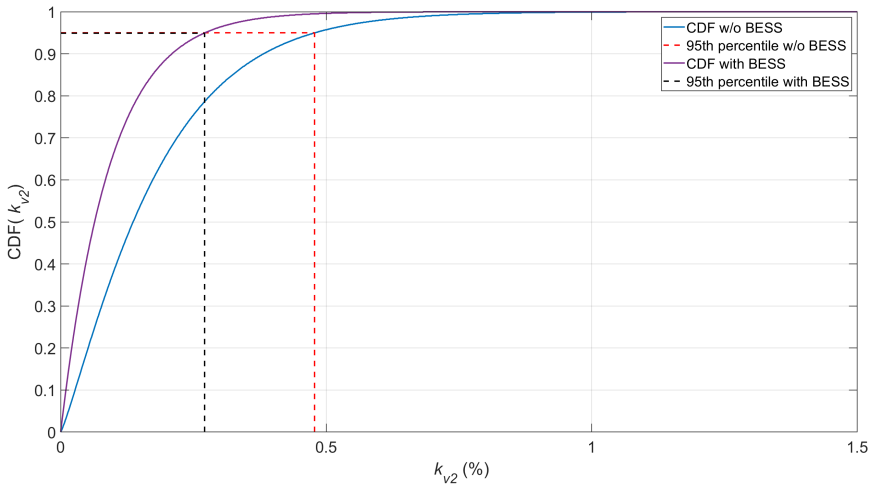

Figure D.45: Cumulative distribution function of k_{v2} at bus D4 for 0% EV penetration level, with and without the BESSs in service.

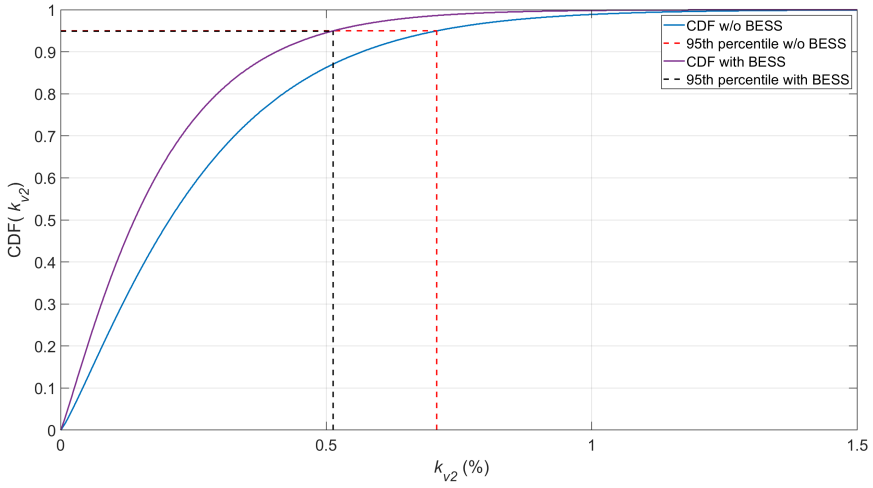

Figure D.46: Cumulative distribution function of k_{v2} at bus E4 for 0% EV penetration level, with and without the BESSs in service.

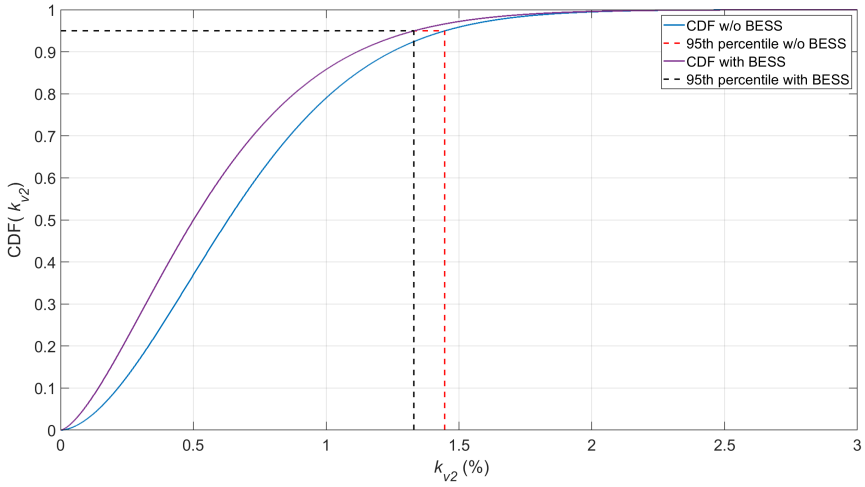

Figure D.47: Cumulative distribution function of k_{v2} at bus A4 for 20% EV penetration level, with and without the BESSs in service.

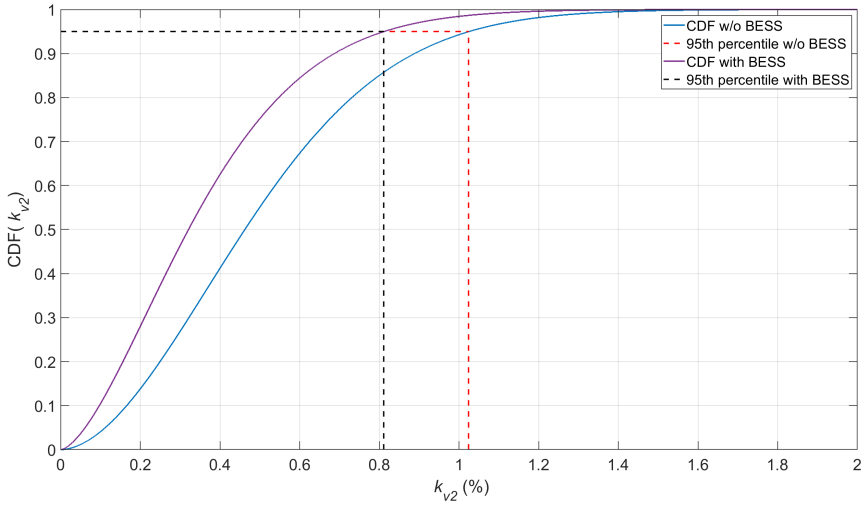

Figure D.48: Cumulative distribution function of k_{v2} at bus B4 for 20% EV penetration level, with and without the BESSs in service.

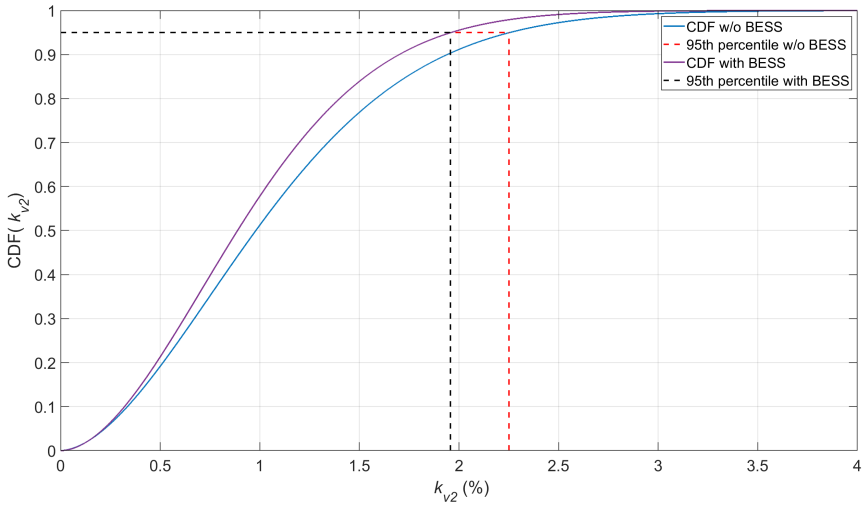

Figure D.49: Cumulative distribution function of k_{v2} at bus C4 for 20% EV penetration level, with and without the BESSs in service.

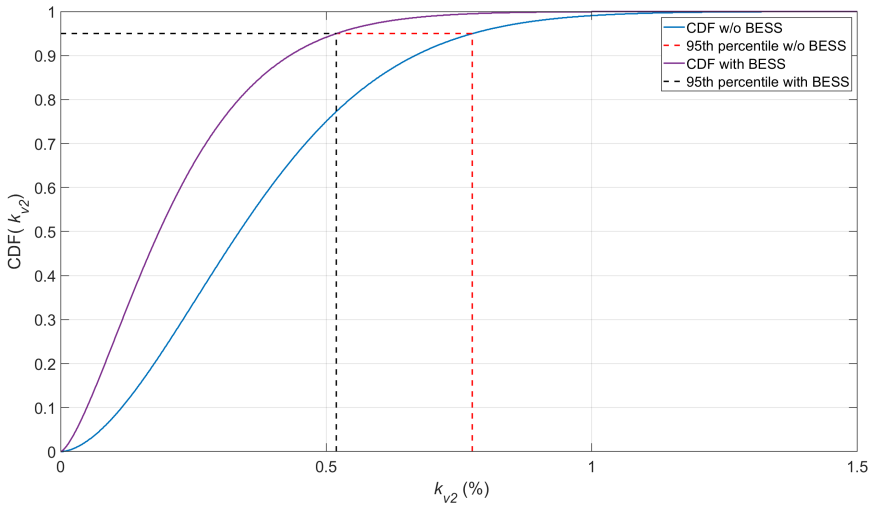

Figure D.50: Cumulative distribution function of k_{v2} at bus D4 for 20% EV penetration level, with and without the BESSs in service.

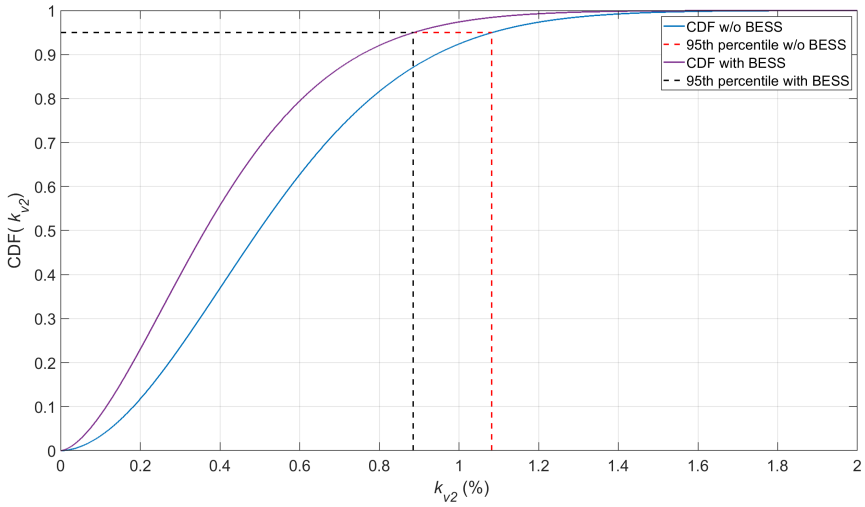

Figure D.51: Cumulative distribution function of k_{v2} at bus E4 for 20% EV penetration level, with and without the BESSs in service.

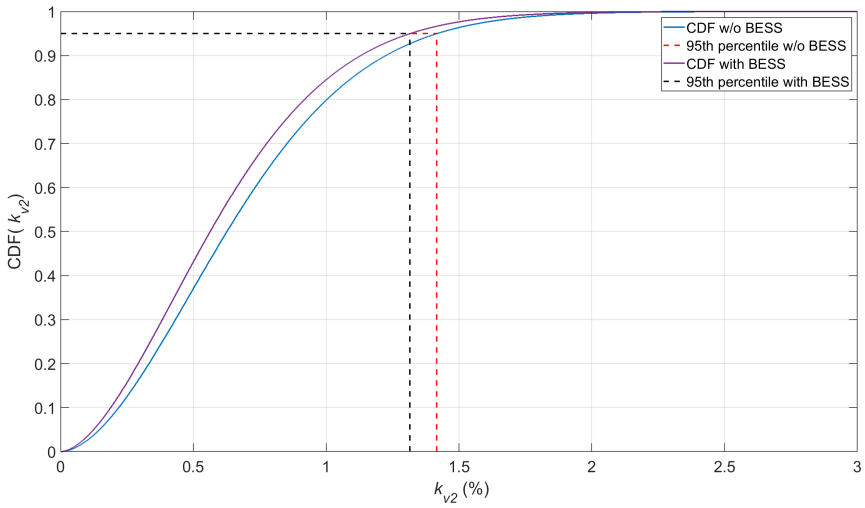

Figure D.52: Cumulative distribution function of k_{v2} at bus A4 for 60% EV penetration level, with and without the BESSs in service.

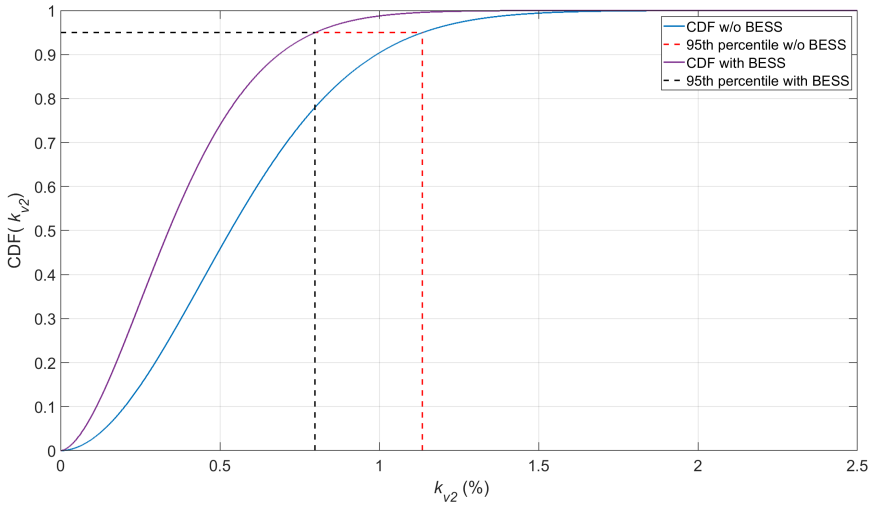

Figure D.53: Cumulative distribution function of k_{v2} at bus B4 for 60% EV penetration level, with and without the BESSs in service.

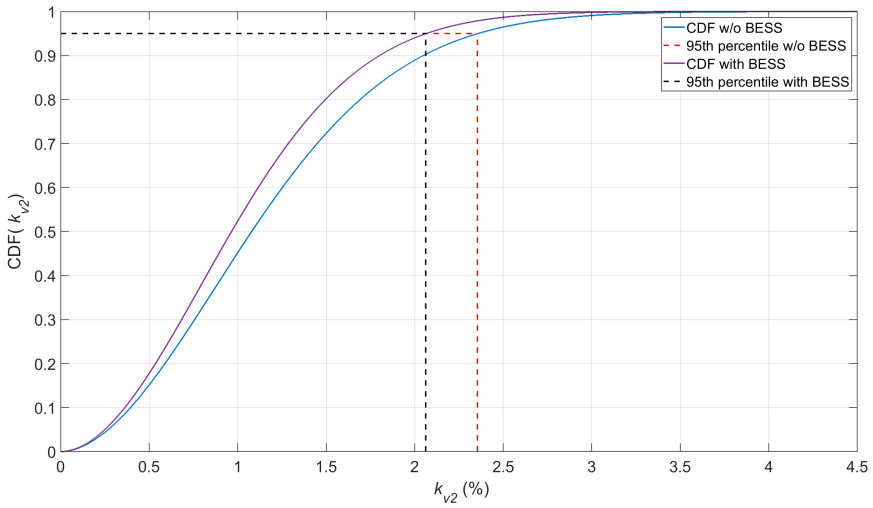

Figure D.54: Cumulative distribution function of k_{v2} at bus C4 for 60% EV penetration level, with and without the BESSs in service.

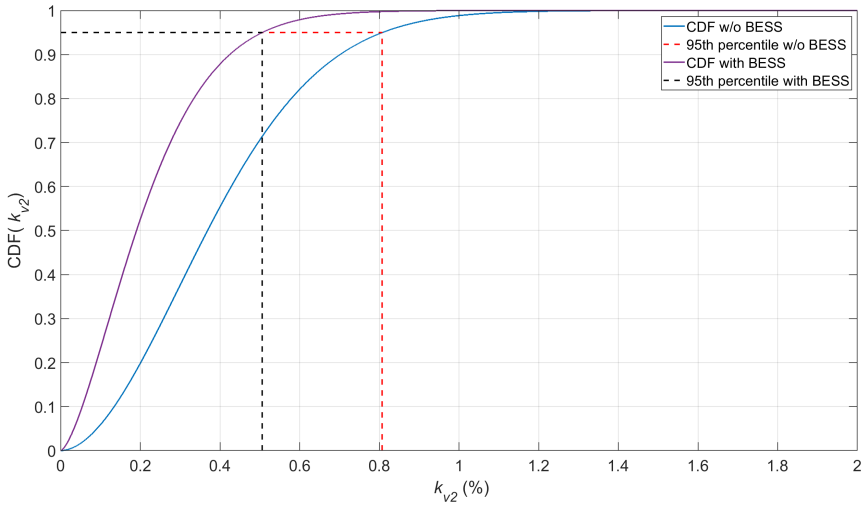

Figure D.55: Cumulative distribution function of k_{v2} at bus D4 for 60% EV penetration level, with and without the BESSs in service.

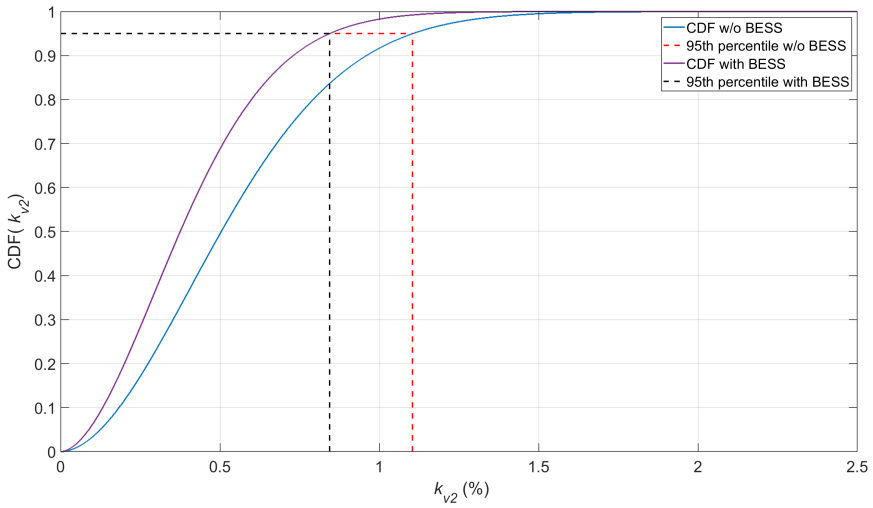

Figure D.56: Cumulative distribution function of k_{v2} at bus E4 for 60% EV penetration level, with and without the BESSs in service.

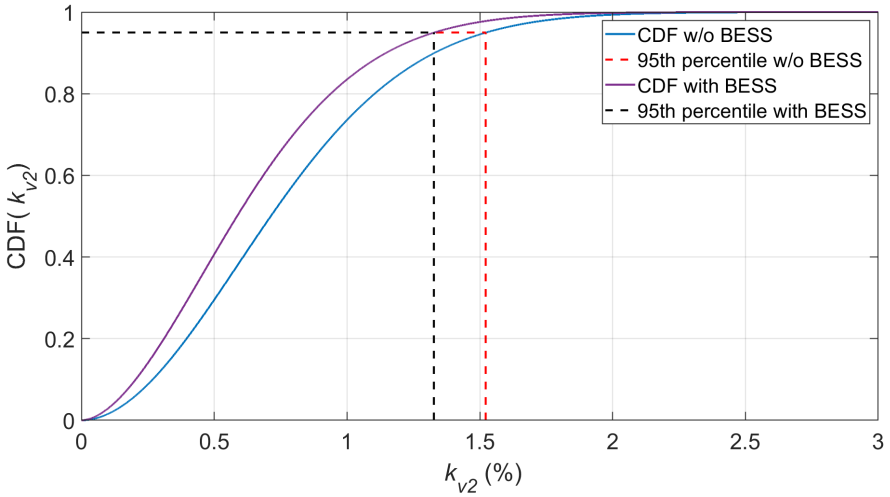

Figure D.57: Cumulative distribution function of k_{v2} at bus A4 for 100% EV penetration level, with and without the BESSs in service.

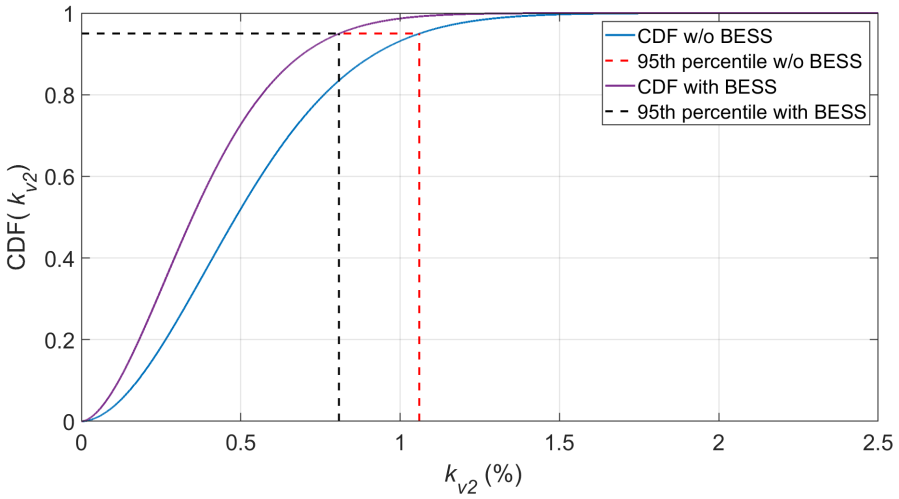

Figure D.58: Cumulative distribution function of k_{v2} at bus B4 for 100% EV penetration level, with and without the BESSs in service.

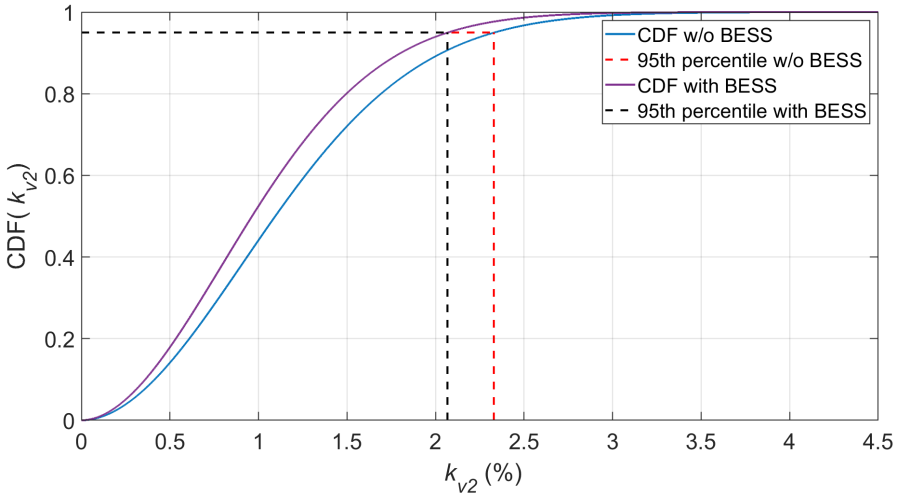

Figure D.59: Cumulative distribution function of k_{v2} at bus C4 for 100% EV penetration level, with and without the BESSs in service.

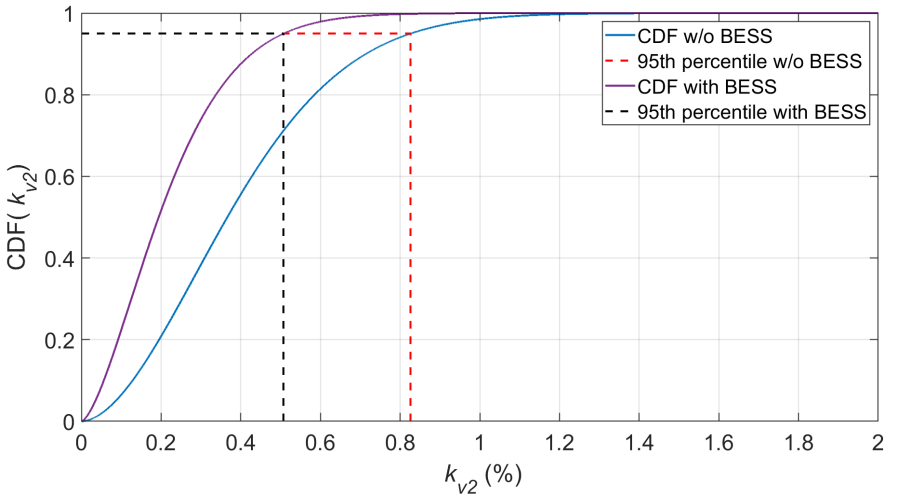

Figure D.60: Cumulative distribution function of k_{v2} at bus D4 for 100% EV penetration level, with and without the BESSs in service.

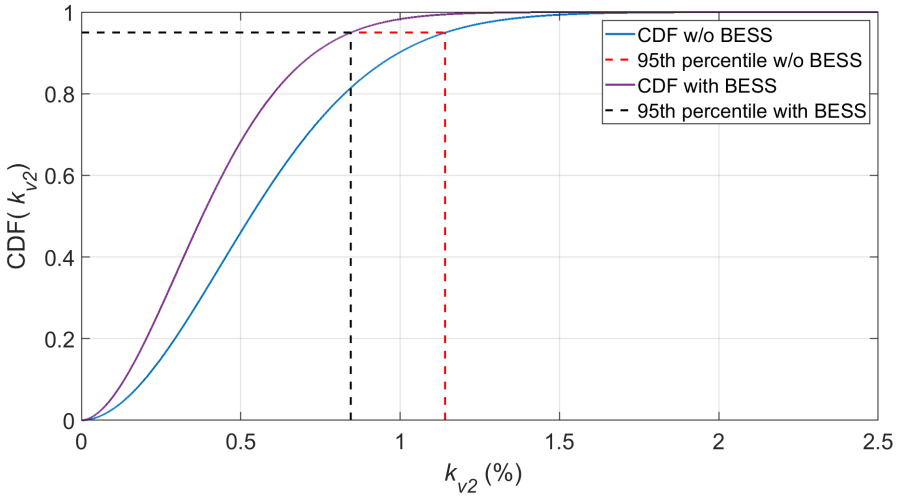

Figure D.61: Cumulative distribution function of k_{v2} at bus E4 for 100% EV penetration level, with and without the BESSs in service.

Appendix E

Experimental Setup

E.1 Preparation process of Simulink model for running in OPAL-RT platform using RT-LAB software

In order for the Simulink model of Figure 6.2 to run in OPAL-RT, a series of modifications have to implemented, including the use of blocks from the OPAL-RT library. The RT-LAB software is used to generate C code from the Simulink model, which is transferred to the OPAL-RT platform via ethernet. More specifically, the steps carried out to run the model to the real-time target machine are described below:

1. **Edit**: Initially, the model was grouped into two subsystems, which are depicted in Figure E.1: the computational subsystem (SM_Grid), which runs on one CPU (Central Processing Unit) core of the simulator, and the graphical subsystem (SC_GUI), which runs on the laptop [127]. The purpose of these two blocks is described next.
   - The computational subsystem contains the models of the grid, inverter (modelled using the ARTEMiS library block Time-Stamped Bridge (TSB) called TSB-RD, RD standing for Real Diodes) and load, as well as the control algorithm. In addition, the configuration of the digital and analog inputs/outputs (I/Os) is done in this subsystem using the Simulink blocks of Figure E.2. The function of these blocks is described next:
     - OpFcnCommonAnalogOut: This block is used to transmit to a physical I/O card the voltage values to be applied to the analog output channels of the OPAL-RT device. In the case under study, the signal of phase-a reference voltage ($v_{a,ref}$) was applied to the analog output channel. The

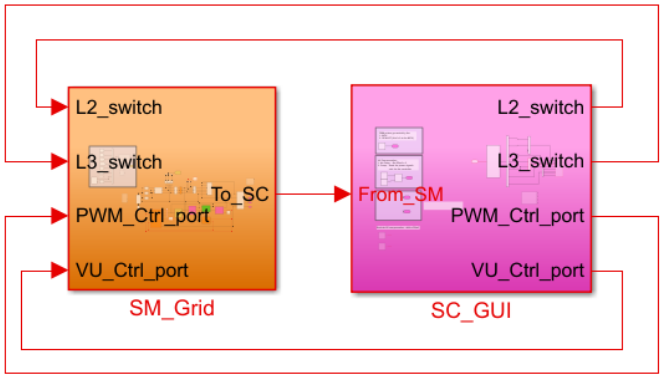

Figure E.1: Computational subsystem and graphical subsystem.

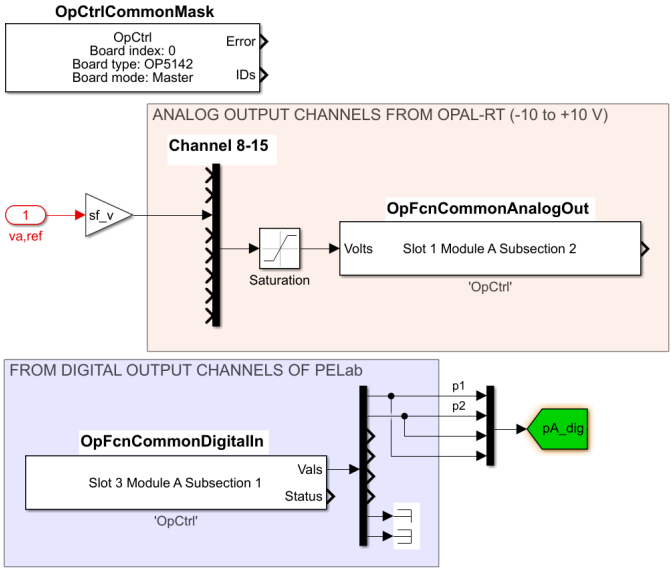

Figure E.2: Simulink I/O blocks.

signal was scaled by a scaling factor equal to $sf_v = 1/1000$ to ensure that it lies within the voltage range for the I/O card, which is ±10 V. A saturation block was added to the signal before sending it to the analog output channel, with the upper and the lower limit set to +10 V and −10 V, respectively.

– OpFcnCommonDigitalIn: This block returns 0/1 state values of a subset of digital input channels of a carrier connected to an FPGA card. Two digital input channels were used to receive the PWM signals from the

digital output channels of the PELab.

- OpCtrlCommonMask: This block controls the programming of the OPAL-RT card, its initialization and the selection of the hardware synchronization mode of the card. It also enables binding of Send/Recv and I/O blocks to that specific card.

- The graphical subsystem contains scopes and displays for the plotting and observation of the signals of interest, as well as constants and manual switches that are used to control various operations occuring in the computational subsystem.

To enable the exchange of signals between the two subsystems, the 'OpComm' block of the RT-LAB library was placed inside each subsystem, being responsible for the TCP/IP communication between the host (SC_GUI) and the target (SM_Grid). All the inports of each subsystem have to pass through this block before being used inside the subsystem. The 'ARTEMiS Guide' block of the ARTEMiS library was used instead of the 'powergui' block, which is typically used for realizing offline simulations in Simulink, and the sample time was set to $T_s = 20$ us. In addition, a fixed-step solver was used to run the model in OPAL-RT, since it is mandatory for executing real-time simulations. The model was run offline before proceeding to the real-time simulations to ensure that it can run without any errors.

2. **Build**: The next step consisted in building the model, during which RT-LAB performs the following procedure: it checks the Simulink model, separates the subsystems, generates code from the subsystems, transfers the code to the target, compiles the code and links it with libraries, and finally it transfers back the executable file to the host PC.

3. **Prepare the model execution**: The real-time simulation mode was set to 'Hardware synchronized', since the analog outputs and digital inputs of OPAL-RT were connected to the analog inputs and digital outputs of the microcontroller, respectively. In addition, the XHP (eXtra High Performance) mode was enabled, since it is strongly recommended for small time steps ($T_s \leq 100$ us), and in the case under study $T_s = 20$ us. Essentially, the XHP mode shields the CPU cores and reserves them for the models, combining the advantages of preventing interruptions from other operating system processes, reducing the jitter considerably and accelerating the simulation.

4. **Load**: Next, the model was loaded. In this stage, OPAL-RT uploads the exe-

cutable file to the target, allocates cores and memory, and launches the user interface (Simulink console).

5. **Execute**: The last step consists in executing the model, i.e. the real-time simulation starts.

Additionally, The 'OpWriteFile' block was used to save the signals of interest. This block makes use of the RT-LAB data acquisition to save all signals without interfering with the real-time simulation. The data was stored in MATLAB file format, and it was plotted in MATLAB.

E.2 Programming of STM32H754 microcontroller using Keil uVision5

As explained in Chapter 6, the control system was implemented in OPAL-RT, while the PWM signals for phase-a inverter were generated using the PEController, which is the internal embedded controller of PELab. The PEcontroller is built using the ST Microelectronics ARM Cortex M7 and M4 dual core STM32H745BI microcontroller, in which two application examples have been implemented by the manufacturer: a V/f control strategy for AC induction motors and a control scheme for three-phase grid-tie inverters with boost converter. While these control algorithms were not run in the context of this work, some of the implemented functions were used and appropriately modified for the purpose of generating the PWM signals. The code was run on the Cortex M7 processor. The aim of the following paragraphs is to provide a high-level description of the microcontroller programming and the modifications made in the code to generate the PWM signals that control the duty cycles of the single-phase inverter switches.

The generation of PWM signals can be achieved with the high resolution timer (HRTIM) peripheral of the microcontroller by programming a number of HRTIM registers. More specifically, the desired switching frequency $f_{sw} = 5$ kHz (see Section 6.2) was programmed in the period register (pTimeBaseCfg.Period) by using the formula:

$$PER = \frac{f_{HRCK}}{f_{sw}} \tag{E.1}$$

where the clock frequency of the timer, f_{HRCK}, was calculated based on the frequency of the kernel clock, $f_{HRTIM} = 480$ MHz, and a prescaler which can take 3 distinct values, as shown in Table E.1. It was observed that the required switching frequency can be achieved either by setting the prescaler value equal to 1 or 2. The prescaler value was chosen equal to 2, which yields $f_{HRCK} = 240$ MHz. Substituting this value and $f_{sw} = 5$ kHz in

Table E.1: Timer's clock frequency as a function of the prescaler for f_{HRTIM} = 480 MHz.

pTimeBaseCfg.PrescalerRatio	f_{HRCK}
HRTIM_PRESCALERRATIO_DIV1	$\frac{f_{HRTIM}}{1}$
HRTIM_PRESCALERRATIO_DIV2	$\frac{f_{HRTIM}}{2}$
HRTIM_PRESCALERRATIO_DIV4	$\frac{f_{HRTIM}}{4}$

(E.1), the value of the period register is obtained as PER = 48000, i.e. its corresponding hexadecimal value is 0x4B00.

The phase-a inverter reference voltage is an analog signal which is sent from an analog output channel of OPAL-RT to an analog input channel of the microcontroller, and it needs to be converted to its digital form so that it can be read and processed by the microcontroller. This can be realized by the external analog-to-digital converter (ADC) used in PELab, which is a 16-bit ADC with an analog voltage range of ±10 V and a resolution equal to $\frac{10}{2^{16}}$, where 0 corresponds to -10 V and 65535 corresponds to 10 V. Therefore, a scaling factor equal to $M_a = \frac{10}{32768}$ was used for the ADC. Additionally, the sampling time of the microcontroller was chosen equal to 200 μs corresponding to a sampling frequency of f_s = 5 kHz, which is equal to the switching frequency. The reference voltage was scaled by a factor divduty = 0.5 to obtain the duty cycle outputs, which are connected to the PWM Channels to generate the switching signals that are sent from the microcontroller's digital output channels to the OPA-RT's digital input channels.

Appendix F

Supplementary Results for Chapter 4

This appendix presents the results obtained from the simulation of the load distributions for cases 2-4 of Table 4.2 in Chapter 4. In contrast to case 1, the results for these cases are briefly summarized, and only the most important figures are plotted with the aim to explain the developed voltage unbalance compensation method.

F.1 Case $\mathrm{C_{2p}}$ (pq–mode) : [6.5 1.5 8] kW

In this case, a purely resistive load is considered and a three-phase unbalance is introduced, with phase-b having the lowest load. The compensating action of the inverters reduces k_{v2} from 1.4 % to 0.15 %. Based on Figure F.1, phase-a and phase-c BESS units are discharging $p_{ga} = 1.15$ kW and $p_{gc} = 2.37$ kW, respectively. As a result, the power flows at the corresponding phases of the transformer are reduced. On the other hand, phase-b BESS unit is charging $p_{gb} = -3.5$ kW, thereby causing an increased power flow at that phase.

Before the compensation, the largest current is drawn from phase-c of the transformer ($I_{LV,c} = 32$ A), since the nominal load at that phase is 8 kW, while $I_{LV,a} = 26.32$ A and $I_{LV,b} = 6.8$ A, as demonstrated in Figure F.2(a). To compensate the unbalance, Figure F.2(c) shows that phase-b inverter injects the largest current, followed by phase-c and phase-a inverter, therefore eliminating the negative- and zero-sequence components at the transformer, as can be seen in Figure F.2(b).

More specifically, the compensation of voltage unbalance is achieved via the injection

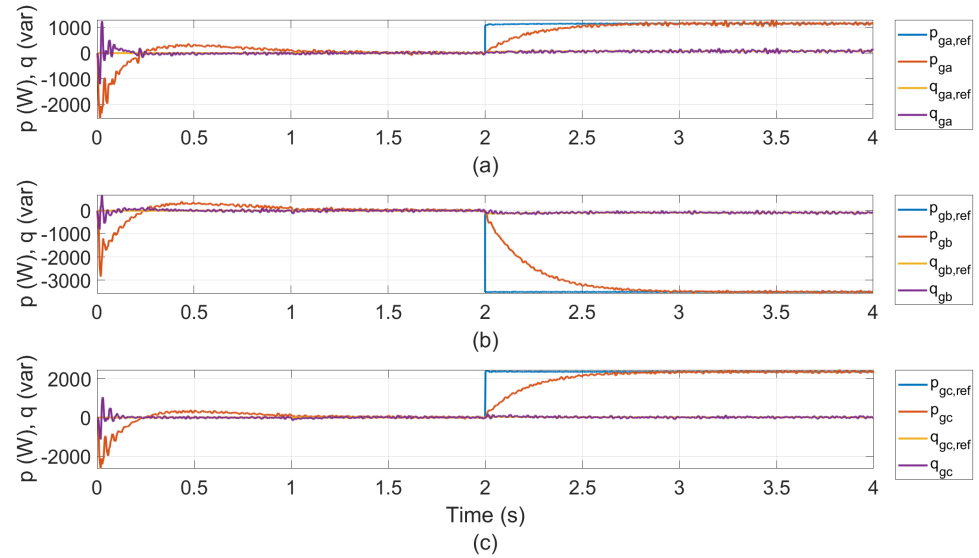

Figure F.1: Reference and measured active and reactive power at the terminal of each inverter: (a) phase-a, (b) phase-b and (c) phase-c.

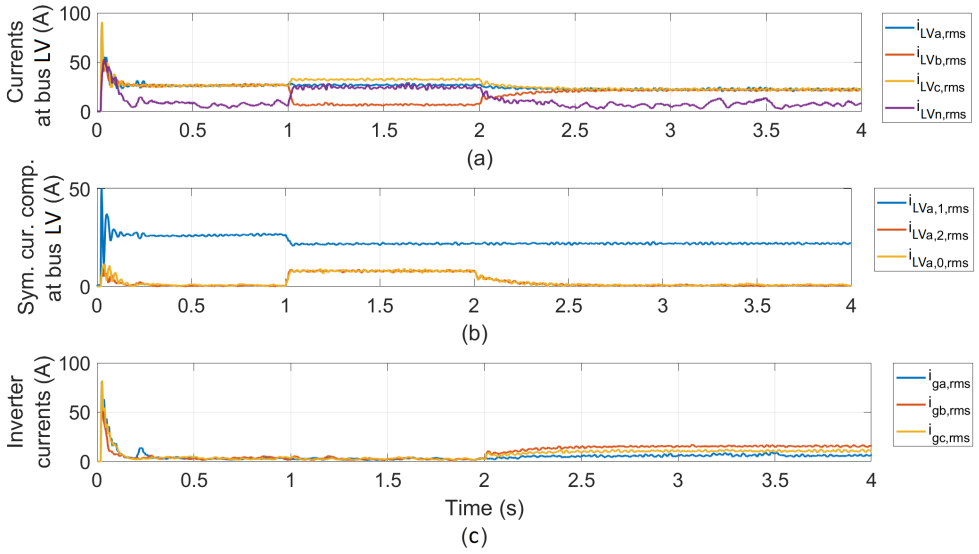

Figure F.2: rms values of (a) phase and neutral currents at bus LV, and (b) symmetrical current components at bus LV, and (c) inverter currents.

of the zero- and negative-sequence load current components by the inverters, with both these values being equal to 12 A, as depicted in Figure F.3.

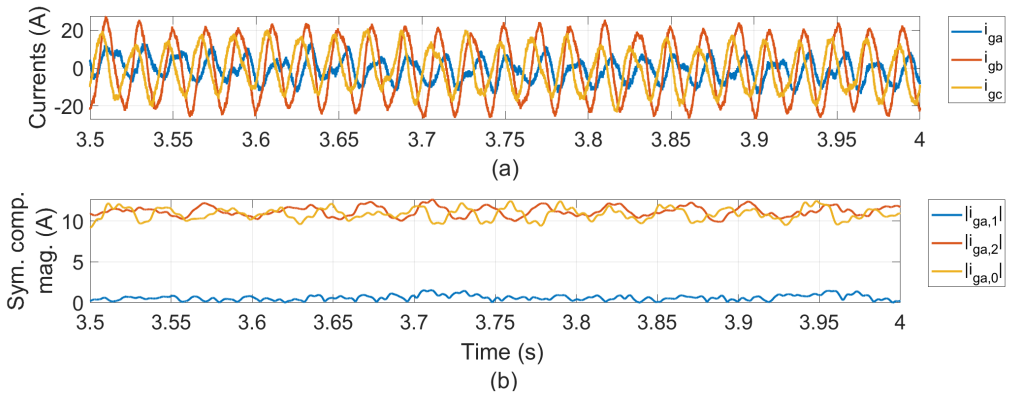

Figure F.3: Currents measured at inverter terminal (a) instantaneous values and (b) magnitudes of their symmetrical components.

The results obtained when the BESS inverters operate in p-mode and q-mode are provided next:

- **p-mode**: The results obtained for inverter operation in p-mode are similar to those obtained throughout this section, since the unbalance is caused due to the load active power unbalance.
- **q-mode**: The voltage unbalance factor value is the same with the value calculated for the base case, since the reactive power injection/absorption has no effect on the active power unbalance.

F.2 Case C_{2q} (pq–mode): [5.5 1.75 4.75] kvar

In this case, the load is purely inductive, and the voltage unbalance factor is reduced from $k_{v2} = 0.8$ % to 0.14 % due to the compensating action from the three inverters. More specifically, Figure F.4 demonstrates that phase-a and phase-c BESS units provide reactive power equal to $q_{ga} = 1.37$ kvar and $q_{gc} = 0.734$ kvar, respectively, while phase-b inverter absorbs reactive power equal to $q_{gb} = -2.11$ kvar with the aim to equalize the reactive power flows at the transformer.

Similar to case C_{2p}, Figure F.5-F.6 demonstrate that the inverters compensate the voltage unbalance by injecting the zero- and negative-sequence load current components. In this case, the values of these components are lower, i.e. $|i_{ga,2}| = |i_{ga,0}| = 7.5$ A, since the amount of reactive power dissipated by the load is lower than its active power consumption.

The results obtained when the BESS inverters operate in p-mode and q-mode are

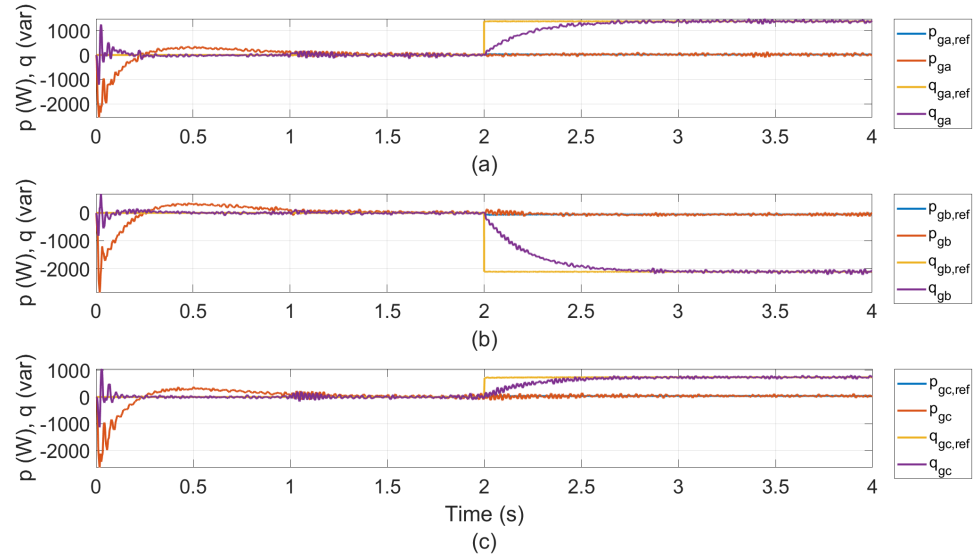

Figure F.4: Reference and measured active and reactive power at the terminal of each inverter: (a) phase-a, (b) phase-b and (c) phase-c.

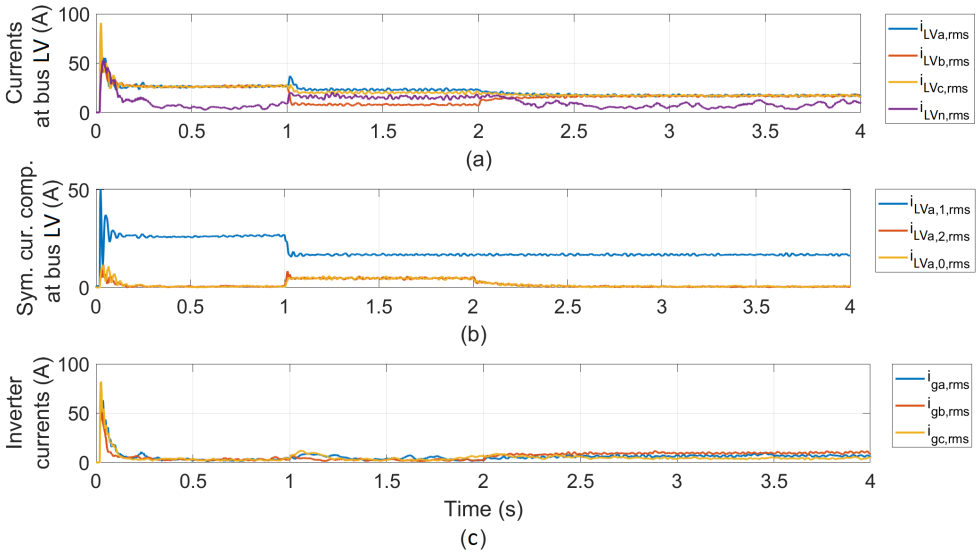

Figure F.5: rms values of (a) phase and neutral currents at bus LV and (b) symmetrical current components at bus LV, and (c) inverter currents.

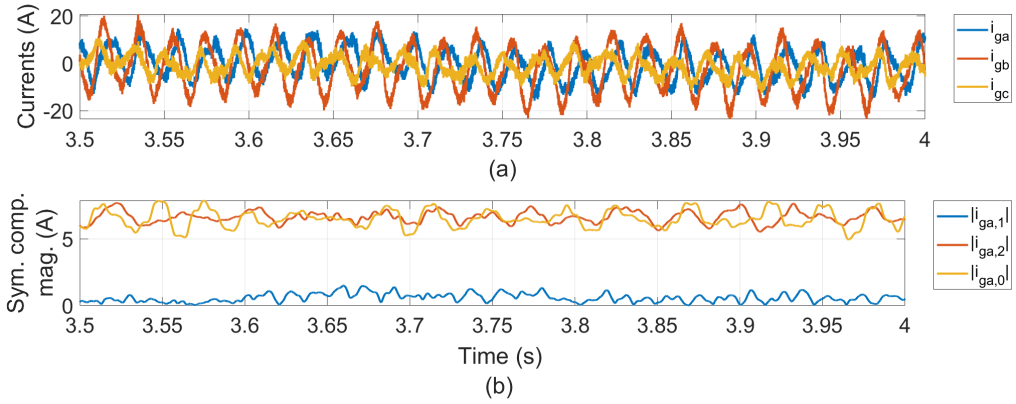

Figure F.6: Currents measured at inverter terminal (a) instantaneous values and (b) magnitudes of their symmetrical components.

provided next:

- **p-mode**: The voltage unbalance factor is not affected by active power injection, therefore its value is the same with that calculated for the base case.
- **q-mode**: The voltage unbalance factor is reduced to the value calculated in this section, i.e. $k_{v2} = 0.15$ %.

F.3 Case C_{2s} (pq–mode) : [8.66 2.68 9.45] kVA

A mixed resistive–inductive load is modelled. When the inverters operate in pq–mode, k_{v2} is reduced from 1.8 % to 0.14 %. Based on Figure F.7, the active power flows are equal to $p_{ga} = 1$ kW, $p_{gb} = -3.25$ kW and $p_{gc} = 2.1$ kW, while the reactive power flows are equal to $q_{ga} = 1.3$ kvar, $q_{gb} = -2$ kvar and $q_{gc} = 350$ kvar.

The zero- and negative-sequence current components injected by the inverters are equal to 10 and 14 A, respectively, as shown in Figure F.9(b).

The results obtained when the BESS inverters operate in p-mode and q-mode are provided next:

- **p-mode**: The value of k_{v2} is similar with the one obtained for the base case of Case C_{2q}.
- **q-mode**: The value of k_{v2} is similar with the one obtained for the base case of Case C_{2p}.

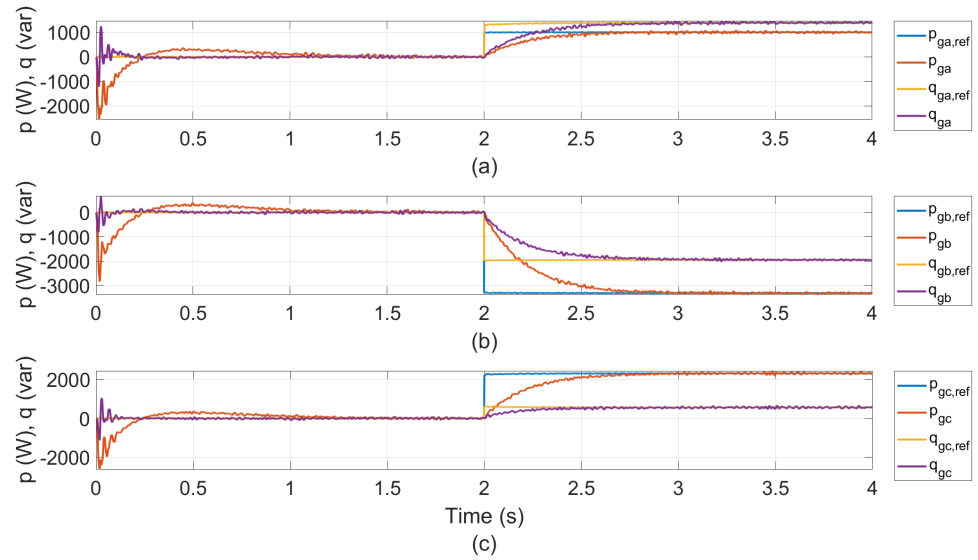

Figure F.7: Reference and measured active and reactive power at the terminal of each inverter: (a) phase-a, (b) phase-b and (c) phase-c.

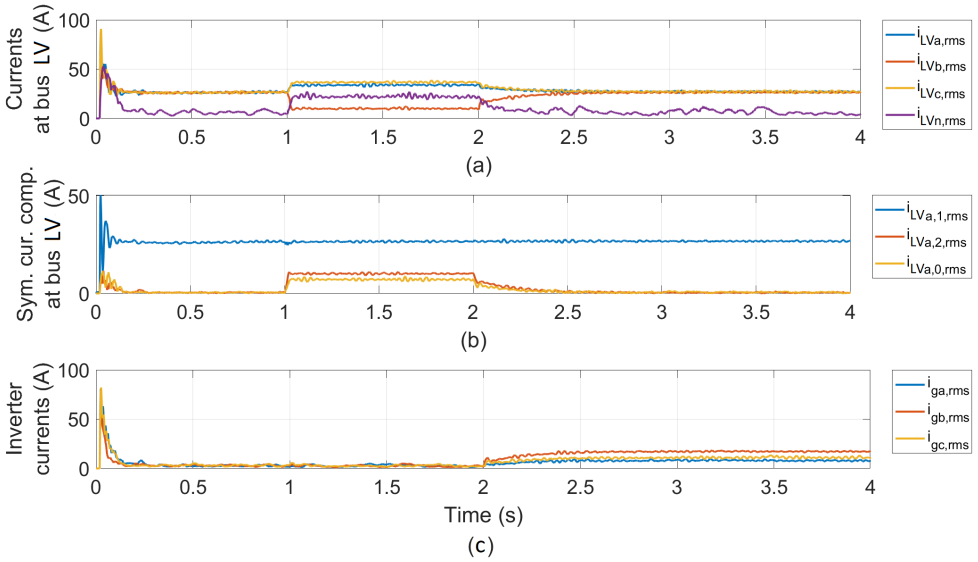

Figure F.8: rms values of (a) phase and neutral currents at bus LV and (b) symmetrical current components at bus LV, and (c) inverter currents.

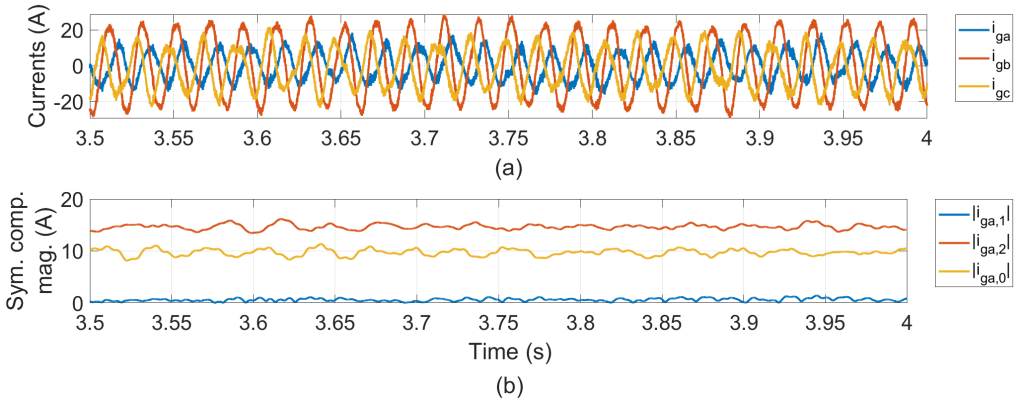

Figure F.9: Currents measured at inverter terminal (a) instantaneous values and (b) magnitudes of their symmetrical components.

F.4 Case C_{3p} (pq–mode): [4.5 9.5 2] kW

In this case, a purely resistive load is considered and a three-phase unbalance is introduced. The voltage unbalance factor k_{v2} is reduced from 1.5 % to 0.15 %. The detailed plots are omitted for this case, since it is very similar to Case 2, with the only difference being that phase-b has the largest load. As a results, two of the three BESS units, i.e. phase-a and phase-c BESS, charge and absorb reactive power, while phase-b BESS discharges and injects reactive power to mitigate the voltage unbalance.

F.5 Case C_{3q} (pq–mode) : [3.5 6 2.5] kvar

The obtained results are given in Table 4.3.

F.6 Case C_{3s} (pq–mode): [6 11.3 3.74] kVA

The obtained results are given in Table 4.3.

F.7 Case C_{4p} (pq–mode) : [16 0 0] kW

In this case, a very high unbalance is introduced at phase-a with the aim to illustrate the operating condition when the output of one or more inverters saturates. Figure F.10 shows that the active power injected from phase-a inverter saturates at $p_{ga} = 9$ kW, while phase-b and phase-c inverters draw $p_{gb} = p_{gc} = -4.6$ kW. The active power unbalance

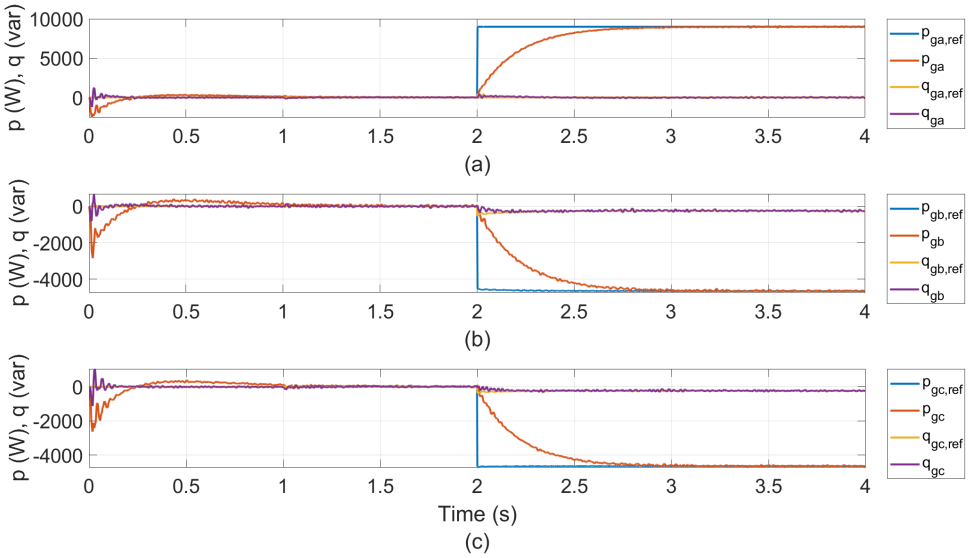

Figure F.10: Reference and measured active and reactive power at the terminal of each inverter: (a) phase-a, (b) phase-b and (c) phase-c.

causes a small reactive power flow at phase-a, therefore phase-b and phase-c inverters absorb reactive power equal to $q_{gb} = -0.245$ kvar and $q_{gc} = -0.264$ kvar, respectively, in order to equalize the reactive power flows at busbar LV, while $q_{ga} = 0$ kvar due to the saturation. The total active and reactive power is non-zero due to the power saturation, as shown in Figure F.11.

Figure F.12 presents the active and reactive power flows at busbar LV. From $t_1 = 0$ s to $t_2 = 1$ s, the load is balanced, and each phase draws equal amount of active and reactive power from the transformer. When the unbalance is introduced, all the power is drawn from transformer's phase-a, i.e. $p_{LV,a} = 13.5$ kW. At the same time, a reactive power flow equal to $q_{LV,a} = 0.79$ kvar is introduced at phase-a. At $t_3 = 2$ s, the active power flows start to converge: $p_{LV,a}$ is reduced to 5.3 kW, while phase-b and phase-c flows are increased to $p_{LV,b} = p_{LV,c} = 4.45$ kW. Also, positive reactive power is flowing at phase-b and phase-c, showing that the inverters absorb reactive power at these phases with the aim to equalize the reactive power flows at busbar LV.

Figure F.13 shows that initially, the three phases of the transformer are equally loaded, therefore the negative– and zero–sequence current components are zero. The unbalance is introduced at $t_2 = 1$, and all the current is drawn from phase-a, i.e. $i_{LV,a,rms} = 60$ A. Thus, the rms values of the symmetrical components are equal to 20 A, as it can be derived from Equation (B.7). The rms value of phase-a inverter current is $i_{ga,rms} =$

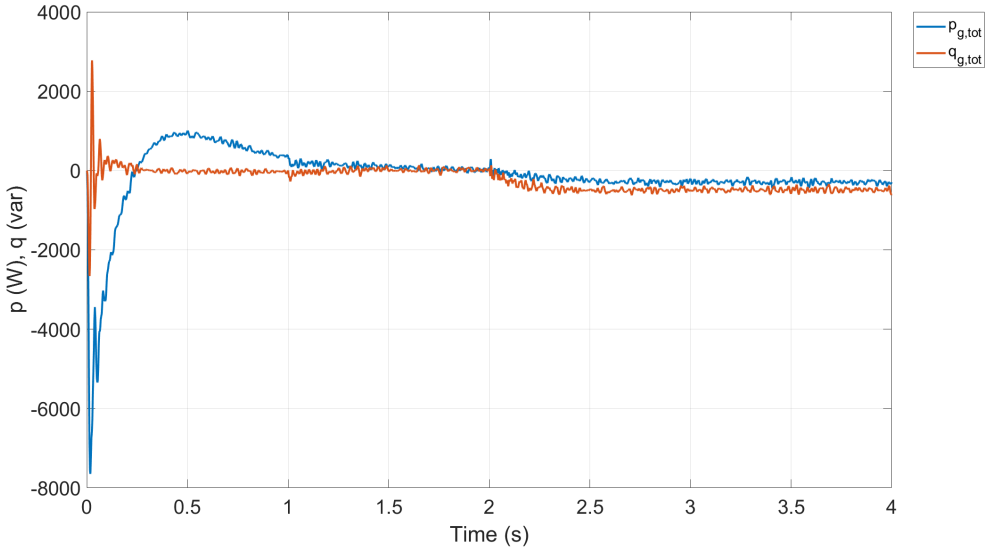

Figure F.11: Sum of active and reactive power measured at the terminals of the three inverters.

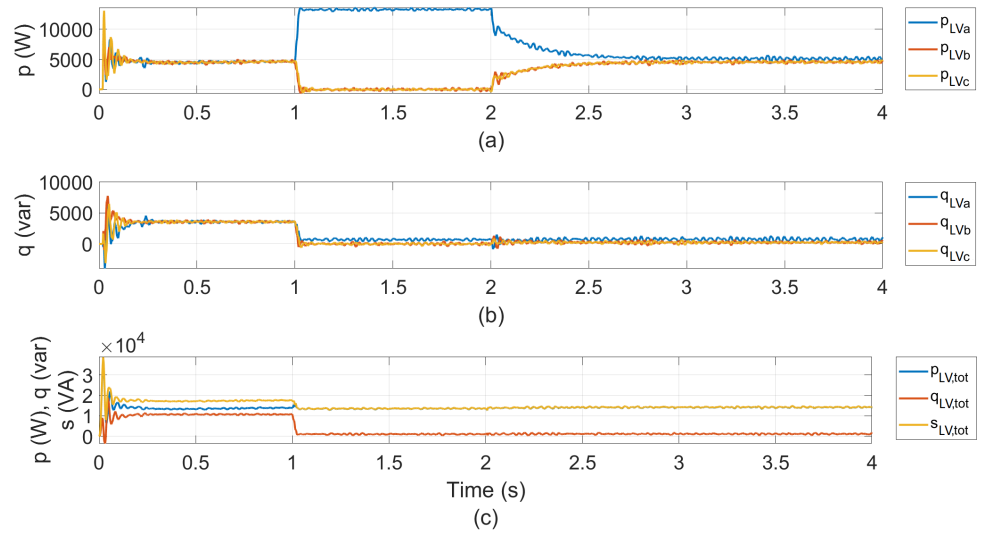

Figure F.12: (a) Active and (b) reactive power at each phase, and (c) total active, reactive and apparent power measured at bus LV.

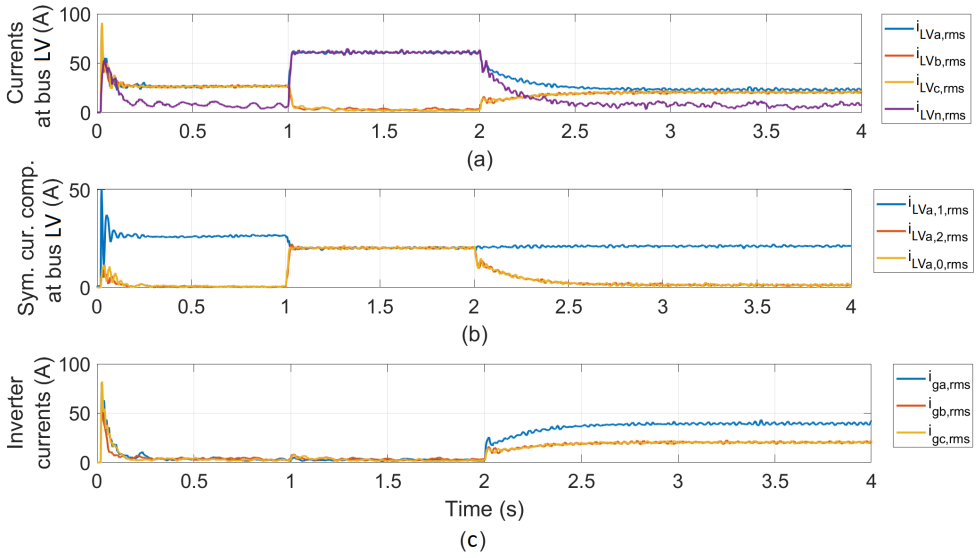

Figure F.13: rms values of (a) phase and neutral currents at bus LV and (b) symmetrical current components at bus LV, and (c) inverter currents.

42 A, while the rms values of phase-b and phase-c inverter currents are $i_{ga,rms} = 21$ A. Therefore, phase-a transformer current reduces to 22 A, while phase-b and phase-c transformer currents are increased to 22 A. The positive–sequence current component is slightly increased to 21 A, while the negative– and zero–sequence components are decreased to 1.5 A.

The currents at the inverter terminal, busbar LV and feeder A of each phase are coplotted in Figure F.14. Initially, all the load current is provided by the transformer. When the unbalance is introduced, there is current flow only at phase-a. When the compensation is activated, the current contribution from phase-a inverter to the load starts to increase, while phase-a transformer current starts to decrease. Since no load is connected at phase-b and phase-c, the feeder currents at these phases are zero. The inverters draw some amount of current from phase-b and phase-c of the transformer to make the transformer currents balanced. The instantaneous currents of the inverter and transformer at phase-b and phase-c are equal and in anti–phase.

Finally, the zero- and negative sequence current components of the inverter are shown in Figure F.15, which shows that both components are equal to 31 A.

The results obtained when the BESS inverters operate in p-mode and q-mode are provided next:

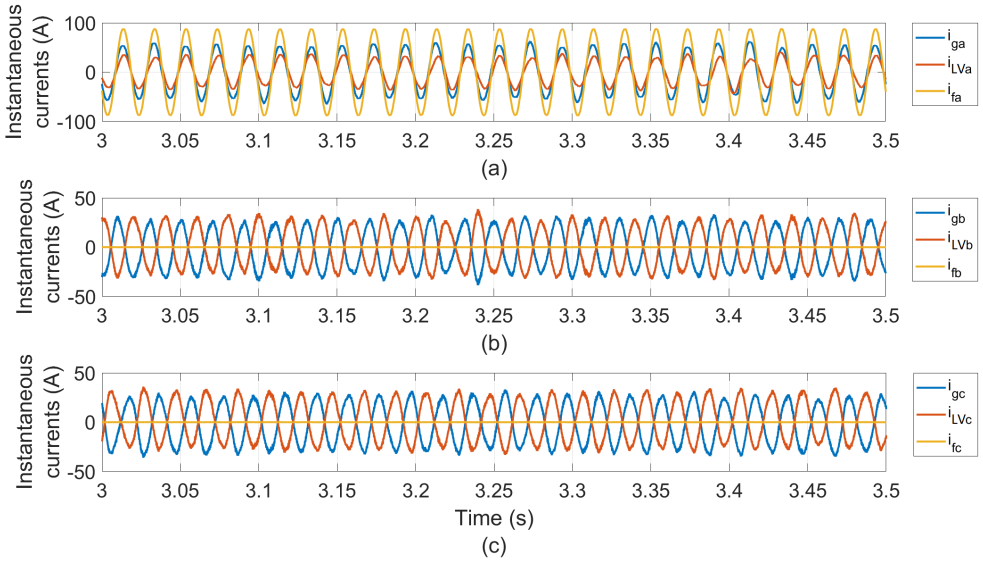

Figure F.14: Instantaneous values of currents at bus LV, inverter and feeder at (a) phase a, (b) phase b and (c) phase c.

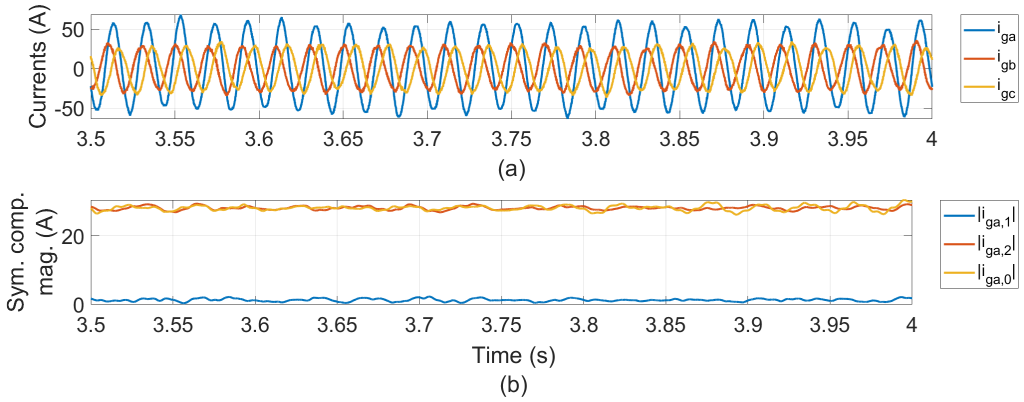

Figure F.15: Currents measured at inverter terminal (a) instantaneous values and (b) magnitudes of their symmetrical components.

- **p-mode**: The results are similar with those obtained in this section.
- **q-mode**: The voltage unbalance factor is not affected by the injection/absorption of reactive power.

F.8 Case C_{4q} (pq–mode) : [12 0 0] kvar

The load is purely inductive. In this case, k_{v2} is reduced from 2.75 % to 0.2 %. The reactive power of the inverters follows a similar pattern with the active power of Case C_{4p}. Specifically, phase-a reactive power is positive, while phase-b and phase-c reactive power are negative. Figure F.16-F.17 show the phase and total reactive power curves, showing that no saturation occurs in this case.

Figure F.18 shows that at $t_2 = 1$ s, when the unbalance is introduced, all the reactive power flows at phase-a, and a small amount of active power starts to flow at that phase. After the compensating action, the reactive power flows of the three phases at busbar LV start to converge.

Regarding the current curves of Figure F.19–F.20, similar comments with the case of the purely resistive load apply.

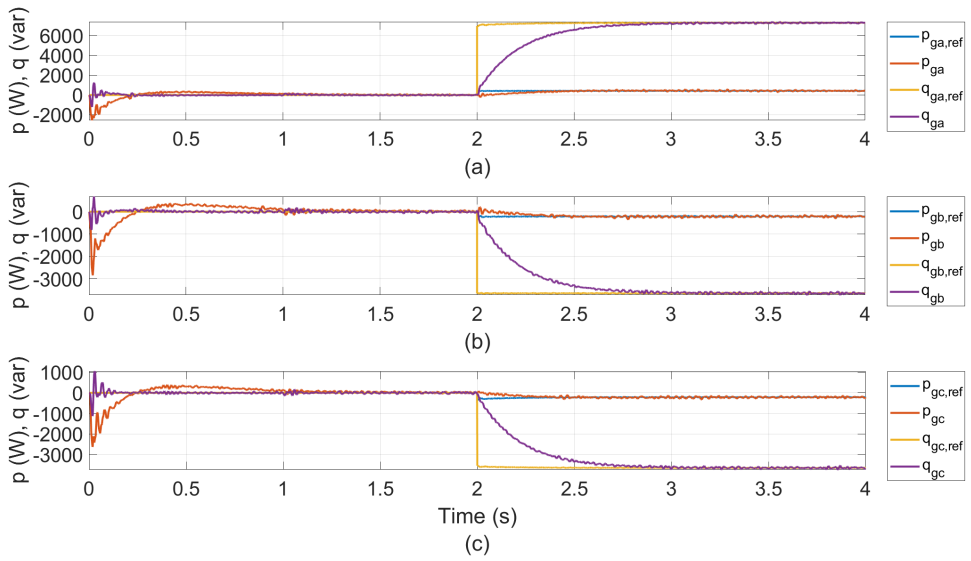

Figure F.16: Reference and measured active and reactive power at the terminal of each inverter: (a) phase-a, (b) phase-b and (c) phase-c.

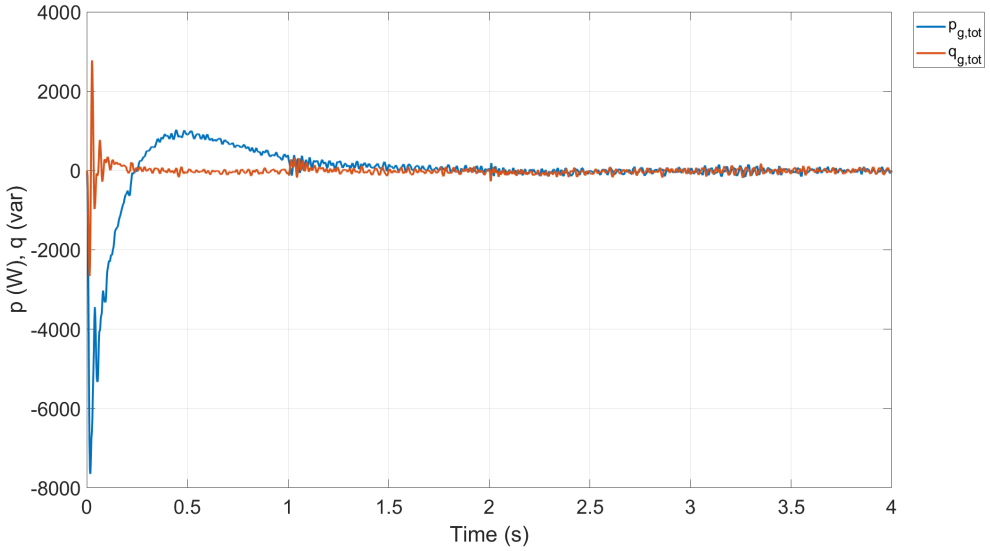

Figure F.17: Sum of active and reactive power measured at the terminals of the three inverters.

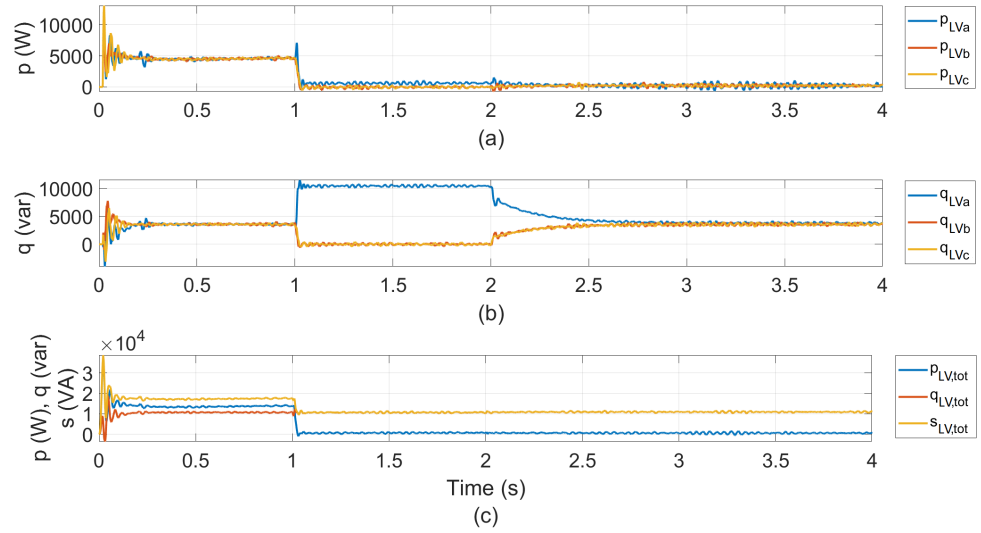

Figure F.18: (a) Active and (b) reactive power at each phase, and (c) total active, reactive and apparent power measured at bus LV.

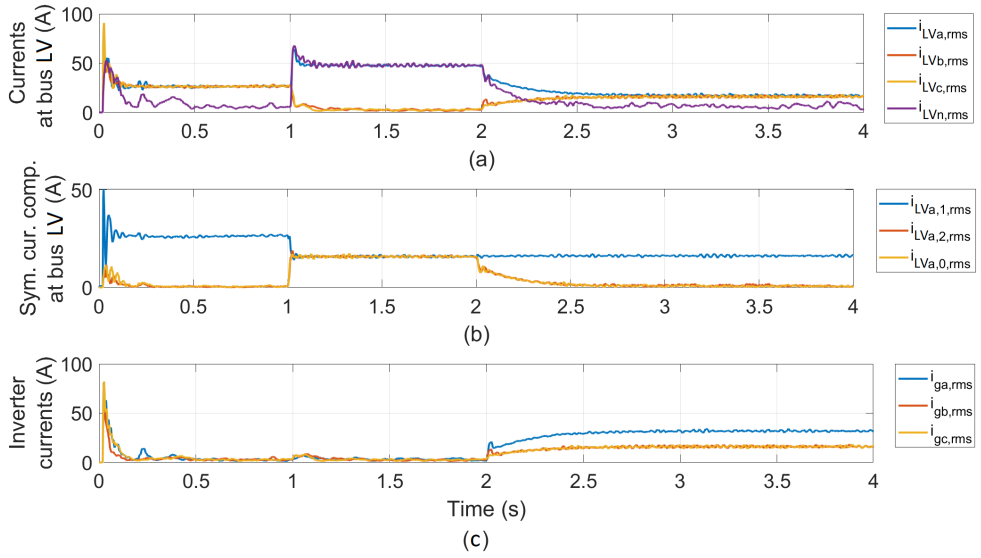

Figure F.19: rms values of (a) phase and neutral currents at bus LV (b) symmetrical current components at bus LV, and (c) inverter currents.

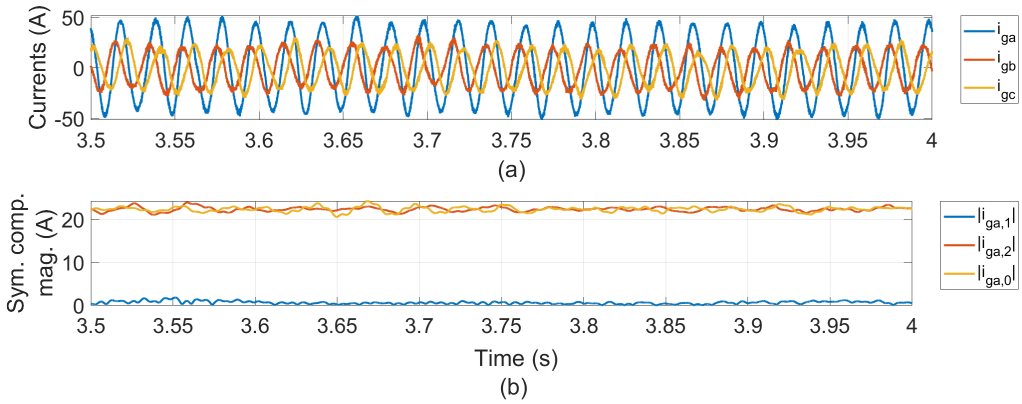

Figure F.20: Currents measured at inverter terminal (a) instantaneous values and (b) magnitudes of their symmetrical components.

The results obtained when the BESS inverters operate in p-mode and q-mode are provided next:

- **p-mode**: The voltage unbalance factor is not affected by the active power injection/absorption.
- **q-mode**: Similar results with those obtained in this Section F.8 are obtained.

F.9 Case C_{4s} (pq–mode): [20 0 0] kVA

Finally, a mixed resistive-inductive load is considered. The voltage unbalance factor is reduced from 4.15 % to 1%. Figure F.21 shows that since the provision of active power is prioritized, the injected reactive power of phase-a inverter is limited. As a result, the total reactive power of the inverters is negative, as shown in Figure F.22. Therefore, the reactive power flows will not fully converge, as can be observed from Figure F.23.

In addition, Figure F.24(b) shows that the negative- and zero-sequence current components are not fully compensated. As a result, there is a considerable amount of current flowing to the transformer's neutral conductor, as depicted in Figure F.24(a).

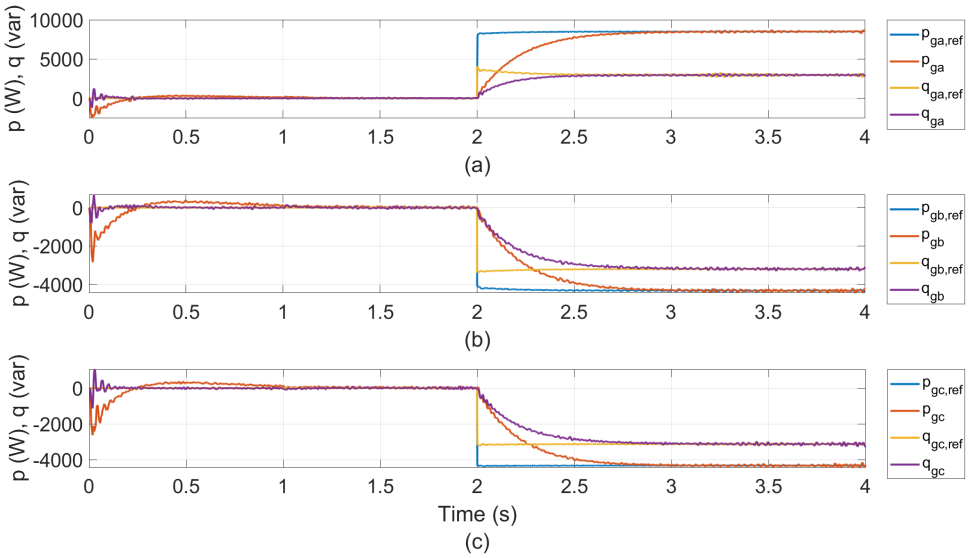

Figure F.21: Reference and measured active and reactive power at the terminal of each inverter: (a) phase-a, (b) phase-b and (c) phase-c.

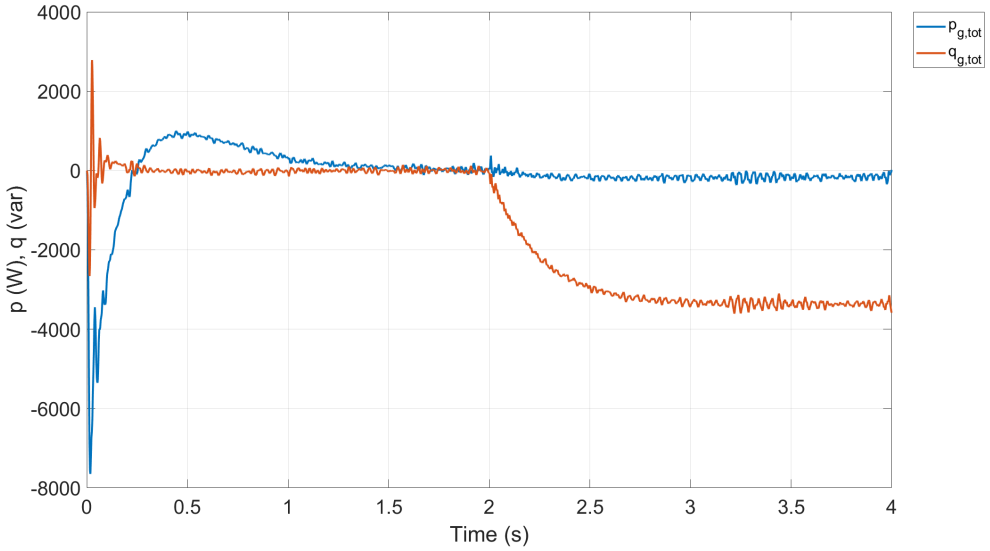

Figure F.22: Sum of active and reactive power measured at the terminals of the three inverters.

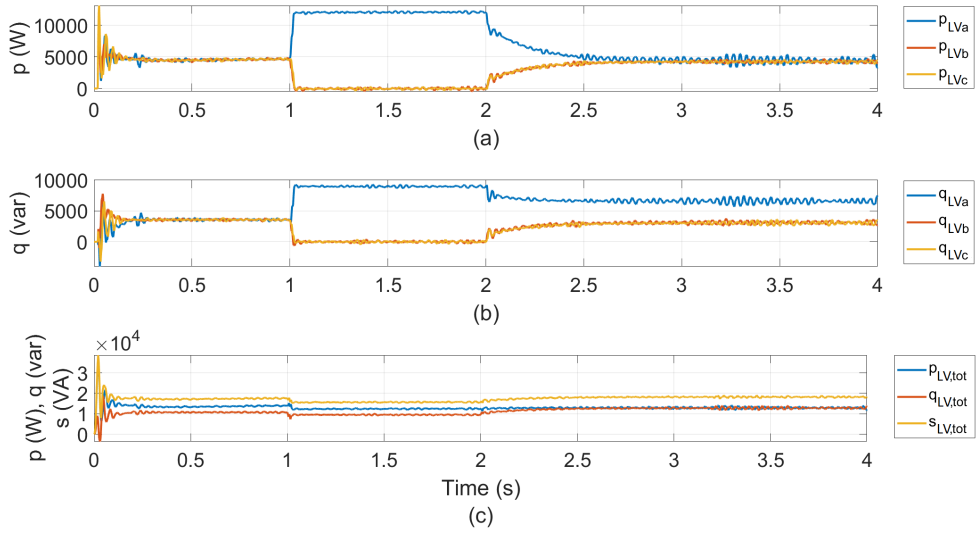

Figure F.23: (a) Active and (b) reactive power at each phase, and (c) total active, reactive and apparent power measured at bus LV.

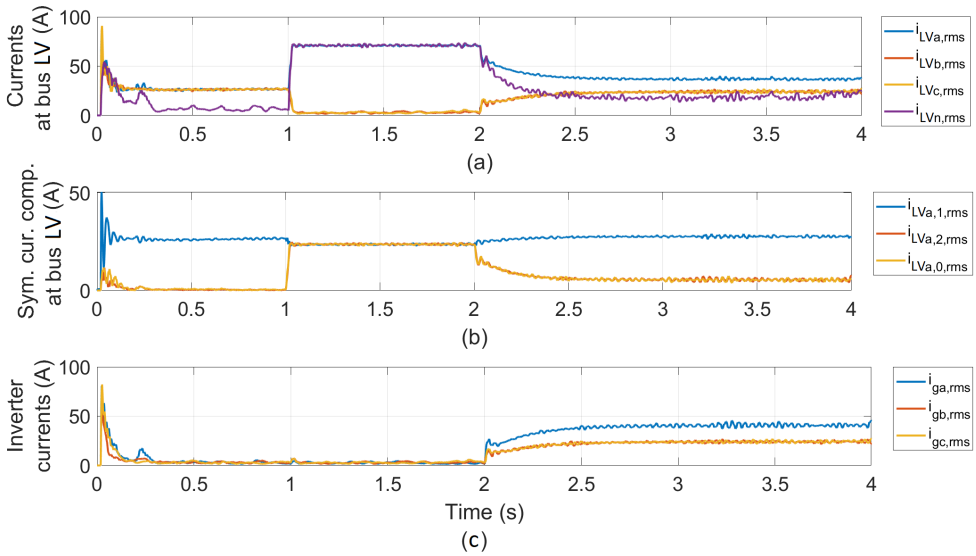

Figure F.24: rms values of (a) phase and neutral currents at bus LV, and (b) symmetrical current components at bus LV, and (c) inverter currents.

The results obtained when the BESS inverters operate in p-mode and q-mode are provided next:

- **p-mode**: The value of k_{v2} is similar to that obtained for the base case of case C4q.
- **q-mode**: The value of k_{v2} is similar to that obtained for the base case of case C4p.

F.10 Formulation of reference apparent powers for the case when the unbalance is at one phase

In this section, the formulas of the reference apparent powers are derived for the case when the unbalance is at one phase (such as in case 1 examined in Chapter 4). It is shown that under this unbalanced operating condition, the BESS units connected at the other two phases contribute to voltage unbalance mitigation with the same amount of apparent power.

The power exchanged between the three BESS units and the grid under steady state conditions are given from (3.6)-(3.8). If the positive-sequence components of phase-a and phase-c inverter voltage are expressed as a function of phase-b voltage, i.e. $\boldsymbol{V_{ga1} = aV_{gb1}}$ and $\boldsymbol{V_{gc1} = a^2 V_{gb1}}$, the above formulas can be rewritten as follows:

$$\boldsymbol{S_{a,ref} = -V_{gb1}(aI^*_{f2} + aI^*_{f0})} \tag{F.1}$$

$$\boldsymbol{S_{b,ref} = -V_{gb1}(a^* I^*_{f2} + I^*_{f0})} \tag{F.2}$$

$$\boldsymbol{S_{c,ref} = -V_{gb1}(I^*_{f2} + a^2 I^*_{f0})} \tag{F.3}$$

Based on Eq. (3.1), the negative- and zero-sequence components of the load current are expressed as:

$$\boldsymbol{I_{f2} = \frac{1}{3} I_{fa} + a^2 I_{fb} + aI_{fc}} \tag{F.4}$$

$$\boldsymbol{I_{f0} = \frac{1}{3} I_{fa} + I_{fb} + I_{fc}} \tag{F.5}$$

For the operating condition examined in case 1 of Chapter 4, phase-b and phase-c loads dissipate the same amount of power, i.e.:

$$\boldsymbol{I_{fc} = a^2 I_{fb}} \tag{F.6}$$

Substituting (F.6) into (F.4)-(F.5), it is found that the two symmetrical components are equal, and they can be expressed as follows:

$$\boldsymbol{I_{f2} = I_{f0} = \frac{1}{3}[I_{fa} + (a^2 + 1) I_{fb}]} \tag{F.7}$$

Substituting $\boldsymbol{I_{f0} = I_{f2}}$ into (F.1)-(F.3), the apparent power references can be expressed as a function of the negative-sequence current component:

$$\boldsymbol{S_{a,ref} = -V_{gb1} I^*_{f2}(2a)} \tag{F.8}$$

$$\boldsymbol{S_{b,ref} = -V_{gb1} I_{f2}^{*}(a^{*} + 1)} \tag{F.9}$$

$$\boldsymbol{S_{c,ref} = -V_{gb1} I_{f2}^{*}(a^{2} + 1)} \tag{F.10}$$

Since $\boldsymbol{a^{*} = a^{2}}$, it can be deduced that phase-b and phase-c BESS units exchange the same amount of apparent power with the grid. By adding (F.8)-(F.10), the following expression is obtained for the sum of the apparent power references:

$$\boldsymbol{S_{g,tot} = -2V_{gb1} I_{f2}^{*}(a + a^{*} + 1)} \tag{F.11}$$

Since $\boldsymbol{a + a^{*} + 1} = 0$, the total apparent power exchanged between the BESS and the system will be zero.